

THE SEASONAL BEHAVIOR OF WATER VAPOR
IN THE MARS ATMOSPHERE

Thesis by

Bruce Martin Jakosky

In Partial Fulfillment of the Requirements

for the Degree of

Doctor of Philosophy

California Institute of Technology

Pasadena, California

1983

(submitted 14 September 1982)

Copyright 1982
Bruce Martin Jakosky
All Rights Reserved

To my parents.

Acknowledgements

I would like to thank C.B. Farmer for stimulating my interest in Mars water and for guiding me via lively discussions throughout much of this investigation; A.P. Ingersoll for many useful discussions, for providing some much-needed insight into atmospheric physics, and for encouraging me to go as far as possible in this work; and R.W. Zurek for always being willing to spend time discussing the relevant physics or the results of this work and for being sufficiently (but not too) skeptical. I am grateful to each of them also for reading and commenting on an early draft of this thesis.

P.E. Doms provided invaluable assistance in the initial stages of this work, R. Mehleman aided in understanding and using the computer, and L. Wainio assisted in reducing some of the data, and I thank them for their assistance.

I am grateful to E. Barker for providing me with results of his unpublished observations of Mars water vapor, and to F.D. Palluconi, D.A. Paige, P.R. Christensen, and T.Z. Martin for many hours of useful discussions.

Additionally, the support provided by fellow students Todd (and Maria), Randy, Eric, Wings, Judy, Alan (ARP), Lucien, Carolyn, Mike, and Jon, and former students Tony, John, Jobea, Quinn, and Alan (ARG) is gratefully acknowledged.

K. Campbell deserves credit for guidance and assistance during my five years at Caltech, and D. Lathrop for patiently and efficiently typing this thing.

Finally, I would like to express my appreciation to H.H. Kieffer for stimulating my interest in planetary science and for providing an initial opportunity to pursue it in research, and to D.O. Muhleman for his constant encouragement, for innumerable discussions on all topics, and for showing me by his example about being a good scientist.

This work was funded in part by the National Aeronautics and Space Administration through the Mars Data Analysis Program. Parts of this dissertation have been published previously in the *Journal of Geophysical Research*.

Abstract

Understanding the evolution of volatiles on Mars requires understanding the processes which are currently acting to cause exchange between the various reservoirs on annual and longer timescales. On the seasonal timescale, exchange of water can occur between the atmosphere and reservoirs of ice in the polar caps and of adsorbed water in the near-surface regolith covering the remainder of the planet. This exchange is driven by the seasonally-varying insolation and its consequent effects on the surface and subsurface temperatures and on the advance and retreat of the predominantly-CO₂ polar caps. On a longer timescale, exchange can occur between these same reservoirs, and is driven by the changing annual insolation patterns which result from the 10⁵-year timescale variations in Mars' orbital elements (predominantly the orbital obliquity). Observations of the seasonal water cycle and its variations from year to year from the Viking spacecraft and from Earth provide clues as to the importance of the various reservoirs and provide boundary conditions against which models of the various processes can be compared.

The water vapor content of the Mars atmosphere was measured from the Viking Orbiter Mars Atmospheric Water Detectors (MAWD) for a period of more than one Martian year, from June, 1976, through April, 1979, and the results are presented here. The data reduction incorporates spatial and seasonal variations in surface pressure, and supplements earlier published versions of less-complete data. Column abundances vary between zero and about 100 precipitable microns (pr μm), depending on location and season, while the entire global abundance varies seasonally between an equivalent of about 1 and 2 km³ of ice. The first appearance of vapor at non-polar latitudes as northern summer approaches, and the drop in abundance at mid-latitudes as summer ends, both strongly imply the existence of a seasonal reservoir for water within

the regolith. There appear to be no net annual sources away from the poles that contribute significant amounts of water. However, the strong annual gradient of vapor from north to south implies a net annual flow of vapor toward the south; this southward flow may be balanced in part by a northward flow during the global dust storms, by transport in the form of clouds or adsorbed onto dust grains, or during other years. The perennially-cold nature of the south-polar residual cap, along with the relatively large summertime vapor abundances over the cap, implies a net annual condensation of vapor onto the cap. Estimates are made of the southward transport, and are consistent with the movement of ice being important in the formation and evolution of the polar layered terrain, and with the formation of the individual layers at the rate of one per obliquity cycle (10^5 years).

The global distribution of the annual average abundance of vapor is found to correlate well with Martian topography, as might be expected for a uniform constant atmospheric mixing ratio. If this topographic effect is divided out, the resulting residual map correlates with maps of surface albedo and thermal inertia; this correlation may be related to the control exerted by the surface and subsurface temperatures on the adsorption/desorption process and on the atmospheric temperature profile and, hence, the vapor holding capacity of the atmosphere.

The vertical distribution of vapor within the atmosphere is inferred through comparison of the observed water vapor abundances with measurements of atmospheric temperatures. In order to not saturate, the vapor must be confined to the lowermost 1 to 3 scale heights (~ 10 - 30 km), with this height varying with location and season. Near-surface water vapor can condense out overnight and form a morning fog; estimates of the optical thickness of the resulting fog are made, and they agree well with observations of

diurnal variations of opacity due to fog formation.

Previous Earth-based near-infrared observations are re-interpreted here; they show that water ice condenses out onto the seasonal polar caps, but not during midday near the equator. Earth-based observations of the vapor column abundance are compared with the Viking MAWD results, and indicate that the seasonal cycle shows a remarkable repeatability, except during 1969 when large vapor abundances were present during southern summer. This difference is explained by postulating that all of the CO_2 had sublimed off of the south residual cap that year, exposing the underlying water cap which would subsequently sublime and produce large amounts of atmospheric vapor; the rate and amount of CO_2 sublimation may depend on the degree of dust storm activity each year and hence on the different thermal loads placed on the cap.

The possible processes for producing seasonal changes in the atmospheric vapor abundances have been modeled in order to infer the relative importance of each process in the seasonal cycle. The equilibrium between water vapor and water adsorbed onto the regolith grains is sufficiently temperature-dependent that seasonal surface temperature variations are capable of driving a large exchange of water between the atmosphere and subsurface. For the likely range of regolith properties, this exchange is found to be from 10-150% of the observed seasonal change in atmospheric abundance; the differences between this exchange and the observed behavior result from transport of vapor due to the atmospheric circulation. Due to the latitudinal gradient of atmospheric vapor, there will also be a gradient of adsorbed water, with the south regolith containing much less water than that in the north; this gradient in the regolith will result independent of the vapor diffusivity in the regolith, as the near-surface water will be able to equilibrate on some timescale.

Models have been constructed which include regolith exchange, polar cap formation, and atmospheric transport. Comparison of the model results with the vapor observations and with other data regarding the physical nature of the surface allows constraints to be placed on the relative importance of each process. The models are capable of satisfactorily explaining the gross features of the observed behavior using plausible values for the regolith and atmosphere mixing terms. In the region between the polar caps, the regolith contributes as much water to the seasonal cycle of vapor as does transport in from the more-poleward regions, to within a factor of two. Globally, 10-50% of the seasonal cycle of vapor results from exchange of water with the regolith, about 40% results from the behavior of the residual caps, and the remainder is due to exchange of water with the seasonal caps. It is difficult to determine the relative importance of the processes more precisely than this because both regolith and polar cap exchange of water act in the same direction, producing the largest vapor abundance during the local summer. The system is ultimately regulated on the seasonal timescale by the polar caps, as the time to reach equilibrium between the atmosphere and regolith or between the polar atmosphere and the global atmosphere is much longer than the time for the polar caps to equilibrate with the local atmosphere. This same behavior will hold for longer timescales, with the polar caps being in equilibrium with the insolation as it changes on the obliquity timescale, and the atmosphere and regolith following along.

TABLE OF CONTENTS

Acknowledgements	iv
Abstract	vi
List of Figures	xii
List of Tables	xv
Chapter I Introduction	1
Chapter II Observations of the Seasonal Cycle of Water on Mars	8
II.A. Viking MAWD Observations of Atmospheric Vapor	10
1. Introduction	10
2. Data Reduction Technique	12
3. Global and Seasonal Vapor Behavior	19
a. Global data set	19
b. Evidence for seasonal reservoirs	34
c. The polar caps	38
d. Behavior at specific sites	39
4. Annual-Average Water Vapor Distribution	47
a. Annual-average map	47
b. Comparison with topography	53
c. Latitudinal gradient and net transport of water	65
d. Comparison with surface thermophysical properties	67
II.B. The Saturation State and Vertical Distribution of Water Vapor in the Mars Atmosphere	80
1. Introduction	80
2. The Vertical Distribution of Vapor	85
3. Early-morning Ground Fogs	95
4. Discussion	102
II.C. Interannual Variability of the Seasonal Cycle	105
1. Introduction	105
2. Mariner 9 Observations of Atmospheric Vapor	107
3. Earth-based Observations of Atmospheric Vapor	110
4. Discussion	130
5. Conclusions and Summary	134
II.D. Near-Infrared Observations of Surface Water Frost	135
1. Introduction	135
2. The Polar Caps	136
3. The Equatorial Regions	141

Chapter III The Role of Seasonal Reservoirs in the Mars Water Cycle	148
III.A. Seasonal Exchange of Water with the Regolith	149
1. Introduction	149
2. Regolith Diffusion and Adsorption	152
3. One-dimensional Model for Seasonal Exchange	162
4. One-dimensional Model with Boundary Conditions	181
5. Discussion	191
III.B. Coupled Models of the Regolith, the Polar Caps, and Atmospheric Transport	193
1. Introduction	193
2. Estimates of Global Atmospheric Mixing Times	195
3. Mid-latitude and Equatorial Processes and Models	200
4. Global Processes and Models	211
5. Discussion	237
Chapter IV Concluding Remarks	241
Bibliography	249

List of Figures

Chapter II, Section A

1. The temporal coverage obtained by the Viking MAWD instrument.	20
2. Observed water vapor abundance in each 10° latitude strip as a function of Martian season.	21
3. The latitudinal behavior of water vapor abundance at each period.	23
4. Cross-plot of the water vapor abundance versus albedo during period 10.	26
5. Contour plot of water vapor abundance as a function of season and latitude.	30
6. The global vapor content of the atmosphere as a function of L_s	32
7. The seasonal behavior of vapor over several specific sites.	41
8. Contour maps of annual average vapor abundance and of the same divided by airmass.	48
9. Averaging scheme for producing Figure 8.	51
10. Latitudinal behavior of annual average vapor abundance and of the same divided by airmass.	54
11. Global map of airmass.	57
12. Cross-plot of annual average vapor abundance versus airmass.	61
13. Global maps of the surface albedo and thermal inertia.	68
14. Cross-plot of annual average vapor abundance/airmass versus thermal inertia.	72
15. Cross-plot of annual average vapor abundance/airmass versus albedo.	74
16. Cross-plot of thermal inertia versus airmass.	76

Chapter II, Section B

17. Atmospheric temperature structure at 20° latitude and $L_s = 100^\circ$	82
18. Atmospheric structure observed by Mariner 9, $L_s = 43$ to 54°	86
19. Observed T_{15} and $T_{saturation}$ at different latitudes and seasons.	90

20. The height to saturation, h , at different latitudes and seasons.	92
21. Global maps of fog density for several seasons.	97

Chapter II, Section C

22. Earth-based observations by Barker plotted versus Viking MAWD observations made at the same time.	112
23. The same as Figure 22, except that data obtained within a span of several days were averaged together.	115
24. The seasonal variation of vapor as would be seen from Earth if the global distribution of vapor was like that seen by Viking.	118
25. Comparison of the Earth-based seasonal variation predicted from Viking data with PPCM observations made from Earth.	120
26. Observed latitudinal distribution of vapor at nine seasonal periods, 1972-1974.	127

Chapter II, Section D

27. Behavior of B , R_1 and R_2 at the south polar cap edge, as observed by the Mariner 6 and 7 IRS.	142
28. Composite Mars surface spectra obtained by McCord et al. and of a surface composed of water ice.	145

Chapter III, Section A

29. Adsorption isotherms for basalt and montmorillonite.	150
30. Seasonal surface temperature variations, as predicted by the thermal model of Kieffer et al. (1977).	164
31. Results of the 1-D model for regolith exchange, varying only D	171
32. Results of the 1-D model for regolith exchange at $\pm 25^\circ$ and $\pm 45^\circ$ latitude.	173
33. Results of the 1-D model for regolith exchange, keeping the amount of water adsorbed at depth constant.	175
34. Seasonal variation of amount of water adsorbed at different depths.	178
35. Contour plot of column vapor abundance, from a smooth line drawn through the data.	182
36. Results of the 1-D model using appropriate boundary	

conditions.	184
37. Latitudinal gradient of amount of water adsorbed at depth.	190
Chapter III, Section B	
38. Contour plot of the correlation coefficient comparing the mid-latitude/equatorial model with the data.	203
39. Results of the mid-latitude/equatorial model for $D = 0$ and various τ_a	204
40. Results of the mid-latitude/equatorial model for $\tau_a = 3$ and various D	206
41. The relative importance of regolith exchange and atmospheric transport in the mid-latitude/equatorial region.	209
42. Time-evolution of the global model.	214
43. Contour plot of the correlation coefficient comparing the global model with the data.	217
44. Results of the global coupled model for $D = 0$ and various values of τ_a	218
45. Results of the global coupled model for (a) $\tau_a = 2.5$ and $D = 1.0$, and (b) $\tau_a = 5.0$ and $D = 1.0$	223
46. The seasonal variation of global water abundance as observed by the MAWD and as predicted by the global model with $\tau_a = 2.5$ and $D = 1.0$	227
47. Seasonal behavior of water vapor at latitude $+55^\circ$	232
48. The relative importance of the regolith and polar caps in the global spring behavior.	235

List of Tables

1. L_e Ranges of the Period Maps.	15
2. Possible Annual-Average Distributions of Vapor.	60
3. Correlation Coefficients Obtained in Comparing Various Data Sets.	64
4. Comparison of Mariner 9 and Viking Observations of Water Vapor.	108
5. Diffusion Depths through a Porous Medium.	157
6. Diffusion Depths through an Adsorbing Porous Medium.	159
7. Results from Atmospheric Circulation Models.	196

Chapter I

Introduction

A key question regarding the evolution of volatiles on Mars centers about the behavior of its water. Although estimates indicate that enough water has been outgassed from the interior to form a layer of liquid between several tens and several hundreds of meters deep (e.g., Pollack and Yung, 1980), only an equivalent of less than several meters can be directly accounted for in the polar caps and atmosphere today, with most of that being in the caps. The presence of large channels on Mars implies that climatic conditions were different and that liquid water flowed at some time in the past, as the liquid is not stable under present conditions (e.g., Sharp and Malin, 1975). Long-term climatic change is thus implied, along with reversible or irreversible exchange of water between various locations. The nature of the polar laminated terrain also argues for exchange of water, with the individual layers being formed by intermixed deposits of dust and water ice (see Pollack, 1979, for a recent discussion). The important questions then revolve around understanding how much water has outgassed over the age of the planet, and its evolution since then regarding exchange of water between various reservoirs on all timescales.

Direct examination of the amounts of water held in various reservoirs and possibly released or exchanged during the 10^5 year timescale variations of the orbital obliquity (Ward, 1979) is not possible. Purely theoretical models of the long-term behavior (e.g., Toon et al., 1980) predict large amounts of volatiles exchanged, although tremendous uncertainties arise from a lack of knowledge of some of the relevant shorter-term behavior. One can, however, attack the problem by observing the changes in the amounts of atmospheric vapor during a single Martian year and infer from them the existence and accessibility of various sources and sinks of water on that shorter timescale. These results

would provide an important guide to predicting the long-term behavior of water.

Observations of Martian atmospheric water vapor were first made by Spinrad et al. (1963), who observed a column abundance of ~ 15 pr μm ; this amount is significant in that it indicates that the Martian atmosphere may be near saturation at some places. Since then, water vapor has been observed over a timespan of about two decades by Earth-based observers (see Barker, 1976, for a synthesis of these observations) and by the Mariner 9 IRIS experiment (Conrath et al., 1973). It wasn't until the observations by the Viking Mars Atmospheric Water Detector (MAWD) instrument (Farmer et al., 1976, 1977; Farmer and Doms, 1979; and others) that the large spatial and seasonal variability of Martian water which occurs was realized. Discussion has centered on how the atmospheric amounts vary with local time of day (Barker, 1976; Flasar and Goody, 1976; see, however, Farmer et al., 1977, and Davies, 1979a), latitude and season (Barker, 1976; Farmer and Doms, 1979; Davies, 1981). From these and other observations, inferences have been made regarding the amounts and the global distribution of water, in the form of liquid water (Ingersoll, 1970; Farmer, 1976; Brass, 1980), water of hydration (Pimental et al., 1974; Houck et al., 1973; Clark, 1978), permafrost (Fanale, 1976; Carr and Schaber, 1977; Farmer and Doms, 1979), and adsorbed water (Anderson et al., 1967, 1978; Pollack et al., 1970; Fanale and Cannon, 1974; Flasar and Goody, 1976).

To date, few attempts have been made to estimate the amounts of water in each of these phases that may exchange seasonally with the atmosphere. That some exchange does occur is evidenced by the appearance of large amounts of water vapor over the warm north polar cap during summer (Farmer et al., 1976) and by the seasonal variation of the total amount of vapor present in the entire atmosphere (Farmer and Doms, 1979). Once the seasonal cycle of

exchange is understood, analysis can be extended to the longer timescale of the changing orbital elements. Discussion at that time will center on exchange of water between the two polar caps (driven by the cyclical heating and cooling of the two caps, each one out of phase with the other) and on the long-term response of the regolith. The understanding of these long-term exchanges will in time yield an understanding of the variability of Martian climate, the total amount of volatiles which may have been outgassed, and the formation of various geologic features (including the polar layered terrain, channels and valleys, and possibly rampart craters).

In the present work, the seasonal cycle of water vapor in the Mars atmosphere will be discussed. Analysis will consist of two main parts: First, presentation, analysis, and synthesis of observations of the seasonal cycle of water vapor, including implications for the seasonal exchange of water between various seasonally-accessible reservoirs. Second, modeling of the possible processes which may be controlling the water cycle, and a discussion of the contributions of each possible process and reservoir to the entire global and seasonal cycle. The candidate processes for controlling the seasonal behavior of water include: buffering of the atmospheric water by a surface or subsurface reservoir of ground ice (Farmer and Doms, 1979; Davies, 1981), physically adsorbed water (Anderson et al., 1967, 1978; Pollack et al., 1970; Fanale and Cannon, 1974), or chemically-bound water (Clark, 1978); supply of water from the residual or seasonal north polar ice cap (see Davies et al., 1977; Davies, 1981); redistribution of the vapor resulting from atmospheric circulation; and control of the vapor holding-capacity of the atmosphere by the local atmospheric temperatures (see Davies, 1979b). All of these processes are probably important at some locations and on some timescales.

The most complete information regarding the seasonal and spatial variability of water vapor over the course of a Mars year comes from observations of water vapor made by the Viking MAWD experiment, presented in complete form for the first time in Chapter II.A. Observations extended over nearly the entire planet for longer than a Mars year, and provided less-complete coverage for an additional year. Analysis of these data, also in Chapter II.A, allows inferences to be made about the possible seasonal sources and sinks for water vapor and the relative importance of some of the processes which may be responsible for the variations. The completeness of the data allows a quantitative comparison between the vapor abundance and various global properties which may exert some control over the vapor; these properties are the local topography, and the thermal inertia and albedo of the surface. Previous analysis of the water vapor data has concentrated on presentation of the data itself (Farmer et al., 1977). Farmer and Doms (1979) do discuss the implications of the observations for possible equilibrium of atmospheric vapor with subsurface permafrost or ice, but are only able to delimit those locations where ice may be present. The analysis here extends the work of Farmer and Doms in terms of more-detailed comparisons and possible alternative viewpoints.

By examining the relationship between the water vapor abundances and the observed atmospheric temperatures, information can be gained about the vertical distribution of the vapor and the degree of saturation of the atmosphere (Chapter II.B). This section builds on the work of Hess (1976), who used models of the atmospheric temperatures to constrain where the water could be without saturating and forming clouds; the models erred in not including the radiative effects of airborne dust, so yielded temperatures which were too low. Davies (1979b) compared the observed vapor abundances with

temperatures obtained by radio occultation, but suffered from a lack of good coverage in space and time. In this section, thermal observations from Viking provide excellent spatial and temporal coverage. Useful comparisons can then be made and results obtained regarding the vertical distribution of vapor and possible saturation of the atmosphere at night at the surface and at high altitudes.

Comparison of the observations of vapor made by the Viking MAWD with those made by Earth-based observers allows the time-base of information to be extended to nearly two decades, and provides information regarding the year-to-year variability of the water cycle (Chapter II.C). This analysis makes use of previously published Earth-based observations (Barker, 1976) along with unpublished data obtained more recently (E. Barker, personal communication, 1981), and provides the basis for conclusions to be drawn regarding the behavior of water vapor over the course of a half dozen Mars years. Additionally, Earth-based observations of the near-infrared reflectance of Mars have been previously interpreted in terms of the possibility of water ice being present on the surface or incorporated into the polar caps; these observations are discussed and critically reviewed in Chapter II.D.

All of the above observations can serve as boundary conditions or constraints for numerical models of the processes which may be controlling the water cycle. Some simple (and not so simple) models of these processes are constructed and presented in Chapter III. The processes explicitly considered include seasonal exchange with a subsurface reservoir of adsorbed water, exchange with the seasonal and residual polar caps, and transport in the vapor state resulting from the atmospheric circulation. Seasonal exchange with a regolith reservoir of sorbed water has been previously suggested by Anderson et al. (1967, 1978), Pollack et al. (1970), and Fanale and Cannon (1974) based on

experimental measurements of the sorptive properties of candidate surface materials; exchange with the polar caps has been discussed by Leovy (1973) based on the circulation of the atmosphere, and by Farmer et al. (1976) based on observations of polar water vapor; only Leovy (1973) and Leighton and Murray (1966) have considered transport of water vapor through the atmosphere in any detail. While the physics of the adsorption/desorption process is included directly into the models, the transport through the atmosphere is taken to be diffusive and exchange of water with the polar caps is parameterized and governed by the surface temperatures. The possible processes which are not considered are transport of water through the atmosphere in the form of clouds or sorbed onto airborne dust, exchange with subsurface ice deposits (except as the discussion of adsorbed water indicates that ice will form when all of the adsorption sites are filled), or transport horizontally through the regolith. Results of the several models will allow an understanding as to how each of the processes may affect the water cycle and as to the possible suite of physical properties of the atmosphere and surface. Coupled models are constructed, which contain all of the processes acting in parallel, and allow discussion of the relative importance of each of the processes to the entire water vapor cycle and of the ability of each possible reservoir for water to exchange seasonally with the atmosphere. It will be seen that the basic processes considered here can readily account for the observed global and seasonal behavior of the water. Some of the implications for longer timescale behavior will also be addressed.

The final chapter contains a summary of the discussion and conclusions regarding the seasonal water cycle. Additionally, ideas are presented for possible future modeling, analysis, and observations (both Earth-based and from spacecraft) that will serve to further illuminate the nature of the Mars atmospheric water vapor cycle and climate.

Chapter II

Observations of the Seasonal Cycle of Water on Mars

The seasonal and global cycle of water on Mars has been observed by many techniques over the last thirty years. Detection of atmospheric vapor was first made spectroscopically by Spinrad et al. (1963). Subsequently, data were obtained from Earth covering the entire range of Martian seasons (e.g., Barker, 1976). Vapor abundances were measured and mapped from experiments aboard the Mariner 9 and Viking spacecraft, respectively (e.g., Conrath et al., 1973; Farmer and Doms, 1979; and others). In the latter, relatively complete coverage was obtained both spatially and temporally. Near-infrared spectral measurements have also been made, both from spacecraft (Pimentel et al., 1974) and from Earth (e.g., Moroz, 1964; McCord et al., 1982), and have been interpreted in terms of the presence of water frost on the surface.

All of these observations serve to place constraints on the annual cycle of water on Mars and on the possible exchange between the various seasonal reservoirs. In this chapter, the various observations will be discussed, and implications for the seasonal reservoirs inferred. In Section A, data regarding atmospheric vapor, obtained from the Viking orbiter MAWD experiment, are presented, covering the complete seasonal cycle at most locations on the planet, and interpreted in terms of the seasonal cycle. Some of the implications regarding the vertical distribution of the vapor and its possible saturation at some locations and seasons are discussed in Section B. The year-to-year variations in the seasonal cycle are seen in Section C, in which comparison of the Viking data with earlier Mariner 9 and Earth-based observations is made. In Section D, previous near-infrared spectral measurements are reviewed, along with their possible interpretation regarding water ice.

While detailed numerical modeling of the various processes responsible for the seasonal cycle must play an important role in the analysis, discussion in this chapter is limited to the observations and what can be deduced from them directly. Models of some of the processes, and implications regarding the relative importance of seasonal exchange of water between the regolith, atmosphere, and polar caps, will be discussed in Chapter III.

II.A. Viking MAWD Observations of Atmospheric Vapor

1. Introduction

Observations of the column abundance of atmospheric water vapor, made from the Viking orbiters, extend over a time period greater than a Martian year and provide nearly global coverage of Mars for much of that time. These data provide valuable boundary conditions against which various models of the seasonal cycle can be compared. Inferences can also be made directly from the observations regarding the possible importance of those processes which may be controlling the vapor behavior on a seasonal basis. The possible processes include buffering of the atmospheric vapor by reservoirs of water in the regolith, supply of water from the polar caps, transport of water due to the atmospheric circulation, and control by the capacity of the atmosphere for holding vapor.

The MAWD instrument is described briefly in the next section of this chapter, along with details of the data reduction techniques and the possible errors and uncertainties in the data. The section following contains the basic results of column abundance of vapor as a function of location and season. Although Farmer et al. (1977), Farmer and Doms (1979), and Davies (1981) discussed earlier reductions of various subsets of this data, the entire global data set is discussed here, incorporating for the first time both spatial and seasonal variations in atmospheric pressure. The analysis of the data presented here goes beyond that in earlier papers by making quantitative arguments regarding the implications for seasonal storage of water, and by presenting new ideas concerning the seasonal and spatial behavior of the vapor. The seasonal behavior of water vapor over the Viking landing sites and over the classical feature Solis Lacus is also discussed.

In the fourth section, the water vapor distributions are compared with

the distribution of properties which might be exerting control on the water: the surface topography and the albedo and thermal inertia of the surface. Regardless of which of the above-mentioned mechanisms dominates the seasonal water cycle, the surface properties are expected to play a role; the reasons are discussed in this section along with the data comparisons.

2. Data Reduction Technique

The Viking Orbiter MAWD instruments are reflectance spectrometers observing in five channels at wavelengths of about $1.38 \mu\text{m}$ (see Farmer and La Porte, 1972, and Farmer et al., 1977, for a detailed discussion of the instrument and observations). Operating in this spectral region, the results do not depend on the atmospheric temperature extant, except insofar as it affects the shapes of the water absorption bands. Three of the channels are centered on water vapor absorption lines while the other two are located in adjacent continuum regions. Ideally, the use of three vapor channels should allow a unique determination of the vapor column abundance and of the effective pressure and temperature of the region in the atmosphere in which the vapor resides. In practice, however, the noise in the observations does not allow a sensitive determination of P and T and these values are input in order to derive the vapor abundance. A temperature of 200 K is used universally. Using the Curtis-Godson approximation and assuming uniform vertical mixing of the vapor, a value of one-half the local surface atmospheric pressure is used for the effective pressure of line formation; this takes into account the effects of the spatial variation of topography (U.S. Geological Survey, 1976) and the seasonal variation of surface pressure (Hess et al., 1979). Although dynamical phenomena will affect the surface pressure (e.g., Leovy and Mintz, 1969; Conrath et al., 1973), this effect will be relatively small and is ignored. If the vapor is not distributed uniformly vertically then the pressure used in the calculations differs from the actual effective pressure, and the derived water abundances will be in error. The conclusions reached in the present analysis will not be affected by this because the relative abundances would not change significantly (see below).

Atmospheric dust will modify the observed column abundances because dust will scatter some of the incident sunlight, such that the observed radiation will not have sampled the entire column of atmosphere equally (Farmer et al., 1977; Davies, 1979a). This will result in observed vapor abundances which are less than the actual column abundances. Davies' (1979a) empirical model of scattering by airborne dust predicts that a normal extinction opacity of 0.5 will result in derived vapor abundances about 10% less than actual for an observational airmass of 3 (the observational airmass is $1/\cos(\text{emission angle}) + 1/\cos(\text{incidence angle})$), with a lesser effect at lower airmass. An opacity of 1.0 would only reduce the observed vapor abundance by about 20%. For about half of the Martian year, the opacity at the Viking landing sites is less than 0.5, and it is seldom greater than 1.0 except during the global dust storms (Pollack et al., 1979). It is found that the distribution of observing geometries is such that the derived vapor abundances are essentially unaffected by dust as long as both the incidence and emission angles are separately restricted to values less than 60° , except during the global dust storms (Farmer et al., 1977; Farmer and Doms, 1979). Systematic effects may occur for observations at high latitudes, where larger observing angles may have affected some of the vapor determinations.

During southern summer, local dust clouds of limited extent and high opacity ($\tau \gg 1$) are observed even when there is no simultaneous global storm (Briggs et al., 1979; Peterfreund and Kieffer, 1979). Only a small number of such events were observed, each one only several hundred kilometers in size, such that they will be unimportant with respect to the global or zonally-averaged vapor observations. They will, however, affect the observations of specific regions, yielding observed vapor abundances less than the amount actually present. Except for the local storms associated with the retreating polar cap

boundary, those storms which were observed occur almost exclusively during the time period near perihelion, when the global dust storms occurred (Peterfreund and Kieffer, 1979). As will be discussed in the next section, water vapor data from this time period are largely not used in the subsequent analysis in order to avoid the effects of dust. Additionally, the locations of the local dust storms do not have storms at all times, as can be seen in the thermal mapping data of the region; even at the location of the widely-discussed Solis Planum storm (Briggs et al., 1979; Peterfreund and Kieffer, 1979) a storm is not present at all times during the southern summer and more often than not does not have a local dust cloud present during other times of year (A.R. Peterfreund, personal communication, 1982).

In the data presented here, no correction has been made for opacity. Thus, the water abundances will represent lower limits during the dusty time periods. Incidence and emission angles are restricted to values less than 60° , as already discussed. The local time of day has been restricted to values between 1000 hrs and 1600 hrs in order to reduce the effects of either diurnal variation of vapor or morning or afternoon fogs or clouds. This is done despite the absence of significant observable diurnal variation (Farmer et al., 1977; Davies, 1979a) or ubiquitous morning or afternoon clouds (Briggs et al., 1977). The time of day constraint is not centered about noon because of the expectation that morning fogs and clouds may be more significant than those in the afternoon. As in earlier presentations of the data, the Martian year is divided into twenty-four time periods, each one spanning 15° of L_s (planetocentric longitude of the sun; $L_s = 0^\circ$ at the time of the vernal equinox); the values of L_s corresponding to each period are given in Table 1. For each period map of water vapor column abundance, data are placed into spatial bins 10° in latitude by 10° in longitude. While higher spatial resolution is possible in some places and at

Table 1. L_s Ranges of the Period Maps

Period	L_s Range
1,25	80-95
2,26	95-110
3,27	110-125
4,28	125-140
5,29	140-155
6,30	155-170
7,31	170-185
8,32	185-200
9,33	200-215
10,34	215-230
11,35	230-245
12	245-260
13	260-275
14	275-290
15	290-305
16	305-320
17	320-335
18	335-350
19	350-5
20	5-20
21	20-35
22	35-50
23	50-65
24	65-80

some times, 10° bins provide for reasonably complete spatial coverage and for relatively low uncertainties in the water determinations.

Possible errors and uncertainties in the water vapor column abundances in the period maps can result from several sources. The noise in the observations produces an estimated uncertainty of the water value in each bin of, typically, 5-10% of the value, depending in part on the number of observations falling within the bin. Spatial and temporal variability of abundance within a bin appears to be generally unimportant compared to the noise of the individual observations. A more subtle effect is that all of the spatial bins are not necessarily observed at the same time during the period, due to the nature of the Viking orbit and the observational sequences, possibly producing a striping effect or a gradation of water amount with longitude on the maps. That neither of these effects seems to occur implies that they are unimportant compared to the first-order spatial and seasonal variation of water vapor abundances.

The largest uncertainty in the vapor determinations lies in the choice of the effective pressure of line formation, which is in turn dependent on the actual vertical distribution of vapor within the atmosphere. The absorption of solar radiation by water vapor is nonlinear in vapor abundance, pressure, and temperature (see Farmer et al., 1977, for examples of the curves of growth for each line), such that placing the effective height of line formation at the surface (instead of at the half-surface-pressure height, about 7 km altitude for an atmospheric scale-height of 10 km) can result in a lowering of the derived water abundance by as much as a factor of two. The effect is systematic, however, such that although absolute values of abundance would be affected, relative values would not be significantly changed. Our choice of the uniform-mixing assumption for determining the effective pressure is based on the lack of

evidence for water being concentrated nearer to the surface. Unless saturation of the vapor and condensation are occurring daily over a substantial portion of the atmospheric column, the vapor will be distributed nearly uniformly. In Chapter II.B, it will be seen that the vapor is in fact not uniformly distributed, except possibly within the lowermost 1 to 3 scale heights. The vertical range of this distribution varies as a function of both latitude and time, such that the vapor determinations here will have some unknown errors associated with them; for the water uniformly distributed within this range of 1 to 3 scale heights, however, the effective pressure will vary by only about 15%, resulting in a possible systematic uncertainty in the vapor abundance of less than 15%.

It is the assumption of the effective pressure of line formation, along with including the seasonal change of atmospheric pressure, that causes the values of vapor abundance reported here to differ somewhat from those reported in earlier papers. In the work of Farmer et al. (1977) and Farmer and Doms (1979) the spatial (but not temporal) variability of surface pressure was taken into account in the choice of the effective pressure, and the water was assumed concentrated very near the surface. That is, the effective pressure was taken as $P_e = P_0 \exp(-z/H)$, where P_0 is 6 mbar, z is the local surface elevation, and H is the assumed atmospheric scale height. In the presentation by Davies (1981), a spatially- and temporally-constant effective pressure was used, and a correction factor was applied globally to attempt to correct for the effects of atmospheric dust opacity assuming that the opacity behaves everywhere with time like that observed at the Viking landing sites by Pollack et al. (1977, 1979) and that the vapor is uniformly mixed throughout the atmosphere.

Finally, clouds will mask any water vapor beneath the cloud level. Optically-thick clouds are known to occur (Briggs et al., 1977; Smith and Smith, 1972; French et al., 1981). Even optically-thin clouds can have a marked effect if

the vapor is beneath the cloud level. This effect is systematic by always yielding water abundances less than the actual values, yet random in terms of its occurrence at specific locations or seasons (see, however, Smith and Smith, 1972; and French et al., 1981) and cannot be readily dealt with quantitatively. Clouds do not in general dominate the atmospheric behavior, however, such that masking of vapor by clouds will not usually be important.

3. Global and Seasonal Vapor Behavior

In this section, the observational results of atmospheric water vapor column abundance as a function of location and season on Mars are presented, some of the implications regarding the storage and release of water from seasonal reservoirs are addressed, and the seasonal behavior of water vapor over the polar caps, the Viking landing sites, and Solis Planum are discussed.

a. Global data set

The temporal coverage of the MAWD observations is shown in Figure 1. In this work data from the first 35 periods, from $L_s = 85^\circ$ up to almost $L_s = 245^\circ$ during the second Martian year of observations, will be discussed (see Table 1, Figure 1). The data for the first two periods and for periods 31 to 35 do not cover the entire planet; no data were taken during period 6, which corresponded to solar conjunction. Plate 1 (as presented in Jakosky and Farmer, 1982; hereafter referred to simply as Plate 1) shows color representations of the period water maps for periods 1 to 35. In the discussion below of the details visible in the maps, reference will be made to Figures 2 and 3, which show the data in a zonally averaged sense.

The two global dust storms of 1977 are evident in all three representations of the data. The storms began at $L_s \approx 205^\circ$ and 274° (Pollack et al., 1979), and can be seen as dramatic decreases in the apparent water abundance in periods 10 and 14, respectively (Farmer and Doms, 1979). The first storm actually began during period 9 but is not completely evident until the following period. The decrease in observed vapor is much more marked in the second storm (Figure 2), consistent with the larger visual opacities observed by the Viking landers (Pollack et al., 1979). Interestingly, the period 10 and 11 water maps, during the first storm, have an appearance similar to the visual

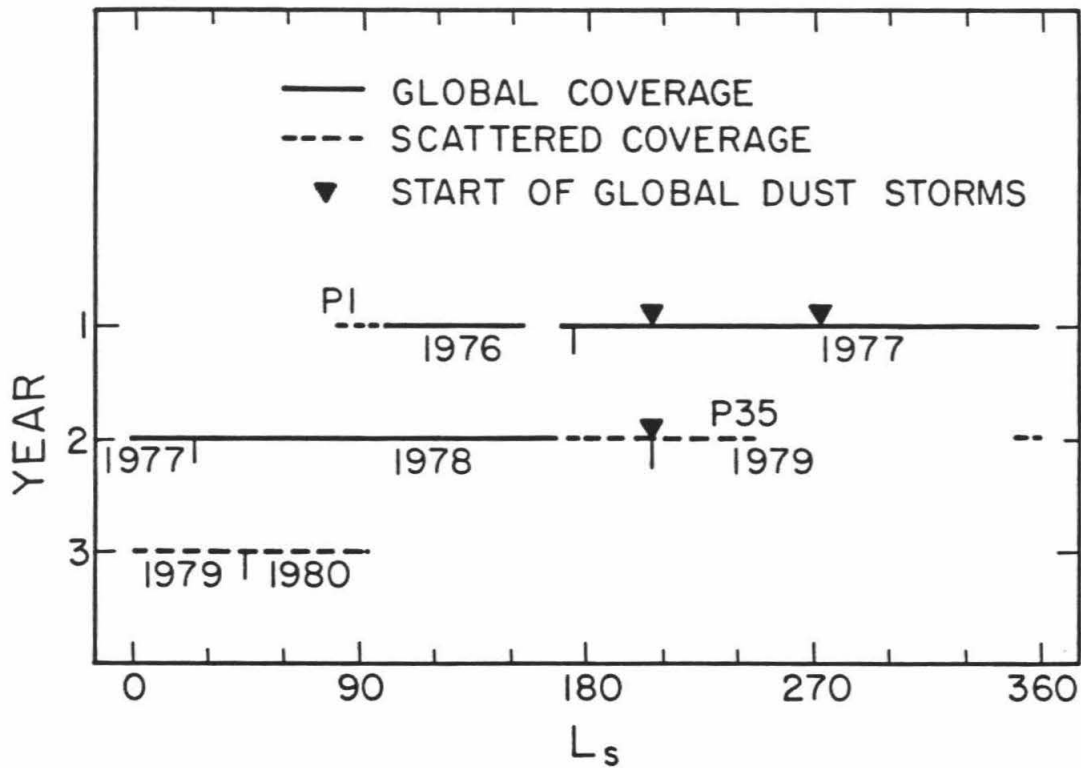


Figure 1: The temporal coverage obtained by the MAWD instrument. The times of the start of the dust storms are taken from Pollack et al. (1979) and Leovy (1981). The times of occurrence of selected periods (see Table 1) are shown, as are the Earth years.

Figure 2: Observed water vapor abundance in each 10° latitude strip as a function of Martian season. The dashed lines are data taken during the second year of observations. The arrows mark the times of the global dust storms. The horizontal lines represent the base level for each plot, and the tick marks along the ordinate are spaced $5 \text{ pr } \mu\text{m}$ apart.

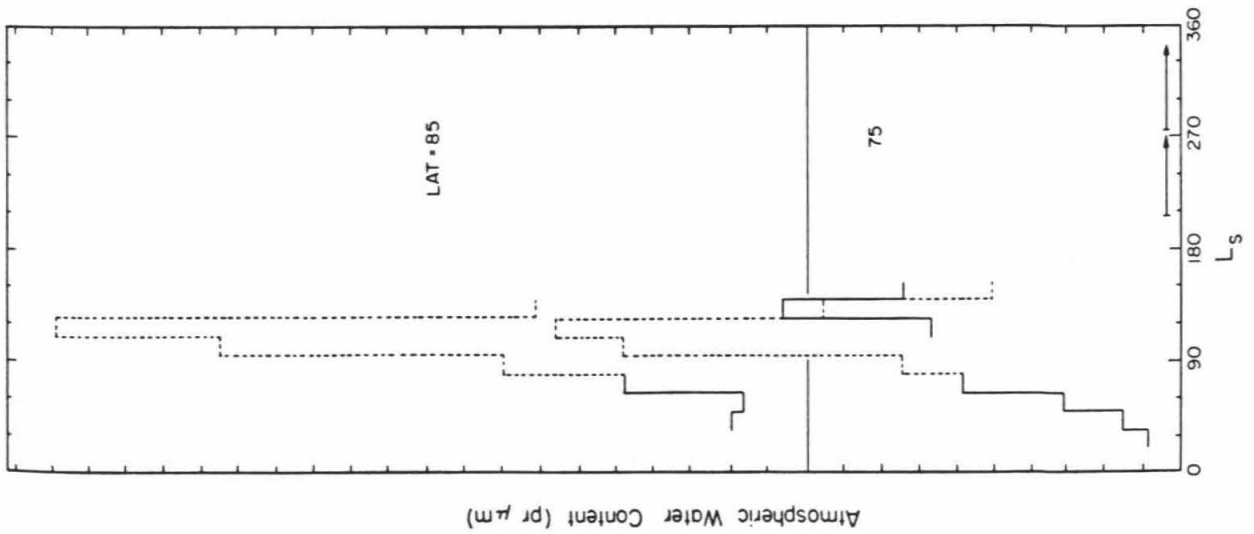
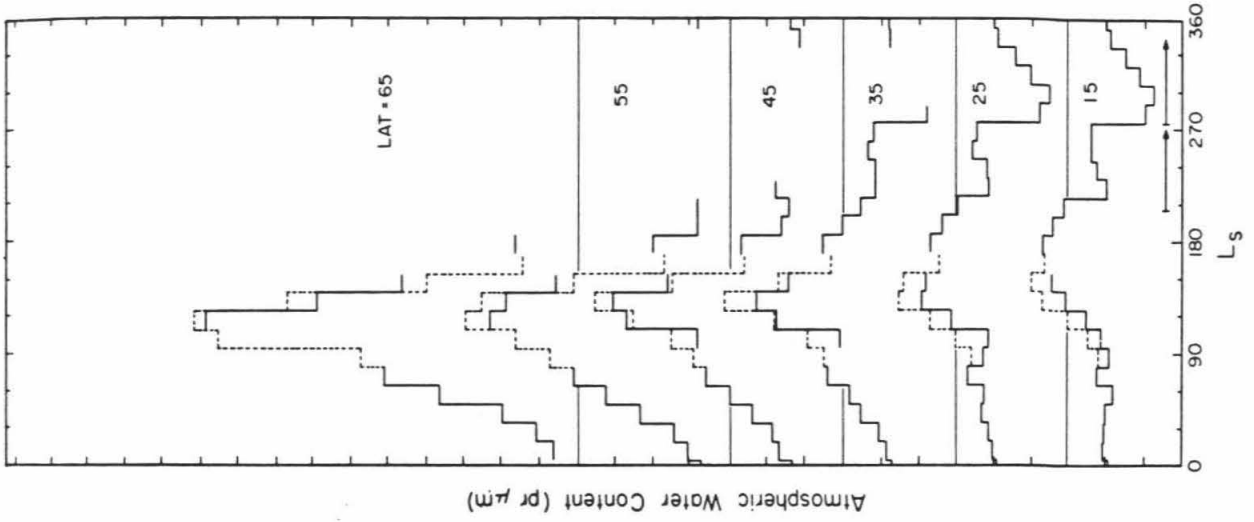
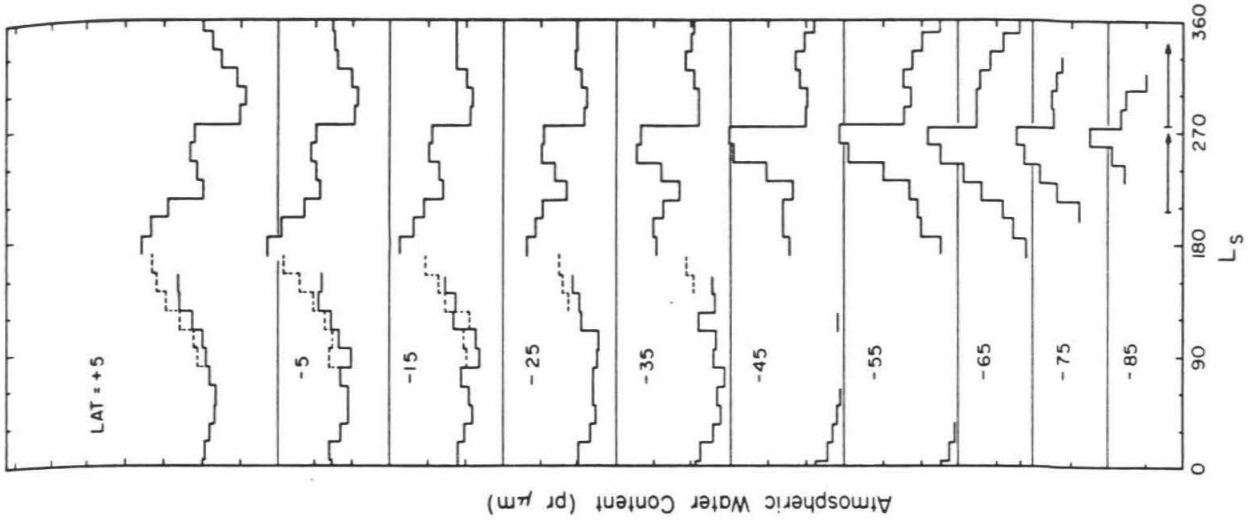
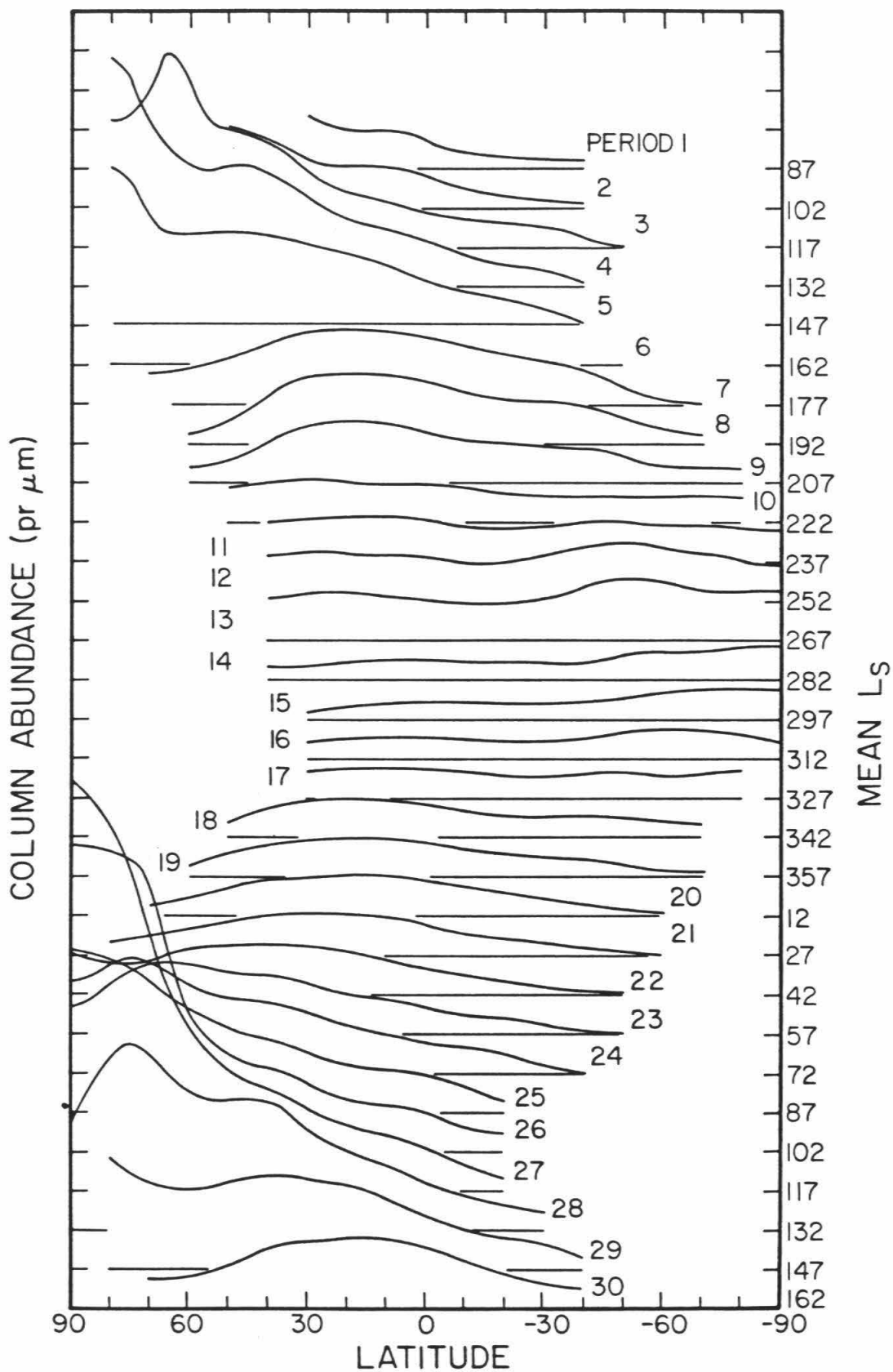


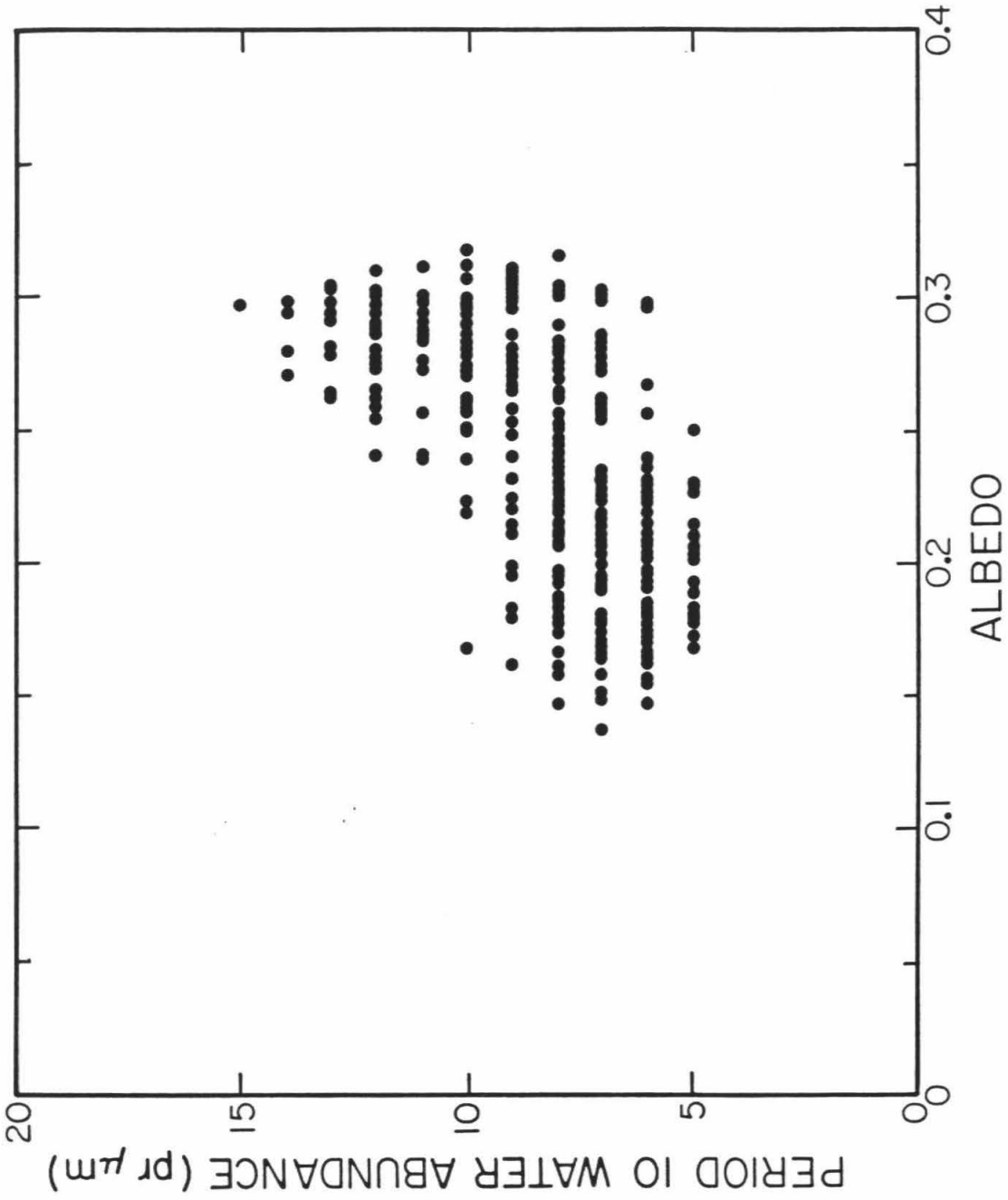
Figure 3: The latitudinal behavior of vapor abundance at each period. The horizontal lines represent the base level for each plot, and the ticks along the ordinate represent 10 pr μm each. The L_s values corresponding to each period are listed in Table 1 and the L_s value at the center of each period is shown along the right margin.



albedo map of Palluconi and Kieffer (1981) (reproduced here in Figure 13a and b), while that of period 14, during the height of the second storm, bears little resemblance. Figure 4 shows a cross plot of the period 10 water abundance versus the local surface albedo, from which this correlation is evident. At this time, more water appears over the bright surface regions than over the dark regions. This is consistent with a larger fraction of the observed radiance having been reflected from the surface in the bright regions than in the dark and hence a deeper effective sampling of the atmosphere. That is, with some of the observed radiance having been reflected off of dust in the atmosphere, varying the surface albedo will change the fraction of the observed radiance which was reflected off of the surface and which has thereby sampled the entire atmospheric column. A simple model verifies that this effect will produce a correlation like that observed, with observed water vapor abundances over bright areas being 25% or more greater than over dark areas, assuming identical actual abundances and moderate opacities due to dust; this simple model is based on the Monte Carlo calculations by Davies (1979a), and includes the effects of light scattered off of airborne dust and light reflected off of the surface, with the partitioning between the two being determined by the dust opacity and the surface albedo.

The water maps prior to the two dust storms, periods 8 and 13, respectively, show little correlation with albedo, suggesting that dust effects do not dominate the water observations at these times, although they may be present. The lack of correlation of vapor with albedo prior to each dust storm also supports our assertion that the cause of the effect here is dust-related and not representative of the actual vapor distribution. The lack of such a correlation during the height of the second storm implies that very little of the observed radiance has been reflected from the ground (i.e., that most of it is

Figure 4: Cross-plot of the water vapor abundance during period 10, during the first dust storm, versus the surface albedo.



scattered back by the atmospheric dust). Interestingly, the period 16 map, during the decay phase of the second dust storm, bears a similar resemblance to the albedo map, indicating that the dust amount has decayed sufficiently for the surface albedo to play a role in the light-scattering process. It is important to realize that when the atmosphere contains large amounts of dust, the observed flux samples only the top part of the atmosphere; when there is no dust in the atmosphere, the entire column is sampled equally at all places. Only when there is a moderate amount of dust present is the column sampled deeper over bright than over dark regions, producing a correlation of water abundance with albedo. The average dust opacity during period 10 was about 2, while that during periods 14 and 16, during the second dust storm was greater than 3 and about 2.2, respectively (Pollack et al., 1979), consistent with these ideas. Additionally, it should be pointed out that, although this albedo effect can explain the observed correlation, spatial variations of atmospheric dust content are also capable of producing such a dependence. There is no reason, however, to expect the dust content to depend on surface albedo during the dust storms. By about period 19 ($L_s \approx 360^\circ$), the second dust storm has decayed sufficiently for the dust to no longer play an important role in the measurement of the water abundances.

Each hemisphere has its maximum of vapor abundance during the local summer (see Plate 1, Figures 2 and 3). The north polar latitudes have as much as 100 pr μm of vapor at $L_s \approx 120^\circ$. More-equatorial regions peak later in the year and have less vapor at the peak; for instance, the band at $+35^\circ$ latitude peaks with about 30 pr μm at $L_s \approx 130^\circ$, while the peak at the equator (about 18 pr μm) occurs at $L_s \approx 180^\circ$. In the south, the maximum polar abundance is much less than in the north, being less than 15 pr μm , and occurs at $L_s \approx 270^\circ$ during southern summer. The actual peak southern abundance and the time at

which it occurs are difficult to determine due to obscuration by the second global dust storm.

There is a marked asymmetry during the year observed by Viking between vapor behavior in the northern hemisphere and that in the southern hemisphere, discussed earlier by Farmer and Doms (1979). The northern hemisphere maximum vapor abundances are nearly all greater than the maxima at the corresponding latitudes in the southern hemisphere. Although observations are less definitive, the same seems to hold true during local winter, with the north having more water at its minimum than does the south. This effect can be seen in Figures 5 and 6. Figure 5 again shows a zonally-averaged representation of the data and readily shows the difference between the two hemispheres.

In Figure 6 the total global abundance of water as well as the total global abundance in each hemisphere is shown as a function of season. Again, the hemispherical asymmetry is readily observed. The total abundance is seen to vary with season by a factor of two, from an equivalent of about 1 km^3 to 2 km^3 of ice. This variation is direct evidence for vapor being held in a seasonal reservoir rather than just being redistributed throughout the atmosphere with time. For comparison, Earth's atmosphere contains typically $13,000 \text{ km}^3$ of water (Trenberth, 1981); this larger abundance causes the dynamics of the Earth's atmosphere to be driven in part by the energy tied up in the water cycle. The much smaller abundance in the Mars atmosphere causes the latent heat of the water which is present to be insignificant compared to the solar input, such that the dynamics are not affected by the presence or absence of water.

Figure 5: Contour plot of vapor abundance (in μm) as a function of season and latitude. Shaded areas represent regions where no data met the geometry constraints. The arcs bound the regions of polar night. The arrows represent the times of the dust storms. The heavily-shaded box (lower-right) shows the size of the bins from which this figure was drawn (10° in latitude by 15° in L_s).

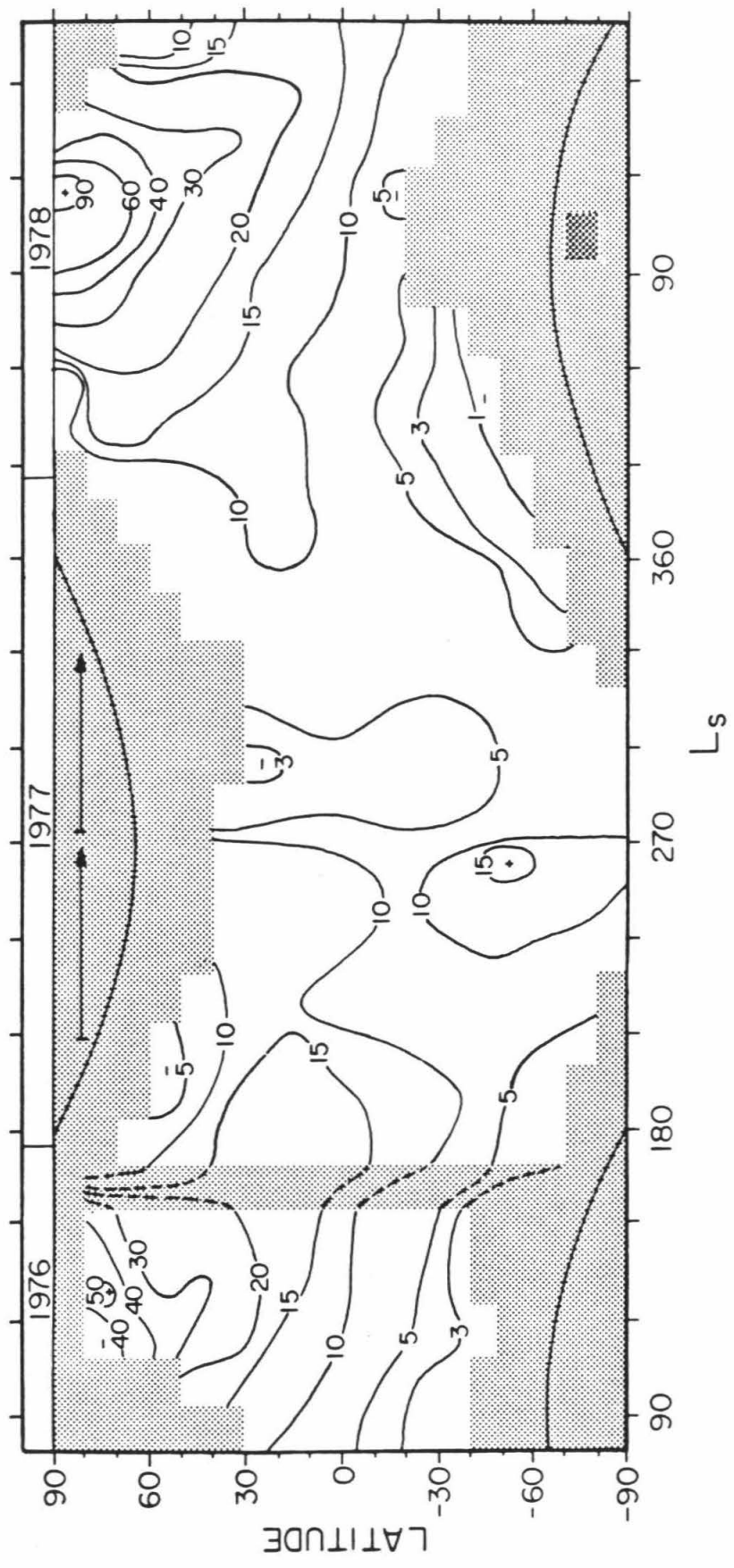
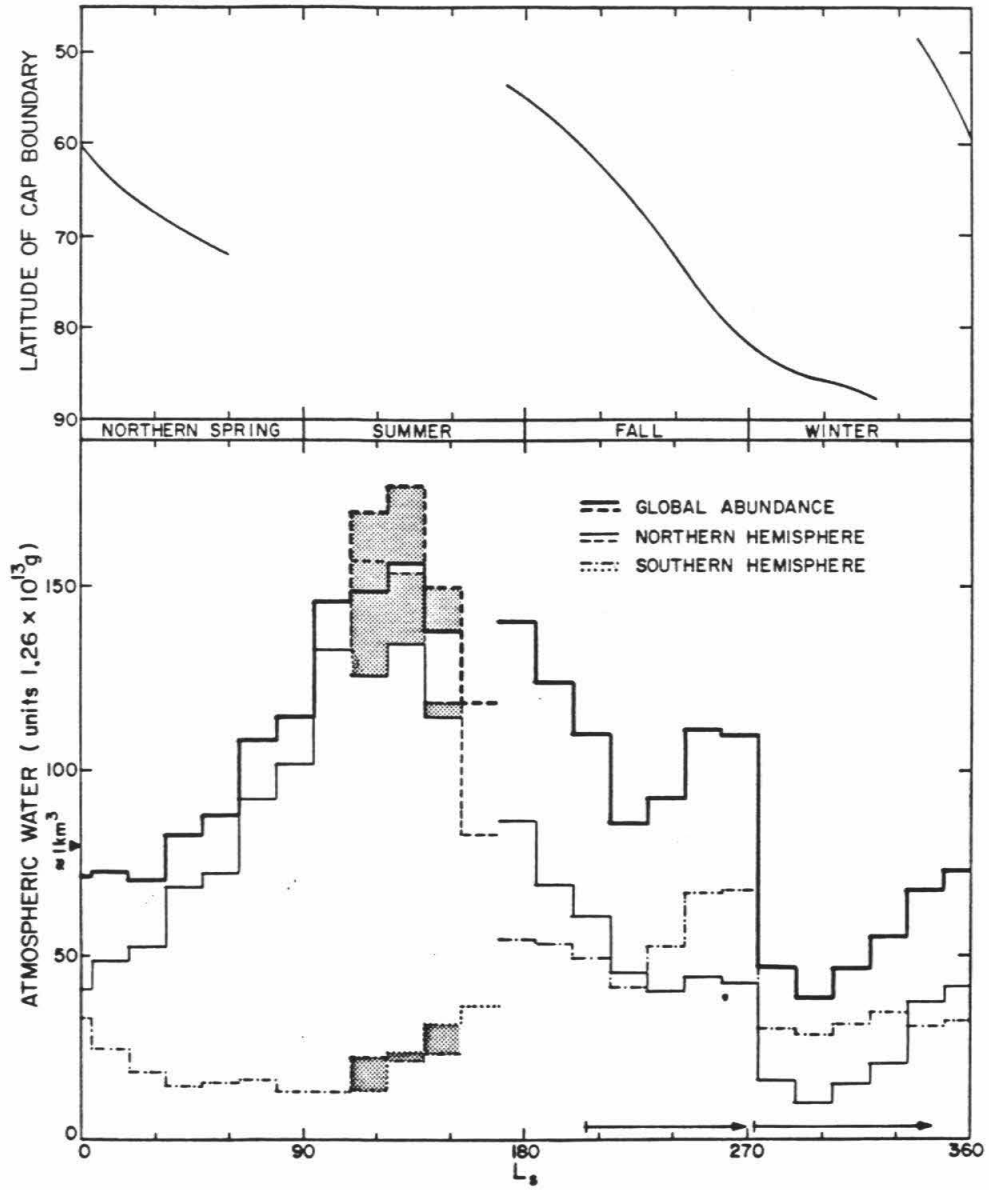


Figure 6: The total global vapor content of the Martian atmosphere as a function of L_s . The dashed and dotted lines represent the second year of observations at the same season; the shading illustrates graphically the differences between the two years. Shown for comparison are curves of the regression of the north and south seasonal polar caps during the same years as the water observations, drawn smoothly through the data of James (1979) and James et al. (1979).



b. Evidence for seasonal reservoirs

It is important to identify the sources and sinks of the seasonal water and to determine whether the data can indicate them uniquely. One would expect that, in the absence of competing dynamical phenomena (see Section 4), the locations of discrete maxima in vapor abundance would coincide with local sources of vapor. Figure 5 shows that local maxima occur near the north pole at $L_s \approx 120^\circ$ and near -50° latitude at $L_s \approx 265^\circ$. The north polar residual cap is known to consist of water ice at a temperature of about 205 K (Farmer et al., 1976; Kieffer et al., 1976a). At this temperature, water can readily sublime and be carried away from the immediate vicinity of the cap, consistent with the region being a local source. In the southern hemisphere, the maximum at -50° latitude occurs nearly 90° of L_s after the seasonal polar cap has receded south past this latitude (James et al., 1979; Figure 6). Although there is considerable uncertainty in the location of this maximum, due to the absence of a strong gradient of water with latitude, it would seem to rule out water tied up in the seasonal cap as the predominant source. The vapor cannot come from the south residual cap, due both to its distance and to polar temperatures too cold to allow significant sublimation of water ice to occur (Kieffer, 1979). Thus, the source of the vapor is likely to be within the regolith, connected to the seasonal warming at this latitude.

Consider also the increase of vapor abundance in the northern hemisphere as northern summer approaches. As water abundances increase at all latitudes the location of the peak vapor abundance should be indicative of the source region. If the receding polar cap is the source of the vapor, the peak should be in that region. It appears from Plate 1 and Figure 3 that the dust storm has dissipated by about period 19. At this time, observed vapor abundances in the south begin to drop after rising as the dust opacity decays;

abundances in the north continue to rise (Figure 2). The rise in vapor following period 19, well after the dust storm has decayed, is seen at all observed latitudes north of $+20^\circ$. The peak of abundance as the water rises lies within the region between $+20^\circ$ and $+50^\circ$ (Figure 3), while the edge of the receding polar cap is at about $+70^\circ$ latitude (see Figure 6). The location of this peak indicates that the source region of the initial part of the seasonal vapor increase must be within the regolith, at these mid-latitudes and away from the edge of the receding seasonal cap. Not until $L_s \approx 40^\circ$ does this trend change, to indicate larger vapor abundances nearer the edge of the retreating cap. This behavior is in contrast with models of the seasonal behavior based on the assumption that the vapor varies only in response to the sublimation of the receding polar cap (e.g., Leovy, 1973; Davies, 1981). A similar examination of the behavior in the southern hemisphere is hindered by the occurrence of the two dust storms as southern summer approaches; Davies and Wainio (1981) do show, however, that at least some of the vapor in the southern hemisphere may be coming from the edge of the receding south polar seasonal cap.

Additional results can be derived from the data regarding the seasonal sinks for atmospheric vapor. At the north pole, the water abundances are consistent with the vapor being in equilibrium with surface ice at the appropriate summertime temperatures (Farmer et al., 1976). Thus, as summer ends and the surface temperatures decrease, the water abundance undergoes a corresponding decrease. At lower latitudes, even as far south as $+25^\circ$, similar behavior is observed — atmospheric vapor undergoes a significant decrease well before $L_s = 180^\circ$ (Figure 2). Because the seasonal CO_2 cap does not begin to form at any latitude until almost $L_s = 180^\circ$ (Paige, 1981; Kieffer et al., 1977), and because the daily temperature variations yield maximum temperatures more than sufficient to sublime any ice as long as the CO_2 cap is not there (T.Z.

Martin, 1981), the vapor must be going into a reservoir other than the seasonal cap. Rapid circulation could be returning vapor to the residual cap, although the pre-summer behavior makes it apparent that the *residual* cap is not the source of the bulk of the seasonal vapor (see previous section). There is no corresponding rise of comparable magnitude in southern hemisphere vapor (see Figure 6), such that southward transport of the water is not important. This factor of two drop in the northern-hemisphere abundance as summer ends (Figure 6) may also be due to water vapor entering the regolith, as either subsurface adsorbed water or ground ice.

The possibility exists that this decline in vapor is due to obscuration by the north polar hood. Historically, these clouds develop sometime between $L_s \approx 150^\circ$ and 180° , and extend to as far south as $+40^\circ$ latitude (L.J. Martin, 1975). However, Viking orbiter imaging observations show that a significant hood did not develop that year until nearly $L_s = 180^\circ$, although the data are scant (P. James, personal communication, 1981). Also, VL-2 data indicate that significant obscuration by the hood at that location (at $+48^\circ$ latitude) was sporadic. Lander-measured visual opacities show values of less than 0.4 through $L_s = 163^\circ$ (Pollack et al., 1979); later measurements, up until the time that the first global dust storm begins, yield values as high as 1.4, but these are interpreted as precursors to the dust storms due to the occurrence of similar values at both sites (Pollack et al., 1979). Tillman et al. (1979) discuss evidence for brief passage of the hood over the VL-2 site at $L_s = 205^\circ$. The observations all point to occurrence of the hood late enough seasonally that the observed decline in vapor abundance cannot be due to obscuration by the hood. Additionally, the decline in vapor occurs as far south as $+25^\circ$ (Figure 2), much further south than the extent of the hood when fully developed.

Obscuration by dust also fails to account for the decline in observed vapor abundance. Again, the lander-measured opacities do not increase early enough to cause the drop. Also, vapor abundances do not decline further south than about $+20^\circ$ at this time, although there is likely atmospheric dust behavior in the south similar to that in the north. The increase in opacity observed after $L_s = 163^\circ$ must affect the water measurements; however, the decline in observed abundance *during* the first storm is sufficiently small with respect to the increase in opacity (about a 25% drop at most latitudes; see Figure 2) that it is unlikely that dust is the major cause of the lowered abundances prior to $L_s = 205^\circ$.

The end-of-summer behavior of vapor in the southern hemisphere is again confounded by obscuration of the vapor during the global dust storms. Farmer and Doms (1979) pointed out that the seasonal drop in southern hemisphere vapor abundances coincided in time with the occurrence of the second global dust storm, with abundances after the storm being half of what they were prior to the storm while northern hemisphere abundances return to their prestorm values (Figure 6). They suggested that the southern water was carried north along with atmospheric dust (T.Z. Martin and Kieffer, 1979) and deposited on the northern winter cap. A simple and plausible alternative exists. The dust storm dissipated near the end of southern summer; at the corresponding northern season the northern vapor abundances had dropped by a large amount with the water likely entering the regolith, as discussed above. The possibility exists that, as in the north, the vapor re-entered the regolith as the winter approached, and that this action was simply masked by the presence of dust in the atmosphere. That is, had the dust storms not occurred, the vapor behavior might have been the same as it was, dropping to low values by $L_s = 360^\circ$. The timing of the decline in southern vapor abundance is consistent

with the seasonal thermal behavior as discussed by Kieffer et al. (1977, appendix I). That the southern vapor did not go north also readily explains why the northern hemisphere did not also lose vapor as a result of the dust storms, as would be expected if enhanced atmospheric mixing and consequent deposition at the north were the cause of the southern drop in abundance.

c. The polar caps

The behavior of water vapor over the north polar cap has been discussed by Farmer et al. (1976). The vapor content during the northern summer is consistent with a uniformly-mixed atmosphere saturated at the surface at a temperature of about 205 K. This temperature is consistent with radiative equilibrium between the surface and the solar irradiation using the measured surface albedo of the north residual cap (~ 0.43), and is also consistent with the observed surface temperatures (Kieffer et al., 1976a). These observations led to the conclusion that the residual north polar cap is water ice.

The same type of analysis will not yield such a simple conclusion for the south pole, however. The peak summertime abundances over the south pole are approximately 13 pr μm (see Figure 2). If the atmospheric vapor were saturated and in equilibrium with water ice at the surface and uniformly mixed throughout the atmosphere, the corresponding surface temperature would be about 193 K. This temperature could result if the surface thermal emission were in equilibrium with the insolation and if the surface albedo were 0.65. While this is close to the inferred albedo (~ 0.64), the observed thermal emission is too low to be consistent with a kinetic temperature of 193 K (Kieffer, 1979; Paige, 1981). Instead, the 20 μm brightness temperature varies between 160 K and 175 K and the total thermal emission yields a bolometric brightness temperature of about 172 K prior to the second dust storm (Paige, 1981); both

are consistent with emission from a surface near the CO₂ condensation temperature and transmission through a dusty atmosphere (Kieffer, 1979). If this interpretation is correct, uniformly-mixed vapor would rapidly condense out of the atmosphere.

An isothermal atmosphere saturated up to several scale heights would not be capable of holding as much water as is observed unless the temperature were greater than about 190 K. A temperature inversion over the pole is thus implied, and is consistent with the infrared and radio occultation measurements made concurrently by Viking (Kieffer, 1979; Lindal et al., 1979) and at a similar season by Mariner 9 (Conrath et al., 1973) (see also Davies and Wainio, 1981, for a discussion of the evidence for an inversion). Thus, we expect that the vapor is present over the south pole due to advection in from elsewhere and that some of this vapor diffuses downward to condense onto the much-colder cap. The fact that the CO₂ on the cap does not disappear in summer (Kieffer, 1979; Paige, 1981) does not rule out the presence of copious amounts of water ice. In fact, if the CO₂ ice does indeed survive the summer then the underlying water ice will not sublime at any season, and a net annual growth of the water ice component of the south cap will occur.

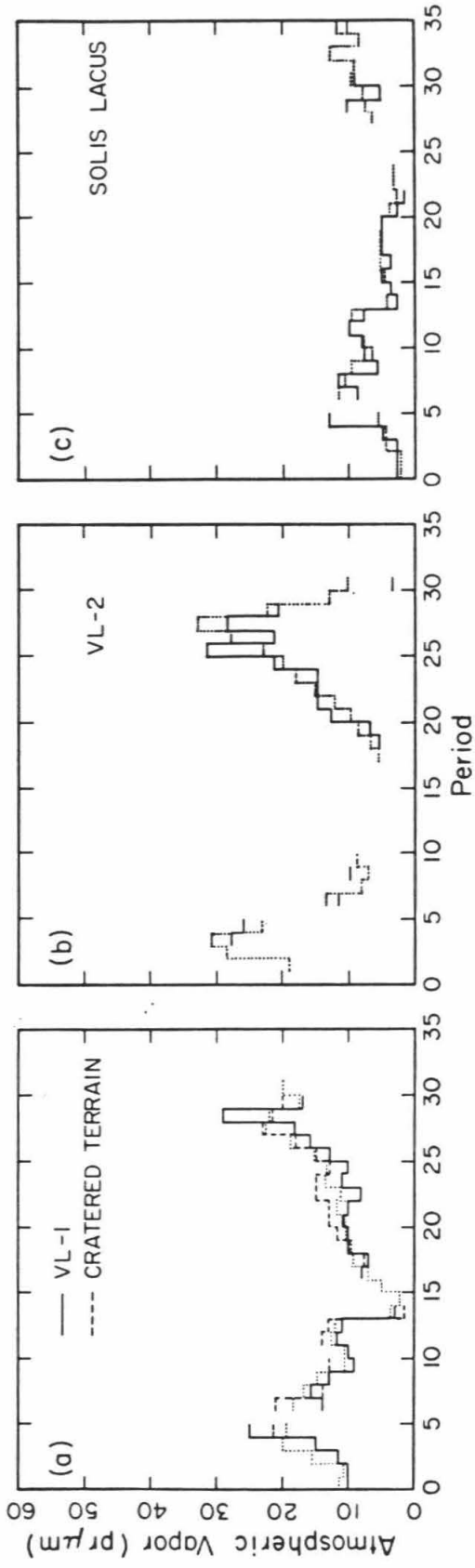
It should be stressed that the above discussion applies only to the year that the cap was observed by Viking. As will be seen in Chapter II.C, the possibility of significant inter-annual variability in the water cycle exists. Observations of large vapor abundances during the southern summer season (Barker et al., 1970) indicate that all of the CO₂ on the south cap may sublime away in some years to expose the underlying water ice cap.

d. Behavior at specific sites

Several locations on the planet are of intrinsic interest due to the application of a variety of data sets from several sources. Here the seasonal behavior of atmospheric vapor over the two Viking landing sites and over the classical region Solis Lacus will be discussed.

Over the VL-1 site, the vapor abundance goes from a minimum of perhaps 10 pr μm (during mid-winter when masking of the water during the global dust storm occurs) to a maximum of nearly 30 pr μm at $L_s \approx 150^\circ$ (Figure 7a). If the vapor were uniformly mixed with height at all times of day, this would imply a saturation temperature at the surface of between about 190 K and 198 K. The surface temperature drops below these values each night throughout the year (Kieffer, 1976), so that one might expect daily condensation of near-surface vapor to be a possibility. Temperature inflections near the surface that are attributed to the frost point being reached are in fact observed (Ryan and Sharman, 1981), but the interpretation is ambiguous. Viking lander opacity measurements also indicate the existence of a thin early-morning fog (Pollack et al., 1977, 1979). If nighttime condensation occurs, the optical thickness of the resulting fog may be estimated. Based on the atmospheric models of Pollack et al. (1979) and the condensation temperatures obtained assuming uniform vertical mixing of the vapor, fog would be expected to form within the lowermost 100 m or so of the atmosphere. If there are 30 pr μm of vapor distributed uniformly within the atmosphere, then 0.3 pr μm will be within this condensable region. Condensation of this amount of vapor onto the dust grains already present in the atmosphere, with an effective particle size of 2.5 μm (Pollack et al., 1979), would produce an opacity change of ~ 0.2 . This value is remarkably close to the diurnal variation observed from the Viking landers and attributed to ground fog (Pollack et al., 1977) (see Chapter II.B for further discussion of this point).

Figure 7: The seasonal behavior of vapor over (a) the VL-1 site, (b) the VL-2 site, and (c) Solis Lacus. In each case, the abundances shown are those of the 10° bins (from Plate 1) which contain the location, and the period (along the abscissa) has the same meaning as in Plate 1 and Table 1. The dotted line in each figure is the average behavior at the appropriate latitude, and is the same as is in Figure 2.



Shown also in Figure 7a is the history of vapor above a location at the same latitude as the VL-1 site but in the cratered terrain, as well as the average vapor behavior at that latitude. The cratered terrain shows a lower peak water abundance, consistent with its being at a higher elevation than the landing site, but otherwise shows little difference. The observed variation of abundance with season at this latitude is a factor of several times greater than that predicted by the global model of Davies (1981). The small variation in his model results from use of a very low coefficient for mixing between latitudes, required by him in order to fit the data, with most of the seasonal water variation resulting from a seasonal cycle of condensation and sublimation of local surface ice.

The vapor abundance at the VL-2 site varies from a low of less than 5 pr μm in winter to about 30 pr μm in summer (Figure 7b). Examining data with observing geometry that did not meet the earlier geometry criteria shows that the minimum is about 4 pr μm during period 13 ($L_s \approx 270^\circ$), while the average at this latitude at this time is 7 pr μm . If the vapor is uniformly-mixed vertically, the resulting surface frost point temperatures would be between 185 K and 198 K, depending on season. Lander temperature inflections and diurnal opacity variations are both observed at the VL-2 site (Ryan and Sharman, 1981; Pollack et al., 1977) and seem to occur at about the same time of day as each other, again indicating that the atmosphere may be reaching the saturation point at night at the surface (Ryan and Sharman, 1981). The site shows little significant difference from the other locations at that latitude.

Condensate has been observed on the surface at the VL-2 site (Jones et al., 1979) and has been interpreted as a mixture of CO_2 and H_2O frost (Jones et al., 1979; Wall, 1981). The frost is present during the winter, appearing at $L_s \approx 243^\circ$ and disappearing completely by $L_s \approx 16^\circ$ (although most has disappeared by $L_s \approx 360^\circ$). Comparison of the observed color with that

expected for frost overlying a surface suggests that the frost layer is between 0.2 and 0.6 mm thick, or is greater than 0.5 mm thick if dust is incorporated into the frost (Clark, 1980). Because a large fraction of the surface at the VL-2 site is covered with frost, sublimation of this amount of water ice would produce between 100 and 500 μm of atmospheric vapor locally. However, the annual behavior of vapor shown in Figure 2 indicates that there is no large increase in atmospheric vapor abundance at this latitude until well after all of the VL-2 frost has disappeared. In fact, the entire hemisphere shows no increase until after this time also (Figure 6). Additionally, most of the seasonal decline in vapor occurs about 60° of L_s prior to the first appearance of the frost. This timing indicates that the condensate cannot be a significant reservoir for the seasonal water. The timing is also not consistent with this location being a reservoir for southern hemisphere water which might be carried north during the dust storms, due to its first appearance between the two dust storms, prior to the observed decline in southern vapor. There are several arguments against the condensate being CO_2 , dealing with the thermal balance of the surface (see Jones et al., 1979). The timing of the frost's occurrence is more consistent, however, with that expected for CO_2 (Kieffer et al., 1977, appendix I) than for H_2O . Based on the timing of the occurrence and the amount present, either the condensate is CO_2 ice with little H_2O mixed in; the VL-2 site is a special location and only a very small part of the planet has similar deposits at these seasons; or the estimates of the amount of water contained within the deposits are much greater than the amount actually present. Nevertheless, the amount of water ice contained within this frost deposit, and within like deposits elsewhere at the seasons discussed, must be negligible in comparison with the global seasonal budget of water vapor.

The region in the vicinity of the classical region Solis Lacus (located in Solis Planum, at about -25° latitude, 90° longitude) has generated much discussion recently as a candidate site for the injection of large amounts of water vapor into the atmosphere from a subsurface reservoir (e.g. McCord et al., 1977; Huguenin and Clifford, 1981; Huguenin, 1979, 1980) or for the possible presence of near-surface liquid water (Zisk and Mouginis-Mark, 1980). The Solis Lacus region appears in Plate 1 to be identical to its surroundings in terms of the water vapor behavior. In Figure 7c, it is seen to be not significantly different from the average behavior at that latitude. If as much water is being injected yearly into the atmosphere as is estimated by Huguenin (1980), greater than 10% of the atmospheric water content of the entire planet, the region would show anomalously high vapor content. Continuity of the gradient of vapor across this latitude (see the next section) makes it clear that there can be no source of vapor from this latitude strip that is significant with respect to the global water budget. If vapor were being injected into the atmosphere only at the times of the dust storms, it might not appear in the MAWD data at that time due to the discreteness of the observations and to the simultaneous masking by dust. It appears from Figures 2 and 5, however, that there are no detectable increases in local or global vapor abundance at that time, at -25° or at any other latitude. Therefore, any vapor so injected must be negligible with respect to the global water budget or must be removed from the atmosphere prior to the decay of the dust storms. The minimum amount of vapor required by Huguenin (1979) to produce the bright rings observed by McCord et al. (1977) around the early phases of the dust storms is, of course, a completely negligible amount with respect to the global budget. It is even small compared to the column abundance of vapor present above Solis Lacus at that time. This bright ring, if real and not an observational artifact, can instead be readily understood as

arising from condensation of the water vapor already present in the atmosphere as a result of the active convection associated with the dust storm.

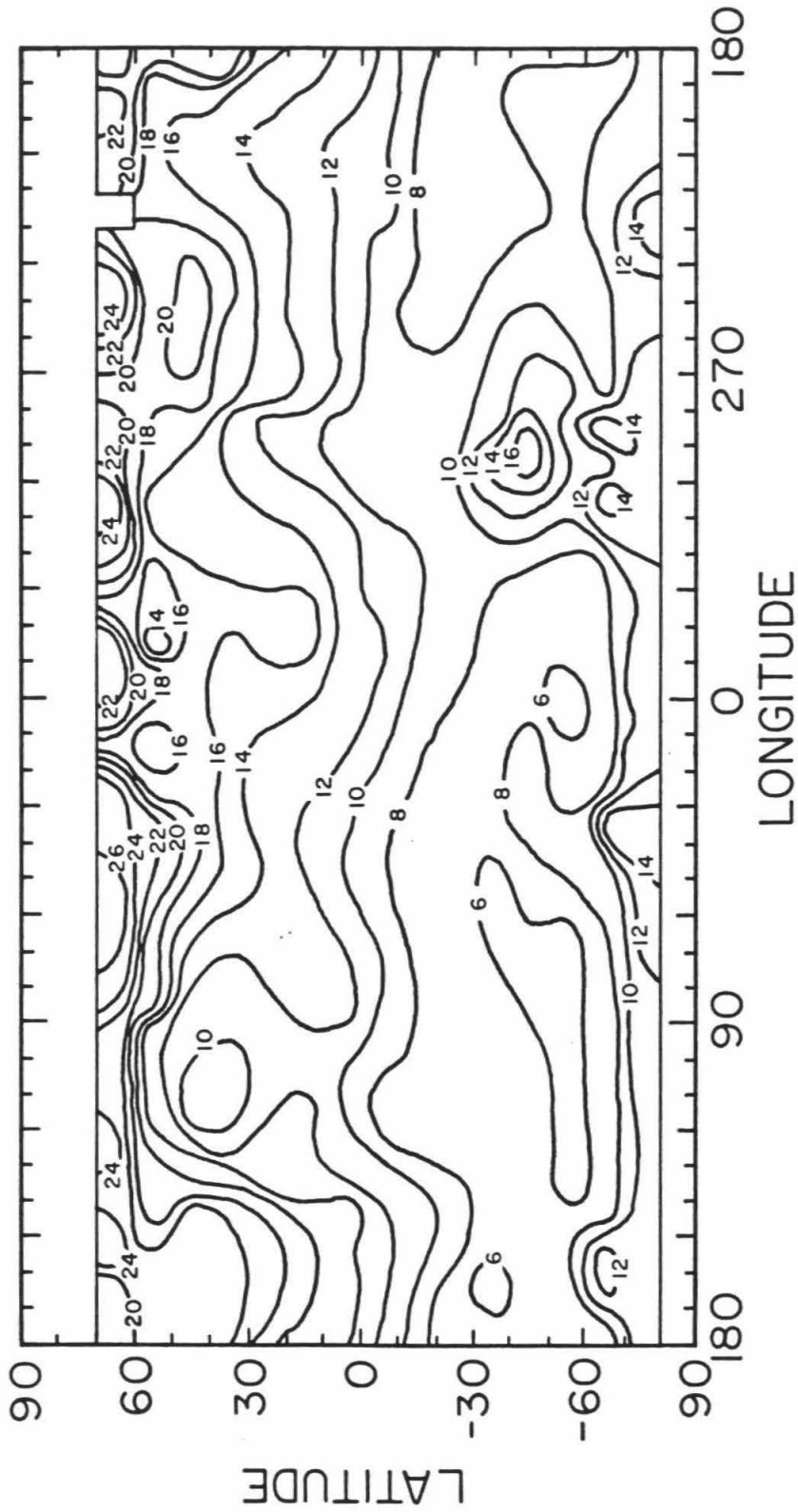
4. Annual-Average Water Vapor Distribution

a. *Annual-average map*

The seasonal water vapor behavior is expected to depend in part on the physical properties of the surface because of the control exerted by these properties on the subsurface, surface, and atmospheric temperatures and thereby on the water holding capacity of both the subsurface and atmosphere. The circulation of the atmosphere is not uniform with respect to longitude (e.g., Pollack et al., 1981), however, so that perturbations due to mass motions will in some sense be superimposed on any correlations of water vapor with surface properties.

One should not initially expect any of the period maps shown in Plate 1 to resemble maps of surface properties, due to the difference in seasonal behavior of water vapor between the northern and southern hemispheres. The resemblance between the period 10 map and the albedo map, discussed earlier, is an exception to this due to the presence of significant quantities of atmospheric dust. The period maps have therefore been combined in order to yield a measure of the annual average column abundance of water vapor at each point (Figure 8a) and to allow some first-order comparisons. The averaging scheme, shown in Figure 9, was devised in order that the times of year when significant dust was present would not be included yet equal time periods would still receive equal weighting in the final average. Because the period maps are equally-spaced in L_s , rather than time, averaging obtains not a true "time-average" of behavior, but instead a "season-average" behavior. This averaging scheme must be building a bias into the results because the vapor behavior is not completely symmetric in time and all periods are not included equally. The salient features to be discussed below, however, would likely be apparent in any averaged set of the data and their appearance should not be dependent on our

Figure 8: a) Contour map of annual average atmospheric water vapor abundance, in μm . b) Contour map of annual average vapor/airmass, in μm . See text for details.



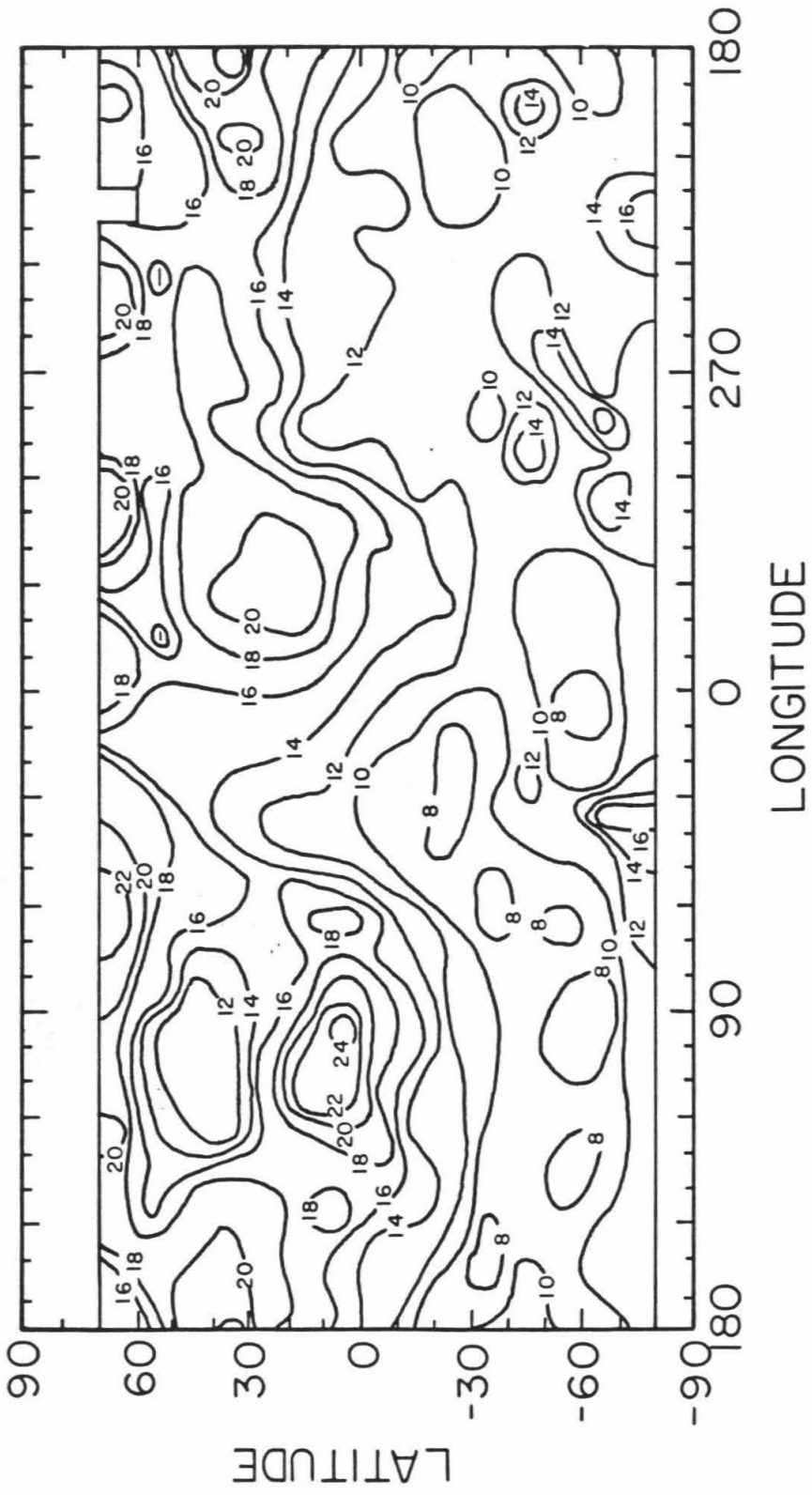
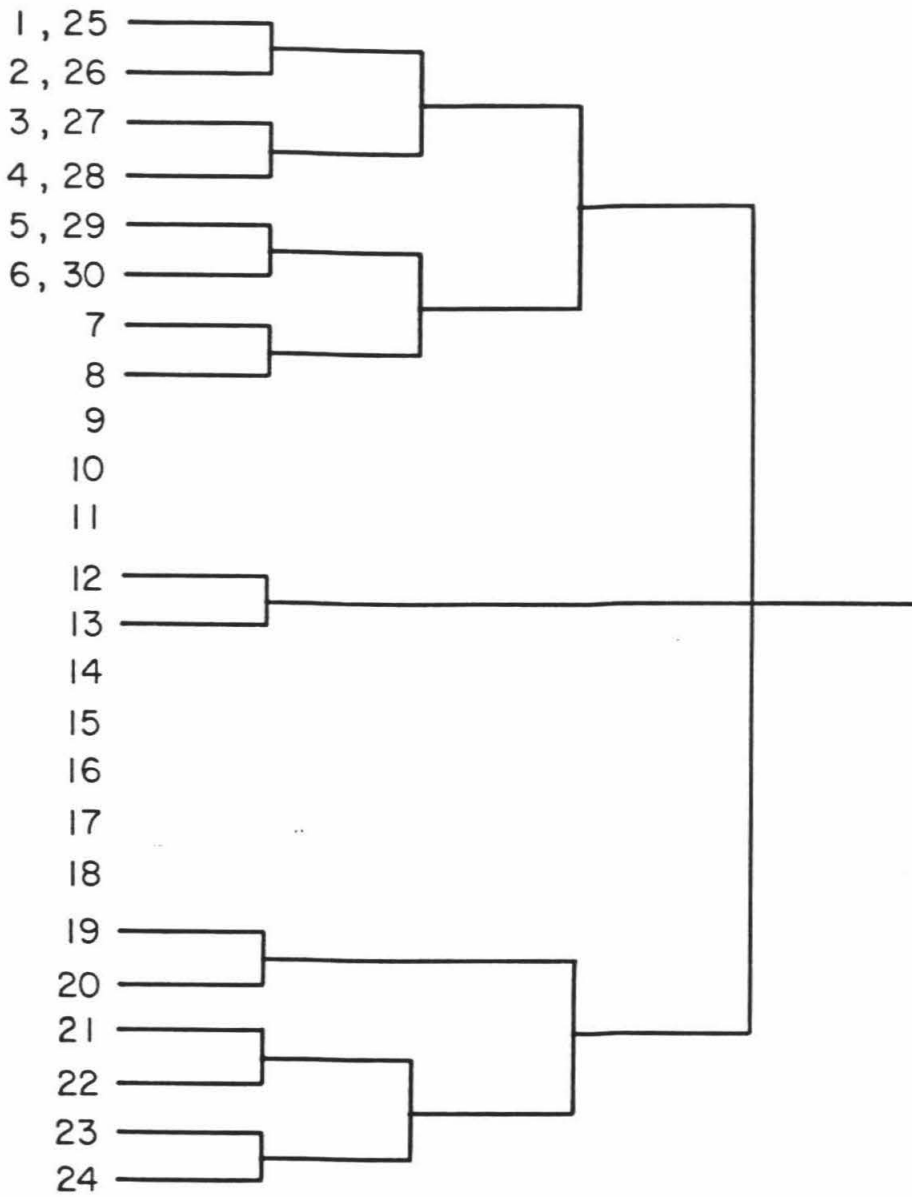


Figure 9: Averaging scheme for producing the annual average water vapor abundance map (Figure 8a). Converging lines indicate periods which were averaged together, with the resulting map subsequently being averaged with other resulting maps, as shown. Periods 9 to 11 and 14 to 18 are not included in the averaging due to the obscuration of vapor by atmospheric dust at these times. By averaging in this way, one can largely eliminate any bias that would otherwise result due to lack of coverage in some locations at some seasons.



averaging method.

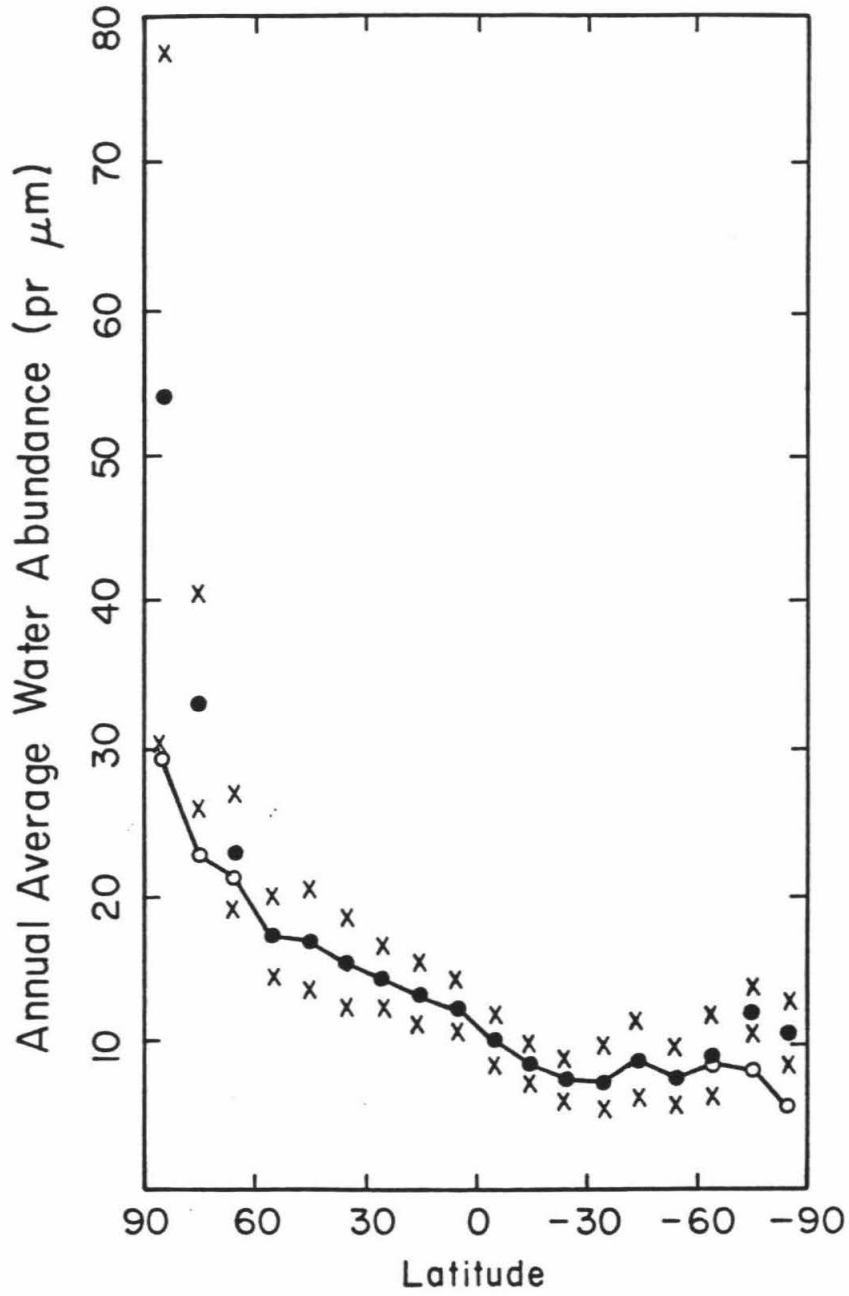
The most striking feature in the annual-average map (Figure 8a) is, again, the strong asymmetry between abundances in the two hemispheres. The northern hemisphere has typically twice as much vapor as the southern. This latitudinal gradient is seen most dramatically in Figure 10a, which shows the average abundance as a function of latitude. The near-polar abundances have been corrected (open circles) to account for the lack of polar-nighttime observations by assuming zero vapor abundance during the polar night.

If account is taken of the uncertainties in the derived vapor abundances, the abundance is essentially monotonically decreasing from north to south. Because the behavior is monotonic and smooth, there are no significant *net annual* sources or sinks of vapor at any latitude except the poles. Because the circulation of the atmosphere will generally act to lessen the vapor abundance gradients present, at least in the absence of other concurrent processes, this implies a net annual flow of vapor toward the south (see below for further discussion of this point).

b. Comparison with topography

Interestingly, the annual average vapor abundance shows a strong correlation with the surface topography (compare Figure 8a with Figure 11). The lowest place in the southern hemisphere, Hellas Basin (located at -45° latitude, 290° longitude), has the largest average vapor abundance, and in fact has almost twice as much vapor at its peak as does any other location at that latitude. Argyre Basin (-55° , 40°) also has more vapor than do most places at that latitude, but is not nearly as prominent in Figure 8a as is Hellas. The Tharsis Plateau region (centered at about 0° , 105°) appears as a relative low in vapor abundance. The Elysium region (centered at 30° , 210°) is also a

Figure 10: a) Latitudinal behavior of the annual average vapor abundance. The x's represent the one-sigma variation at each latitude rather than errors. The near-polar data have been corrected (open circles) for lack of observations during the polar night by assuming zero abundance at that time. b) Latitudinal behavior of the annual average vapor abundance/airmass.



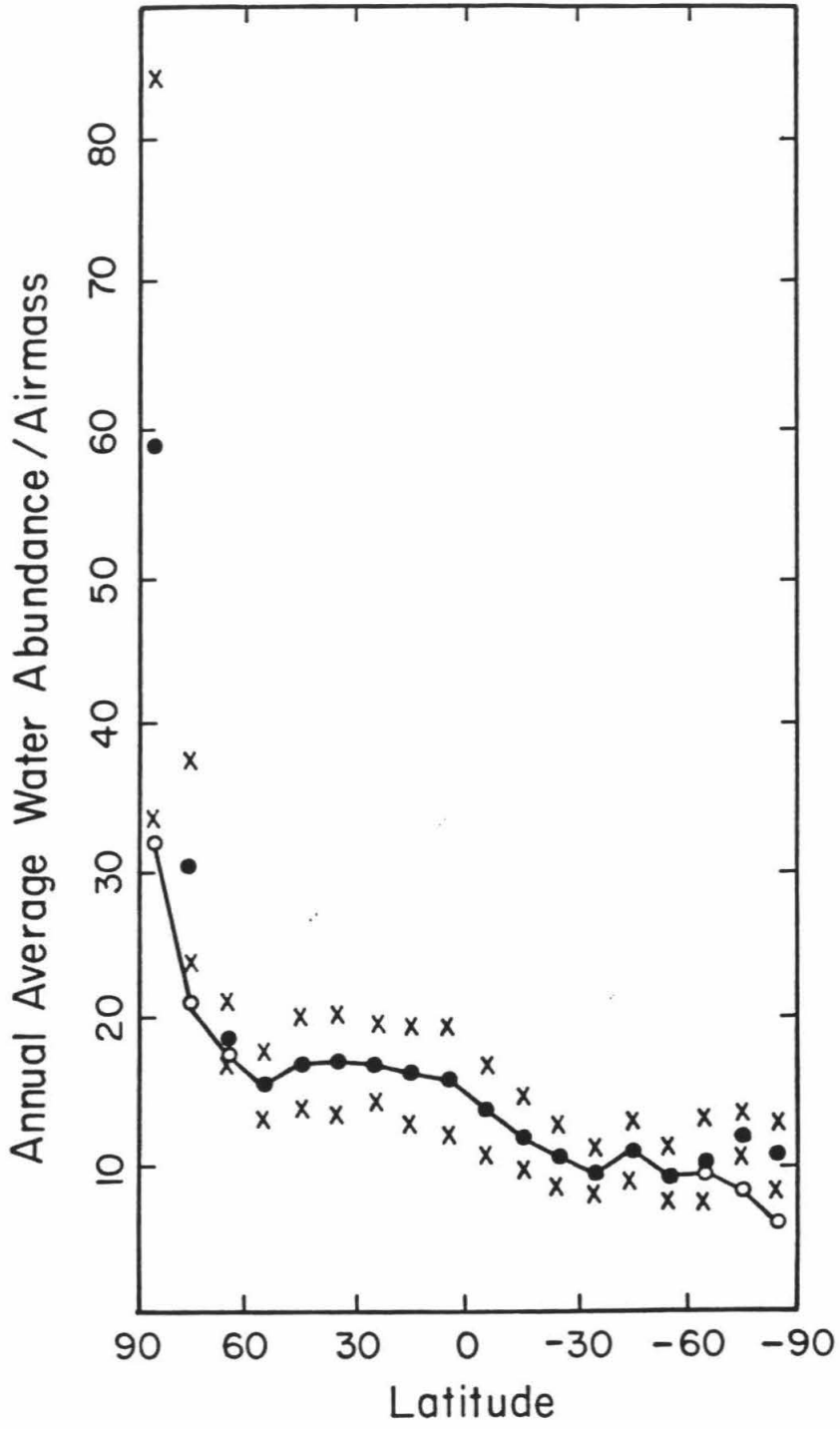
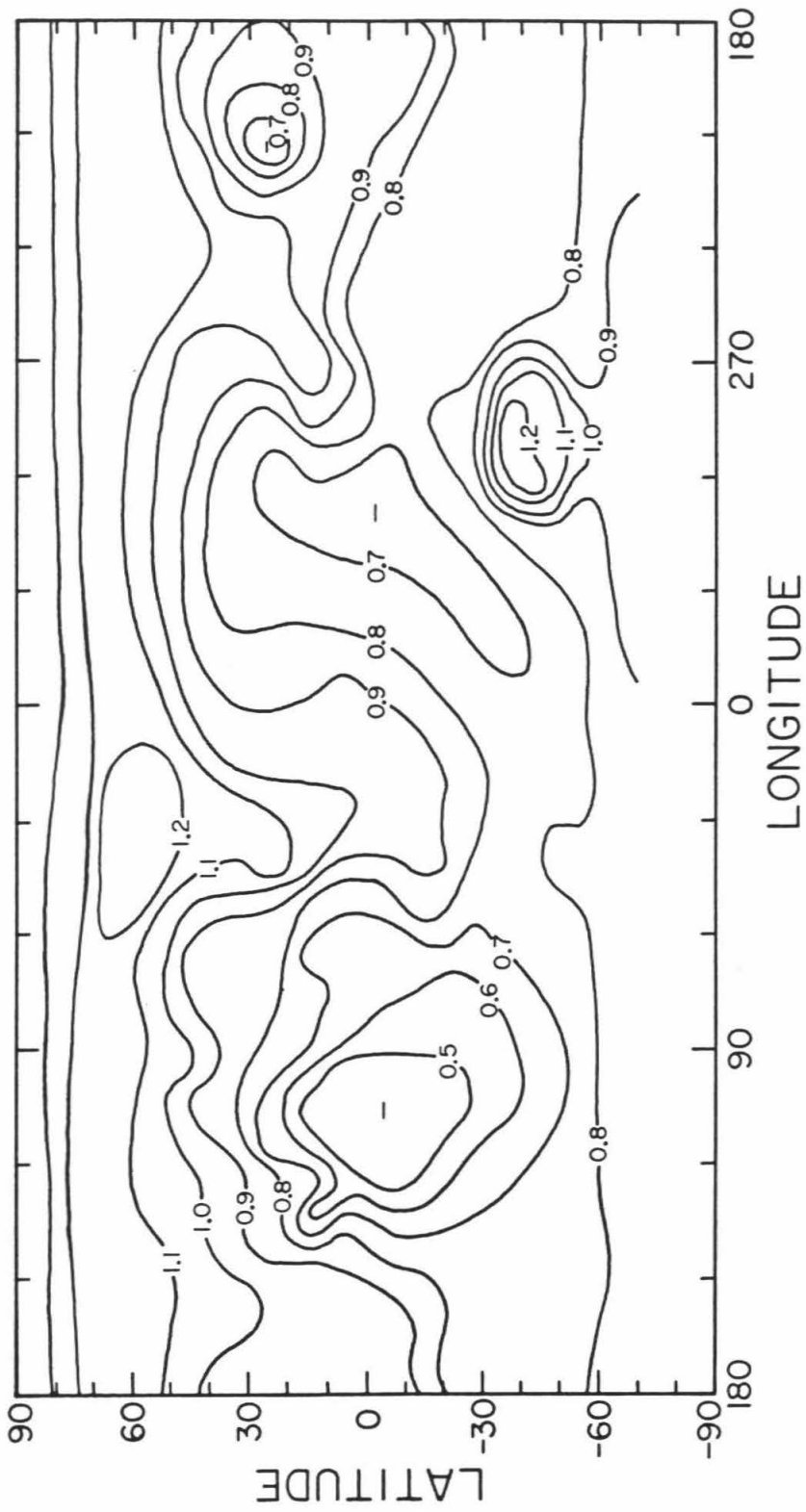


Figure 11: Global map of the airmass, given by $a = \exp(-z/H)$. A value of 1.0 represents an elevation of 0 km; H is taken to be 10 km everywhere. Local topography is taken from U.S. Geological Survey (1976); no data exists south of -70° latitude. The contours were drawn from an array of the average airmass within each 10° latitude by 10° longitude bin.



topographic high and appears as a low-vapor region. While the vapor abundance in Alba Patera (45° , 110°) is low it appears on the maps as a relatively subdued region in comparison with other topographic highs. Figure 12 shows a scatter plot of the year-average abundance versus the local airmass (here, airmass is given by $\exp(-z/H)$, where z is the local surface height above the geoid and H is the scale height of the atmosphere, taken to be 10 km everywhere). There is a strong correlation between the vapor abundance and airmass. Although there are many counter-examples to this trend, as exemplified by the deviations from a perfect one-to-one correspondence in Figure 12, the overall trend is striking. One can imagine several types of global vapor distributions that would result in distinctive behavior when plotted versus airmass as in Figure 12. These are listed in Table 2 and discussed below:

(i) If the surface vapor concentration (in molecules/cm³) averaged over a year were everywhere the same, and the vapor were uniformly mixed vertically, then the average column abundance would be the same everywhere and Figure 8a would appear bland.

(ii) If the mixing ratio were, instead, a simple function only of altitude above the local surface, a slight correlation with airmass would result due to the assumption of uniform mixing applied in the reduction of the data; even for the most-extreme cases, however, this correlation would not be significant with respect to the scatter in the data.

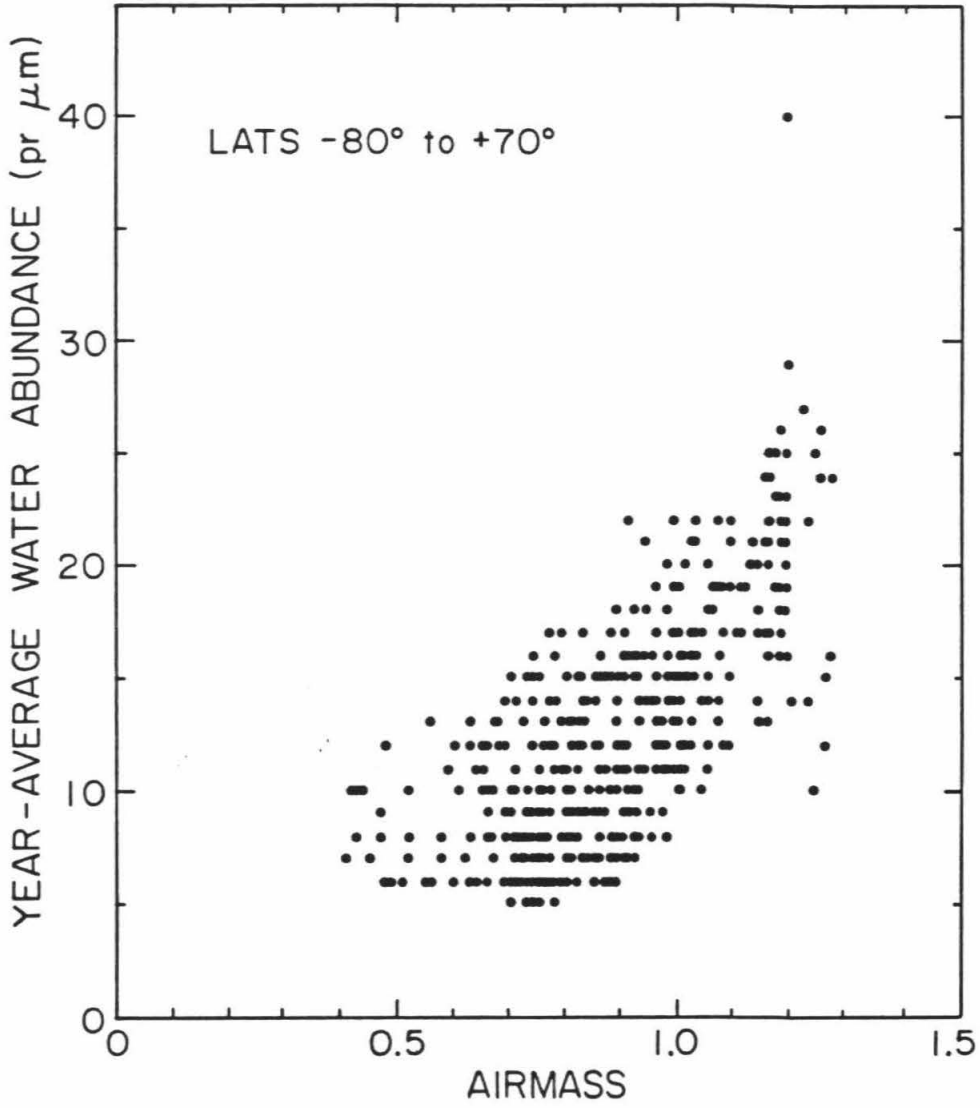
(iii) If, averaged over a year, the vapor mixing ratio were the same everywhere in the atmosphere, then the average column abundance would be a linear function of the airmass at the surface. The data in Figure 12 would then fall along a straight line through the origin.

(iv) If the mixing ratio were a simple function of altitude above the geoid,

Table 2. Possible Annual-Average Distribution of Vapor.

Distribution	What is Seen on a Map of	
	Water	Water/Airmass
$N_{surf} = \text{constant}$ $H_{H_2O} = H_{CO_2}$ $H_{H_2O} < H_{CO_2}$	uniform slight correlation with airmass	
$f_{H_2O} = \text{constant}$	linear function of airmass	uniform
$f_{H_2O} = \text{fn (altitude)}$	Monotonically- increasing function of airmass	correlated with air- mass

Figure 12: Cross-plot of the annual average vapor abundance (Figure 8a) versus the local airmass (Figure 11).



the water abundance would be a monotonically increasing function of the airmass.

These cases are summarized in Table 2.

The data indicate that one of these last two possibilities occurs. Dividing the average water abundance by the airmass allows one to decide between them. Figure 8b shows a map of the annual average abundance (Figure 8a) divided point-by-point by the airmass (Figure 11). It is in fact not uniform but still correlates positively with airmass (see Table 3). A possible explanation that can easily be tested is whether the correlation seen in Figure 12 is fortuitous, resulting from the strong north-to-south gradient of water being superimposed upon the strong north-to-south gradient of topography (see Figure 11). In fact, this seems not to be the case uniquely. The correlation occurs not only when the global data set is examined but also when the data for the individual latitude bands are examined. As an example, the Tharsis plateau is the highest region on the planet and has less water than most places at that latitude, while Hellas Planitia is the lowest place in the southern hemisphere and has more water than any place at that latitude. Additionally, the highest places in the southern hemisphere, in the cratered terrain and south of Tharsis, have the least water amounts in that hemisphere. Further south both the airmass and the water abundance increase.

Although the cause has yet to be determined, one can conclude that an important affect on the Martian water abundance is the relative height of the surface. The scatter in the data precludes an accurate determination of an "average scale-height" of the water vapor by reading off the slope of the best-fit line through the data. In fact, the scatter also prevents such a concept from being uniformly applicable over the whole of the planet.

Table 3. Correlation Coefficients Obtained in Comparing Various Data Sets.

Data Sets	Latitude Range of Comparison	
	-60° to +60°	-20° to +30°
year-avg. water, airmass	0.706 ¹	
year-avg. water/airmass, airmass	0.210 ¹	-0.444
year-avg. water, thermal inertia	0.017	-0.271
year-avg. water, albedo	0.429	0.553
year-avg. water/airmass, inertia	-0.297	-0.657
year-avg. water/airmass, albedo	0.556	0.658
thermal inertia, airmass	0.466	0.434
albedo, airmass	0.097	-0.076
thermal inertia, albedo	-0.621	-0.713

¹Latitude range -80° to +70°.

c. *Latitudinal gradient and net transport of water*

Even after dividing by the airmass there is a hemispherical asymmetry of water, with the northern abundances generally being larger (Figure 10b). On the average, the north still has over 50% more water than the south. This asymmetry is seen also in Figure 8b by comparing the average abundances over Hellas and Argyre with the abundances over places in the northern hemisphere that have similar surface elevations (about -2 to -4 and 2 to 3 km, respectively). Vapor over Hellas averages about 14-18 pr μm , while Argyre has about 8-10 pr μm . At places of similar heights in the north there are about 16-22 pr μm and 14-16 pr μm , respectively (Figure 8a). This same asymmetry obtains when comparing the higher southern elevations with like elevations in the north.

In the absence of other major processes, the annual average gradient of water vapor will result in the transport of water toward the south on a *net annual* basis. This results because diffusive flow and mixing will both tend to reduce atmospheric gradients of water. There are examples where transport of species can be up-gradient rather than down-gradient, but these have complications that do not apply here. Water vapor in the Earth's tropic regions can travel up-gradient, for example, but this results because vertical mixing causes cooling and saturation of water higher up in the atmosphere, with consequent rain and near-surface concentration of the water; the circulation pattern then moves water in one direction down low with no return flow in the other direction up high. On Mars, the vapor is likely to be mixed much more uniformly vertically, even given the slight near-surface concentration of vapor discussed in Chapter II.B, such that transport will tend to be down-gradient. There are other Earthly examples of non-down-gradient flow, such as ozone or volcanic dust in the stratosphere, but these also involve complications not present in the Mars water system.

Therefore, the latitudinal gradient of water (Figure 10 a and b) will result in a net annual transport of water toward the south. This southward flow may be balanced to some degree by transport of vapor north during the global dust storms, or in the form of condensates or in other years. Global mixing of the atmosphere is enhanced during the storms (Haberle et al., 1980), but the distribution of atmospheric vapor is sufficiently uniform with respect to latitude at this time (Figure 3) that it is unlikely that mixing would significantly redistribute the vapor except by promoting condensation of a small amount of water onto the cold polar caps. Certainly, vapor which condenses onto the south polar cap as a result of southward flow cannot return north under any conditions as long as the presence of CO₂ ice at the pole keeps the temperatures depressed and allows no sublimation of water ice. In the model by Davies (1981), no net southward flow results due to the implicit assumption that flow south down the gradient is balanced each year by flow north during the season of the global dust storms.

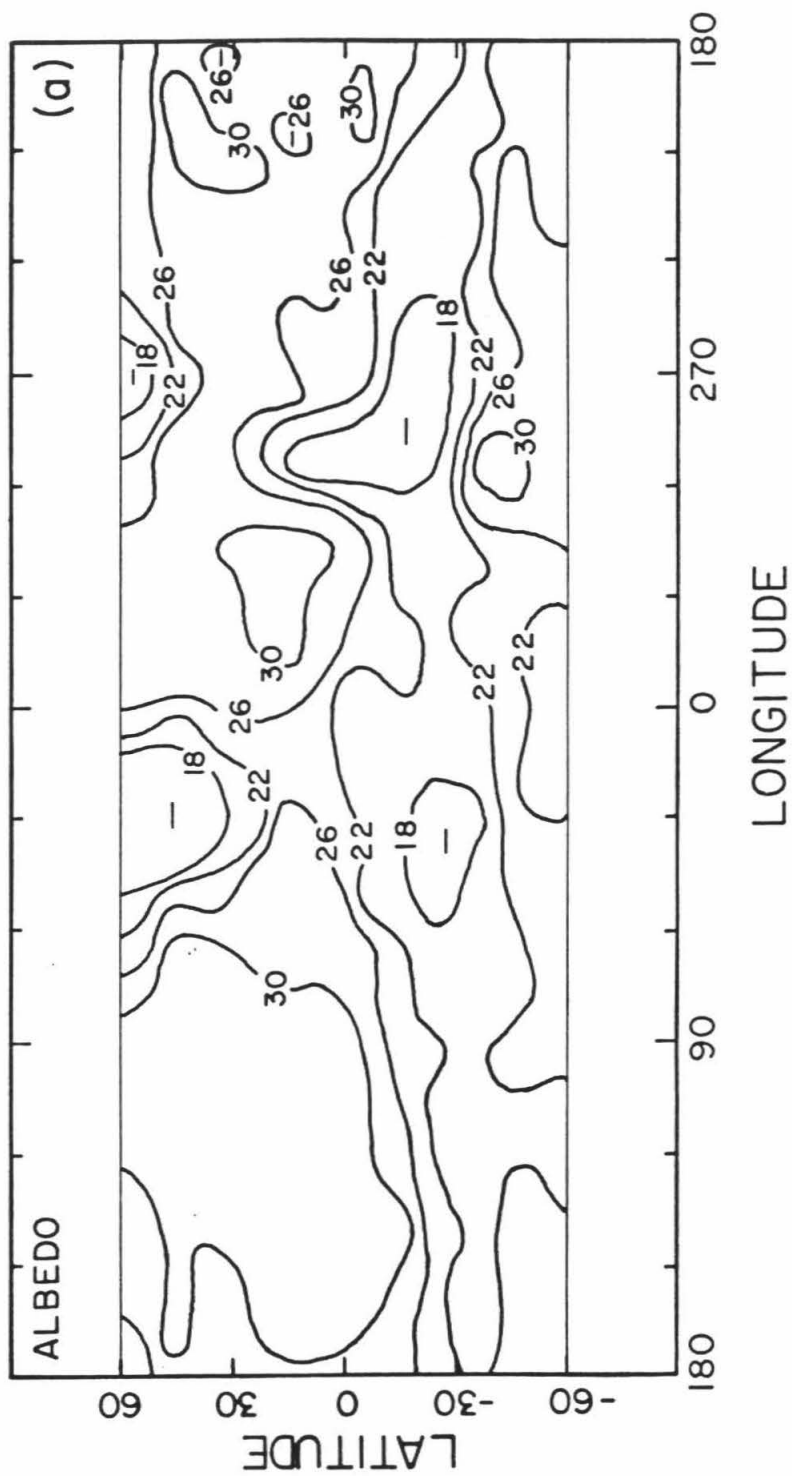
An upper limit to the amount of water transported toward the south in a year may be obtained by assuming that none of the vapor sublimed off of the north polar cap in the summer returns in the winter, and that all of the increase in vapor abundance in the northern hemisphere after $L_s = 80^\circ$ is due to vapor released from the north residual polar cap. $L_s = 80^\circ$ is chosen because this is when the seasonal covering of CO₂ ice in the north completely disappears (Paige, 1981). From Figure 6, this increase is equivalent to about 4×10^{14} g H₂O. In 10^5 years, the approximate time period during which the obliquity of Mars' orbit cycles from minimum to maximum and back to a minimum (Ward, 1979), this southward transport would remove a layer of water ice about 140 m thick from the north polar cap. The actual amount of water transported will be lower than this because not all of the water sublimed is lost from the cap (some will

return at the end of summer), not all of the vapor increase at this season is necessarily due to the subliming polar cap, and because flow toward the south may be mitigated in part by mechanisms not explicitly considered here. Interestingly, the thickness of the layers in the polar laminated terrain, thought to form one per obliquity cycle, have individual thicknesses of about 30 m (Cutts et al., 1979), a value which is of the same order as our upper limit estimate. Thus, although transport of dust is a key element in the formation of the polar laminated terrain (e.g., Pollack et al., 1979; Pollack, 1979; Cutts et al., 1979), transport of water from pole to pole is likely to play a major role and must not be ignored.

d. Comparison with surface thermophysical properties

Irrespective of the precise mechanisms which are controlling the seasonal behavior of atmospheric vapor, it is likely that the thermophysical properties of the surface will play a role in determining that behavior. This is because of their control on the diurnal and annual surface and subsurface variations in temperature and consequent control of the amounts of water that both the atmosphere and subsurface are capable of holding. Both the thermal inertia (I) and the bolometric albedo (A) of the surface have been mapped over a large fraction of the surface of Mars by Palluconi and Kieffer (1981). For comparison purposes, the resolution of these maps has been degraded to 10° in latitude and longitude from the original 2° ; contour maps made from the 10° binning are shown in Figure 13. The thermal inertia controls the diurnal variation of surface temperatures as well as the depth beneath the surface to which thermal energy can penetrate in a fixed time. The variations in inertia are controlled primarily by variations in the effective particle size of the surface material. The albedo determines the amount of solar radiation absorbed at the

Figure 13: Global maps of the albedo (a) and thermal inertia (b) of the surface. Contours were drawn from data placed into bins 10° in latitude by 10° in longitude. Units of albedo are percent, of thermal inertia 10^{-3} cal/cm² s^{1/2} K. Data are taken from the work of Palluconi and Kieffer (1981).



surface and hence controls the average value of the surface temperature. For a more detailed discussion of these properties, see Kieffer et al. (1977), Jakosky (1979), Palluconi and Kieffer (1981), or Jakosky and Muhleman (1981).

Comparison of the water vapor abundances, both from the period maps (Plate 1) and the annual average maps (Figure 8), with the inertia and albedo maps reveals some interesting relationships. With the exception of the dusty time periods, as discussed earlier, the period maps show no unique trend with respect to either of these properties. There also is very little correlation of the year-average water amounts with thermal inertia (see Table 3). The albedo seems to correlate better, but the dominant trend is by far that of the year-average water with airmass.

Dividing the year-average abundance by airmass takes out the largest part of this correlation. The resulting map of year-average water vapor abundance/airmass (hereafter, YAW/AM) appears remarkably like the albedo and inertia maps (compare Figure 8b with Figures 13a and b). Quantitatively, the degree of correlation can be seen in Table 3 and in Figures 14 and 15, which are cross-plots of YAW/AM versus thermal inertia and albedo, respectively. For simplicity, only data from the equatorial region (latitudes -20° to $+30^{\circ}$) are shown in these figures. The global correlation for albedo is very similar to that of this equatorial region while that for inertia is not nearly as good, as seen in Table 3. Table 3 also shows that the correlation of annual-average vapor abundance with airmass is the best of any correlations examined, and that the correlations seen in Figures 14 and 15 are secondary to this.

One can test whether the correlation of YAW/AM with albedo and inertia is coincidental, arising as a result of dividing by airmass and building in any existing correlation of I or A with airmass. Figure 16 shows the correlation of

Figure 14: Cross-plot of annual average vapor abundance/airmass versus thermal inertia.

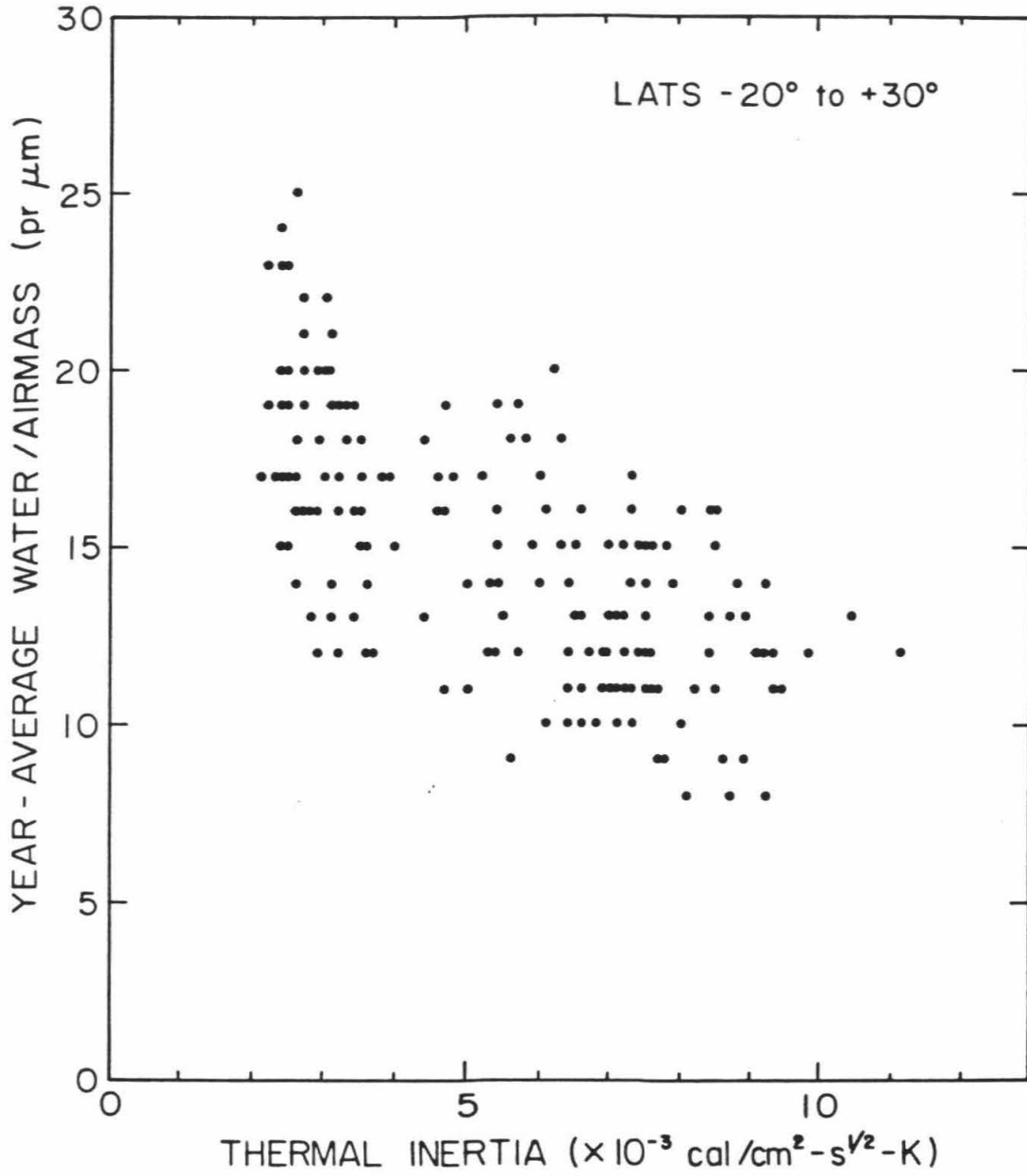
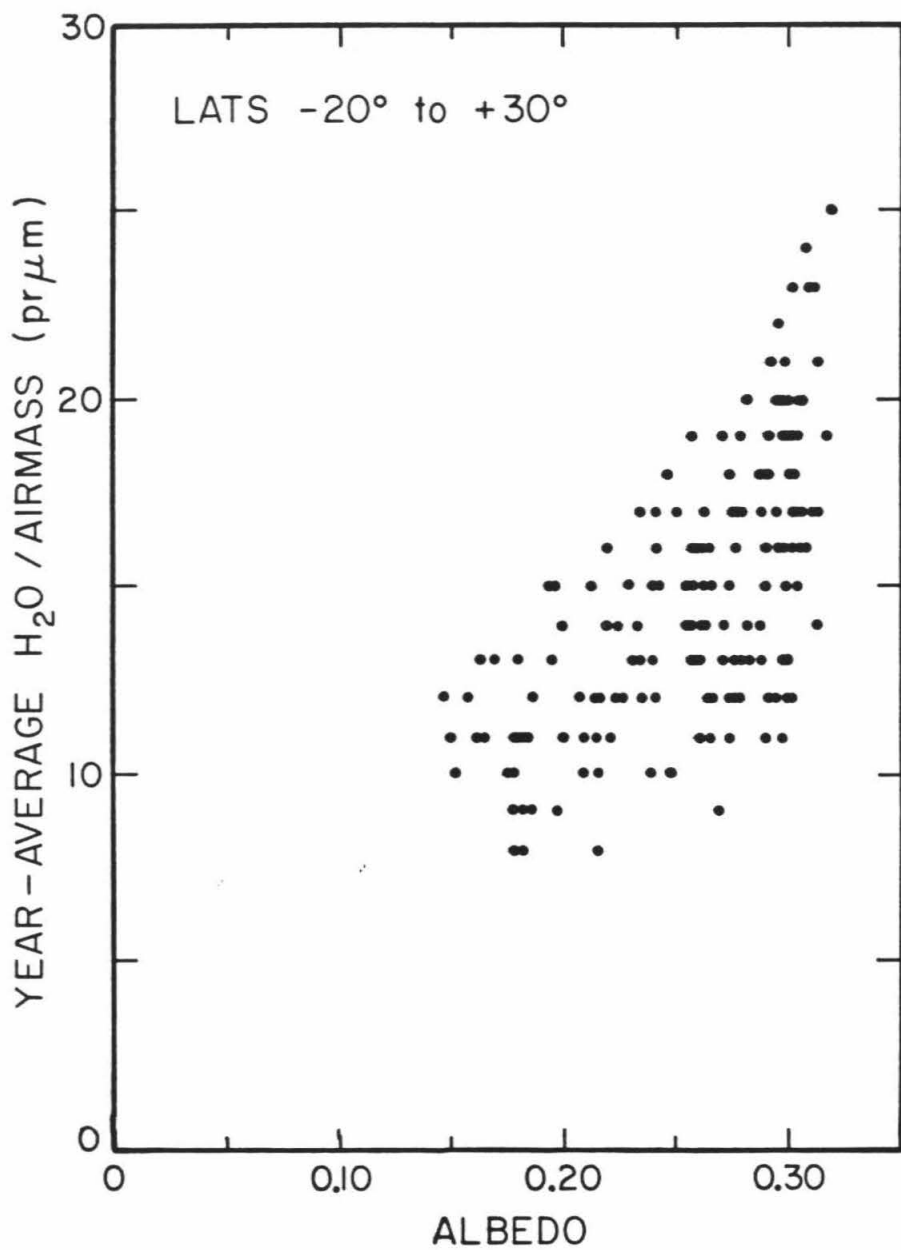


Figure 15: Cross-plot of annual average vapor abundance/airmass versus albedo.



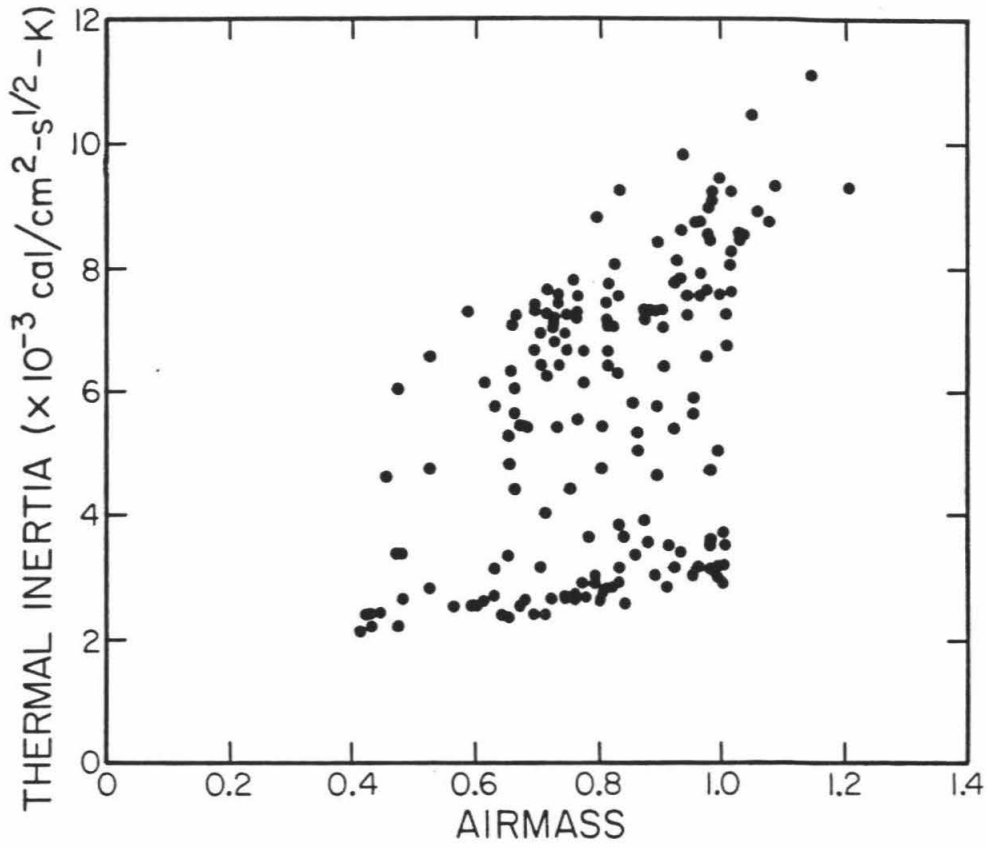


Figure 16: Cross-plot of the surface thermal inertia versus local airmass, including data between -20° and $+30^\circ$ latitude.

inertia with airmass, and Table 3 gives the correlation coefficients for both inertia and albedo. Although there is a correlation, with the lowest places on the planet having the highest inertias, and vice versa, the trend is by no means simple or unique (Jakosky, 1979; Palluconi and Kieffer, 1981). The correlation is dominated by the occurrence of two populations, one at low and one at high inertias, with elevation being a small affect within each population and between populations. The overall correlation is not as strong as in Figures 14 and 15, and the magnitude of any resulting built-in bias is not important.

The possibility exists that the dust present in the atmosphere even far away in time from the dust storms could produce this type of behavior, as it did for the period 10 water map during the dust storm. Compare the correlation of water vapor with albedo for the period 10 map (Figure 4) and for the YAW/AM map (Figure 15). In the former, going from low to high albedos corresponds to a change in observed water abundance from about 6 to 9 pr μm ; in the latter, the water changes from about 10 to 18 pr μm . The fractional change is larger for the YAW/AM map. For this map, however, dusty time periods were explicitly excluded, and the dust opacity was typically a factor of five or more smaller than it was during period 10 (see Pollack et al., 1979). It is estimated that if dust were producing this effect in the YAW/AM map, the largest part of the reflected energy would be coming from the atmosphere rather than the surface throughout most of the year; this is inconsistent with the low extinction opacities and strongly forward-scattering behavior of the atmosphere away from the dust storm periods (Pollack et al., 1977, 1979). Based on a simple model of light scattering from the surface and atmosphere, an atmospheric-dust-caused trend with albedo will, for opacities typical of the non-dust storm periods, be several times smaller than is observed. While variations in dust opacity related to albedo or thermal inertia may also produce these observed correlations, it is

unlikely that the variation would be large enough to produce this trend; a factor of two change in vapor abundance would require opacities to be significantly greater than one over the dark areas for much of the year. While variations in opacity from region to region are inferred from thermal infrared observations (Christensen, 1982), the magnitude of the opacities and the variations is not large enough to produce the effect.

Thus, the correlations shown in Figures 14 and 15 are real and the atmospheric vapor abundances are affected by the surface thermophysical properties. This behavior can be understood qualitatively as resulting from one of several possible mechanisms, including control of the vapor abundances by interaction with the regolith or by the saturation state of the atmosphere.

If interaction with the regolith is important in the seasonal water cycle, as suggested in the previous section, surface thermal inertia will play a key role in the process. A larger thermal inertia will allow a deeper part of the regolith to undergo diurnal temperature cycling, and will result in the diurnal variation at the surface being smaller. Both effects can affect the adsorption and diffusive transport of vapor due to the temperature dependence of these processes. Also, low-inertia surfaces will usually be composed of smaller particles (see Figure 11 of Kieffer et al., 1973), which will act as a greater reservoir for adsorbed water due to the larger available surface area and will at the same time inhibit vapor diffusion due to the smaller pore space size. If inter-particle bonding (e.g., Kieffer, 1976) is important, however, high-inertia surfaces may instead have smaller pore spaces and thus act to inhibit diffusion. Both the thermal inertia and the albedo exert control on the average temperature of the surface and subsurface. Due to the anti-correlation of albedo with inertia (Kieffer et al., 1977; see also Table 3), the effects add and result in low I -high A surfaces being as much as 18 K cooler on the average over a diurnal cycle than high I -low A

surfaces (Jakosky and Muhleman, 1980). As the processes of adsorption and desorption in the regolith are highly non-linear with temperature (Fanale and Cannon, 1974), these effects can be expected to play an important role.

Finally, the water vapor content of the atmosphere may to a degree be controlled by the saturation state of the atmosphere, as suggested by Davies (1979b). In this case, the atmospheric temperatures would determine the amount of vapor present if the vapor saturates during the coldest part of the day. The atmospheric temperatures are controlled predominantly by radiative processes, including absorption of both incoming solar radiation and emitted surface thermal radiation (Gierasch and Goody, 1972; Pollack et al., 1979), but atmospheric dynamics plays a role also (Pollack et al., 1979). The amount of absorbed sunlight will be albedo-dependent in the presence of a dusty atmosphere due to absorption of sunlight reflected off the surface. Due to the above-mentioned role of albedo and inertia in determining the surface temperatures and hence the emitted thermal energy, atmospheric absorption of thermal energy will also depend on these properties.

The above discussion of the effects of the thermophysical properties is not intended to be categorical, but rather to show the plausibility of a dependence of atmospheric vapor on the physical properties of the surface. Detailed modeling of each of the possible processes mentioned is complicated by the uncertainty in our understanding of the detailed structure of the surface and subsurface and by the large number of physical possibilities.

II.B. The Saturation State and Vertical Distribution of Water Vapor in the Mars Atmosphere

1. Introduction

Knowledge of the vertical distribution of water vapor and of temperature within the Mars atmosphere allows information to be obtained regarding the degree of saturation as a function of height. These are important inputs into analysis regarding the location and abundance of water in clouds or fogs, the transport of water due to the atmospheric circulation, the exchange of water with the regolith on diurnal or seasonal timescales, and even possible surface chemistry and biology.

The vertical distribution of vapor has been inferred by several means. Farmer (1976) pointed out that the effective temperature of formation of the water vapor absorption lines as determined by earth-based observers is higher than the mass-weighted atmospheric temperature (225 K as compared to 204 K), implying that the vapor is concentrated nearer to the surface. Analysis of MAWD spectra by Farmer and Doms (1979), however, indicates an effective temperature of $195\text{-}200\text{ K} \pm 10$, implying a more-uniform mixing. Davies (1979a) modeled the effect of masking of vapor due to reflection of sunlight off of atmospheric dust and found that the vapor is distributed with height about the same as the dust, which is itself nearly uniformly distributed (Pollack et al., 1977; Kahn et al., 1981), although both of these results may be off by as much as 50%.

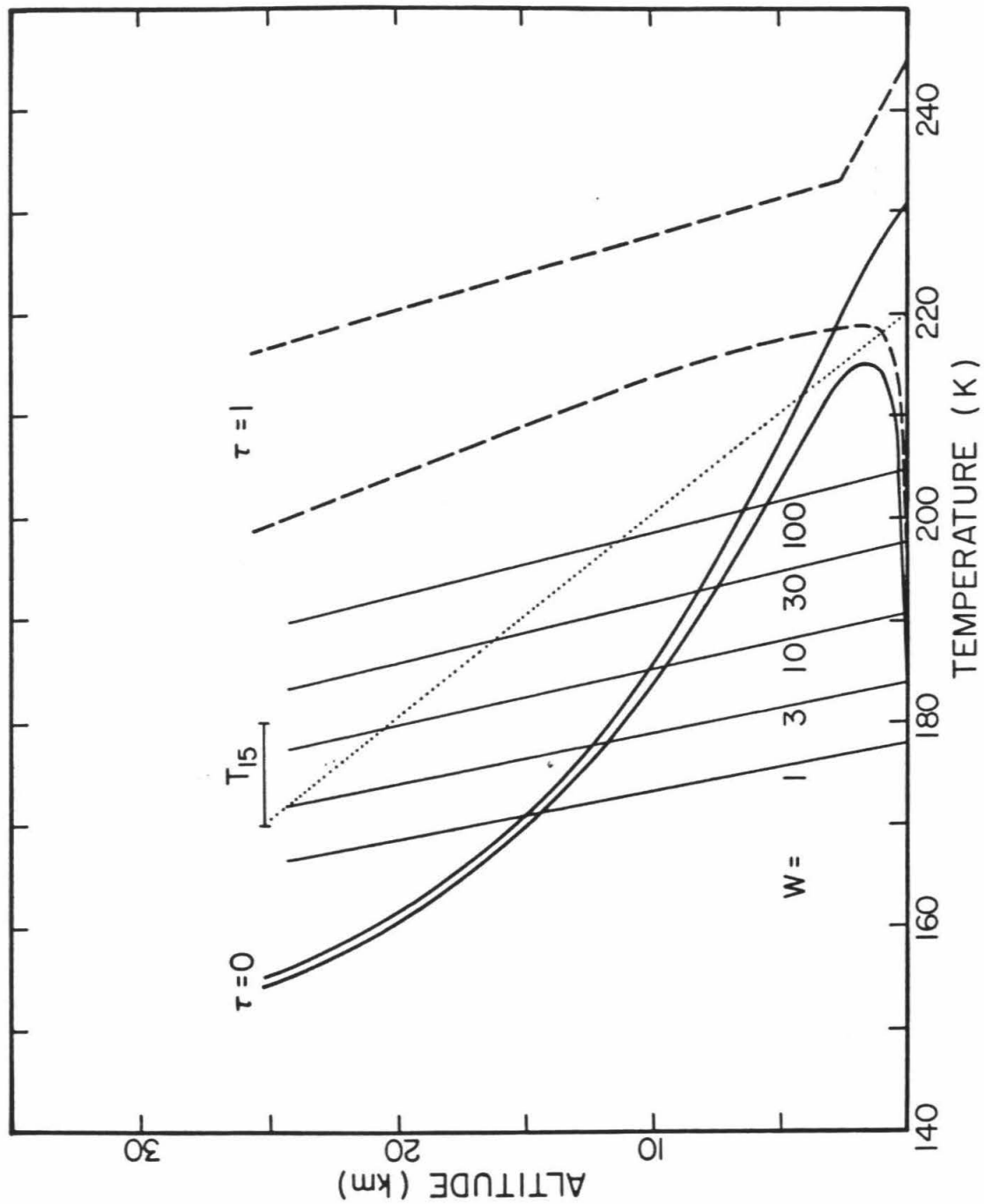
Possible vertical distributions can also be examined by comparing the known vapor column abundances with observed or modeled temperatures and looking for regions of possible saturation. Davies (1979b) compared observed column vapor abundances with radio-occultation-derived temperature profiles.

His results indicate that the bulk atmosphere is not near saturation at any time except over the polar caps. During the day over much of the planet, the atmosphere can hold orders of magnitude more water than is present; even at night it can hold more water than is seen.

Based on models of the temperature structure obtained by Gierasch and Goody (1968), Hess (1976) concluded that if the vapor were distributed uniformly it would saturate very low in the atmosphere, and that the vapor must therefore be confined to within the lowermost scale height (about 10 km). This effect can be seen in Figure 17, which shows possible temperature profiles as predicted by the model of Pollack et al. (1979) for two values of the atmospheric opacity. Also shown are vapor saturation temperature curves for various column vapor abundances (using the Goff-Gratch formulation for the saturation vapor pressure over ice, contained in List, 1951), assuming uniform vertical distribution. Hess (1976) in essence compared the vapor abundances with the $\tau = 0$ profile. In this case, the atmosphere would saturate below 10 km for even as little as about 6 pr μm of atmospheric vapor distributed uniformly vertically; the observed values of about 30 pr μm would require that the vapor be predominantly below about 7 km. The presence of atmospheric dust raises the temperatures at all altitudes due to absorption of both solar and emitted thermal radiation. For the $\tau = 1$ case shown in Figure 17, the temperatures are all high enough that saturation would not occur below 30 km. The observed amounts of vapor could then be distributed nearly uniformly with height. Actual values of the opacity are typically 0.5 (Pollack et al., 1977, 1979).

As can also be seen in Figure 17, the near-surface temperatures undergo large diurnal variations, regardless of the atmospheric opacity. Thus, if the vapor were mixed uniformly, it is possible that the near-surface vapor would saturate at night to form low-lying fogs. The formation of a fog would depend on

Figure 17: Atmospheric temperature structure at 20° latitude and $L_s = 100^\circ$. The curves labelled " $\tau = 0$ " and " $\tau = 1$ " are model profiles at 4 and 16 H local time, incorporating atmospheric dust with the total opacity indicated, and are taken from Pollack et al. (1979). The bar labelled T_{15} shows the observed diurnal range of temperature at that location and season at the height indicated; the dotted line indicates the temperature for a lapse rate Γ of 2 K/km. The lighter lines are vapor saturation temperatures, assuming that the indicated amount of vapor (in μm) is uniformly distributed with a scale height of 10 km.



the amount of vapor present as well as its vertical distribution, and on the temperatures which the lower atmosphere would attain at night. Widespread morning fogs and hazes have been reported by many observers (e.g., Slipher, 1962; Smith and Smith, 1972; Carr et al., 1976; Briggs et al., 1977; Soderblom et al., 1978). Diurnal opacity variations have been seen at the Viking landing sites and are attributed to fog formation (Pollack et al., 1977, 1979), and possible saturation of the lower atmosphere and consequent fog formation has also been reported (Ryan and Sharman, 1981).

In the following sections, the column vapor abundances observed by Viking are compared with atmospheric temperatures as observed by both Viking and Mariner 9. This will allow discussion regarding the vertical distribution of the vapor and possible saturation at the top and bottom of the atmosphere.

2. The Vertical Distribution of Vapor

If the column vapor abundances could be compared with simultaneous information regarding the atmospheric temperatures, the possible vertical distributions could be deduced. Unfortunately, only the atmospheric temperatures at about 25 km elevation were measured by Viking (e.g., Martin et al., 1979; Martin, 1981). While useful comparisons can still be made (see below), their utility is limited due to the poorly known variation of temperature with height.

The Mariner 9 IRIS experiment did obtain temperatures as a function of both location and height during 1971-1972 (e.g., Hanel et al., 1972; Conrath et al., 1973); these can be compared to the 1976-1978 Viking observations of water vapor. Such a comparison is likely to be valid because the Mars atmosphere is nearly in radiative-convective equilibrium (Goody and Belton, 1967; Gierasch and Goody, 1968), such that the structure would be expected to repeat from year to year except for the time periods of the global dust storms and except when different amounts of dust may be present in the atmosphere. Figure 18 shows the temperature structure as inferred from Mariner 9 data for the period $L_s = 43^\circ$ to 54° in 1972 (presented by Pollack et al., 1981). This time period is well after the complete decay of the global dust storms during both years (Conrath, 1975; Pollack et al., 1979), when the dust abundance in the atmosphere has decayed to its background (lowest observed) level. The minimum daily temperature at the 25 km level, as observed in 1978 by the Viking IRTM (see Martin, 1981), in fact agrees quite well with the IRIS temperatures. Also shown in Figure 18 are contours of the saturation temperature, obtained assuming that the observed vapor ($L_s = 35^\circ$ to 50°) is distributed in height uniformly. Were the vapor to actually be uniformly mixed, saturation (and condensation) would occur anyplace that the actual

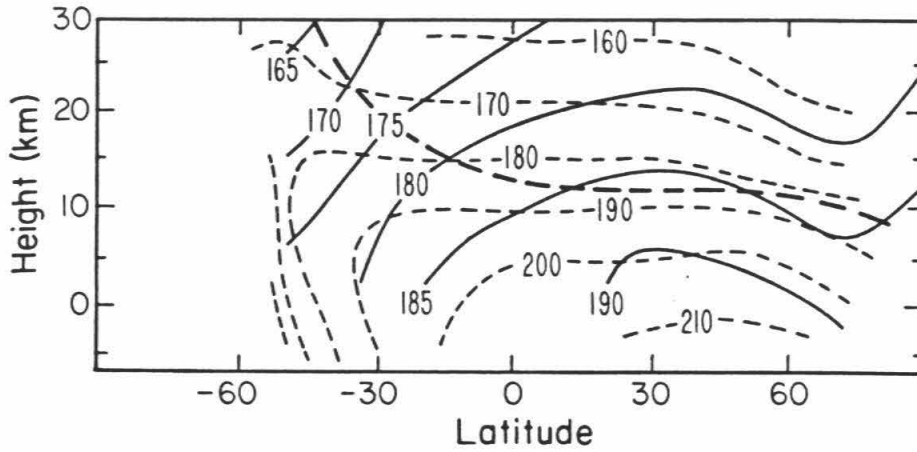


Figure 18: Atmospheric structure observed by Mariner 9, $L_s = 43$ to 54° . The light dashes indicate the observed temperature structure, and are taken from Pollack et al. (1981). The solid lines are the inferred vapor saturation temperatures (see text). Above the heavy-dashed line, temperatures are lower than the saturation value and vapor would condense; the vapor must therefore be generally confined to beneath this level.

temperature was less than or equal to the condensation temperature. This region of possible condensation is marked in Figure 18 by the heavy dashed line, above which saturation would occur. This is not to say that saturation actually does occur, but rather that the vapor present must be confined to the region below the line in order for saturation to not occur. The absence of ubiquitous optically-thick clouds at this season indicates this to be the case. Therefore, the vapor is contained within the lowermost scale height in the northern hemisphere. In the south, the region of confinement is higher, going up to as high as 30 km (about three scale heights) at -45° latitude. Again, these altitudes represent upper limits to the regions of vapor confinement, above which the vapor would saturate. Similar analysis at other seasons is hindered by the uncertainty in the temperature structure and in the relative atmospheric dust abundances during the decay of the global dust storms.

The analysis can be extended to other seasons by using the Viking IRTM measurements of upper atmospheric temperature. Measurements of T_{15} are shown in Figure 17, as measured by the IRTM at the same latitude and season as the models shown in that figure (Kieffer et al., 1976b). The bar represents both an uncertainty in the individual measurements of several degrees and a diurnal variation of about 10 K. The T_{15} weighting function is very broad within the atmosphere and the measured brightness temperature corresponds to the actual temperature, for reasonable temperature profiles, at about the 0.63 mbar level, at an altitude of about 25 km (Kieffer et al., 1976b,c). This serves to pin down the actual temperature profile and shows that saturation will occur at this altitude at night for a uniformly distributed vapor with column abundance of greater than $3 \text{ pr } \mu\text{m}$. Because the abundance at this latitude ($+20^\circ$) at this season is about $10 \text{ pr } \mu\text{m}$ the vapor must be predominantly below 25 km.

If the temperature lapse rate Γ at this altitude were known, a more precise determination of the maximum height of the vapor layer could be made. Estimates of Γ based on the emission angle dependence of T_{15} indicate values in the range 1.5 to 2.0 K/km (Martin and Kieffer, 1979; T.Z. Martin, unpublished data, 1981). The uncertainties in these values are large, however, and the interpretation is difficult due to the large vertical extent of the weighting functions. Examination of the radio occultation temperature profiles of Fjeldbo et al. (1977) and Lindal et al. (1979) also reveal lapse rates at these altitudes in the vicinity of 2 K/km (for those profiles away from the polar regions). The value of 2.0 K/km is adopted here. Although Γ must be a function of season, location, and altitude, there is no accurate and complete information as to its variations. Applying this lapse rate to T_{15} in Figure 17 indicates that 10 pr μm of vapor could be distributed uniformly up to a height of about 20 km. Above this height, vapor abundance must drop off sharply due to the temperature dependence of the saturation curve.

This type of analysis is applied here to the latitudinal variation of vapor for six periods throughout the Martian year. The vapor abundances used are zonal averages binned 10° in latitude by 15° in L_s , as discussed in Chapter II.A. The T_{15} values taken were the minimum diurnal values at each latitude, as presented by Martin (1981). The season used was that which overlapped most closely in time with the periods chosen from the water vapor data. T_{15} values were averaged into 10° latitude bins from the original 2° bins of Martin (1981) for easier comparison with the vapor abundances. The value of T_{15} was taken to apply to the 0.6 mbar level (at height z_{15}), taking into account the seasonal variation of pressure (Hess et al., 1979) and the latitudinal variation of topography (U.S. Geological Survey, 1976), and assuming a constant bulk atmospheric scale height of 10 km. Atmospheric temperatures at other heights

were obtained from

$$T(z) = T_{15}(z_{15}) + \Gamma(z_{15} - z) \quad (1)$$

where z_{15} is the height above the surface to which T_{15} corresponds. In the analysis which follows, it must be recalled that there is an uncertainty in the atmospheric temperature at a given height, which is proportionate to the departure from the ~ 25 km height to which T_{15} applies, due to the uncertainty in Γ .

Figure 19 shows the T_{15} values as a function of latitude at each season. Also shown are the saturation temperatures at z_{15} , assuming that the observed vapor is distributed uniformly with height. Wherever the values coincide, uniformly distributed vapor would first saturate at z_{15} . If $T_{\text{sat}} > T_{15}$, saturation would first occur at a lower level. If $T_{15} > T_{\text{sat}}$, saturation would first occur at a higher level. The height to saturation (h) was determined in each case such that the vapor is distributed uniformly up to this height, with no vapor present above this height. The results are shown in Figure 20.

Most often the height to saturation is in the range of 10 to 25 km. The values of 30 to 40 km which occur during period 13 ($L_s \approx 267^\circ$) are a consequence of the high values of T_{15} which occur between the two global dust storms of 1977, and which presumably result from solar heating due to the presence of high-altitude dust at this time. The values of h near the poles are probably not dependable due to the likely inapplicability of the assumed lapse rate. At the south pole there must be a temperature inversion at $L_s \approx 267^\circ$, as discussed earlier. At the north pole, the measured T_{15} and surface temperature would imply $\Gamma \approx 1$ K/km over the cap material (Kieffer et al., 1976a). Even away from the poles, values of h as low as 10 km may be significantly in error if the lapse rate is not exactly 2 K/km between about 25 km and 10 km. The sense of

Figure 19: Observed T_{15} values and T_{sat} at z_{15} corresponding to the observed vapor abundances, shown as a function of latitude at several seasons. The numbers in the upper right are the period numbers from which the data were taken (see Table 1). L_s values are also shown for each period.

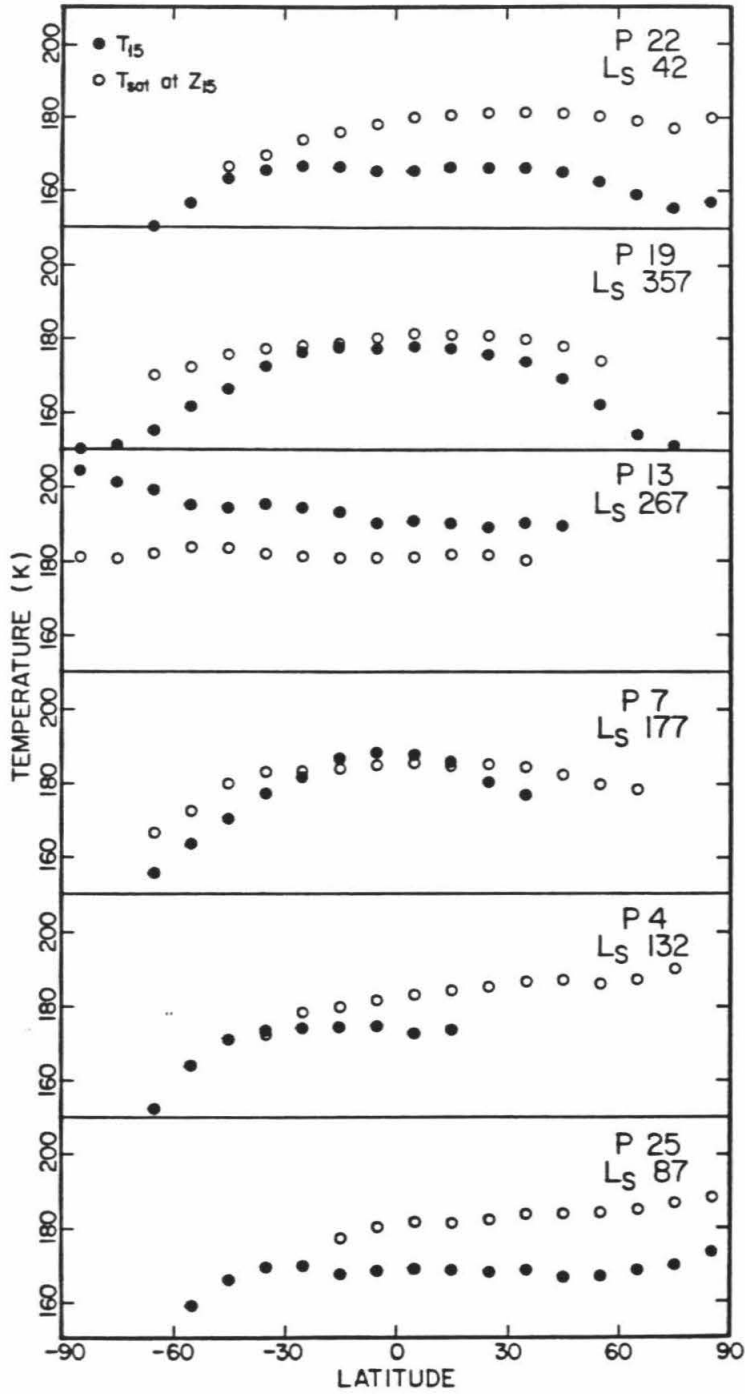
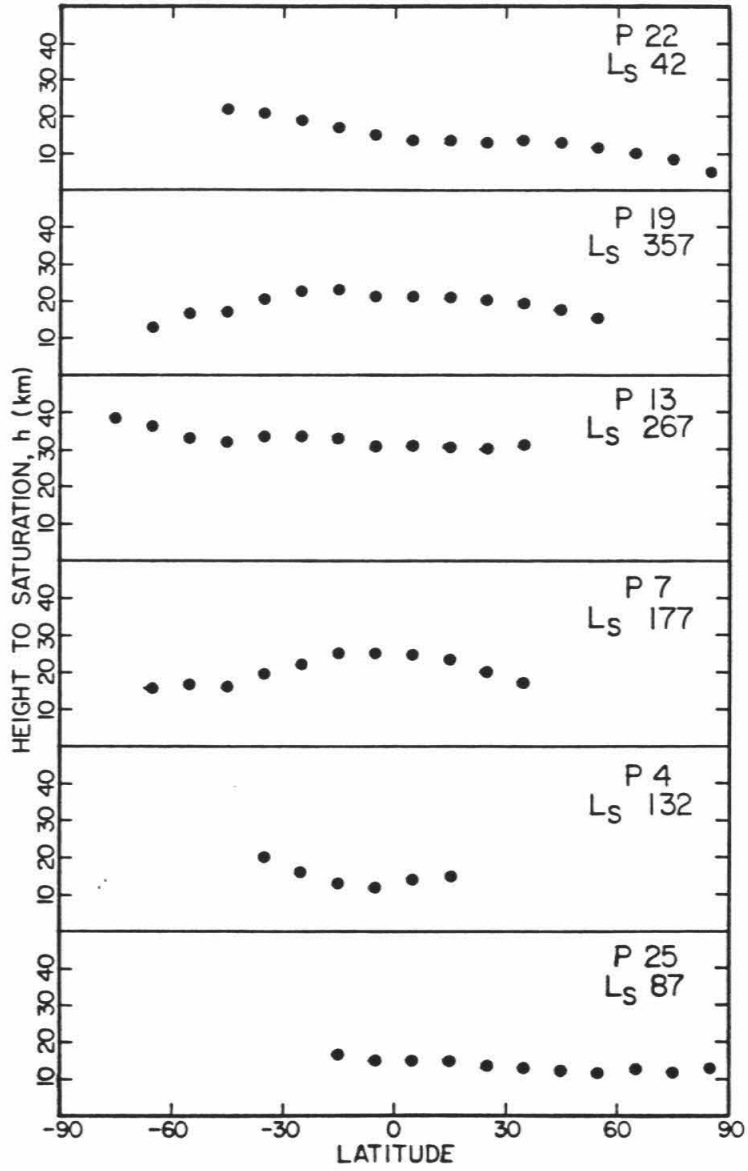


Figure 20: The height to saturation h as a function of latitude for the same periods as were discussed in Figure 19. See text for details.



h will be correct however, in that it must be much less than 25 km in those cases in order to explain the large temperature differences seen in Figure 19.

There seems to be no unique trend of h with latitude. There is a trend with L_s , with values in the northern hemisphere typically being lower during summer and higher during winter. This results from the fact that the vapor abundances are largest in the summer and the fact that the T_{15} values are largest in winter due to the presence of dust. It should be emphasized here that the results in Figures 18 to 20 show that the data are not consistent with uniform mixing of vapor. They are, however, consistent with uniform mixing up to a height h of between 10 and 30 km at which point saturation would occur. There is no general way to determine if the vapor is concentrated more toward the surface than this, however. The temperatures between this height and the surface are generally high enough that there is no difficulty with the atmosphere holding as much water vapor as is observed (see Figure 17).

3. Early-Morning Ground Fogs

The formation of a low-lying widespread ground fog may occur because the near-surface atmospheric temperatures undergo a large-amplitude diurnal variation, dropping below the local saturation temperature at night. This will result in the formation of a fog within the lowermost hundred meters or so of the atmosphere prior to dawn. Any condensate which settles out of the atmosphere and onto the surface will sublime rapidly after sunrise and contribute to the morning fog as it contacts the cooler atmosphere (Hess, 1976). The complete radiative transfer solution to the temperature profile would provide information as to the properties of this expected fog (e.g., Flasar and Goody, 1976), but the results would be very model dependent. A simpler approach is taken here which should provide some basic first-order results regarding fog formation.

The amount of fog formed in the immediate vicinity of the surface is determined by knowing the temperature and the water vapor concentration within the lowest part of the atmosphere. The vapor concentration is obtained from the column abundance of vapor measured at a given location and season assuming uniform vertical distribution with a scale height of 10 km. Although the vapor may be concentrated in the lowest part of the atmosphere, as just discussed, the condensation temperature is not a sufficiently strong function of the vapor partial pressure to significantly change the results to be discussed. A factor of two change in surface vapor pressure corresponds to only about a 3 K change in the saturation temperature (see Figure 17).

The atmospheric temperature near the surface just prior to dawn is taken to be equal to the surface temperature at that time. Viking lander meteorology measurements show this to be a valid assumption (Hess et al.,

1977). The predawn surface temperature is determined at any season and location using the values of thermal inertia and albedo derived from surface temperature information by Palluconi and Kieffer (1981) in conjunction with the thermal model of Kieffer et al. (1977). Because the inertia and albedo were determined simultaneously so as to match the observed infrared brightness temperature, the inverse process leads directly back to the temperatures. A kinetic temperature was obtained from the brightness temperature assuming a bolometric emissivity of 0.97 (see, e.g., Christensen, 1982).

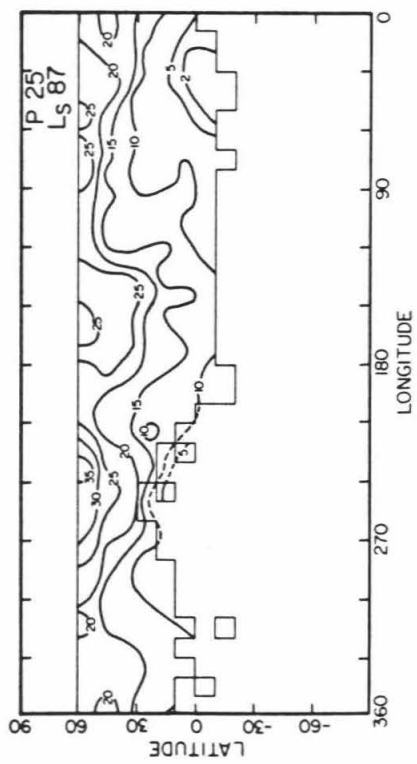
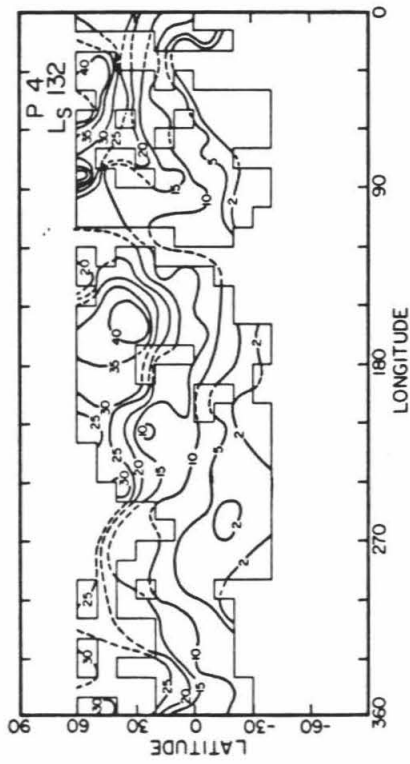
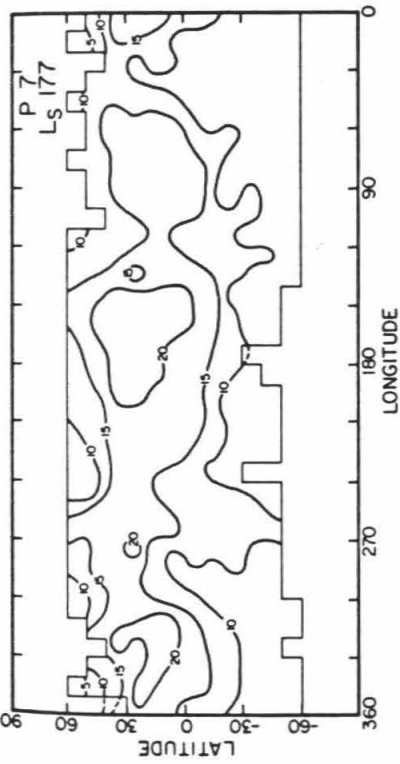
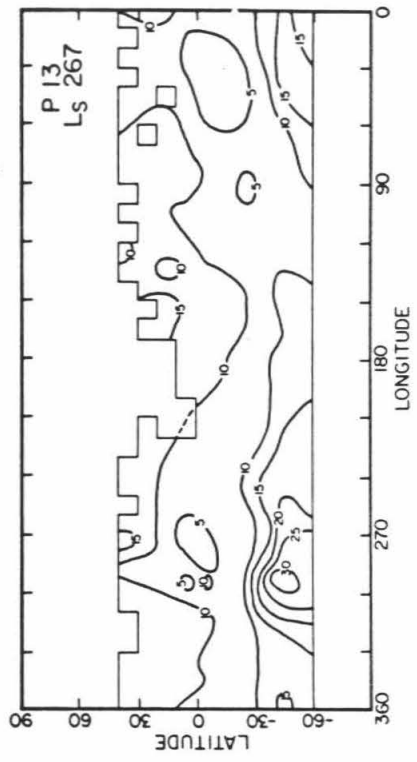
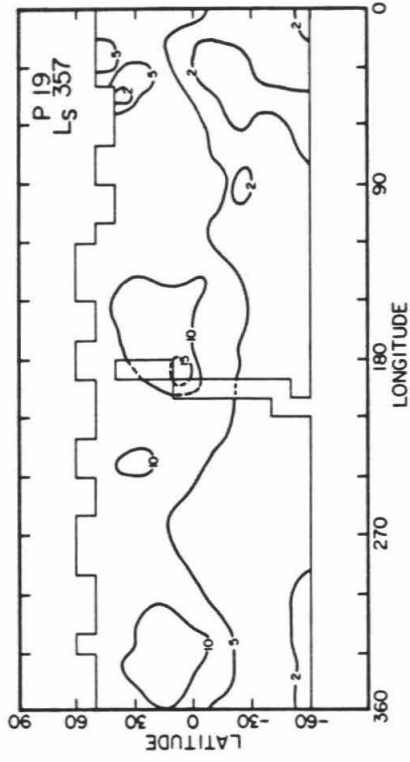
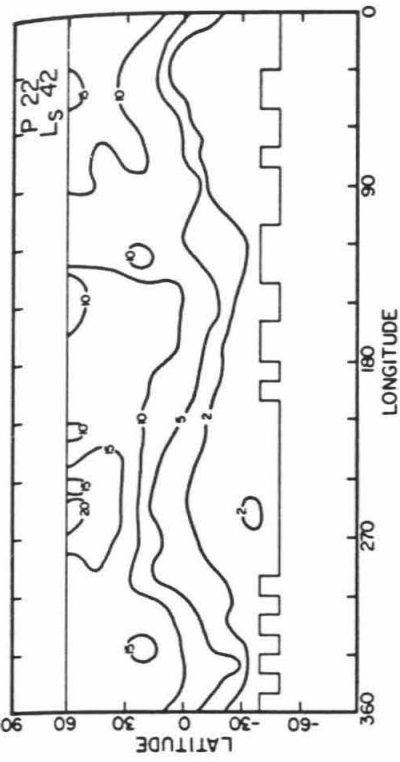
The saturation pressure at the predawn temperature determines how much water can be present in the vapor state. Any remaining water is taken to be in the form of condensates in the atmosphere. Thus, the method used here determines a fog density near the surface. The total amount of fog present and the corresponding optical thickness that will obtain depend on the assumed or modeled change of temperature with height.

Maps of the expected fog density are shown in Figure 21 for the same time periods as were discussed in the previous section. The maps were constructed from data placed into bins 10° in latitude by 10° in longitude. The contours shown are in units of 10^{-10} g/cm³ (or 10^{-6} pr $\mu\text{m}/\text{cm}$) of condensate in the atmosphere near the surface. The fog density is a function of both the minimum daily temperature and the column vapor abundance. The general trend appears to be for the fog density to be greatest in the summer when the vapor abundances are greatest and over regions of low thermal inertia, where temperatures are lowest. That more of the vapor present will condense out at night in the winter when the temperatures everywhere are lowest is tempered by the relative dearth of vapor at that season in each hemisphere.

Whether these fogs will be visible depends on both the thickness of the

Figure 21: Global maps of fog density for the same periods as were discussed in Figures 19 and 20. Units are 10^{-10} g/cm³ or 10^{-6} pr $\mu\text{m}/\text{cm}$.

See text for a detailed discussion.



condensing layer and on the size of the condensate particles formed. Based on the models shown in Figure 17, condensation might be expected to occur within approximately the lower 100 m of the atmosphere. Assuming that all of the vapor within this layer contributes to the fog, the optical depths are calculated as the condensate particle effective projected area/unit area:

$$\tau \approx 3m/2r \quad (2)$$

where m is the condensate mass in grams/cm² and r is the particle radius in centimeters. Because the vapor would condense onto the airborne dust grains already present, the particle size would be nearly that of the dust, yielding an effective size of about 2.5 μm (Pollack et al., 1979). For 30 pr μm of vapor, this results in a fog opacity of about 0.2. Interestingly, Viking lander observations of diurnal opacity variations inferred to be due to overnight formation of fog yield a contribution to the total opacity from the fog of about 0.13 (Pollack et al., 1977). Although this near-agreement may be fortuitous, owing to the possible errors in the assumptions of particle size and fog layer thickness, it still presents an interesting correspondence.

Ryan and Sharman (1981) have discussed evidence in the Viking lander atmospheric temperature variations for passing through the frost point and forming a ground fog during the predawn hours as temperatures fall. They conclude that inflections in the curve of temperature versus local time of day are likely to be due to saturation and condensation near the surface. Of the events that they discuss, many of the temperatures at which the inflections occur are consistent with the total column abundances observed by the MAWD if uniform mixing of vapor is assumed. At least two of the events, however, have inflections at temperatures that would indicate saturation with one to two orders of magnitude less vapor than is observed. Whether this indicates a flaw

in the inflection/saturation hypothesis or an increasing vapor abundance with height at that season cannot be readily determined. In either case, it points out an ambiguity in the interpretation of the lander temperature curves which must be considered when interpreting them in terms of the column vapor abundance.

Based on Figure 21, the optical thickness of the fogs mapped might be expected to vary from zero to about 0.3. This is not thick enough to drastically reduce the visibility of surface features when viewed normally, especially when compared with the dust contribution to the opacity of, typically, 0.5 (Pollack et al., 1979). It can, however, explain the repeated observation of widespread morning haze at a variety of locations and seasons (Slipher, 1962; Smith and Smith, 1972; Carr et al., 1976; Briggs et al., 1977; Soderblom et al., 1978).

Due to the nature of the analysis, the fogs expected on the basis of Figure 21 are widespread, diffuse hazes. In the discussion by French et al. (1981) of clouds observed by Viking, diffuse hazes were ignored and only discrete fogs associated with topographic barriers were mapped. It is thus not clear what the relationship between the two should be. French et al. (1981) found discrete fogs most abundant in the southern hemisphere, opposite from the distribution expected on the basis of the water vapor distribution. They may have been affected by an observational bias, however, related to the actual distribution of observed images on the planet. There seems to be no correlation between the location of the diffuse fogs predicted here and the discrete fogs mapped by them. There is also no correlation between the occurrences mapped by French et al. and the distribution of vapor column abundance. Again, this is no surprise due to the differences in nature and resolution of the types of fogs discussed. The discrete fogs may be due to a localized enhancement of vapor, or to a localized variation of surface thermophysical properties on a scale smaller than the 10° bins used here and associated with the individual relief features in

which the fogs occur. It will be very interesting to compare the diffuse fogs predicted here with those diffuse fogs actually observed by the Viking orbiters (Kahn and Gierasch, 1982); differences between the two may yield information on boundary layer processes or on the actual vertical distribution of water vapor within the atmosphere.

4. Discussion

Several interesting conclusions can be reached regarding the vertical distribution of vapor and the saturation state of Mars' atmosphere. The vertical eddy diffusion coefficient in the lower atmosphere is of order 10^7 cm²/s or greater. This result is based on observations of dust storm dissipation (and applies to the lower 30-50 km of the atmosphere; Conrath, 1975), photochemical modeling (20-50 km; Kong and McElroy, 1977), and atmospheric tidal theory (30-80 km; Zurek, 1976). The lowermost 5-10 km is actively convecting each day (Gierasch and Goody, 1968, 1972; Pollack et al., 1979), so would have an effective value of the eddy diffusion coefficient at least this large. Thus, mixing of the atmosphere is rapid compared to the seasons and the vapor is likely to be uniformly mixed on a timescale of days throughout the atmosphere except where saturation would occur. The timescale for seasonal variation of the column vapor abundance is much longer than that for vertical mixing, such that addition or removal of vapor from the bottom of the atmosphere will not cause an enhancement or depletion of vapor at any altitude relative to uniform mixing. At some height h , the vapor abundance must drop off much more rapidly with height in order that the atmosphere not be supersaturated. This height to saturation h varies between about 10 and 30 km, depending on location and season.

Flasar and Goody (1976) discussed the diurnal variation of water vapor within the atmosphere as caused by fog formation and daily exchange with the regolith. Because the atmosphere is stable, only vapor within the lowermost ~ 1.5 km can make it to the surface each night. If the vapor is distributed up to 10-30 km, then only ~ 10 -20% of the vapor, at most, can cycle daily into the regolith or as fog.

At the bottom of the atmosphere, the daily temperature variations will cause saturation to occur near the surface at night at most locations and most seasons. If the vapor is concentrated more toward the surface than is indicated by the range of the height to saturation, then saturation temperatures are higher than assumed here and condensation will occur to a greater degree than discussed. It should be noted that, even at the extreme, the atmosphere is not at anytime saturated at all altitudes and is capable of holding much more vapor at all times of day (except possibly over the polar caps, where the situation is more complicated). This can also be seen in the calculation by Davies (1979b) of saturation vapor abundances using radio occultation temperature profiles. Of those predawn profiles analyzed, only those over the polar caps show saturation abundances near the observed abundance. The two predawn profiles not over the caps yield saturation abundances greater than twice the observed abundance, and the daytime non-polar profiles yield saturation abundances much greater than the observed abundance. Thus, the amount of vapor present must depend on the relative magnitudes of the sources and sinks for vapor on a daily and seasonal timescale and not simply on the vapor holding capacity of the atmosphere being filled at some particular time of day.

Also, recall that the discussion of saturation at the base of the atmosphere centers on the minimum daily temperatures. Except near the poles and on the seasonal polar caps, the daily maximum of temperature is generally high enough to cause any surface or near-surface condensate which forms at night to completely sublime. In a sense, it is the maximum daily temperatures which control the amount of vapor that the atmosphere can hold. This is because evaporation of condensate is a very rapid process (Ingersoll, 1970; Farmer, 1976), and a reservoir of surface ice would fill the available vapor holding capacity of the atmosphere very rapidly. That such a reservoir does not

exist is seen by the relatively low vapor abundances which occur despite an atmosphere warm enough to hold much more vapor.

Farmer (1976) has suggested that the daily cycle of condensation near the surface may cause vapor to be removed from the atmosphere into the regolith on a seasonal basis, accounting for the seasonal cycle. It is apparent, however, that the atmospheric water abundance cannot be controlled uniquely by the minimum temperature saturation abundance. In order for this mechanism to be effective, any condensed vapor must be partly removed from the system on a daily timescale. Burial of ice is not likely, because the aeolian deposition rates are too slow to bury any surface ice deep enough to allow it to survive a night (see Arvidson et al., 1979). More likely is the diffusion of vapor through the porous regolith and the seasonal storage at some depth in the form of adsorbed water or ground ice. Ice within the top meter of the regolith is stable at some seasons poleward of about $\pm 40^\circ$ latitude (Leighton and Murray, 1966; Fanale, 1976; Farmer and Doms, 1979), and diffusion to this depth through a non-adsorbing regolith is rapid. In an adsorbing regolith, the seasonal temperature variations cause changes in the equilibrium between vapor and adsorbed water, and are capable of driving a diffusive exchange of vapor with the atmosphere (see Chapter III). In either case, the seasonal process is more complicated than condensation of vapor at night and the consequent loss of the vapor on a seasonal basis from the atmosphere.

I.I.C. Interannual Variability of the Seasonal Cycle

1. Introduction

The Viking MAWD observations of Mars have provided detailed information on the seasonal and spatial variability of atmospheric water vapor for almost $1\frac{1}{2}$ Martian years. Whether or not the observed behavior is characteristic of the typical or average behavior during the current epoch remains to be determined. Comparison of the seasonal cycle of water as observed during many different years should provide information on its variability from year to year, and aid in understanding the processes controlling the behavior.

Some limited information about the interannual variation can be obtained by comparing the MAWD observations during the overlap of seasons in consecutive years (Chapter II.A; Zurek, 1982b); no significant differences are seen in the observed behavior. Additionally, observations of the vapor abundance made at some seasons by the Mariner 9 IRIS experiment can be discussed (Hanel et al., 1972; Conrath et al., 1973; Kunde, 1973). The most detailed information regarding other years, both in terms of the seasons observed and the number of different Mars years covered, can be obtained from Earth-based observations of the vapor abundance. Successful Earth-based spectroscopic observations were first reported by Spinrad et al. (1963). Subsequently, observations have been published by a wide variety of groups; these data have been summarized and synthesized by Barker (1976). The time period from the first detection up through the Viking observations encompasses about seven distinct Mars years, and should allow significant information to be learned about any possible interannual variations in the vapor cycle.

In the following sections, first the Mariner 9 and then the Earth-based

observations of the vapor cycle will be compared with the Viking data. Observations from Earth by E. Barker (personal communication, 1981), made simultaneously with the Viking measurements during 1976-1978, allow direct comparison to be made, thereby validating both of these techniques and allowing discussion and comparison of the earlier data. The comparisons between the various data sets are presented for the first time here and allow significant discussion of the observed year-to-year variations of the water cycle and its implications.

2. Mariner 9 Observations of Atmospheric Vapor

Thermal infrared spectra between 10 and 50 μm , obtained by the Mariner 9 IRIS experiment, have been used to determine the water vapor abundance of the Mars atmosphere (Hanel et al., 1972; Kunde, 1973; Conrath et al., 1973). The observations were obtained between November, 1971, and July, 1972, spanning a range in L_s from 293° to 60°. Table 4 summarizes their results of vapor abundance over the north and south polar regions and over the sub-solar latitude region. (The subsolar latitude varied during this time from about -23° at $L_s = 293^\circ$ to 0° at $L_s = 0^\circ$ to +22° at $L_s = 60^\circ$.) Listed for comparison are the vapor abundances over the same latitudes at the same season as observed in 1977-1978 by the Viking MAWD. The MAWD results are taken from the period maps, as presented in Chapter II.A, for the closest relevant seasons.

Direct comparison of the IRIS and MAWD results is hampered by the global dust storms which occurred during each year. The effect of dust on the MAWD reflectance measurements is to mask from view the water vapor in the lower part of the atmosphere, causing the measured abundance to be less than the actual abundance (Davies, 1979a). The values given in parentheses in Table 4 are estimates of the actual column vapor abundance in the atmosphere, as would likely have been observed by the Viking MAWD in the absence of significant dust. IRIS measurements are less sensitive to the dust, due to the nature of the observational method, but are strongly dependent on knowledge of the atmospheric temperature profile. Even small errors in the temperatures can lead to large errors in the water vapor abundance.

Basically, the sub-solar values agree with each other to within the uncertainties in the measurements. Small differences may be present, but there is no evidence for significant variability. The south polar summertime

Table 4. Comparison of Mariner 9 and Viking Observations of Mars Atmospheric Vapor.

Location	Vapor Abundance (pr μm) from		
	L_s	M9*	Viking**
South pole	297	10-20	8
	321	10-20	5
North pole	~ 300	< 8	†
	60	20-30	16
Subsolar latitudes	293	10-25	4 (10)
	314	10-20	5 (9)
	336	7-17	7 (8)
	~ 5	7-17	9

*From IRIS measurements, as reported by Hanel et al. (1972), Kunde (1973), and Conrath et al. (1973).

**From the MAWD period maps, taking the closest relevant period.

†Not observed.

measurements, which will be seen to be of especial interest later, show no evidence of being significantly different between the two years.

Observations were also made at the same seasons from the Russian Mars-3 spacecraft using reflectance measurements in the $1.38 \mu\text{m}$ water vapor bands (Moroz and Ksanfomaliti, 1972). Their results indicate between 1 and 3 pr μm of water vapor over most of the planet (at $L_s \approx 350^\circ$), with less than 1 pr μm over the north polar cap. These abundances are significantly lower than those reported by other observers, both from spacecraft and ground-based data.

3. Earth-Based Observations of Atmospheric Vapor

Earth-based determinations of the column abundance of water vapor in the Mars atmosphere are made by observing one of the water absorption bands at about 8200 \AA , Doppler-shifted due to a relative velocity between Earth and Mars and superimposed on the much larger absorption due to water in the Earth's atmosphere. The spectrometer slit can be oriented on Mars either parallel to the line between the poles and centered on the disk (pole-to-pole on the central meridian, or PPCM) or perpendicular to this line and at any latitude (parallel to the equator, or EQ). Observations to determine a time-of-day dependence of water vapor were also done (see Barker, 1976), but will not be discussed here.

Data obtained between 1976 and 1978 (E. Barker, personal communication, 1981) can be compared directly with simultaneous measurements by Viking, in order to validate both techniques. This will allow us to examine earlier years of Earth-based observations with confidence, in order to look for interannual variations. In order to compare Barker's data with the Viking observations, the latter must be integrated spatially to reproduce the poorer spatial resolution of the former. This is done numerically, using data interpolated to the appropriate season from the seasonal period maps (described in Chapter II.A). Spatial integration is done along a line oriented on the disk of Mars from limb to limb, approximating the Earth-based spectroscopic slit. At each point on this line, the vapor abundance w_i is determined from a look-up table and the geometrical airmass α_i is calculated using the appropriate Earth-sun-Mars geometry. The airmass in this case includes the paths travelled by a ray through the atmosphere from the sun to the surface and from the surface to the observer. The Earth-based equivalent vapor abundance is then obtained using

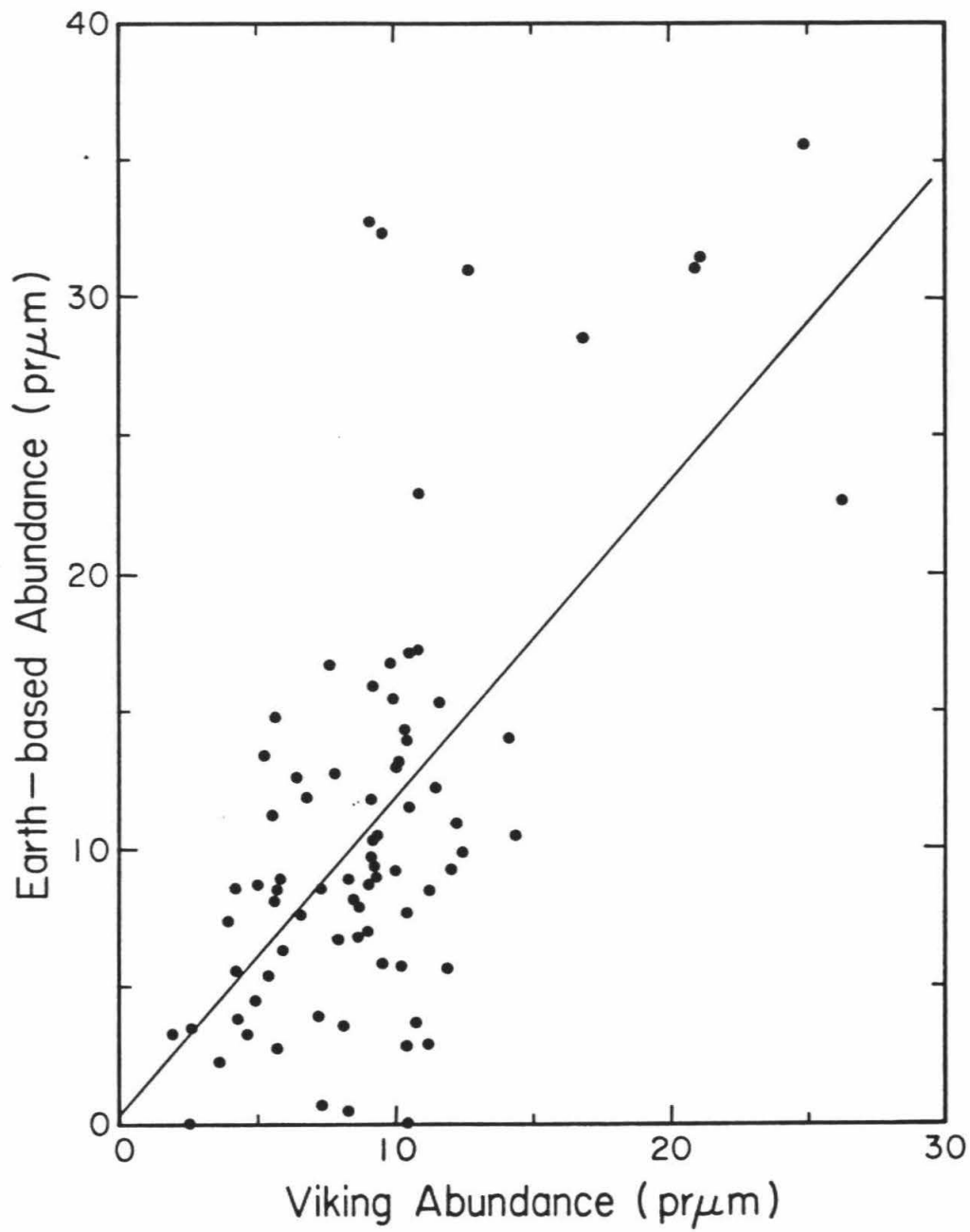
$$w = \frac{\sum_i a_i w_i}{\sum_i a_i} \quad (3)$$

This makes the reasonable assumption that the absorption bands are not near saturation, such that the additive process is indeed linear, and ignores the different weighting of regions due to spatial variations in albedo. Any decrease in the apparent column abundance of vapor at high emission or incidence angles (see Davies, 1979a; Chapter II.A) is ignored. This is done because only a very small fraction of the planet is observed sufficiently-obliquely to affect the result.

Figure 22 shows the comparison between the Earth-based and the Viking observations of vapor abundance. Included are 78 separate observations of type EQ (parallel to the equator). The correlation coefficient between the two data sets is 0.64, and the linear regression line through the points has a slope of 1.15 (as opposed to the expected value of unity). It is apparent that, except for a large degree of scatter in the data, the Earth-based and Viking measurements of atmospheric vapor agree. The question remains as to whether the scatter is due to uncertainties resulting from the detection method or calibration of either instrument or to a rapid temporal variability of the amount of water vapor actually present in the Mars atmosphere.

The Viking measurements have an uncertainty of about $\pm 5-10\%$ (see Chapter II.A). This estimate is based on the known signal-to-noise ratio of the detectors and on the number of points used in the time and space averaging technique (see Farmer and LaPorte, 1972). Examination of the data within some of the individual bins reveals a standard deviation similar to these estimates, indicating that any temporal or spatial variations within an individual bin (10° in both latitude and longitude and 15° in L_s) were smaller than the

Figure 22: Earth-based observations of vapor by Barker plotted versus Viking MAWD observations made at the same time. The data were all obtained in 1976-1978, and were of the type EQ (slit oriented parallel to the equator). The best-fit straight line through the 78 data points has a slope of 1.15 and a y-intercept of 0.26; the correlation coefficient is 0.64.

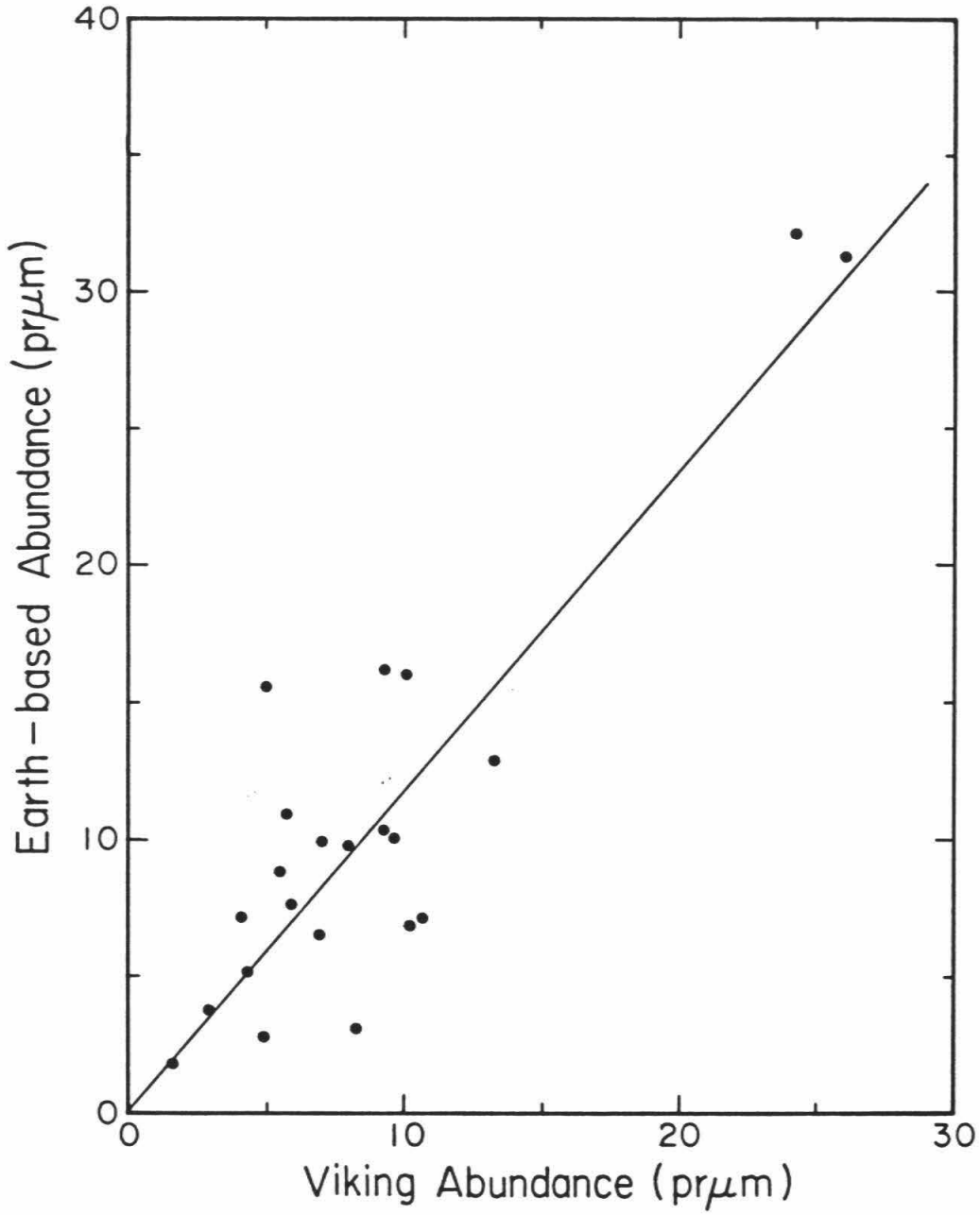


uncertainties in the measurements and that the noise estimates are indeed accurate.

The stated uncertainties in the Earth-based observations are typically about 5-25% of the observed value (Barker, 1976, and personal communication, 1981). However, the scatter seen in observations of Mars taken within a very short time period is generally much larger than this, often showing variations of greater than a factor of two in column abundance (see Barker, 1976). Large variations are possible depending on which face of the planet is being observed (due to longitudinal structure in vapor abundance; see below). However, this large a variation occurs only during northern summer ($L_s \approx 90-180^\circ$), when the largest amounts of vapor are present. At other seasons, there is much less spatial structure in vapor behavior. Also, the large scatter in the Earth-based data is evident even when account is made of the differences in the sub-Earth longitude observed. Therefore, the variation observed must be due to uncertainties inherent in the observing or reduction techniques.

That most of the scatter seen in Figure 22 is due to uncertainties in the Earth-based observations is consistent with the fact that the scatter decreases if data from a given day or short series of days are averaged. Figure 23 shows this trend, with the 78 points of Figure 22 averaged into 22 points based on when they were obtained. The best-fit line is essentially identical to that in Figure 22, but now the correlation coefficient for the data set is 0.88, a much improved value. Thus, the two data sets agree to within the probable uncertainties and errors in the observations, as expected because it is the same planet being observed by the two methods at the same time. This agreement serves as a consistency check on both techniques, and now allows us to examine the behavior seen from Earth during other years.

Figure 23: The same comparison as in Figure 22, except that data points obtained within a span of several days are averaged together to reduce the errors. There are now 22 points, the best-fitting line is essentially the same as that indicated in Figure 22, and the correlation coefficient is 0.88.



For the interannual comparisons, only the data taken in the PPCM mode will be discussed, for simplicity. Except for the 1976-1978 year, this type of observation was the most commonly made. The seasonal variation that would be observed from Earth, based on the Viking measurements and using the method outlined above, is shown in Figure 24. The possible variation due to longitudinal structure in vapor abundance is also shown for four of the twenty-four seasons. As mentioned above, there can be quite a large variation during northern summer, when there is $\sim 42 \pm 17$ (peak-to-peak variation, based on the 10° bins) pr μm of vapor. During southern summer, there is $\sim 12 \pm 4$ pr μm . The seasonal variation seen in Figure 24 is not actually for the geometry of any specific year. Rather, it is calculated assuming that the subsolar and subearth latitudes and longitudes are the same (i.e., zero phase angle). Thus, the water abundance is a function only of L_s (or subsolar latitude) and central meridian longitude (CML). A difference between the subsolar and subearth longitudes will make no difference in the observed vapor in the absence of significant diurnal variability of vapor abundance or large amounts of atmospheric dust. The difference between the subsolar and subearth latitudes is always less than about 20° and most often less than 10° , such that the lack of strong latitudinal vapor gradients will minimize any difference in observed vapor abundance. The effects of masking of the water vapor due to reflection off of airborne dust can readily be seen in Figure 24. The small dip in abundance at $L_s \approx 220^\circ$ and the larger drop at $L_s \approx 275^\circ$ are due to the presence of global dust storms (see Davies et al., 1979a, and Chapter II.A). The vapor present in the atmosphere does not necessarily disappear at these seasons, but is merely hidden from view due to scattering of sunlight by the dust.

These Earth-based abundances predicted from the Viking data are compared with actual observations from 1964 to 1978 in Figure 25a-d. The

Figure 24: The seasonal variation of vapor as would be seen from Earth if the global and seasonal distribution of vapor was like that seen by Viking. The calculations were done for a phase angle of 0° and a spectroscopic slit stretching from limb to limb along the line through the poles of Mars (corresponding to observation type PPCM). Dips due to the global dust storms are evident near $L_s = 210^\circ$ and 280° . The levels shown represent the average of the rotational curve; the vertical bars through the abundance levels of four of the periods represent the *peak-to-peak* variation in what would be observed depending on which face of Mars pointed toward Earth.

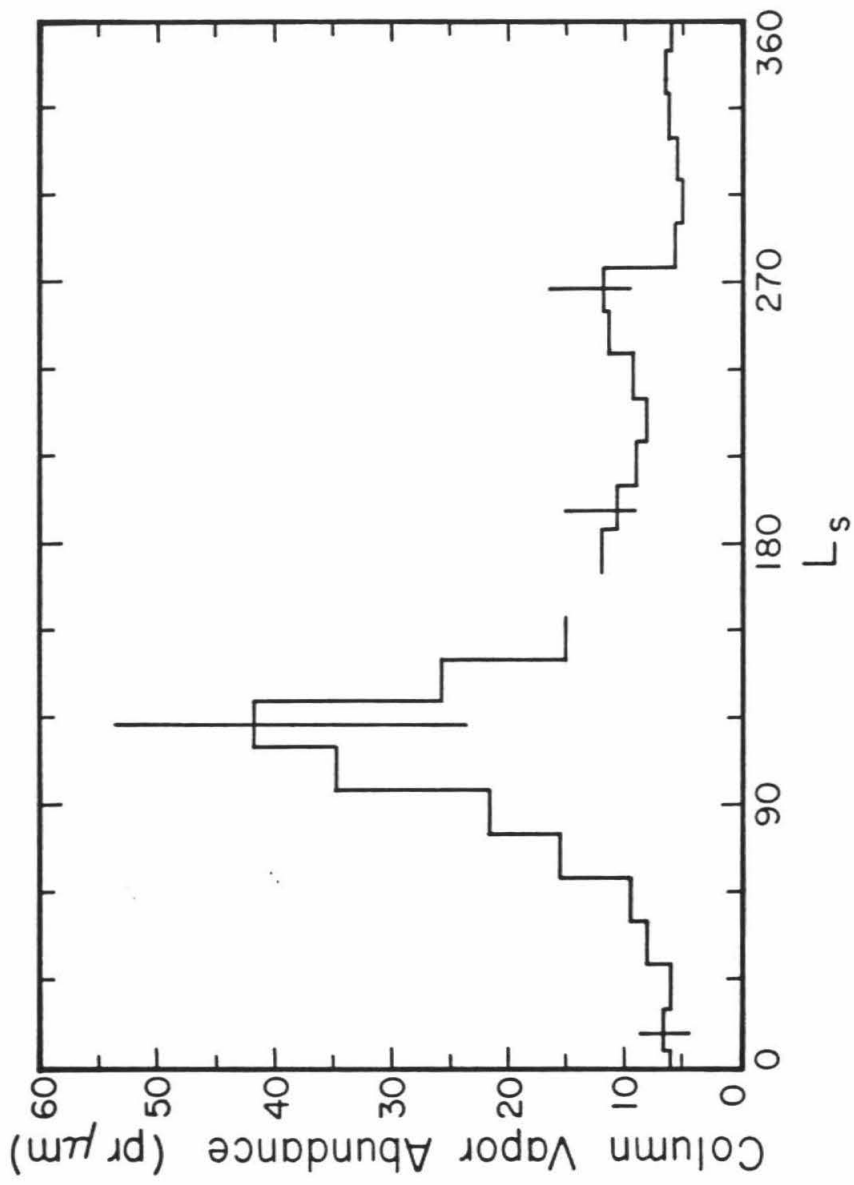
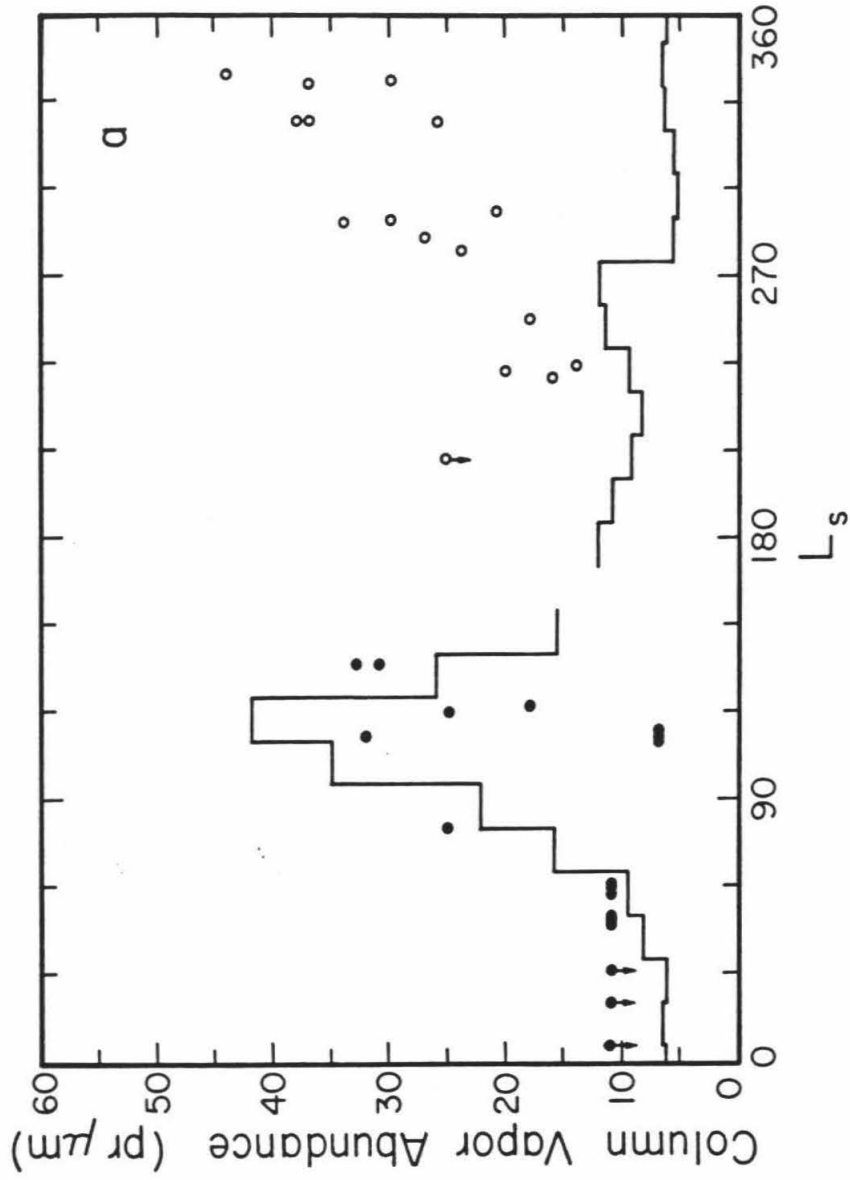
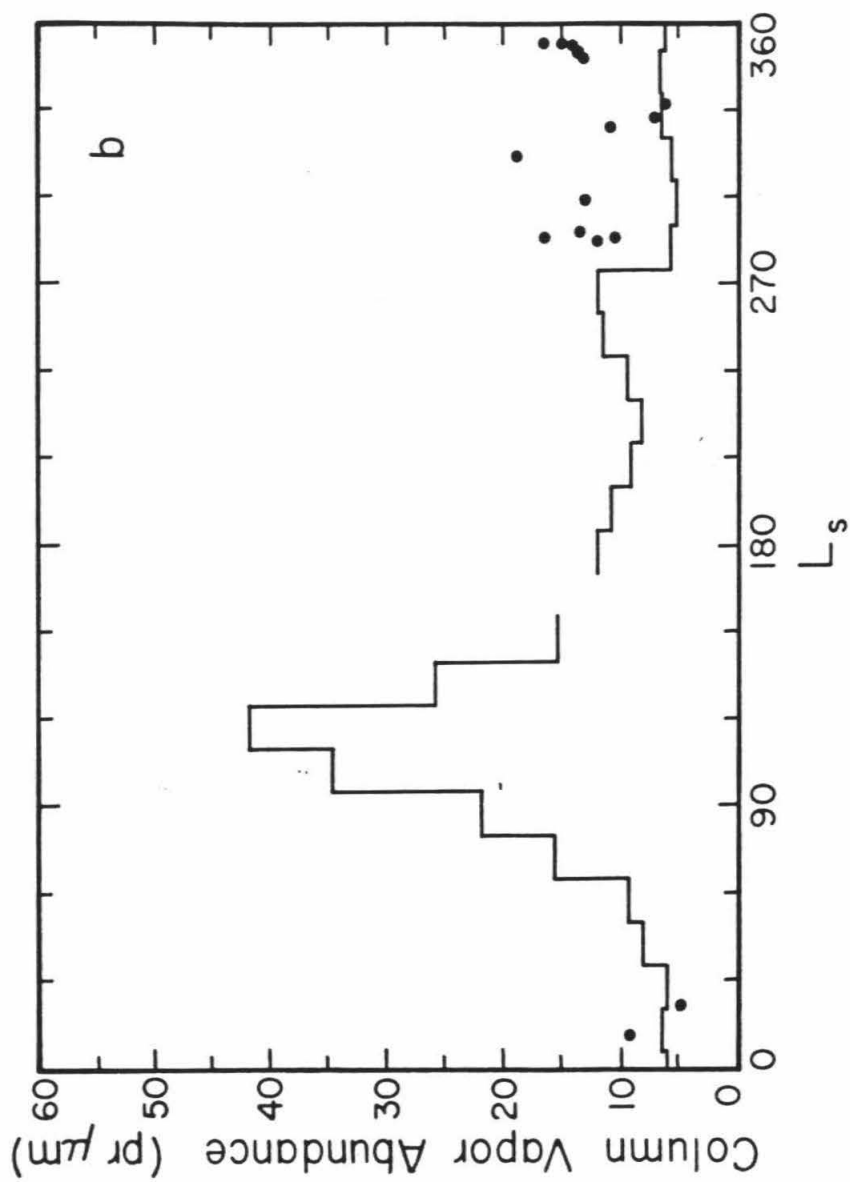
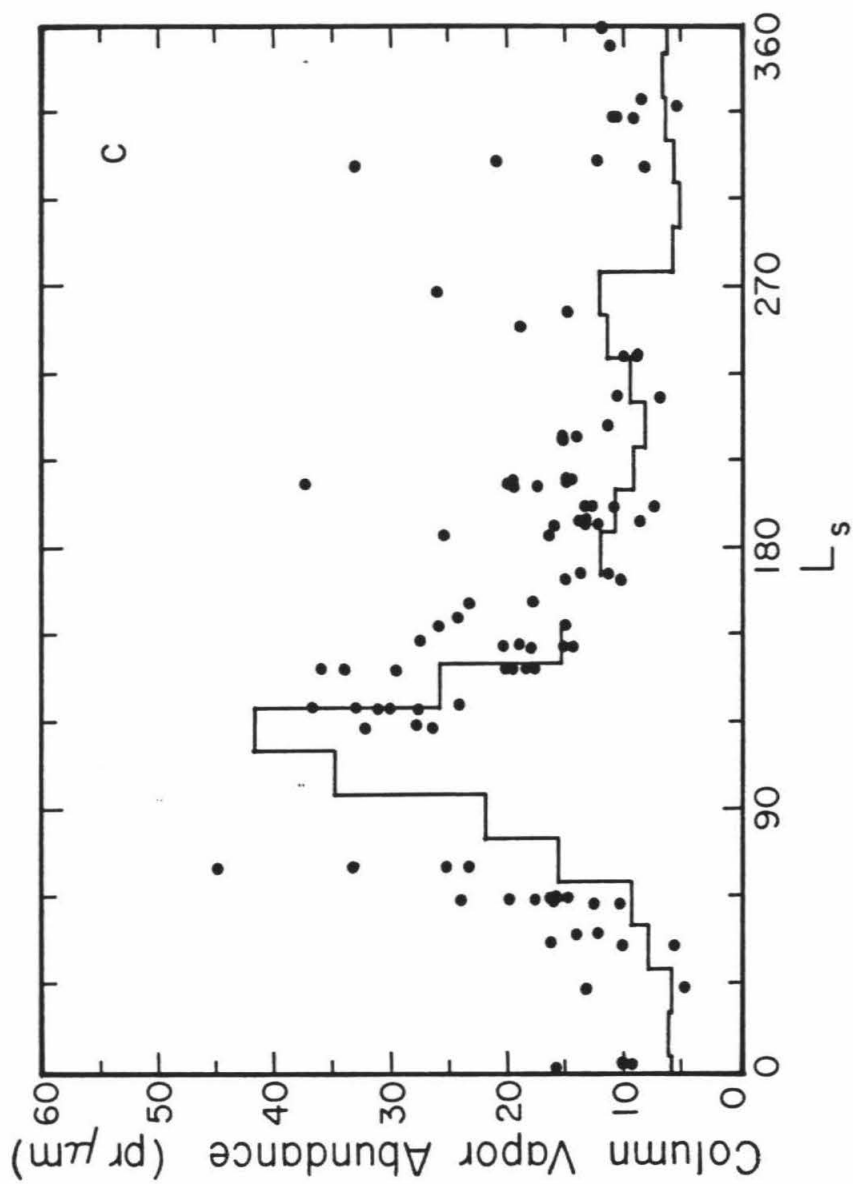


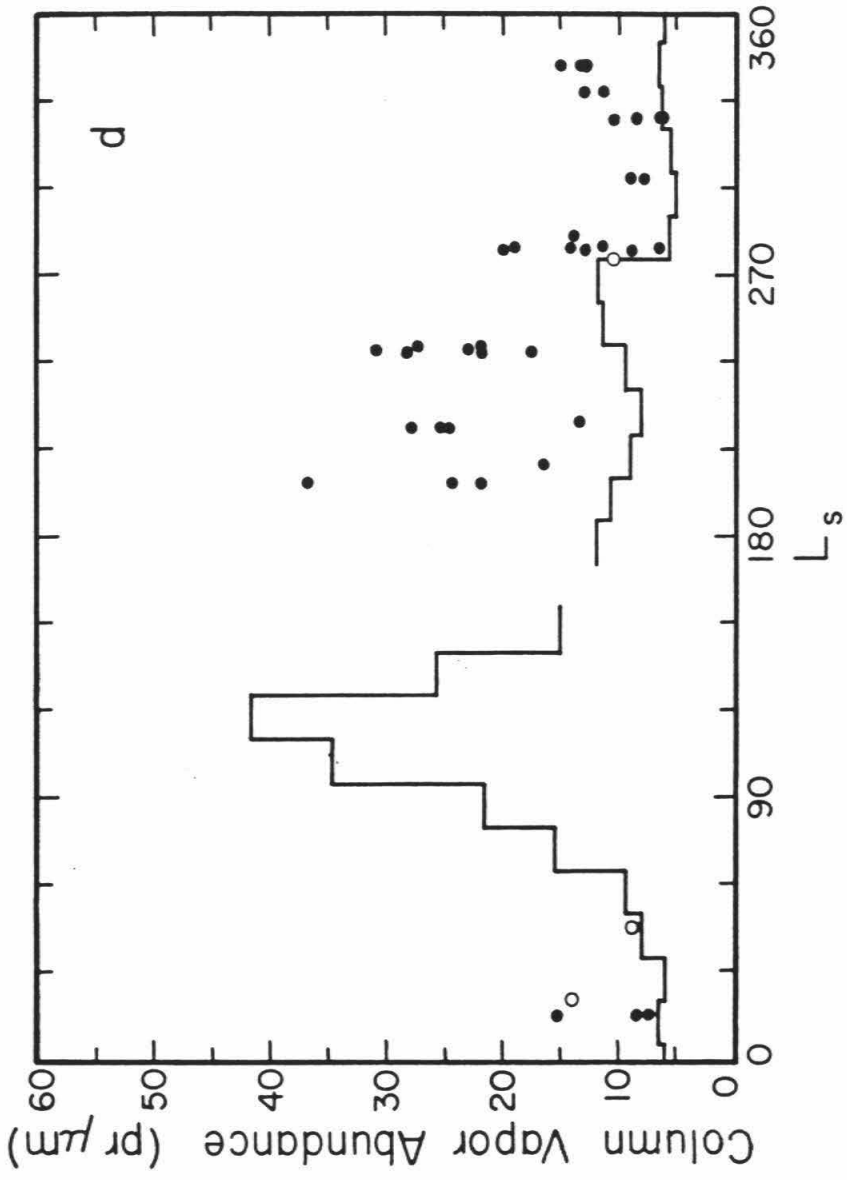
Figure 25: Comparison of the Earth-based seasonal variation predicted from Viking data with PPCM observations made from Earth.

- a) Observations made prior to 1970. Points with arrows represent upper limits. Open circles are data obtained in 1969.
- b) Observations made in 1970-1971.
- c) Observations made in 1972-1974.
- d) Observations made in 1975-1978. The open circles are data obtained in 1978.









Earth-based data are taken from the lists compiled by Barker (1976, and personal communication, 1981), and have all been reduced by him to the same physical assumptions of bulk pressure (6 mbar) and temperature (225 K). The Viking measurements were reduced assuming $T = 200$ K and $P = \frac{1}{2}P_{\text{surface}}$ (or $P \approx 3 \pm 1$ mbar) (see Chapter II.A), but this difference should be a small effect in the comparison.

The seasonal curves seen for each Mars year show both similarities to and differences from the curve obtained from Viking measurements. The data prior to 1970 (Figure 25a) show a rise in vapor abundance during northern summer (see Barker, 1976) and a corresponding rise during southern summer. This led Barker et al. (1970) to conclude that the annual behavior was nearly symmetrical with respect to the two hemispheres and that the water vapor behavior correlated well with the retreat of the polar caps. As will be seen, the observations of the southern summer season in 1969 are the only ones to definitely show this type of behavior. During all of the other years the water vapor abundance during southern summer stayed quite low. Whether or not this is a real effect and some of the implications of these data will be discussed in detail in the next section.

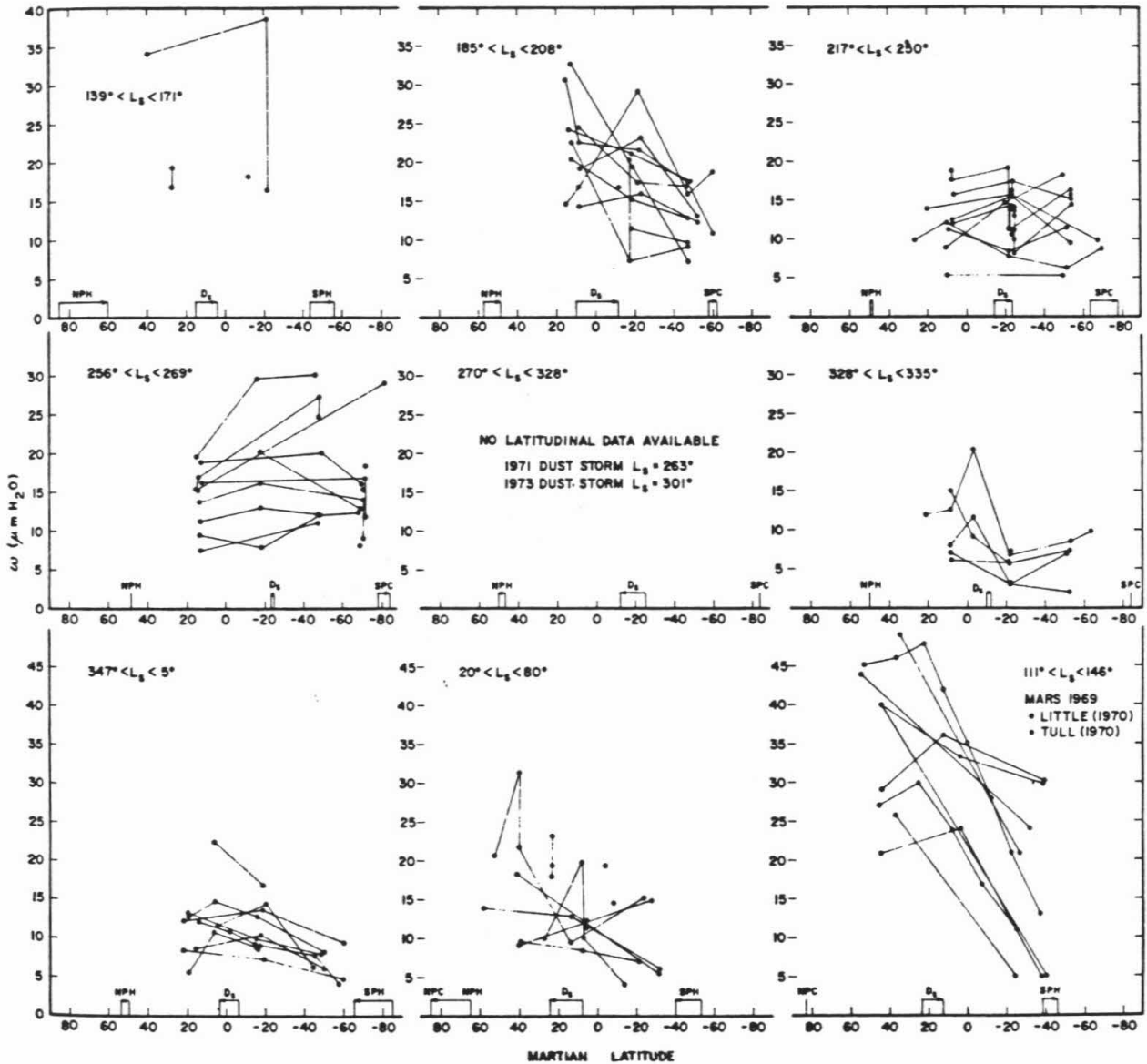
The data for 1970-1971 (Figure 25b) cover only the time period during southern summer and early fall. They show abundances which were much lower than were seen in 1969, and which are more consistent with the Viking observations. Of course, there was a global dust storm in 1971, beginning at about $L_s = 260^\circ$ (e.g., Zurek, 1982a). If the dust masked the water that year to the degree that the MAWD observations were masked (lowering the observed abundances by about a factor of two), there could have been as much as 30 μm of water in the atmosphere. The degree of masking depends, however,

on both the amount of dust in the atmosphere and on the relative vertical distributions of the dust and the water, such that the masking which occurred in 1971 is not known. It is perhaps significant that between $L_s = 330^\circ$ and 360° , when most of the dust should have settled out of the atmosphere, the 1971 data indicates less than 15 pr μm of water while the 1969 data show almost 40 pr μm ; thus, even the Earth-based measurements show there to be significant differences between the two years.

The observations by Barker (1976) for the 1972-1974 Mars year (Figure 25c) yield the most complete seasonal curve as seen from Earth. The data show a rise in vapor abundance during northern summer, but little evidence of a similar rise during southern summer. Again, however, there was a dust storm this year, beginning at $L_s = 300^\circ$ (Zurek, 1982a; Briggs et al., 1979), and the relative degree of masking by dust is not known. Barker (1976) argued that the data from $L_s = 240^\circ$ to 270° showed a rise similar to that seen in 1969, and attributed the largest abundances to the south polar regions (based on latitudinal data taken in the EQ mode). However, the latitudinal data that he presents (reproduced here as Figure 26) show no significant latitudinal gradient, and indicate global abundances near 15 pr μm . These values are very consistent with the Viking observations of about 12 pr μm at this season, such that the apparent rise in vapor may be attributed to scatter and uncertainty in the data. Similarly, the latitudinal data for the period $L_s = 328^\circ$ to 335° (Figure 26) show little evidence for much more than about 15 pr μm of vapor, and this is consistent with the data in Figure 25c. There is certainly no evidence for there being as much as 40 pr μm of vapor near $L_s = 330^\circ$ as there was in 1969. The decline in vapor following northern summer in 1972-1974 follows very closely the decline seen in the Viking data. The rise as northern summer approaches, however, appears to be earlier than in the Viking year. Unfortunately, these are

Figure 26: Observed latitudinal distribution of vapor at nine seasonal periods, 1972-1974. From Barker (1976).

OBSERVED N-S WATER VAPOR DISTRIBUTION DURING ONE MARTIAN YEAR



the only data for this season, so that it is left indeterminate as to which behavior is more normal or whether the differences are significant.

The data for 1975-1978 are shown in Figure 25d. These data were all obtained by Barker (unpublished data, personal communication, 1981). The vapor behavior following $L_s = 270^\circ$ is very similar to that seen by Viking. The earlier behavior appears different, however, with abundances averaging about twice those seen by Viking. While part of this may be due to differences in the amount of atmospheric dust present, it is likely that most of the difference represents a real variation; it is not known whether a global dust storm occurred during southern summer that year.

In summary, the seasonal behavior of water vapor generally follows closely that observed by Viking, with some possible exceptions. In 1975, the decline in vapor following the northern summer peak was less rapid or less complete than in other years (Figure 25d). While some of this difference may be due to differences in the obscuration by dust during the two years, that effect cannot explain all of the discrepancy (it would require significant global obscuration by dust at a season when this is not likely). Rather, removal of water from the atmosphere due to condensation onto the north polar cap or diffusion into the regolith must have been less efficient in 1975.

In 1969, and possibly 1971 and 1973, the global vapor behavior during southern summer mimicked that which occurs annually during northern summer, while other years show no similar increase. If real, this increase is due to the supply of vapor that year from a southern hemisphere source. Discussion of this apparent anomaly and its implications for the south polar cap are contained in the next section.

4. Discussion

Regarding the 1969 southern summer behavior, two questions arise: 1) Is the apparent increase in vapor from $L_s = 270^\circ$ to 360° (Figure 25a) real? And 2) What are the possible causes? Although Mars was not easily observed at that season, there should have been no difficulty with the whole-disk type of measurements made by Barker et al. (1970). The eleven data points during this season yield a mean vapor abundance of 31.6 ± 2.0 pr μm . Even if each point is assigned a random uncertainty of 50% of the mean value (16 pr μm , as opposed to the standard deviation of the eleven points of 6.5 pr μm), the uncertainty in the mean is only ~ 5 pr μm . The Viking observations before and after the global dust storm of that season indicate a global vapor abundance of about 12 and 7 pr μm , respectively. Thus, the 1969 values are more than a factor of three greater than those seen by Viking, and are more than three σ away from them. Thus, it is highly probable that the differences detected are significant. Because the same observers obtained the 1969 data (Barker et al., 1970) as obtained the data during the other years with different behavior (Barker, 1976; Tull and Barker, 1972; Barker, unpublished data, 1975), using similar (though not identical) equipment, one has confidence that the measurements are to be believed.

It is not likely that there would be sufficient atmospheric dust during all of the other years to mask the vapor were there actually 30-40 pr μm of vapor in the atmosphere. The major dust storm during 1977, observed by Viking, had optical opacities possibly as great as 6 at the Viking landing sites (Pollack et al., 1979), but caused the observed vapor abundance to drop only by a factor of two (see Figure 24, or Chapter II.A). Near the end of the storm, at $L_s = 345^\circ$, the opacity had dropped to less than one (Pollack et al., 1979), and the vapor abundance had climbed to about 7 pr μm . Were there actually 35 pr μm of

vapor in an atmosphere with dust of unit opacity, masking of the vapor by the dust would result in at most a drop of half in the observed abundance, rather than the factor of five required here (see Davies, 1979b). The 1971 and 1973 data are ambiguous. There were dust storms which could have masked the water to the degree required prior to $L_s \approx 330^\circ$; after this time, however, there was probably insufficient dust in the atmosphere. The degree of masking which occurred, and the amounts of water present during the 1971 and 1973 southern summers, remains uncertain.

Thus, the large 1969 (and possibly 1971 and 1973) southern summer vapor abundances observed by Barker et al. (1970) seem to represent real observations of an atmospheric vapor abundance very different from that seen in other years. There is little evidence regarding the latitudinal distribution of the vapor at this season in 1969. Scans of the EQ type at $L_s \approx 290^\circ$, centered at $+6^\circ$ and -54° latitude, show significantly less vapor than the pole-to-pole observations, with abundances more nearly like those seen by Viking (Barker, 1976). Although not conclusive, this distribution is consistent with large amounts of vapor in the south polar region. Unfortunately, there is very little data of other types that bear on this problem due to the unfavorable position of Mars at these seasons in 1969. The Mariner 6 and 7 spacecraft flew by Mars that year, but that was at $L_s \approx 200^\circ$, very early in the season.

It is suggested here that the "excess" vapor in 1969 was sublimed from a south polar water ice residual cap which was exposed when all of the seasonal CO_2 cap disappeared. This process occurs in the north each summer, with the CO_2 subliming to reveal the underlying water cap, which subsequently loses sufficient vapor to saturate the polar atmosphere (Farmer et al., 1976; Kieffer et al., 1976a). In the south during summer, however, 1977 Viking data revealed that the residual cap retained a cover of CO_2 (Kieffer, 1979; Paige, 1981).

Because the region was nearly in energy equilibrium on a yearly basis (Paige, 1981), there is no information as to the thickness of the residual covering of CO₂. Were it sufficiently thin, it might disappear in some years to reveal the water cap which must lie beneath it. This disappearance could be tied to the difference in the thermal load placed upon the cap by the presence or absence or the relative strength of global dust storms or of the nominal (non-storm period) atmospheric dust load that year. The presence of atmospheric dust over the cap will cause a change in the net radiative (solar plus atmospheric thermal) flux onto the cap, thereby subliming CO₂ at a different rate (Kieffer, 1979; Paige, 1982). A difference in dust storm activity between the year observed by Viking and the year of the large southern summer vapor abundances observed by Barker et al. (1970) may account for this difference in polar behavior, with all of the CO₂ having sublimed off the south cap in the earlier year, revealing the underlying water ice. This is consistent with the thermal models of the polar caps by Kieffer et al. (1977, Appendix I) and by Briggs (1974), in which there is insufficient CO₂ to last through the summer in the absence of protective atmospheric dust. If the underlying water cap has the same albedo as the north residual cap, it would be capable of reaching a maximum summer temperature of about 215 K, resulting in an atmospheric vapor abundance of greater than 150 pr μm over the cap. Were all of the CO₂ to disappear from the south one year, it would occur at the season of minimum cap extent. Visually, the cap typically reaches its minimum extent at $L_s = 300^\circ$ (James and Lumme, 1982). This is consistent with the temperatures of the south cap, which indicate a minimum size no later than $L_s = 300^\circ$ (Kieffer, 1979). In 1969, a faster cap recession would mean that the water ice would be revealed at a slightly earlier season than this. CO₂ would not begin to condense again until almost $L_s = 360^\circ$ (see Kieffer et al., 1977, Appendix I). The 1969 vapor

behavior (Figure 25a) is consistent with this timing. Polar vapor of column abundance $100 \text{ pr } \mu\text{m}$ would only need to extend to latitude -75° in order to produce the observed abundance of $\sim 25 \text{ pr } \mu\text{m}$ at $L_s = 280^\circ$ to 290° , and it need extend to -57° to result in $35 \text{ pr } \mu\text{m}$ at $L_s = 330^\circ$. Simple transport models of the type discussed in Chapter III.B, with appropriate south polar vapor abundances as a boundary condition, can readily produce the required global abundances; the shape of the resulting seasonal curve, however, depends strongly on the assumed polar abundance variation.

5. Conclusions and Summary

The annual cycle of water vapor in the Mars atmosphere has been observed for several separate Mars years from spacecraft and by Earth-based telescopic observers. The two different techniques yield similar results for simultaneous observations, and thereby allow comparisons to be made between the behavior in each year. The general trend shows a rise in global vapor abundance during northern summer, and a decline during the remainder of the year. The specific timing of the rise and decline vary slightly from year to year, but the overall trend is similar.

In 1969, however, observations showed that the vapor had a similar increase during southern summer. That Martian year is the only one to date for which this type of southern summer behavior has been observed, with four years apparently showing no rise at this season. The timing and magnitude of the 1969 southern summer vapor increases is consistent with sublimation of water from a permanent south polar water ice cap which is revealed when all of the CO₂ sublimates. Although the south polar cap retained CO₂ during 1977, when observed by Viking, the atmospheric dust present during other years may have placed a greater thermal load on the cap causing the CO₂ to completely sublime. Verification of both the "anomalous" observations and the above hypothesis may be best obtained by continuing the Earth-based observations of the water vapor content of the Mars atmosphere, especially during southern summer.

II.D. Near-Infrared Observations of Surface Water Frost

1. Introduction

In addition to water vapor present in the Mars atmosphere, observations which may indicate the presence of water ice on the surface are relevant to the seasonal and global water cycle. A number of observations in the near-infrared have revealed spectral features that may be indicative of surface water ice. The most unambiguous measurements and interpretations regard the presence of water incorporated into the seasonal CO₂ polar cap (Kieffer, 1970b; Pimentel et al., 1974; Clark and McCord, 1982). More speculative is the possible presence of surface water ice in the equatorial regions near local midday (McCord et al., 1982). These data and interpretations are discussed below.

2. The Polar Caps

In a recent paper, Clark and McCord (1982) presented near-infrared spectral measurements of the Mars north polar region. The spectra, taken during northern spring, showed absorption features due to the presence of water ice, and Clark and McCord interpreted these data as confirming the water ice composition of the residual cap as previously determined from spacecraft measurements by Farmer et al. (1976) and Kieffer et al. (1976a). However, Clark and McCord were, in fact, observing the predominantly-CO₂ seasonal cap rather than the residual water-ice cap. When viewed in these terms, one is led to the same conclusions, that water ice must be present on the seasonal CO₂ polar cap, as were reached by Kieffer (1970b) based on analysis of a near-infrared spectrum of the polar cap obtained by Moroz (1964).

The seasonal behavior of the north polar cap involves the condensation of CO₂ onto the surface during winter and the subsequent sublimation during the following spring (e.g., Leighton and Murray, 1966). Visual observations of the recession of the cap during spring have been made from Earth and from spacecraft over the course of many years (see James (1979) for a summary and comparison of most of these data). Additionally, thermal mapping data from the Viking orbiters can pinpoint the recession of the cap edge due to the buffering of the surface temperature which occurs whenever solid CO₂ is present on the surface (e.g., Martin, 1981; Paige, 1981).

Generally speaking, the north seasonal cap extends as far south as ~50° N latitude during the winter. Soon after the vernal equinox ($L_s = 0^\circ$), the hood of clouds which is often present dissipates and the seasonal cap retreats toward the pole. By northern summer solstice ($L_s = 90^\circ$) only a small residual cap is left at the pole, extending to as far south as 80 to 85° N latitude

(depending on longitude). It was this residual cap, observed by Viking at $L_s \approx 108^\circ$, that was determined to be water ice (Kieffer et al., 1976a; Farmer et al., 1976).

The Earth-based data of Clark and McCord were obtained on 20 February 1978, at $L_s = 50^\circ$. They noted that the polar cap at that time extended to as far south as $\sim 60^\circ$ N latitude. Thus, the largest fraction of their field of view contained the seasonal cap, composed predominantly of CO_2 ; the area of the residual part of the cap comprised less than a few percent of their field of view. Of course, even the location of the residual cap is covered with CO_2 at this season; the CO_2 buffering the residual cap temperatures does not completely disappear and reveal the underlying water ice until $L_s \approx 80^\circ$ (Paige, 1981).

Thus, although the spectra of Clark and McCord indicate water ice features, it is not the residual north polar cap that contains this ice. Rather, the water ice may be present either as clouds within the region observed or as surface ice intermixed with the solid CO_2 present on the surface. If optically-thick water ice clouds were present on Mars during the time of Clark and McCord's observations, it would not be surprising to see ice absorption features in the spectra. As they point out, however, no thick clouds were seen in the analysis by James (1979) or in Planetary Patrol or their own Earth-based photographs at nearly the same time. There is evidence for optically-thin clouds during this time period (James, 1979), but were they a significant contributor to the observed near-infrared flux they would have been easily visible to an Earth-based observer.

It is likely, then, that the water ice which produced the absorption features in the spectra of Clark and McCord was present on the surface,

intermixed in some fashion with the solid CO₂. They estimate that 60% of the observed light comes from H₂O frost while 40% is from other, unspecified, components. They have no way of estimating the location of the water frost (i.e., whether it is nearer to the pole or to the southernmost extent of the seasonal cap, or even if it is in the sub-polar regions also included in their field of view). There are two reasons why one might expect water frost to be present on the surface of the seasonal CO₂ cap. First, there is as much as 10 pr μm (precipitable microns) of water vapor in the atmosphere above the retreating seasonal cap at this season (Farmer and Doms, 1979; also, Chapter II.A). The saturation water vapor pressure at the low CO₂-cap temperatures is too low for any significant vapor to exist ($\sim 10^{-6}$ mbar at 150 K, equivalent to $\sim 10^{-3}$ pr μm of water vapor/km of atmosphere at saturation; see Farmer, 1976). Thus, any vertical mixing of or diffusion within the atmosphere will result in condensation of some of the water onto the surface. Second, at $L_s = 50^\circ$ CO₂ from the seasonal cap is subliming and causing the cap locally to thin and disappear. The temperatures are too low, however, for any water ice which may be present to sublime until all of the CO₂ has sublimed. Thus, if any water had been volumetrically incorporated into the seasonal CO₂ cap as it formed, it would be left behind as a surface lag deposit as the CO₂ disappeared.

Uncertainties in the nature of the mixing of the water ice with the CO₂ ice and possibly with dust on the surface make it difficult to establish the total amount of water ice present. These uncertainties include the frost texture (or grain size), the physical nature of the mixing (e.g., whether the water frost is all on the surface or mixed uniformly throughout some volume), and the nature and abundance of any dust contaminants. The effects of these complications on observed frost spectra are discussed by Kieffer (1970a) and Clark (1981a,b), among others. Based on these analyses, and the spectra presented by Clark and

McCord, it is likely that there is greater than about 20 pr μm of water frost on the surface, averaged over the area observed. No upper limit can be established due to uncertainty in the thickness of the water-frost-containing layer. Thus, the amount of water ice contained within the seasonal cap may be little enough to be only a small part of the seasonally-released vapor, or it may be large enough to be the dominant source. This ambiguity remains essentially unchanged if one considers the possibility that the water is present as a water-carbon dioxide clathrate, as the spectra of the clathrate and pure ice are very similar (Smythe, 1975). It is interesting to compare these results with the lack of water ice features seen in the spectra of the south seasonal cap during southern spring ($L_s = 212^\circ$), as observed by Larson and Fink (1972). They place an upper limit of ~ 15 pr μm on the average water frost abundance, similar to the lower limit obtained here for the north; this difference between the north and the south polar caps seems consistent with the observed occurrence of larger atmospheric vapor abundances in the north than in the south (Farmer and Doms, 1979; Chapter II.A). Interestingly, Mariner 6 and 7 observations in 1969 of the south polar cap ($L_s \approx 200^\circ$) indicated the presence of water ice on the surface everywhere south of the cap edge at $\sim 60^\circ$ (Pimentel et al., 1974). Although no estimates of the amount of frost present were made, a latitudinal variation was apparently seen, with larger frost abundances being present near the cap edge.

In summary, the spectral evidence indicates that water ice is present at the surface of the cap, intermixed with the CO_2 frost. This is the same conclusion reached by Kieffer (1970b), who properly interpreted the near-infrared spectrum of Mars taken by Moroz (1964) at $L_s = 63^\circ$, nearly the same season as is discussed here. It would be interesting if similar observations could be performed throughout the entire seasonal recession of the cap or if more-

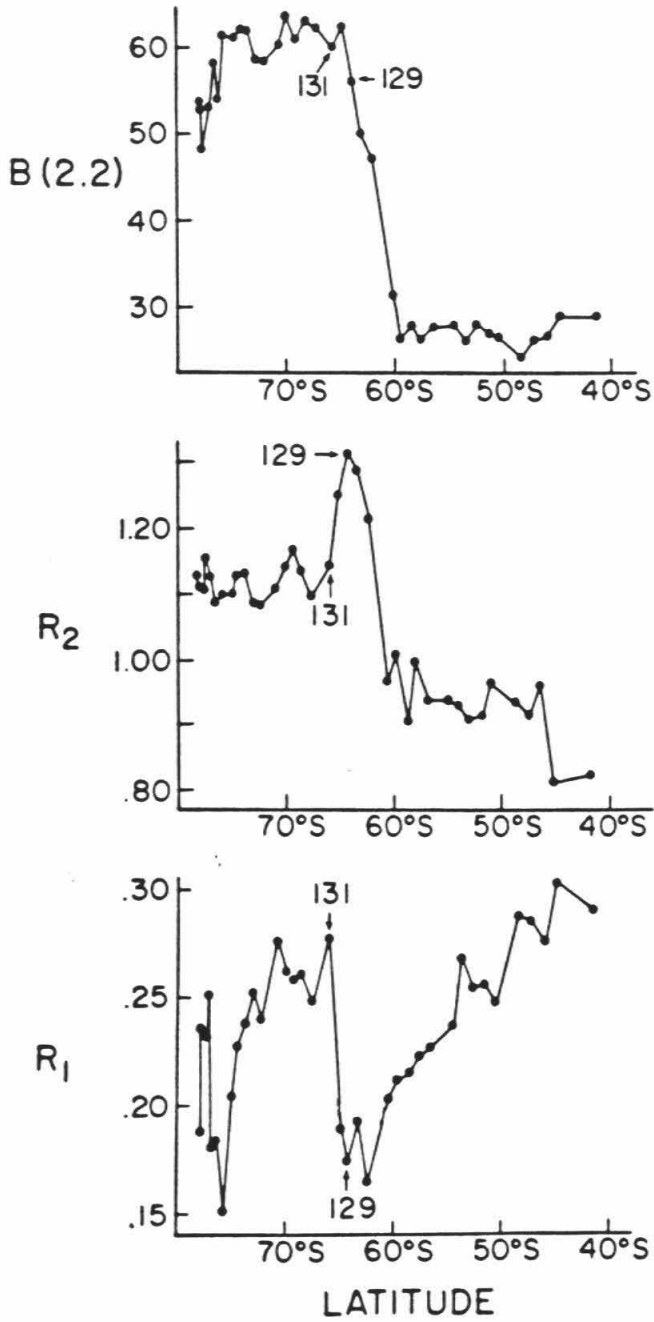
detailed variations with latitude could be mapped over the cap. This could provide harder constraints as to how much water is actually incorporated within the cap, and would in turn constrain models of the seasonal cycle of water which include exchange of water between the atmosphere and the regolith (see Chapter III).

3. The Equatorial Regions

A variety of near-infrared measurements of non-polar, near-equatorial regions on Mars have also been interpreted in terms of the presence of water in the near-surface regolith, either as water of hydration, adsorbed water, or ice (Houck et al., 1973; Sinton, 1967; Pimentel et al., 1974; McCord et al., 1978, 1982). Bound water produces absorption bands near $1.5 \mu\text{m}$, $1.9 \mu\text{m}$, $2.4 \mu\text{m}$, and $2.9 \mu\text{m}$ (e.g., Hunt, 1977; Pimentel et al., 1974). Water ice has bands centered at about $1.6 \mu\text{m}$, $2.0 \mu\text{m}$, and $3.1 \mu\text{m}$ (e.g., Kieffer, 1970a; Pimentel et al., 1974; Clark, 1981a; and others). While bound water can exist in equilibrium with atmospheric vapor under the existing range of pressure and temperature in the equatorial regions, ice is unstable during the day and would be expected to sublime. Thus, the existence of daytime ice would present a significant boundary condition for the behavior of water in the atmosphere as well as for the surface chemistry.

Perhaps the most-interesting data regarding water is that obtained from the Mariner 6 and 7 infrared spectrometers (Pimentel et al., 1974). Although containing only a limited set of observations, the data clearly show the $3 \mu\text{m}$ absorption band, due to chemically- or physically-bound water (sorbates) in the equatorial regions and due to ice in the south polar region. While the data indicate that surface water is present everywhere, they show a clear transition from bound water to water ice at the cap edge. This is seen in Figure 27, from Pimentel et al. (1974), which shows the $2.2\text{-}\mu\text{m}$ brightness B , R_1 (= ratio of intensity at $3.1 \mu\text{m}$ to that at $2.2 \mu\text{m}$), and R_2 (ratio $I(2.9 \mu\text{m})/I(3.1 \mu\text{m})$) as functions of latitude. The reflectance at $2.9 \mu\text{m}$ is indicative of bound water, and that at $3.1 \mu\text{m}$ of water ice; that at $2.2 \mu\text{m}$ does not reflect the existence of water at all. Thus, a relatively low value of R_1 indicates the presence of surface water in some form; a value of $R_2 > 1$ means that the water is in the form of ice,

Figure 27: Behavior of B (at $2.2 \mu\text{m}$), $R_1 (= I(3.1 \mu\text{m})/I(2.2 \mu\text{m}))$, and $R_2 (= I(2.9 \mu\text{m})/I(3.1 \mu\text{m}))$ as a function of latitude at the edge of the south polar seasonal cap, as observed from the Mariner 6 and 7 infrared spectrometer (IRS) experiment, $L_s \approx 200^\circ$. See text for discussion. From Pimentel et al. (1974).



while $R_2 < 1$ means that the water is bound physically or chemically. Contamination of the $2.9 \mu\text{m}$ intensity from the wings of the $2.7 \mu\text{m}$ CO_2 band may occur, but the results should still be qualitatively valid. R_1 has other effects also folded into it, including photometric function, particle size, and chemical composition independent of water content. That all of the values for R_1 are significantly less than 1.0 is interpreted by Pimentel et al. in terms of the presence of significant amounts of water. The decrease toward the south, while consistent with an increase in bound water at colder more-poleward temperatures, can also be explained in terms of particle size variations. Because $R_2 < 1$ north of $\sim 60^\circ\text{S}$, the water in this region is in the form of bound water. The sharp transition to $R_2 > 1$ south of $\sim 60^\circ\text{S}$ indicates the presence of water ice on the polar cap, as mentioned in the previous section. There is no firm evidence for surface water ice in regions other than the polar cap (Pimentel et al., 1974). These results are generally consistent with those of the other observers regarding the presence of bound water.

Recently, McCord et al. (1978, 1982) presented near-infrared spectra of various non-polar regions of Mars and interpreted them in terms of the presence of water ice. The observations were of various bright and dark areas in the Mare Tyrrhenum, Elysium, Amenthes, and Iapygia regions. Composite spectra are shown here in Figure 28. The large scatter near 1.4 and $1.9 \mu\text{m}$ is likely due to telluric water. The vertical lines represent the locations of CO_2 vapor absorption lines (from Kieffer, 1968) which have been approximately removed by McCord et al. from the data by use of a nominal model Mars atmosphere. Also shown is the relative reflectance spectrum of water ice, indicating the location of the absorption features (see McCord et al., 1978, for details of the removal of the atmospheric CO_2 lines, and McCord et al., 1982, for the ice spectrum). McCord et al. (1982) feel that the small intensity decrease in

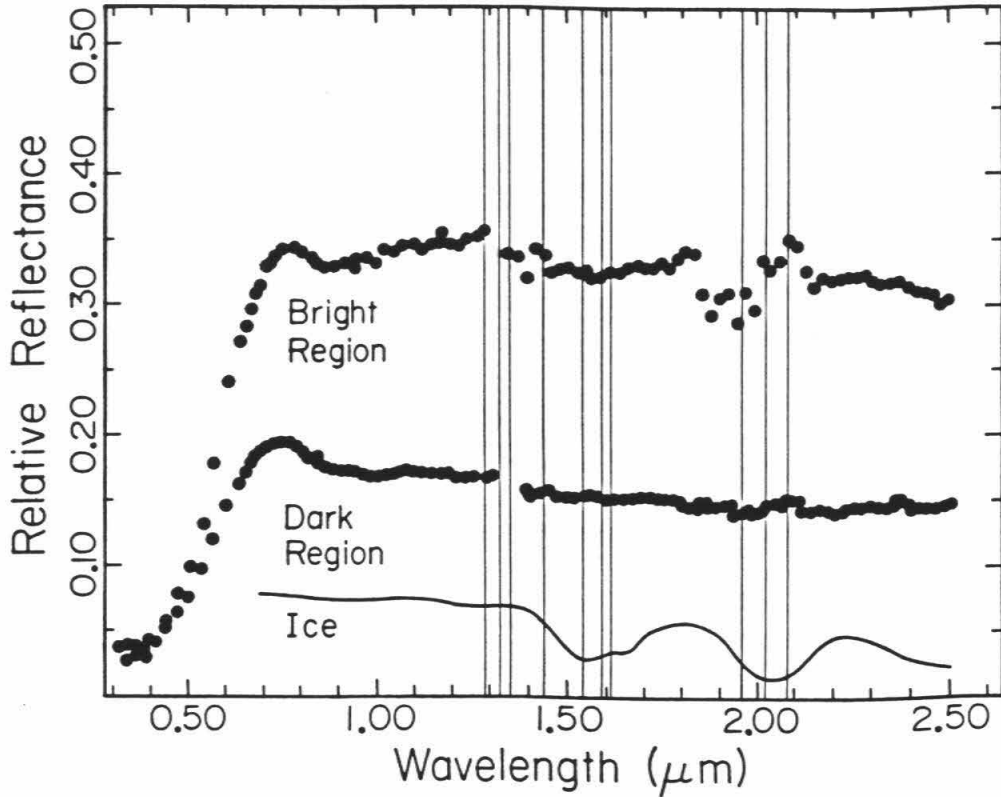


Figure 28: Composite bright and dark region reflectance spectra of Mars, obtained by McCord et al. (1982), and reflectance from a surface composed of water ice. The vertical lines represent the locations of the centers of gaseous CO_2 absorption bands (see Kieffer, 1968). McCord et al. have removed a nominal model CO_2 atmosphere, and interpret the broad dip at $1.6 \mu\text{m}$ to be due to surface ice, despite the absence of the normally-deeper $2.0 \mu\text{m}$ band. See text for discussion.

the bright region spectrum at $\sim 1.6 \mu\text{m}$ can best be explained by the presence of water ice on the surface; about 5% of the surface would need to be covered to produce the band that they feel is present. Interestingly, although the $2.0 \mu\text{m}$ water ice band should be a deeper band, it appears to be absent from the observed spectrum. Instead of water ice producing the band at $\sim 1.6 \mu\text{m}$, much of it may be due to incomplete removal of the CO_2 gas bands at 1.44 and $1.59 \mu\text{m}$. Also, due to the presence in this wavelength range of absorption bands from Fe^{+2} in surface minerals (see Hunt, 1977), a unique assignment cannot be made solely in terms of ice.

At these latitudes (between about $\pm 30^\circ$), the daytime surface temperatures reach maxima of up to 300 K (see Kieffer et al., 1977), such that surface ice would rapidly sublime. McCord et al. (1982) require a highly speculative hysteresis effect between adsorbed water and surface ice to obtain any ice at the time of the observations. If water ice is causing a decrease in the reflected light at this wavelength and location, it is instead likely to be due to high-altitude water clouds rather than surface ice. Because water ice is very absorbing at these wavelengths (e.g., Wiscombe and Warren, 1980), even thin clouds of small particles will cause shallow absorption bands to appear in both transmitted light and light reflected from the clouds. Calculations of the scattering and absorption due to water clouds, done using the Mie theory and a simple delta-Eddington two-stream radiative transfer approximation (D.A. Paige, personal communication, 1982; Joseph et al., 1976), indicate that a water cloud of optical thickness near 1 can produce an adsorption band at $1.6 \mu\text{m}$ greater than several percent deep; the small depth of the band results from the importance of scattering relative to absorption at this wavelength for the cloud particle sizes used. This depth is comparable to the size of the possible decrease discussed by McCord et al. (see Figure 28). A cloud of unit extinction optical

thickness produces only a small rise in the Bond albedo, so may not even be noticed in Earth-based observations.

In summary, the near-infrared data for the equatorial regions are consistent with the ubiquitous presence of bound water in the near-surface region. This water would take the form of either adsorbed water or chemically-bound hydrates. There is no compelling evidence for the presence of surface ice during the midday time period.

Chapter III

The Role of Seasonal Reservoirs in the Mars Water Cycle

Understanding the seasonal cycle of water vapor in the Mars atmosphere requires an understanding of the role played by the seasonally-accessible reservoirs for water. The possible reservoirs include water ice in both the residual and the seasonal polar caps; subsurface water in the regolith, adsorbed onto the individual grains; and subsurface ice or permafrost. All of these reservoirs are thermally-driven, such that the seasonal increase and decrease in temperatures at each location on the planet will tend to drive the water into the atmosphere and back out again, respectively. Additionally, water vapor, once in the atmosphere, can be carried from place to place on the planet due to the circulation of the atmosphere. The water can also be transported as vapor, as solid ice in the form of clouds, or as water sorbed onto airborne dust grains.

The roles of these processes are considered in this chapter. The possible role of regolith exchange of water is discussed in Section A; details of the physics involved are presented, along with results of a simple one-dimensional seasonal model of the atmosphere and regolith. In Section B, the regolith model is coupled with a diffusion-type climate model detailing atmospheric transport and polar cap formation in order to understand the relative importance of each of the processes. The conclusions arrived at here will then feed back into some of the results already obtained regarding the role of each reservoir in the longer timescale behavior.

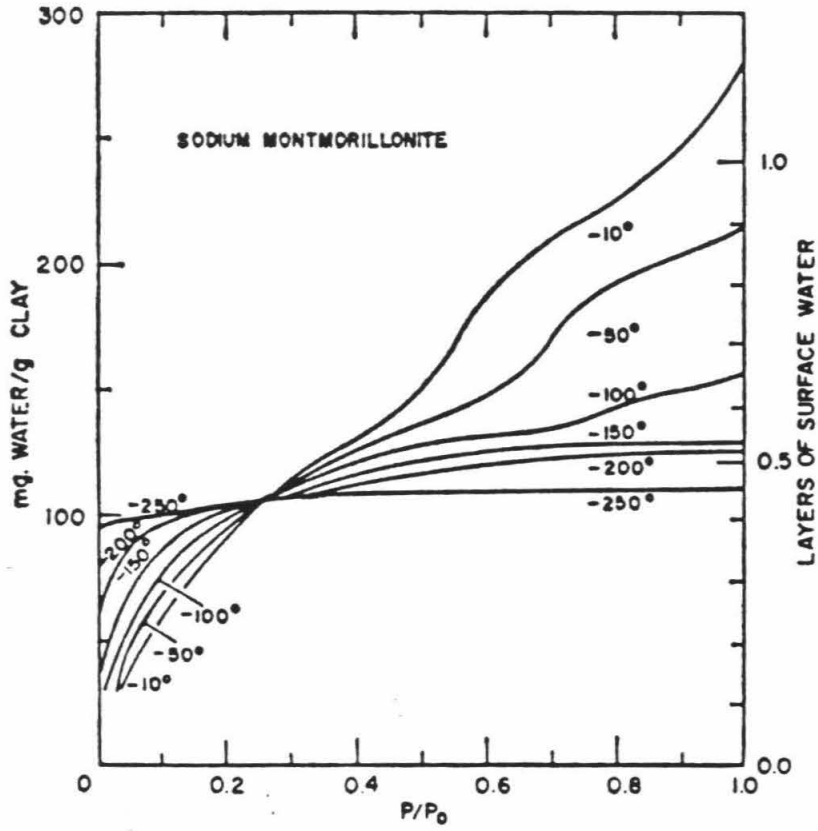
III.A. Seasonal Exchange of Water with the Regolith

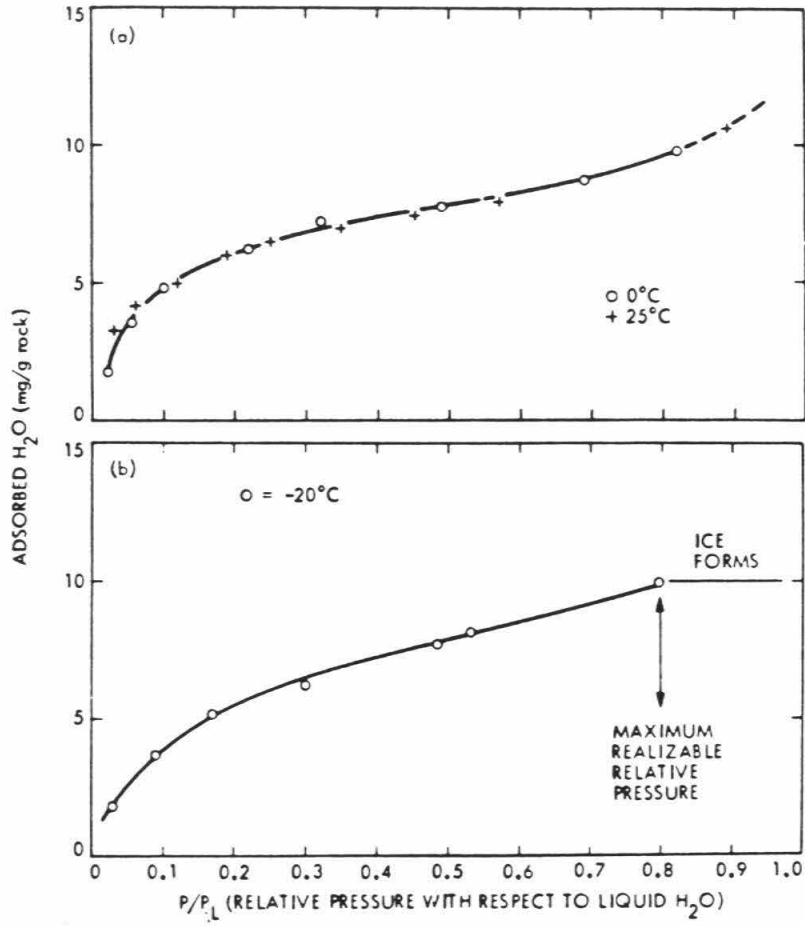
1. Introduction

There is much previous discussion in the literature regarding the existence of subsurface water adsorbed onto the Mars regolith and its ability to exchange with the atmosphere seasonally. Measurements of the adsorption isotherms for water (i.e., the amount of water adsorbed on a material as a function of vapor partial pressure and temperature) have been made for a variety of geologic materials by Mooney et al. (1952), Anderson et al. (1967, 1978), Pollack et al. (1970), and Fanale and Cannon (1974). The strong temperature dependence of the sorption process caused the latter three groups to suggest that exchange of water between the regolith and the atmosphere might be important on Mars on some timescales.

The physics of the adsorption process involves the van der Waals bonding of water molecules onto the surface of individual grains (see, for instance, Brunauer et al., 1967). The number of molecules that will bond onto a unit area of grain surface will depend both on the number available in the surrounding pore space (the vapor partial pressure) and on the ease with which bound molecules can detach (as determined by the temperature extant). Figure 29 shows the measured and inferred isotherms for a granular surface of basalt and of montmorillonite clay. Over the range of pressures and temperatures present on Mars, the amount of adsorbed water can vary up to about 10 mg water/g rock for basalt and up to several hundred mg water/g rock for clay (Fanale and Cannon, 1974; Anderson et al., 1967). In neither case does the water cover the grains to deeper than a complete monolayer of molecules; the clay is more adsorbing due to its greater specific surface area, which results from its more-open molecular construction.

Figure 29: Adsorption isotherms for particulate basalt and montmorillonite clay. (a) Isotherms for adsorption onto clay, as inferred from the measurements of Mooney et al. (1952). From Anderson et al. (1967). (b) Isotherms for adsorption onto basalt. From Fanale and Cannon (1974).





An increase in temperature will thermally activate the adsorbed water molecules and drive them from the surface of the grains into the surrounding pore space as vapor, until equilibrium is re-established. Locally, this is a very rapid process. The ability to then influence the atmosphere depends on the depth beneath the planet's surface to which diffusive contact exists. As an example, consider a case in which the vapor molecule number density in the subsurface pore spaces is initially in equilibrium with the adsorbed water at some temperature, with the base of the atmosphere having the same vapor molecular number density. If the subsurface temperature is increased, water molecules will locally leave the surface and become pore vapor to re-establish the equilibrium. At this point, the water molecule number density is greater in the subsurface than at the base of the atmosphere, and vapor will diffuse out into the atmosphere, again until equilibrium is established. In this manner, the seasonally-changing temperatures can drive vapor out of or back into the regolith.

As was emphasized by Fanale and Cannon (1974), free ice will not form in the subsurface unless all of the particle adsorption sites are filled. While ice, if emplaced onto the surface, is capable of sealing off the subsurface pores, sublimation of this ice into the pores and the subsequent adsorption of the molecules onto the grain surfaces would rapidly occur until equilibrium is established or the sites are filled. Thus, it is proper to consider the adsorption/desorption process first, rather than the possible condensation and sublimation of ice considered by Leighton and Murray (1966), Fanale (1976), and Farmer and Doms (1979).

In the next part of this section, the diffusion distances through the Martian regolith are discussed. These will govern the depth to which vapor may exchange on a seasonal basis. In the sections which follow, a simple one-

dimensional model for seasonal exchange will be presented. The results will indicate the possible importance of regolith exchange in the seasonal cycle.

2. Regolith Diffusion and Adsorption

The ability of vapor to exchange with the atmosphere depends on its ability to diffuse through the porous surface and on the ability of the regolith to adsorb water (and on the temperature dependence of this process). The former depends on the diffusivity, D , of the surface. D is a function of the grain particle size, the bulk porosity, the tortuosity (a measure of the degree of interconnectedness of the pores), and the partial pressure of the CO_2 through which the water molecules must diffuse. Flasar and Goody (1976) examined the dependence of D on its constituent properties, as determined by theory and observations, and found that $0.1 \lesssim D \lesssim 5.0 \text{ cm}^2/\text{s}$. (Notice that these values differ from those quoted by Flasar and Goody; this is because the diffusivities used here include in them the effective porosity, while their discussion has porosity as a separate term.) The lower limit is based on diffusion through $1\text{-}\mu\text{m}$ sized particles, as smaller particles are physically unrealistic; of course, a cemented surface or a frothy lava may not have connected pores at all, such that $D < 0.1$ is possible. The upper limit is obtained for flow through pure CO_2 gas in a porous medium, with the medium not obstructing the diffusion at all. For pore spaces larger than the mean free path for collision ($\sim 5 \mu\text{m}$), Knudsen flow dominates and diffusion is governed solely by gas molecular collisions. For smaller pores it is the collisions of a molecule with the pore walls which are the significant factor.

The ability of a porous material to adsorb water depends predominantly on its specific surface area (surface area per unit mass). This in turn is a function of the particle size of the medium, the structure of the mineral, and the structure of the grains. Fanale and Cannon (1974) measured adsorption isotherms for water on 88- to $246\text{-}\mu\text{m}$ -sized particles of basalt having a specific surface area of $9.8 \text{ m}^2/\text{g}$. Under Martian pressure and temperature conditions,

as much as about 10 mg water can adsorb onto each gram of rock. The behavior of basalt is typical of that of non-clay silicates. Anderson et al. (1967, 1978) examined the adsorption properties of montmorillonite clay under Martian conditions. Clay, with its much more open and regular structure, is capable of holding much more water than basalt; Anderson et al. found that as much as several hundred mg H₂O/g rock could adsorb. The measured and inferred isotherms are shown in Figure 29. The composition of the Mars surface is not well known, however; the evidence for the presence of clays is ambiguous (e.g., McCord et al., 1982), and they may be absent entirely.

Table 5 shows diffusion lengths through porous media for several values of D for a time period of one Mars year (687 Earth days, or 669 Mars days). The actual distances diffused will be much less than these owing to the buffering effects of the adsorbed water; for example, if water is to diffuse out from 10 cm depth, an equivalent amount of water must first be removed from the top 10 cm of the column. Thus, to get a realistic diffusion depth, the values for the diffusion constant must first be scaled by the ratio of the amount of vapor present per unit volume in the regolith to the total amount of water (vapor plus adsorbed water) exchanged:

$$D_{eff} = D \frac{H_2O_{(vapor)}}{H_2O_{(vapor + sorbate)}} \quad (4)$$

Using amounts of adsorbed water of 0.03 mg/g (on particulate basalt) and 3.0 mg/g (on montmorillonite) results in a scale factor for D of 6.7×10^{-5} (basalt) and 6.7×10^{-7} (montmorillonite). The amount of adsorbed water exchanged is much less than the total amount of adsorbed water present in the regolith because feedback of the atmospheric vapor on the equilibrium process will limit the amount of water that can exchange; the values used are more typical of the actual amount of water which would exchange (as obtained using

Table 5. Annual Diffusivity Depths (in Meters) for Various Values of the Diffusivity D (in cm^2/s).

D	0.1	0.3	1.0	3.0
Depth	17.2	29.8	54.5	94.3

the more detailed model in the next section).

These scale factors result in the buffered diffusion depths shown in Table 6. The diffusion depths are typically 0.1 to 1 m through particulate basalt, or 1 to 10 cm through particulate montmorillonite. The diffusion distances through the clay are smaller owing to its larger specific surface area and its increased ability to buffer the diffusion. If an amount of water exchanges which is different from the amounts used in the calculations, of course, the diffusion depths will scale differently. These results imply that typically 100 pr μm of water is available to exchange with the atmosphere on a seasonal basis. This amount is comparable to the variation actually observed (see Chapter II), and indicates that the process can be very important under the right conditions. Of course, the annual process is much more complicated than pure diffusion. Superimposed on that process is the seasonal change in temperature which actually drives the diffusion. The skin depth which obtains when this effect is included will be calculated numerically in the next section, as will be the actual amount of water to exchange in the column for a given value of D .

An additional complication mentioned by F.P. Fanale (personal communication, 1981) is that seasonal exchange of CO_2 with the regolith may influence the H_2O exchange by sweeping up the water molecules and carrying them into or out of the regolith. This is unlikely to be significant: only a small fraction of the atmospheric CO_2 in a column can exchange seasonally with the regolith (Jakosky, 1981; Fanale et al., 1982). Thus, if the CO_2 carries H_2O with it in proportion to its atmospheric mixing ratio (which it would do in a steady state) only a small fraction of the H_2O in the atmosphere could exchange. Regolith diffusion would have to be in the Knudsen flow regime ($D \approx 5 \text{ cm}^2/\text{s}$; mean pore size $\gtrsim 5 \mu\text{m}$) for CO_2 to carry H_2O at all. Otherwise, the dominant collisions experienced by an H_2O molecule will be with the pore walls, and the

Table 6. Annual Diffusion Depths (in Meters) for Various Values of the Diffusivity D (in cm^2/s), Including the Buffering Effects of a Regolith.

D	0.1	0.3	1.0	3.0
Basalt	0.14	0.24	0.45	0.77
Montmorillonite	0.014	0.024	0.045	0.077

CO₂ would be ineffective in transporting water. Given the preponderance of particles smaller than 5 μm in the atmosphere (see Toon et al., 1977, or Pollack et al., 1979) and probably mixed in with the surface material as well, it is likely that diffusion will be somewhat hindered. Of course, if D is large, then thermally-driven exchange of water will dominate CO₂-driven exchange (see next section). If D is small CO₂-driven exchange will be insignificant, and thermally-driven exchange will again dominate. As will be discussed later, D is probably less than about 1 cm²/s, well out of the Knudsen flow range.

A further interaction between the CO₂ and H₂O exchange cycles may occur if the two molecules compete for the same adsorption sites on the regolith grains, and seasonal exchange of CO₂ either opens up additional sites for H₂O, or if the CO₂ molecules are capable of displacing adsorbed H₂O molecules. CO₂ is more volatile than H₂O, however, as evidenced by its much higher saturation pressure at Martian temperatures; and by the fact that fewer molecules of CO₂ adsorb per unit area than of H₂O under Mars conditions, despite the much greater partial pressure of CO₂ than of H₂O (see Fanale and Cannon, 1974, 1979). Thus, it would appear that the CO₂ molecules adsorbed on the grains and their seasonal exchange with the atmosphere would not significantly affect the H₂O adsorption or exchange. In fact, the converse is likely, with water molecules being capable of displacing the CO₂ molecules. This process would act in phase with the seasonal temperatures, hence out of phase with any thermally-driven CO₂ exchange such that the regolith would exchange even less CO₂ during the seasonal CO₂ pressure cycle than predicted by the current models of Jakosky (1981) and Fanale et al. (1982).

Regardless of the value of D appropriate for Mars, the regolith will contain much more water adsorbed within it than is contained in the atmosphere. This is because the surface cannot be a perfect non-diffuser,

isolating the regolith from the atmosphere on all timescales. Because the surface is indeed porous, diffusion of atmospheric vapor into the regolith and adsorption onto the grains will occur on some timescale. This point has been made previously by Fanale (1976) but is worth stressing here. For instance, if there are $10 \text{ pr } \mu\text{m}$ (10^{-3} g/cm^2) of vapor in the atmosphere at the equator, there will be as much as 0.5 g/cm^2 of water adsorbed in the top meter of regolith. How much of this water will be available for seasonal exchange will then depend on the value of D which is appropriate.

3. One-dimensional Model for Seasonal Exchange

To investigate the seasonal exchange of water between the atmosphere and regolith in more detail, a simple one-dimensional numerical model was constructed. This model incorporates the most important physics of the seasonal cycle: the diurnal and seasonal variation of the surface and subsurface temperatures, and the consequent changes in the equilibrium between vapor and adsorbed water; and possible saturation and formation of ice at the base of the atmosphere.

The basic model is a finite-difference time-marching model of vapor diffusion through the regolith. The subsurface is divided into layers, with the daily flux of vapor between layers being

$$J = -D \frac{\partial n}{\partial x} \quad (5)$$

where J is the flux, D is the diffusivity already discussed, and $\partial n / \partial x$ is the vertical gradient of vapor number density. In this formulation, complicated terms such as surface flow of molecules along grains or capillary movement of liquid brines are ignored (see Barrer, 1967).

The term $\partial n / \partial x$ is approximated by the daily average of the finite difference $\Delta n / \Delta x$. That is, the diurnal variation of temperature is calculated at each depth for a particular season. At each time of day, the partial pressure of vapor in the pores which is in equilibrium with the adsorbed water is determined based on the adsorption isotherm. It is this quantity which is averaged over a day to determine the appropriate value of n . In this sense, the diurnal variation of temperature, shown to be important in the adsorption physics by Flasar and Goody (1976), is included in the model. This method is valid in the subsurface so long as significant diurnal variation of the amount of adsorbed water does not occur locally. As Flasar and Goody (1976) have shown, diurnal variation can

be significant only under special circumstances in which the atmospheric vapor lies within the lowermost few kilometers of the atmosphere. This condition is not likely to be satisfied in general (see Chapter II.B, for instance), such that diurnal variation can likely be ignored. To the possible degree that diurnal exchange occurs, the model will be inaccurate in determining the amount of adsorbed water within the diurnally-varying layer; this should not, however, affect the calculations of adsorbed water deeper in the subsurface or of the net daily exchange with the atmosphere. It should be noticed that the depth of the diurnal layer is only about 4% of the depth of the annual layer, so is a very small fraction of the column being considered.

The diurnal variation of surface temperature is obtained from the model by Kieffer (see Kieffer et al., 1977, appendix I) for nominal values of the surface thermophysical properties (thermal inertia of 6×10^{-3} cal/cm²-s^{1/2}-K; albedo 0.30). The seasonal variation of temperature at most latitudes can be seen in Figure 30, which shows the same model as is seen in Kieffer et al. (1977) with temperature as a function of season at each latitude. The model brightness temperatures are converted to kinetic temperatures by assuming a bolometric emissivity (here, 0.95). These diurnal surface temperatures are extrapolated to the subsurface by an analytic solution to the heat conduction equation with known boundary conditions (Carslaw and Jaeger, 1959; see Muhleman, 1972, for a more recent discussion relevant to planetary surfaces):

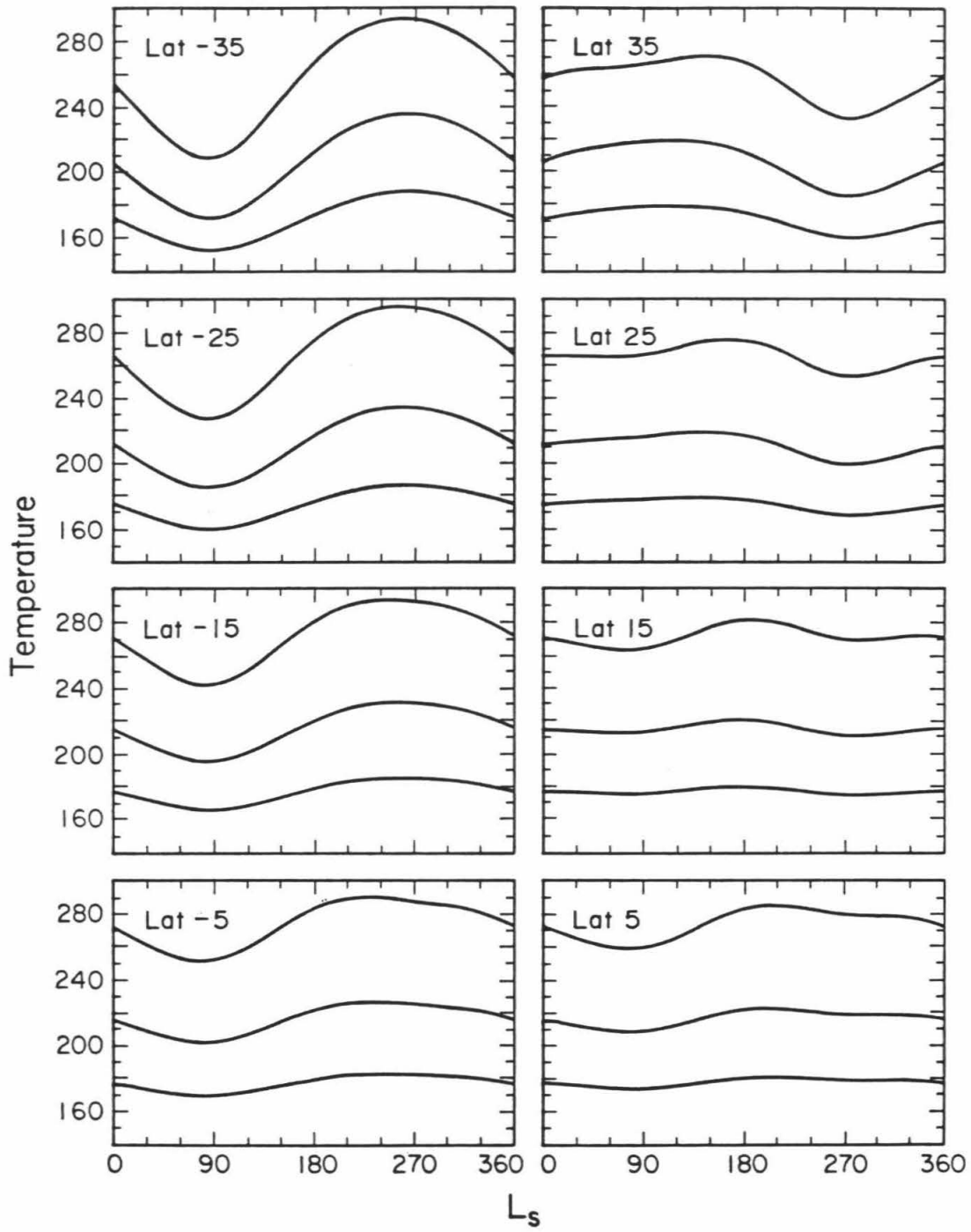
$$T(z,t) = T_0 + \sum_{n=1}^{\infty} T_n e^{-\beta_n z} \cos(\omega t - \varphi_n - \beta_n z) \quad (6)$$

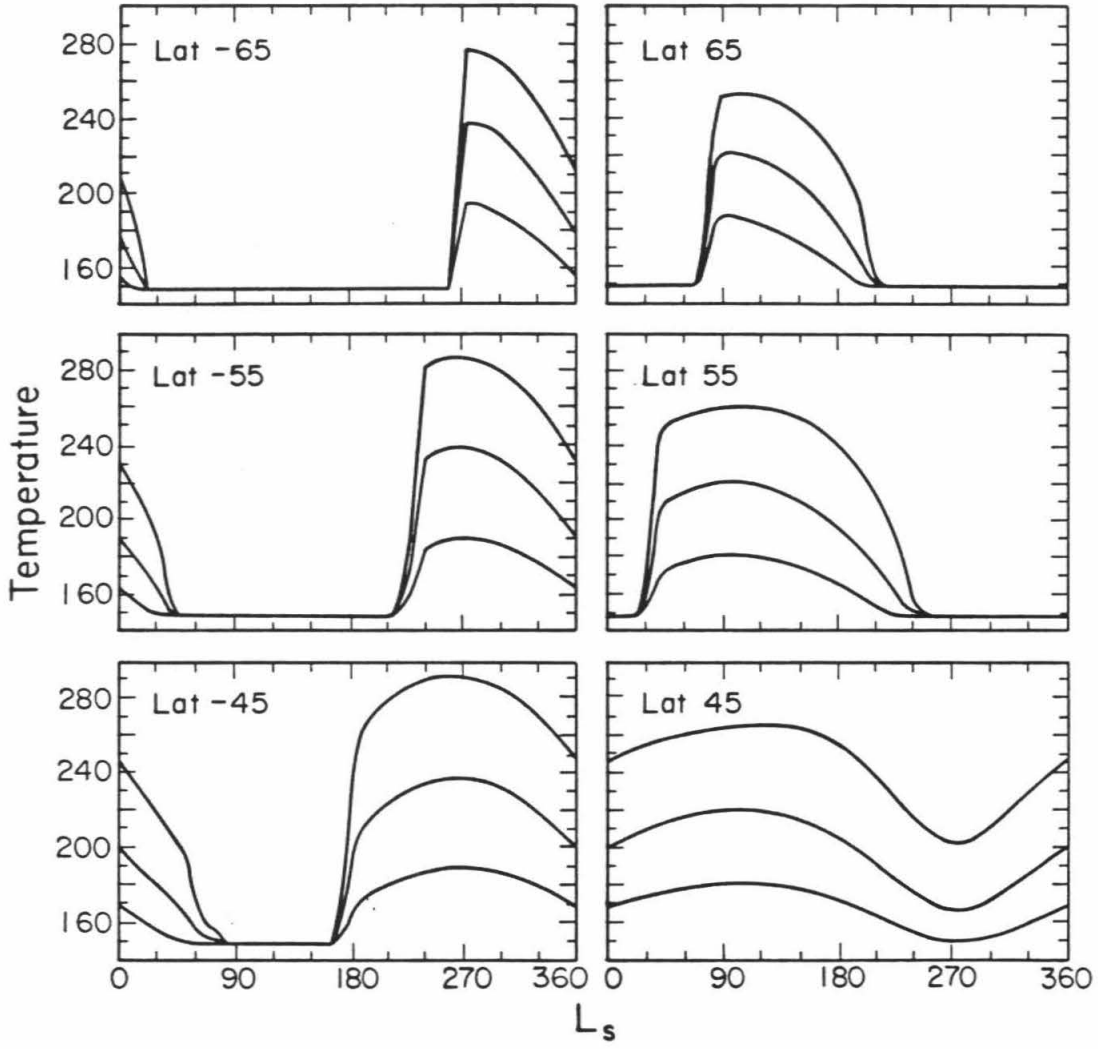
where

$$\beta_n = \left[\frac{n\Omega}{z} \frac{\rho c}{k} \right]^{1/2} \quad (7)$$

k , ρ , and c are the surface thermal conductivity, density, and specific heat,

Figure 30: Maximum, minimum, and average diurnal temperatures as a function of season as predicted by the thermal model of Kieffer et al. (1977) with thermal inertia $6.5 \times 10^{-3} \text{ cal/cm}^2 \text{-s}^{1/2} \text{-K}$ and albedo 0.25. Values of 148 K correspond to the presence of solid CO_2 on the surface.





respectively, Ω is the planetary rotation rate, and the coefficients T_n and φ_n are the values obtained from the Fourier expansion of the surface temperature [equation (2) with $z = 0$]. The assumption is made that the subsurface physical properties and behavior are constant with depth and independent of the amount of water adsorbed. Any gradient of the daily average temperature with depth, as would be caused by the seasonal penetration of the thermal wave, is ignored in the calculations; it will be seen later that the vapor diffusion skin depth is small compared with the annual thermal diffusion depth, such that this assumption is valid.

The adsorption properties used in the model are based on the measurements by Fanale and Cannon (1974) for water bound to 88- to 246- μm -sized particles of basalt, as discussed in the previous section. Although clay would have a significantly greater buffering ability, the additional capacity would be balanced in part by the additional inhibition of diffusion owing to the greater degree of buffering by the clay. Results of one-dimensional models calculated using adsorptive properties more like those of clay do not show a large difference from those calculated for the basalt. This result indicates that the feedback of the atmospheric vapor abundance on the adsorption equilibrium plays an important role in the process, and that conclusions obtained for the basalt would not change significantly if the clay were used instead.

Any hysteresis in the adsorption isotherms is ignored. By hysteresis is meant the equilibrium adsorption of a different amount of water at a given pressure and temperature depending on whether the material has most recently undergone adsorption or desorption of gas. Hysteresis is most prevalent among clays due to the increased importance of capillary adsorption (Fanale and Cannon, 1979), but even there produces a relatively small effect (see Anderson et al., 1978). Finally, the assumption is made that local exchange between

adsorbed water and vapor in the pore spaces is much quicker than a day, such that the regolith is always in local equilibrium.

The atmosphere is treated in a fairly rudimentary fashion in order to isolate the effects of the regolith in the exchange. Atmospheric vapor is assumed to be mixed uniformly with height (i.e., constant mixing ratio). This is a reasonable assumption given the large values for the eddy diffusion constant which have been obtained for the middle part of the atmosphere (Conrath, 1975; Zurek, 1976; Kong and McElroy, 1977), the daily convection occurring within the lower part of the atmosphere (Gierasch and Goody, 1968, 1972; Pollack et al., 1979), the fact that airborne dust is uniformly mixed with height (Kahn et al., 1981), and the unsaturated state of the atmosphere up to a height of 10-30 km (Chapter II.B). Thus, any vapor exchanged one day is assumed to be uniformly mixed within the atmosphere by the following day. Complications such as possible mixing of vapor with an effective scale height different from that of CO₂ or an inversion in vapor abundance (see Chapter II) are ignored. The atmospheric temperature at the surface is taken to be the same as the ground temperature in order to determine whether saturation and condensation occurs at night. These temperatures are very close to each other at night, when fogs or frost may form (Hess et al., 1977). If the frost point is reached, the base of the atmosphere is assumed to hold as much vapor as it can, with no supersaturation or time delays present. The fog or frost which forms is not allowed to affect the energy budget of the surface, consistent with the small amounts of water involved and the low optical thickness of fog (see Pollack et al., 1977). Flasar and Goody (1976) predicted large opacities and significant energy effects because much of the atmospheric vapor was within that part of the lower atmosphere which undergoes diurnal variation of temperature, owing to their assumption of near-surface vapor concentration; these effects will not

occur for a more-uniformly distributed vapor..

The model is constructed, then, with one atmospheric layer and between 5 and 9 subsurface layers. The first (surface) layer is typically 0.2 diurnal thermal skin depths thick (about 0.9 cm), and the thickness of the successive layers increases exponentially with depth. Thicker layers were needed if less water was adsorbed, owing to the consequent larger diffusion distances; in all cases, however, the layers were chosen such that the finite-difference scheme successfully converged and the lowermost layer was deep enough to not significantly affect the seasonal behavior. The entire column conserved water, with no loss from the column across the bottom boundary or from the atmosphere. A one-day timestep was used, and the model reached a steady state after from three to ten Martian years, depending on the initial conditions. The initial distribution of adsorbed water within the regolith was chosen to be in approximate yearly equilibrium with an input initial amount of atmospheric vapor. Thus, in this one-dimensional model, the total amount of water present in the column is a free parameter; the model then calculates the seasonal variations which subsequently occur. Tests of the model using thinner layers and shorter timesteps were done, and show that no significant errors arise from the choice of layer size or timestep.

It is of interest to notice that the basic model is constructed entirely independently from the water vapor behavior that it should predict. In no way do the vapor observations enter into the calculations except as an aid in fixing the initial amount of water present in the column. Even then, this free parameter essentially varies only the average atmospheric abundance predicted by the model; the amplitude and phase of the seasonal variation is nearly independent of the total amount of water in the column. Additionally, even this free parameter will be eliminated in the models in the following sections, such

that the relevant physics will be completely independent of the observations.

Figure 31 shows the seasonal variation of atmospheric vapor at $+25^\circ$ latitude predicted by the model for various values of the diffusivity. For each case, the amount of water placed initially into the column is chosen such that the annual average-atmospheric abundance is equal to the observed average at this latitude. The result is that there is about 1.5 mg of water adsorbed per g of regolith at depth, equivalent to about 0.2 g of water within the top meter (or 2000 pr μm of vapor if it were all placed into the atmosphere). By comparing the predicted variation with the temperature variation seen in Figure 30, it can be seen that the water exchange closely follows the temperatures. Water is forced into the atmosphere during the summer and removed again during the winter. The effect of varying the diffusivity is twofold: First, larger values of the diffusivity allow more regolith to be in communication with the atmosphere, with larger seasonal exchange of water occurring. A diffusivity of $3.0 \text{ cm}^2/\text{s}$ results in a seasonal variation of atmospheric vapor of about 20 pr μm , while a diffusivity of $0.1 \text{ cm}^2/\text{s}$ results in only a couple pr μm variation. The observed amplitude of the seasonal variation at this latitude, about 10 pr μm , corresponds closely to that predicted for $D = 1.0 \text{ cm}^2/\text{s}$. Second, a lower value of the diffusivity will result in a time delay of the vapor appearance and disappearance. For the range shown in Figure 31, $0.1 \leq D \leq 3.0 \text{ cm}^2/\text{s}$, the difference in the time of the vapor maximum can vary by near 30° of L_s (about two Earth months). The delay results from the difference in the amplitude of the response to the forcing function, and is analogous to that seen in the diurnal temperature response of a surface to forcing by insolation, where the temperature maximum occurs well after the maximum insolation.

Because a surface with $D = 1.0 \text{ cm}^2/\text{s}$ can reproduce the amplitude of the seasonal atmospheric vapor variation at this latitude, models were run using

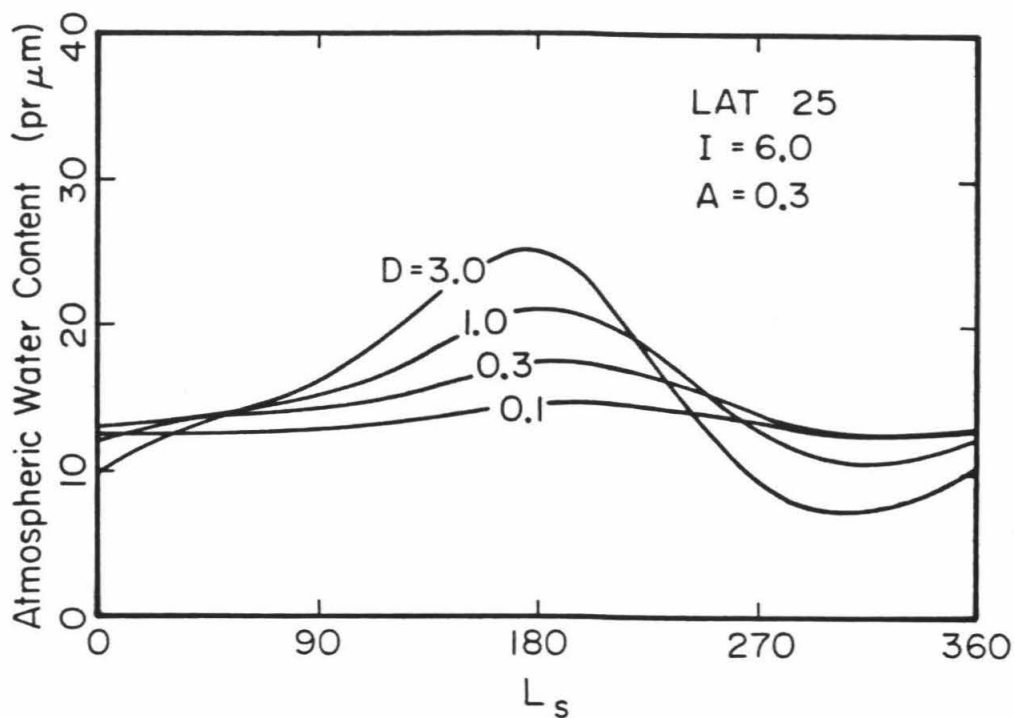


Figure 31: Results of the simple one-dimensional model for regolith exchange obtained by varying only the regolith diffusivity D . The model is for a latitude of $+25^\circ$, and the amount of water in the total column (atmosphere plus regolith) is adjusted such that the average atmospheric vapor abundance is about the same as is observed.

this diffusivity at other latitudes. Figure 32 shows the model variations for $D = 1.0$ compared with the observed vapor variation at latitudes of $\pm 45^\circ$ and $\pm 25^\circ$. In each case the only free parameter in the model was the amount of water contained within the column of atmosphere and regolith at each location; this value was adjusted at each latitude such that the modeled maximum vapor abundance was close to the observed maximum abundance. In comparing the relative amplitudes and phases, recall that the vapor abundances during the dust storm periods are lower limits due to the masking of the vapor by scattering of light from the atmospheric dust (see Chapter II.A); these time periods are approximately $L_s = 205^\circ$ to 245° and $L_s = 275^\circ$ to 345° . Generally speaking, there is a good correspondence between the models and the data. Both indicate that the largest amounts of atmospheric vapor are present during local summer, and the models reproduce the seasonal amplitude at all of the latitudes shown. There are discrepancies, however, between the models and the data: At $\pm 25^\circ$ latitude, the vapor abundance peaks before the model predictions. At $\pm 45^\circ$, the spring rise in vapor is well-modeled, but the fall decline predicted by the model is slower than is observed. That differences occur is not surprising, due to the lack of consideration given atmospheric transport of water and its effects on the regolith exchange. Transport and other processes will be considered in more detail in following sections.

With the southern hemisphere having the more-extreme seasons (see Figure 30), it is of interest to try to understand why the southern hemisphere has so much less atmospheric vapor throughout the year than the north. Figure 33 shows the predicted vapor abundances at different latitudes assuming that the regolith everywhere has the same amount of water adsorbed in it. At depth at each latitude, 1 mg water is adsorbed per gram regolith. Not unexpectedly, the extreme southern summers cause more vapor to be

Figure 32: The results of the simple one-dimensional model for regolith exchange of vapor at $\pm 25^\circ$ and $\pm 45^\circ$ latitude. The smooth curve is the model, calculated for $D = 1.0 \text{ cm}^2/\text{s}$. The bar graph represents the observed vapor abundances (see Chapter II.A).

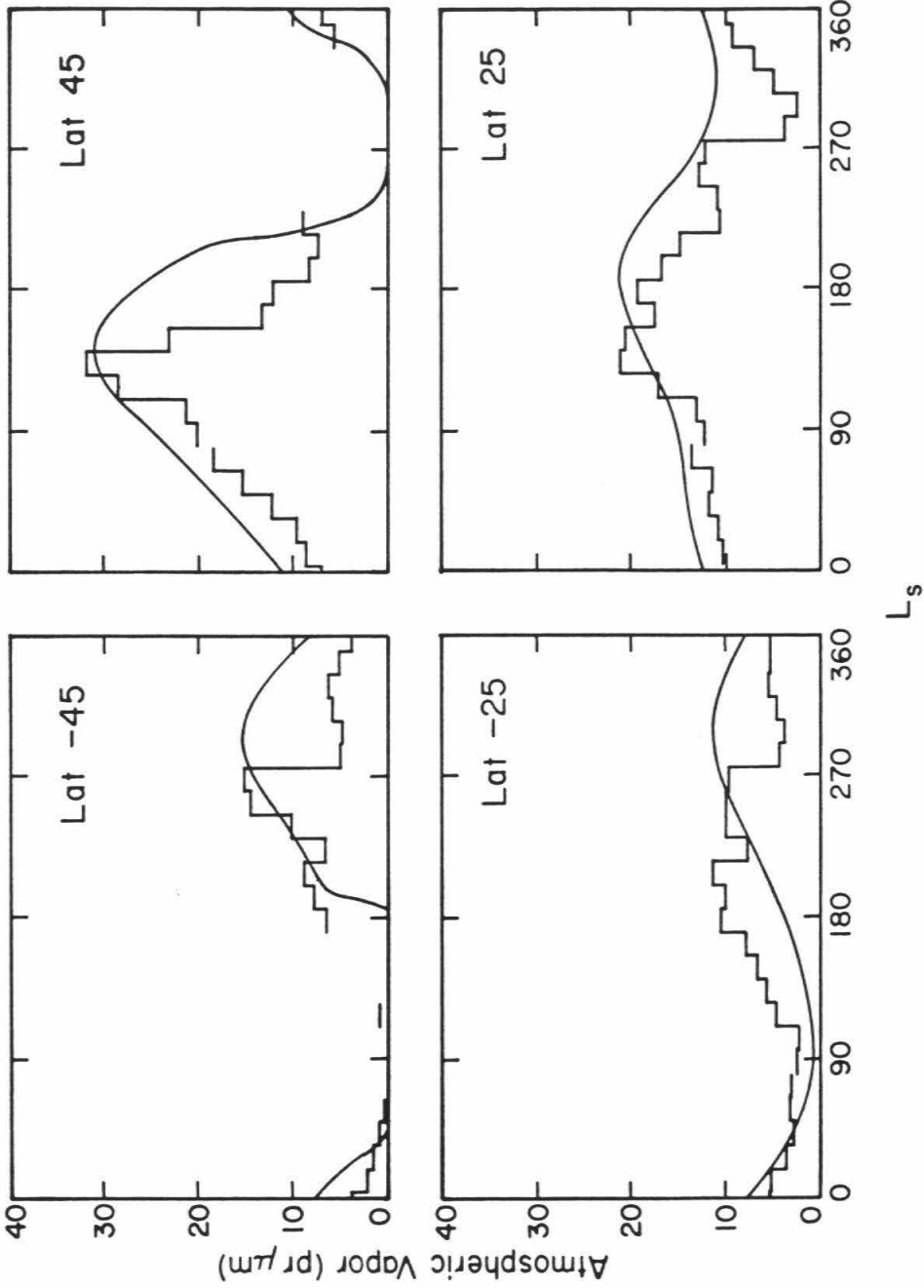
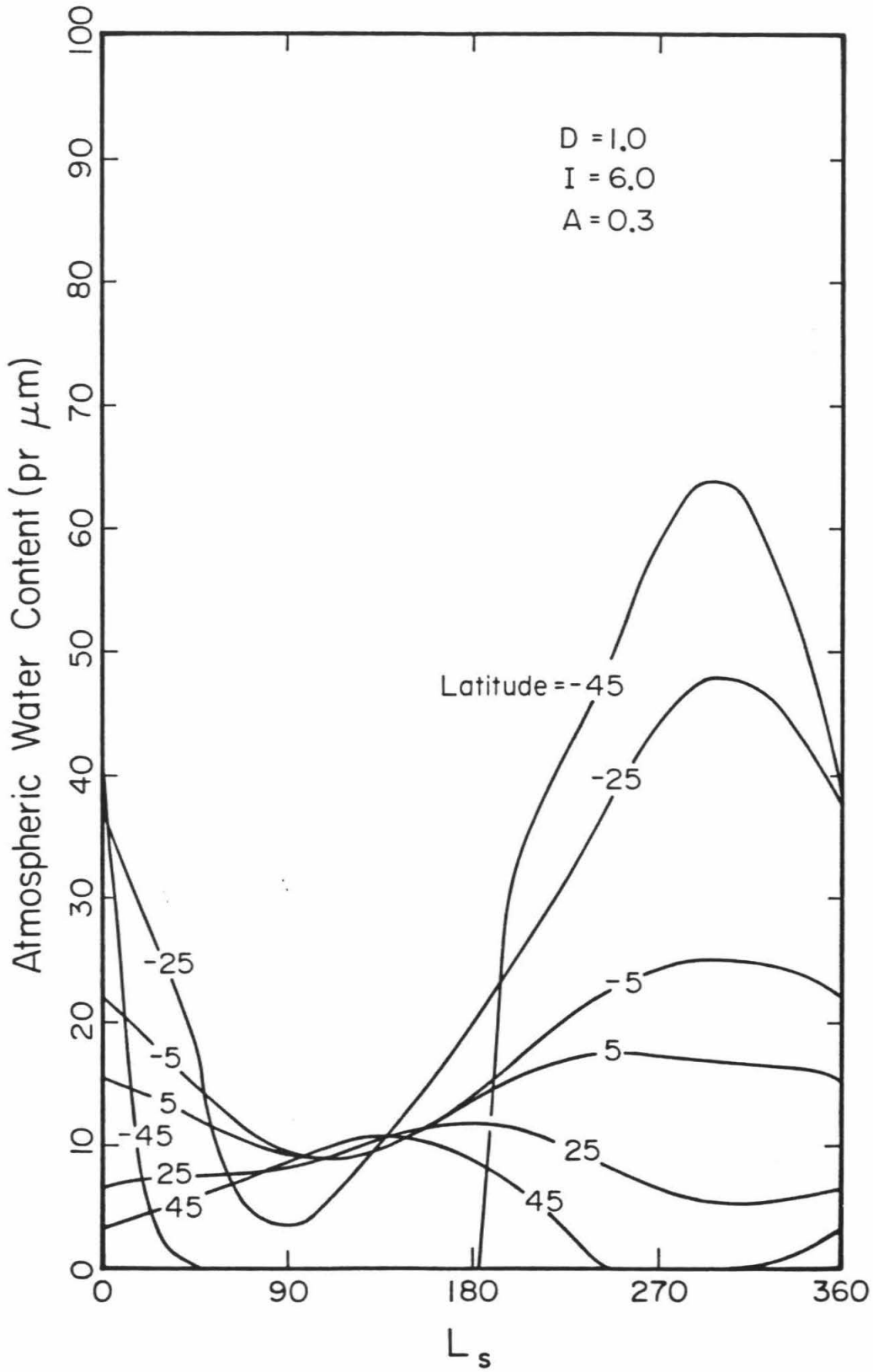


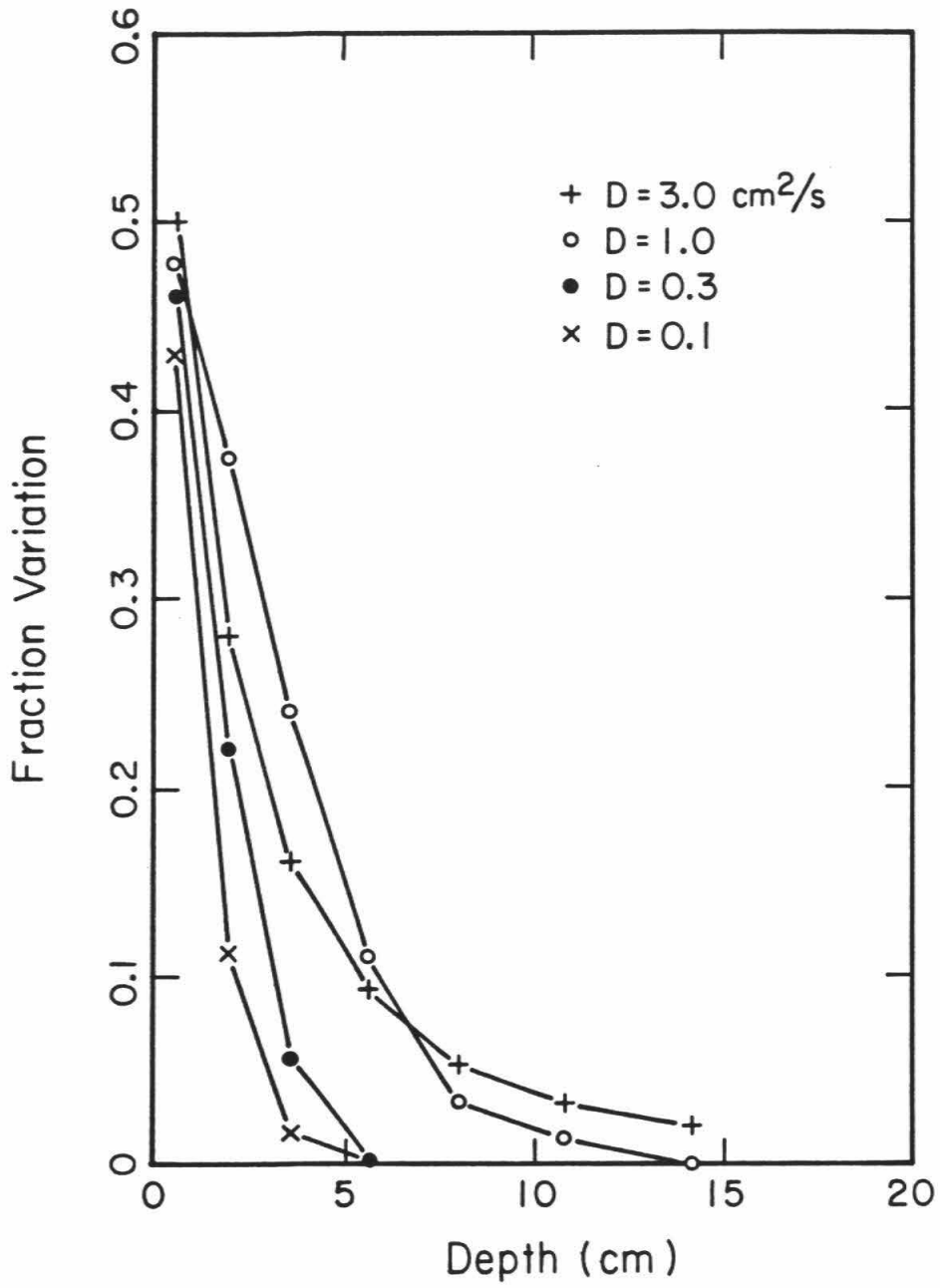
Figure 33: Results of the simple one-dimensional model for regolith exchange, assuming that the same amount of vapor is adsorbed at depth at each latitude. The model assumes 1.0 mg water/g rock at depth, and $D = 1.0 \text{ cm}^2/\text{s}$. The southern hemisphere abundances are all greater due to the more-extreme seasonal temperature variation which occurs in the south.



exchanged in the south than in the north. As much as 60 pr μm of vapor would appear in the south at -45° latitude, compared to only 10 pr μm at $+45^\circ$. The observed abundances indicate that more than 30 pr μm appears at $+45^\circ$, as compared to only about 15 pr μm at -45° (Chapter II.A). This immediately suggests that the regolith in the south must be depleted in water relative to the regolith in the north or that exchange in the south is hindered by a lower regolith diffusivity. A lower diffusivity may be tied to the difference in surface properties between the two hemispheres, as reflected in the map of thermal inertia (Palluconi and Kieffer, 1981). If the south, is depleted in regolith water near the surface, it may be related to the fact that the north residual polar cap is a seasonal source for vapor while the south cap is a sink at all seasons (during the year seen by Viking), thereby depleting the atmosphere in the south of vapor relative to the north. In fact, the southern regolith will be depleted of adsorbed water relative to the north independent of whether significant seasonal exchange of water with the regolith occurs. This is because exchange will occur on some (longer) timescale, and the regolith will seek to be in equilibrium with the overlying atmosphere. The relative dearth of atmospheric vapor seen in the south will eventually translate into a marked decrease in adsorbed water in the south.

The seasonal profile of adsorbed water within the regolith can be examined in these models in order to determine the exchange skin depth, as mentioned in the previous section. Figure 34 shows the fractional seasonal change of adsorbed water at each depth in the regolith for various values of D . The range in effective e-fold skin depths near the surface is from about 2 cm for $D = 0.1 \text{ cm}^2/\text{s}$ to about 5 cm for $D = 1.0 \text{ cm}^2/\text{s}$. It is not immediately clear why the e-fold distance should initially be larger for the $D = 1.0$ case than for $D = 3.0$. This may be related to the larger absolute value of exchange occurring

Figure 34: The seasonal variation of the amount of water adsorbed as a function of depth for various values of D . The variation is expressed as the fractional variation at each depth. The models are calculated for $+25^\circ$ latitude. The e-fold skin depths near the surface range from about 2 cm for $D = 0.1$ to 5 cm for $D = 1.0$.



for $D = 3.0$; or to the fact that diffusion is much more rapid in this case, such that a thicker near-surface layer would be essentially in equilibrium with the atmosphere. In any case, this behavior reverts deeper down to what is expected *a priori*, with the $D = 3.0$ regolith undergoing the larger seasonal variations in adsorbed water. These adsorption skin depths are all comparable to the daily thermal diffusion skin depth of about 5 cm (Kieffer, 1976), and much less than the annual thermal diffusion depth of about 1.3 m. It is for this reason that seasonal-wave thermal gradients have been ignored in the model.

4. One-dimensional Model with Boundary Conditions

The model discussed in the previous section suffers from its inability to include numerous processes which undoubtedly occur. Possibly the most significant of these will be the transport of water vapor from place to place due to the circulation of the atmosphere. Mass transport is a relatively rapid process (e.g., Pollack et al., 1981), and the water vapor would be expected to follow along, except possibly where saturation and condensation occur. This transported water will somehow feed back into the process of regolith exchange, thereby either enhancing or reducing the amount of water exchanged (depending on whether transport is increasing or decreasing the local vapor abundance). Whatever processes may be acting on the surface and atmosphere, they must combine to produce the atmospheric vapor abundances which are observed. The observed abundances can therefore be used as boundary conditions to calculate the amount of water exchanged with the regolith throughout the year.

The model used to calculate this exchange is identical to that in the previous section, except that the observed vapor abundance at a given season is used in the calculations of the flux of water across the surface boundary, rather than using a vapor abundance calculated from the previous history of the regolith and atmosphere at that latitude. Figure 35 shows a contour representation of the boundary condition used. This was obtained from a smooth and continuous line drawn through the observed vapor abundances at each latitude as a function of time. These boundary conditions can also be seen in Figure 36, with the dashed line showing the seasonal behavior at each latitude. The only significant uncertainties in these abundances are during the times of the global dust storms, when the actual abundances were uncertain for several months. The abundances used are obtained so as to be consistent with

Figure 35: Contour plot of the amount of atmospheric vapor at each latitude and season, obtained from a smooth line drawn through the observations (see text for discussion).

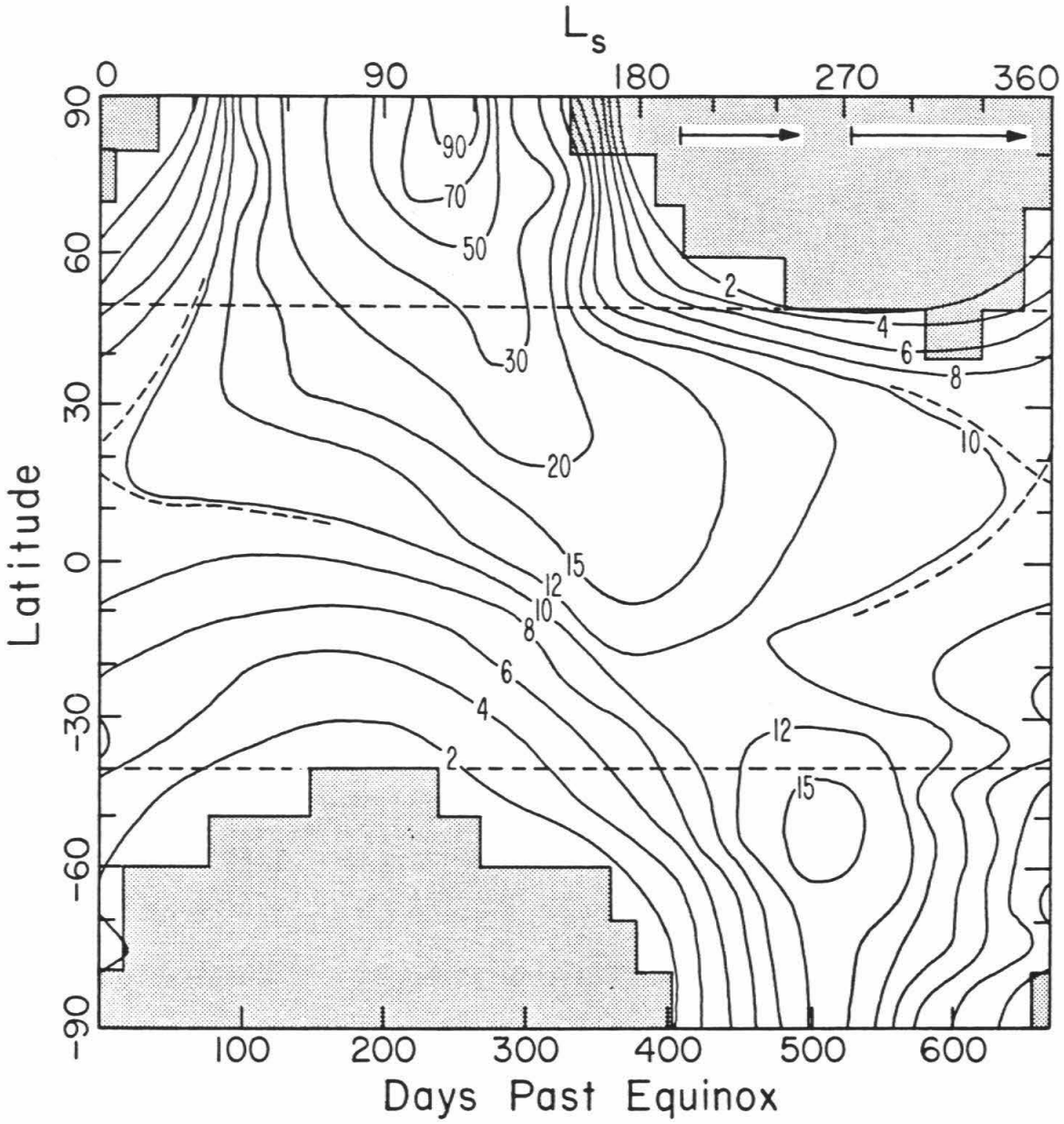
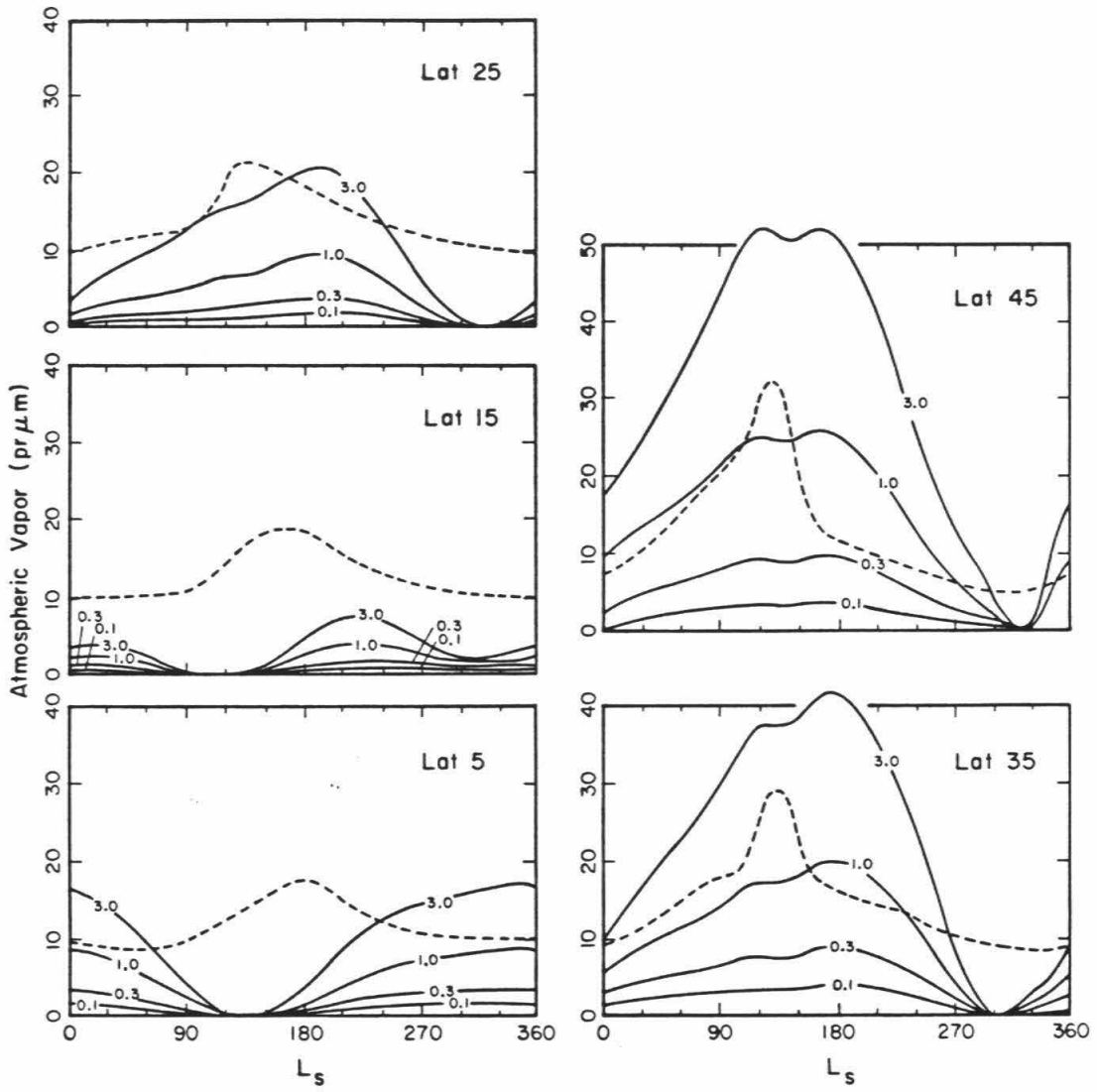
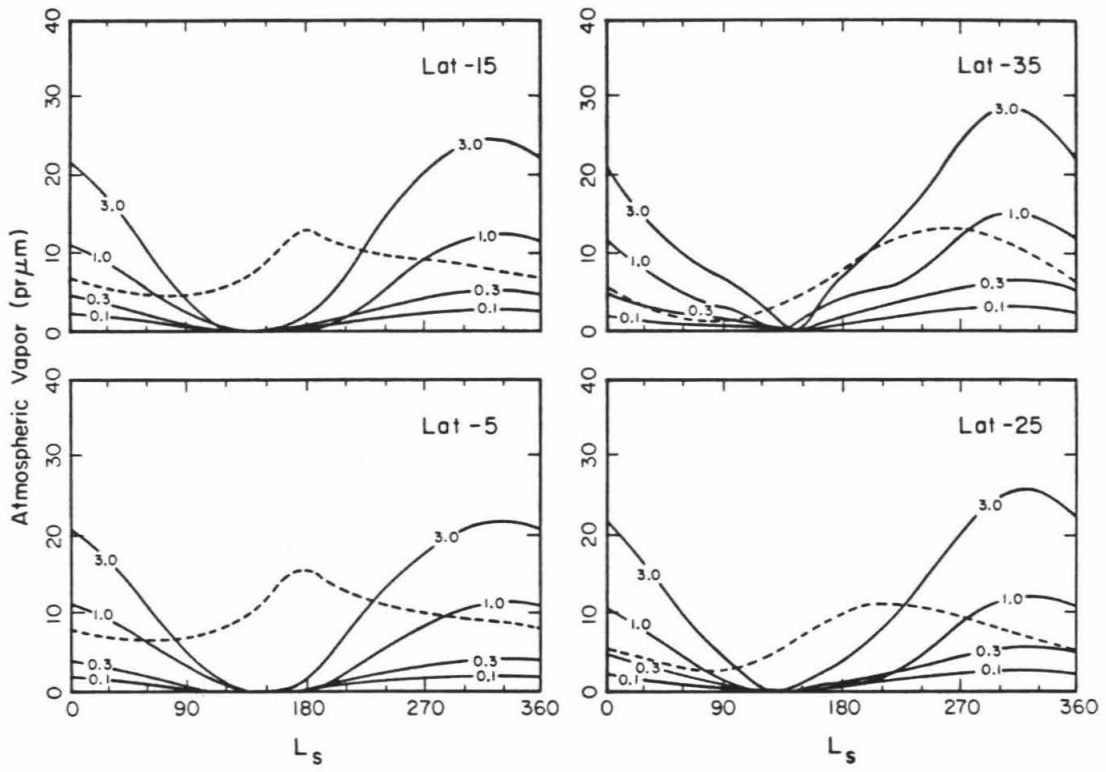


Figure 36: Results of the one-dimensional model using appropriate boundary conditions. The dashed line represents the boundary condition of atmospheric vapor as a function of season at each latitude (as also contoured in Figure 35). The solid lines represent the time integral of the surface flux of vapor at each latitude for several values of D , and are a measure of the amount of vapor in the atmosphere which would have been contributed from the subsurface. The differences of the models from the observations (dashed lines) are indicative of the importance of processes not yet considered, including transport due to atmospheric circulation. See text for further discussion.





the dust storms producing no significant effects on the vapor in the north, and with the seasonal decline in the south (which is partly masked by dust) being approximately symmetric with the seasonal rise at each latitude. Comparing the dashed lines in Figure 36 with the observed abundances in Figure 2 (Chapter II.A) shows that the chosen boundary conditions are a reasonable approximation to the data. Additionally, the shape of the contours in Figure 35 is consistent with those obtained by Davies (1981), who tried to correct for the dust obscuration effects using a model of atmospheric scattering.

The output of the model now is the surface flux of vapor as a function of season. Notice that for a given value of D , this model has no free parameters at all. If too much water is initially placed in the regolith relative to what should be in equilibrium with the atmosphere, there will be a net loss of water from the subsurface the first year, and the excess water will be lost from the system. Similarly, if too little water is chosen initially, there will be a net gain. The model then iterates until the net annual flux across the surface is nearly zero, and a steady state is reached.

Integrating the surface flux over time produces a measure of the amount of water which has come from the regolith at each season. These vapor abundances are compared with the observed seasonal variation in Figure 36. At most latitudes, a diffusivity of $3.0 \text{ cm}^2/\text{s}$ results in more water exchanging seasonally with the regolith than is observed in the atmosphere. In order for this model to be valid, transport must remove the excess water to other latitudes. A diffusivity of $0.1 \text{ cm}^2/\text{s}$ results in only a fraction of the seasonal variation possibly being due to the regolith. This model can be valid only if transport can supply the necessary water to make up the difference. That the models for exchange do not match the observations at most latitudes is again indicative of the fact that atmospheric transport must be important in the

vapor cycle.

The most-poleward latitudes shown in Figure 36 indicate, as before, that the regolith will supply the largest amounts of water during local summer. This results predominantly from the regolith temperature variations. The amount of vapor in the atmosphere also feeds back into the exchange — when the atmospheric vapor increases rapidly, the effect is to inhibit water from coming out of the regolith, or to actually force water back into the regolith, despite the increasing surface temperatures. This effect can be seen in Figure 36 at $+45^\circ$ latitude. The sudden increase in vapor abundance near $L_s = 120^\circ$, presumably caused by transport of vapor in from the polar regions, actually forces water back into the regolith. As the abundance then decreases, water is allowed again to come out of the regolith.

The band at $+15^\circ$ shows the least seasonal exchange, due to the very small variation of temperature with season (Figure 30) and of observed vapor abundance with season (Figure 36). In fact, exchange here occurs twice yearly, as temperature rises occur during both northern and southern summer, with declines during the fall and spring.

The modeled seasonal rise and fall of vapor at most northern latitudes is much less sharp than the observed variations in abundance. This results from the slow seasonal variation of surface temperatures, and the subsequent slow response of the water; and from the fact that some of the sharpness in the observed peak may be from water coming from the polar caps (see Chapter II.A). An additional complication will occur if the vapor is distributed to different heights in the atmosphere at different seasons (see Chapter II.B). Changing the vertical distribution has the effect of changing the surface concentration of water molecules, and will either pump water into or out of the regolith, even at a

constant regolith temperature. Thus, if the vertical distribution changes in the proper manner, it could easily drive the water into the regolith as rapidly at the end of summer in the north as is observed. This point will be discussed in more detail in Chapter III.B.

It is obvious from Figure 36 that the regolith can indeed supply large amounts of water to the atmosphere seasonally. That the regolith does not uniquely explain or reproduce the seasonal variations observed indicates that transport must also play a significant role, as would be expected. Models that include both processes acting simultaneously will be discussed in Chapter III.B.

The models shown in Figure 36 are produced by reaching a steady state with no free parameters. Therefore, the amount of water adsorbed in the regolith should be in equilibrium with the observed vapor abundance at each latitude (independent of D). The latitudinal gradient of the adsorbed water abundance is seen in Figure 37. The regolith in the north has much more water adsorbed than in the south. This is due both to the larger vapor abundances in the north and to the more-extreme seasons in the south, as discussed in the previous section. Again, these results will hold independent of D , so long as the timescale to diffuse into the regolith is more rapid than the timescale for changing the seasonal behavior.

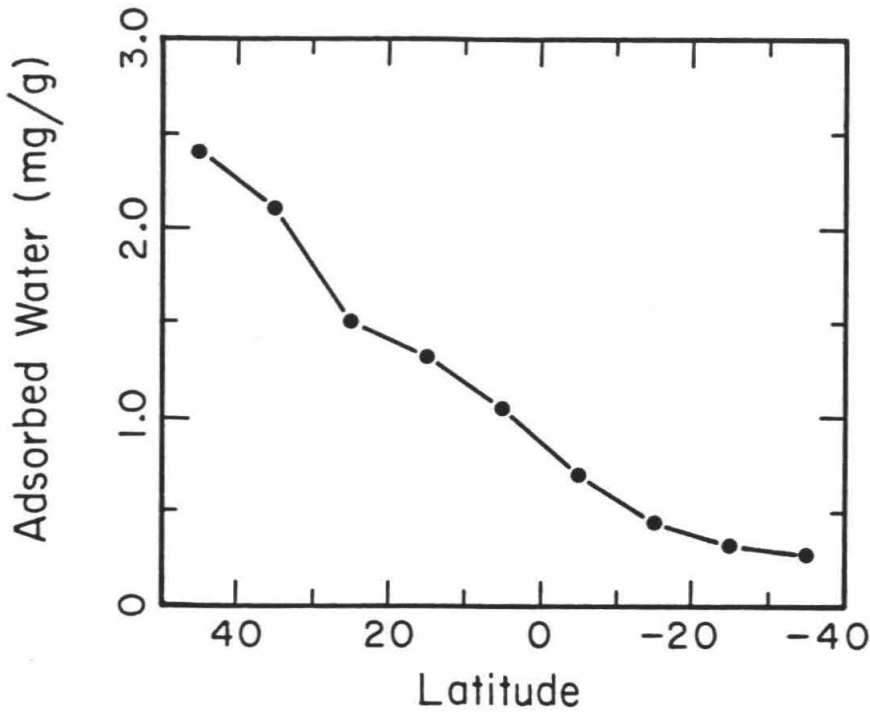


Figure 37: The latitudinal gradient of the amount of water adsorbed at depth (mg of water per g rock). These results are obtained from the one-dimensional model with atmospheric boundary conditions, and represent the subsurface abundance of water *independent* of the value for D which is appropriate. If the regolith were composed of a clay mineral (such as montmorillonite), the values for the amount of adsorbed water would be about 100 times greater at each latitude.

5. Discussion

It is apparent from the models presented in the last several sections that large amounts of water can exchange seasonally between the atmosphere and regolith on Mars. Because it is unlikely that $D \lesssim 0.1 \text{ cm}^2/\text{s}$ (Flasar and Goody, 1976), exchange of vapor must account for at least 10% of the seasonal variation of vapor in the regions discussed. For the largest possible values for D ($\approx 3.0 \text{ cm}^2/\text{s}$), exchange with the regolith results in more water variation locally than is observed; atmospheric transport must then make up for this excess. In fact, the timing of the appearance and disappearance of water due to the regolith does not coincide with the observed variation of vapor except in the more-poleward regions, such that transport must play an important role. The degree to which water actually will exchange will depend on the value for D which applies to the Mars regolith, as well as on possible variations in D from place to place.

The large amounts of dust which are emplaced yearly into the atmosphere during the global dust storms (e.g. Conrath, 1975; Pollack et al., 1977, 1979) are evidence of a loosely-packed, un-cemented surface which would be conducive to diffusion. Deposition of dust has been observed at the Viking landing sites (Guinness et al., 1979), arguing that the porous surface is to some degree widespread over the planet. The thermal inertias measured for the planet range from 1 up to about $20 \times 10^{-3} \text{ cal/cm}^2 \text{ -s}^{1/2} \text{ -K}$ (Palluconi and Kieffer, 1981). These values are much lower than the values which would be measured for any solid rock, about $45. \text{ to } 60. \times 10^{-3}$ (Carslaw and Jaeger, 1959), and are consistent with a porous medium (see Wechsler and Glaser, 1965; Wechsler et al., 1972) with some rocks on the surface (Jakosky, 1979; Christensen, 1982). The low values of thermal inertia also rule out well-cemented particulates which might have low vapor diffusivities.

These observations all imply that Mars is covered globally with a porous surface that is capable of allowing significant diffusion of vapor. Because adsorption will occur on all particulate surfaces, in a strongly temperature- and pressure-dependent manner, seasonal exchange of water between the atmosphere and regolith must occur. The importance of this process to the seasonal water cycle, relative to exchange of water with the polar caps, will depend on the value of D which is appropriate. The relative importance of these processes will be discussed in the next section.

III.B. Coupled Models of the Regolith, the Polar Caps, and Atmospheric Transport

1. Introduction

In the previous section it was seen that seasonal exchange of water between the regolith and atmosphere provides more than about 10% of the seasonal water and possibly as much as about 150%, depending on what value of the regolith diffusivity D is appropriate. Because the timing and rate of the release of this water into the atmosphere did not coincide with the appearance and disappearance of atmospheric vapor observed at all latitudes it is apparent that transport of vapor must play an important role in the seasonal water cycle.

In the following sections, simple models of meridional transport of vapor are developed and applied to the seasonal movement of vapor. The basic model is a simple climate-type model similar to those used in the meridional transport of energy in the atmospheres of both Earth and Mars (see, for instance, Sellers, 1969; North, 1975; Budyko, 1977; James and North, 1982; and many others). Transport of vapor is assumed to be in the down-gradient direction, with an effective transport time constant or atmospheric diffusivity. This model will then be coupled to a model of regolith exchange at each latitude, in order to see the combined effects of both processes. The behavior of water vapor over the polar caps must also be taken into account in any global model; based on the Viking observations (see Chapter II.A) the north residual cap will act as a source of water during the summer and a sink during the winter, and the south cap as a sink at all seasons. The seasonal polar caps in both hemispheres will act as a sink for vapor whenever CO_2 is present but will release the frost as the cap retreats.

By constructing coupled models which incorporate all of the major processes for affecting the seasonal water cycle, it will be possible to examine the relative importance of each of the processes in supplying the seasonal water. The strength of the conclusions reached will rest on the validity of the assumptions built into the several models, the ability of the models to reproduce vapor behavior like that observed, and the uncertainties in the known properties of the regolith and atmosphere.

The next section contains a discussion of the behavior of the simple model for the meridional transport of vapor, including possible values for the atmospheric mixing constant as derived from models and observations of the atmospheric circulation. The two sections following contain the results of the models which incorporate the regolith and polar caps as well as atmospheric mixing. In the last section of this chapter, the results regarding the physical properties of the atmosphere and regolith and the relative importance of the various processes will be discussed. Also included here is a discussion of the implications of these models for the behavior of water on the $\sim 10^5$ -year timescale of the orbital obliquity variations (Ward, 1979).

2. Estimates of Global Atmospheric Mixing Times

In the atmospheric transport formulation used here, movement is quasi-diffusive, with vapor going down the gradient of total atmospheric column abundance of vapor. The parameter used to describe the rate of this transport is the atmospheric time constant, τ_a , which is the e-folding time during which the vapor in two adjacent 10° wide latitude bands will mix together and the column vapor abundances of the two bands will approach the same intermediate value (as determined using the appropriate spherical geometry). In this section, estimates of this mixing time will be obtained using both observations and models of the Mars atmospheric circulation.

The most detailed models of the Mars atmosphere are the three-dimensional global circulation models by Pollack et al. (1976, 1981), Leovy and Mintz (1969), and Moriyama and Iwashima (1980), and the two-dimensional (axisymmetric) model by Haberle et al. (1980). These models are full solutions to the equations of motion for the atmosphere with appropriate heating and cooling terms. They have been run at several different seasons for Mars (see Table 7) and generally show an equatorial Hadley cell as the predominant form of advection. Hadley-cell circulation will produce down-gradient transport of vapor if and only if the water is uniformly mixed vertically; for instance, if the water is all located in one branch of the cell, transport will go in the direction of the motion in that branch, independent of the gradient. The maximum meridional velocity in the region of the Hadley cell allows an estimate of the global mixing time τ_a to be made. The maximum velocities obtained by the various models for the lower branch of the cell are given in Table 7, along with the corresponding time that such a wind would take to travel 10° in latitude. The transport times range from about $\frac{1}{2}$ to $3\frac{1}{2}$ days, depending on the season and on the amount of dust in the atmosphere. These numbers are based on the

Table 7. Results from Atmospheric Circulation Models
(see text for details).

Model	L_s ($^{\circ}$)	Velocity (m/s)	Transport Time (days)	τ_a
Pollack et al.	100	6	1.1	2.2
Leovy and Mintz	270	8	0.8	1.6
	0	2	3.4	6.8
Haberle et al.	270	7-11*	0.9-0.6*	1.8-1.2*
Moriyama and Iwashima	0	2	3.4	6.8

*Depending on atmospheric dust opacity.

maximum velocities, however, and the average velocity of the lower branch will be about half these values, with a corresponding increase in the appropriate value for τ_a , as listed in Table 7. Estimates for τ_a thus lie within the range $1 \lesssim \tau_a \lesssim 7$ days, again depending on season and dust opacity.

The energy balance climate model for Mars by James and North (1982) also allows an estimate of τ_a to be made. Their model incorporates the sublimation and condensation of CO_2 on the polar caps, and they attempt to find a self-consistent set of parameters (polar cap albedo and emissivity, atmospheric mixing constant, and surface and atmospheric emissivity) that provides the proper polar energy balance and hence reproduces the annual variation of atmospheric pressure. While unable to accurately reproduce the curve with a simple model, their best fit occurs with an effective atmospheric diffusivity of $D_a = 0.004 \text{ w/m}^2 \text{ -K}$. D_a may be converted to the equivalent τ_a via:

$$\tau_a = \frac{H\rho C_p(\Delta\theta)^2}{2D_a} \quad (8)$$

where H is the atmospheric scale height, ρ and C_p the atmospheric density and specific heat, respectively, and $\Delta\theta$ the distance diffused (in this case $10^\circ = 0.175 \text{ r}$). Using $\rho = 1.5 \times 10^{-6} \text{ g/cm}^3$, $H = 10^4 \text{ m}$, and $C_p = 845 \text{ J/kg-K}$ results in $\tau_a \approx 5$ days. Because their model is not very sensitive to the value of D_a , this result may be off by as much as an order of magnitude (James and North, 1982); it is consistent, however, with the other values determined here.

An additional estimate of the rate of mixing can be made from the observations of baroclinic waves in the more-poleward regions of the Mars atmosphere. Observations of 3 to 6 day periodicities in the weather (pressure, temperature, and wind velocity) at the Viking landing sites have been interpreted as indicating the presence of baroclinic waves passing to the north of the sites (Ryan et al., 1978; Sharman and Ryan, 1980; Barnes, 1980, 1981).

Although the axisymmetric part of the atmospheric circulation is very weak this far to the north (e.g., Pollack et al., 1981; Haberle et al., 1980), this non-axisymmetric part may be important in the transport of water vapor. Estimates of the peak-to-peak amplitude of the meridional part of the geostrophic wind, made from the several-day pressure oscillations, are in the range of about 5-12 m/s during northern winter (Ryan et al., 1978). These values would translate into atmospheric advection times of $\tau_a \approx 2-6$ days. However, the occurrence of these waves is very seasonally-dependent, with the greatest activity in the north occurring during northern winter and with almost no activity during northern summer (see Hess et al., 1979), such that τ_a might be significantly longer during other seasons.

From the above discussion of various models and observations, it is apparent that the transport of CO_2 and heat occurs with mixing times τ_a of roughly 1-7 days. (There are still uncertainties in these values, however; for instance, Hamilton (1982) suggests that atmospheric tides induced by solar heating of airborne dust may strongly enhance the mixing beyond that predicted by the current models.) The transport of water vapor would generally be expected to follow that of the CO_2 or of heat (see Leovy, 1973), such that these values of τ_a would also be appropriate for calculating the vapor movement. The situation is potentially more complicated than this, however; for instance, baroclinic waves may be totally ineffective in producing a net meridional transport of vapor unless there is a source or a sink for water within the extremes in latitude to which the wave extends, or may transport the vapor up-gradient depending on the superposition of the wave pattern with any longitudinal structure of the water abundance. The values calculated here are only intended as a rough guide to what is plausible, and as a check against which the values of τ_a obtained in the global models for water can be compared.

Although it is obviously a gross oversimplification, the models developed in the next two sections will have $\tau_a = \text{constant}$, both spatially and temporally. Thus, there is no enhanced mixing included during the dust storm periods; this is to first order consistent with the models by Haberle et al. (1980), which show only a 50% variation of mixing rates within the bulk atmosphere due to dust opacity (see Table 7).

3. Mid-latitude and Equatorial Processes and Models

Between the most-equatorward excursion of the polar caps, the only processes which can be important in the water vapor cycle are exchange of water with the regolith and transport of vapor through the atmosphere. Of course, vapor can also be transported into or out of this region entirely, exchanging with the more-poleward atmosphere. In this section, coupled models of transport and regolith exchange are constructed for the region between -40° and $+50^\circ$ latitude. The seasonal CO_2 cap generally does not extend into this region at any season (see, for instance, James, 1979, and James et al., 1979), and complications regarding the seasonal behavior of the cap and exchange of water with the cap need not be considered. In the next section models will be discussed which do extend from pole to pole and which deal with the behavior of the caps.

In this mid-latitudes model, meridional transport of vapor is as discussed in the previous section, moving down the local gradient in column abundance with time constant τ_a . The observed column abundances as a function of season are used as boundary conditions at the north and south borders of the region; these take the form of the smoothed lines through the data at -45° and $+55^\circ$ latitude as shown in Figure 35. In this way, whatever is occurring poleward of -40° and $+50^\circ$ vis-à-vis the vapor abundances and the behavior of the polar caps is implicitly included in this model. At each time step in the model, the flux of vapor into and out of each 10° wide atmospheric bin due to exchange with the two adjacent atmospheric bins is calculated using the time constant τ_a .

The process of exchange of water with the regolith is included by using a look-up table to obtain the flux of water vapor across the surface-atmosphere

boundary at each time step. The fluxes used are those discussed in Chapter III.A and presented in integrated form in Figure 36. These fluxes were calculated using the observed abundance as a function of season as boundary conditions; if the results of a model which incorporates the regolith do not agree with the observations, the fluxes may be slightly in error for that model. Of course, if the model does nearly reproduce the observations, the fluxes are correct and the model is entirely self-consistent.

After the vertical and horizontal fluxes of vapor are calculated at each time step, they are applied to produce a new vapor distribution at the next step. The time step used is one Mars day, and the model is iterated for from two to six Mars years until a steady state is reached.

Figure 35 shows the smoothed version of the data against which models will be compared. In these mid-latitude models, only the region between the horizontal dashed lines is considered. The interesting features which a model should reproduce include: the maximum in vapor abundance at $+50^\circ$ latitude at $L_s \approx 130^\circ$, and the increased delay in the time of the maximum and the decreasing maximum abundance at each latitude closer to the equator; the southern-boundary maximum near $L_s \approx 270^\circ$; and the first increase in vapor nearer to the equator rather than nearer to the edge of the receding north polar cap as northern summer approaches. Of course, no quasi-diffusive model like those considered here can reproduce this early rise as a result of transport of vapor only, as vapor always moves down-gradient and the source of the transported vapor is in the north polar region. It remains to be seen, however, whether models which include the regolith can produce this type of behavior.

To quantitatively compare the results of a particular model run with the observations, a correlation coefficient between the two is calculated. The model

is output as an array of the column vapor abundance at nine latitudes (-35° to $+45^\circ$ in 10° steps) and 67 times of year (every ten Martian days). These are compared with a similar array representing the observations (shown contoured in Figure 35). A perfect correlation would yield a coefficient of 1.0, while no correlation at all would obtain a coefficient of 0.0. In essence, the coefficient is a measure of the deviation from the best-fit straight line which results if the model points are plotted versus the corresponding data points. This method of comparison is limited because all of the 603 points used in the calculation are not independent of each other, because errors or uncertainties of the same fraction magnitude produce different effects at different vapor abundances, and because it does not measure deviation from unity of the slope of the line through the points. It does, however, provide a single number estimate of the fit of the model to the data. Most of the results which will be obtained via this coefficient would also be apparent in comparing the model results directly with the observations.

The model was run for various combinations of the parameters τ_a and D , and the results are shown as a plot of the resulting correlation coefficient in Figure 38. The best fit obtained was for $D = 0$ and $\tau_a = 6$ days, with a correlation coefficient $\alpha = 0.91$. By comparing the various models, it can be understood what features are really being "fit." Figure 39 shows the model results for $D = 0$ and several values of τ_a . All of them show vapor being carried into the region from the north and from the south during their respective summers, and being carried off into the north and into the south during their respective winters. This is exactly what is expected as a result of the imposed boundary conditions at -45° and $+55^\circ$ latitude. The largest difference between the several models is the speed with which the vapor transports into and out of the region. This is manifest in Figure 39 by the line which would be drawn through the maximum

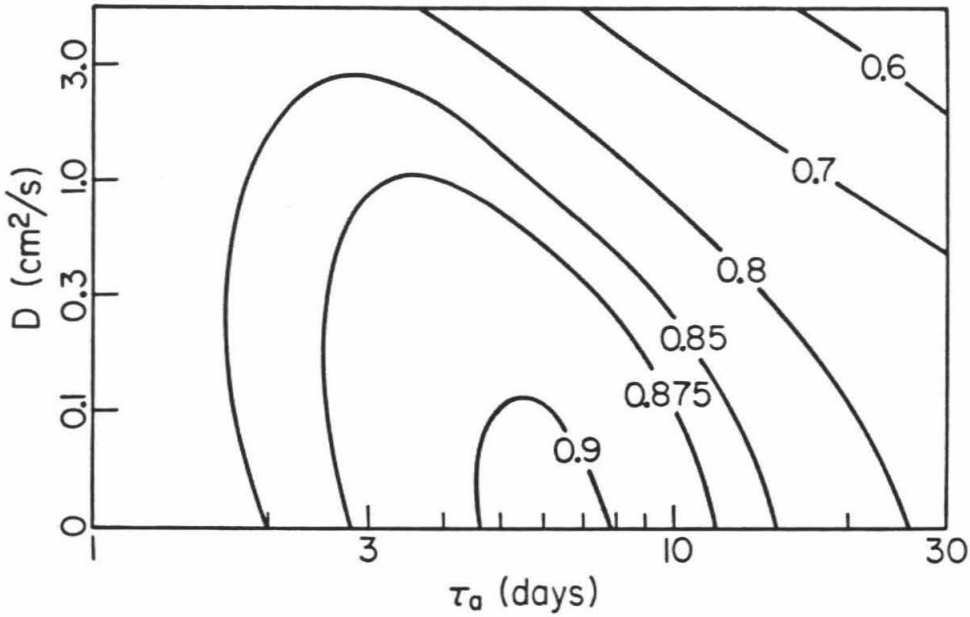


Figure 38: Contour plot of the correlation coefficient obtained comparing the data with the mid-latitude/equatorial model for coupled behavior of atmospheric transport and regolith exchange. Values are shown as a function of the regolith vapor diffusivity D and the meridional transport time constant τ_a . See text for details.

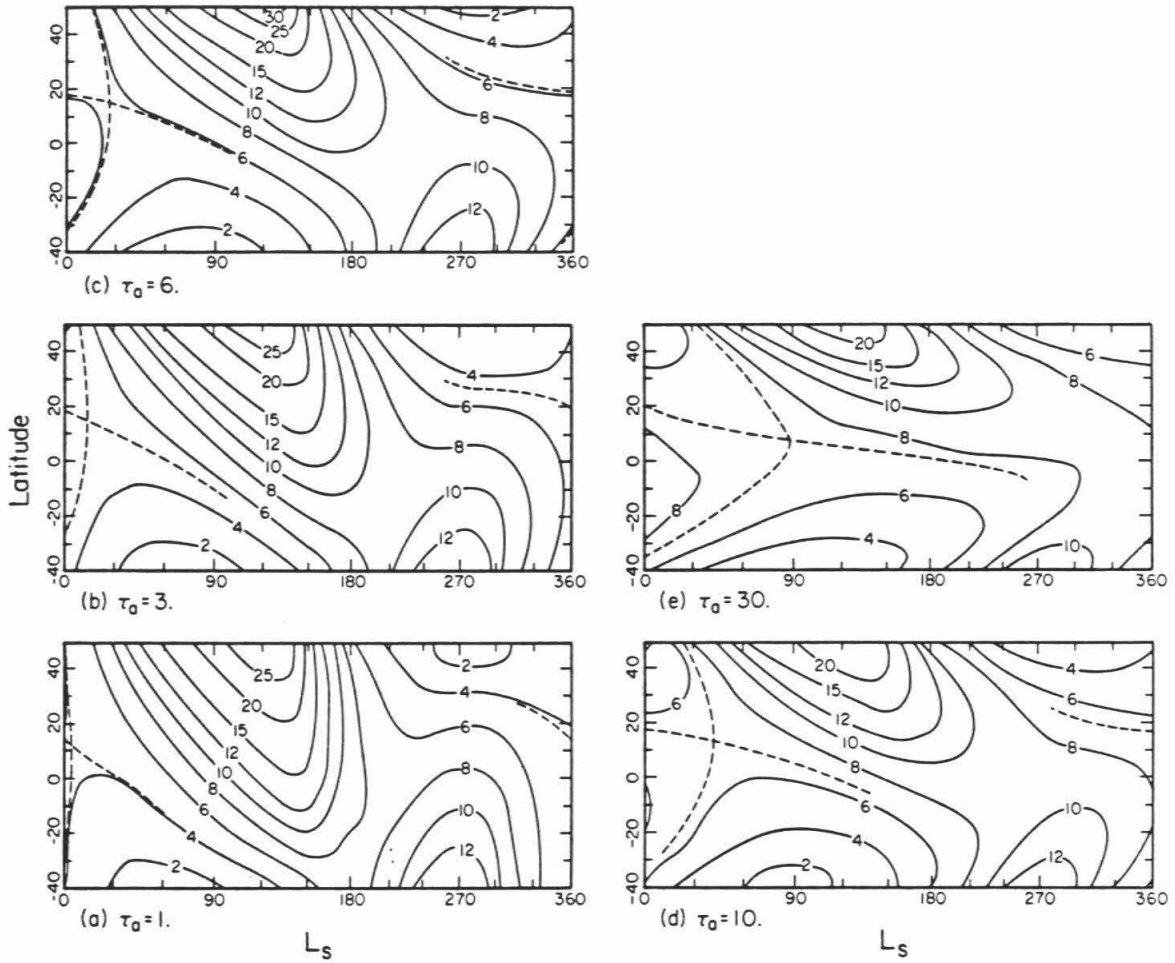


Figure 39: Results of the mid-latitude/equatorial coupled model for $D = 0$ and various values of τ_0 . The contours are column vapor abundances ($\text{pr } \mu\text{m}$), and should be compared with the observations as presented in Figure 35.

abundance at each latitude, extending toward the equator from the northern boundary. More rapid transport results in this line being more nearly vertical, while slower transport yields a more-horizontal line. By comparing the models in Figure 39 with the data in Figure 35, it can be seen that this line in the models most closely matches that in the data for $\tau_a = 6$ days. Given the uncertainty and scatter in the data, however, the models for $\tau_a = 3$ and $\tau_a = 10$ days cannot be ruled out. These values of τ_a all fall within the range expected on the basis of more-complex circulation models and observations of the Mars atmosphere, as discussed in the previous section; this lends credence to the idea that the simple parameterization of the atmospheric circulation used here is sufficient to account for most of the vapor transport, as well as to the idea that transport is very important in the seasonal vapor cycle.

These models ($3 \leq \tau_a \leq 10$ days, $D = 0$) all yield a correlation coefficient $\alpha > 0.88$; it might reasonably be expected, then, that any model, even those incorporating regolith exchange, which results in $\alpha > 0.88$ would also be consistent with the data and could not be ruled out. As seen in Figure 38, this excludes models which incorporate the regolith if $D > 1.0 \text{ cm}^2/\text{s}$, and encompasses roughly the range of values $3 \leq \tau_a \leq 10$ days and $0 \leq D \leq 1.0 \text{ cm}^2/\text{s}$. Figure 40 shows the results of models that have $\tau_a = 3$ days and D ranging from 0. to $3.0 \text{ cm}^2/\text{s}$. The major effect of increasing D is to increase the amplitude of the seasonal variation near the north and south borders of the region. As the amplitude increases, the model tends to deviate more from behavior like the data, such that α decreases also. Although the best-fit model has no regolith exchange, the range of satisfactory models includes those that do include regolith exchange.

All of the models within this range are capable of explaining the gross features of the data, those being the seasonal increase and decrease of vapor at

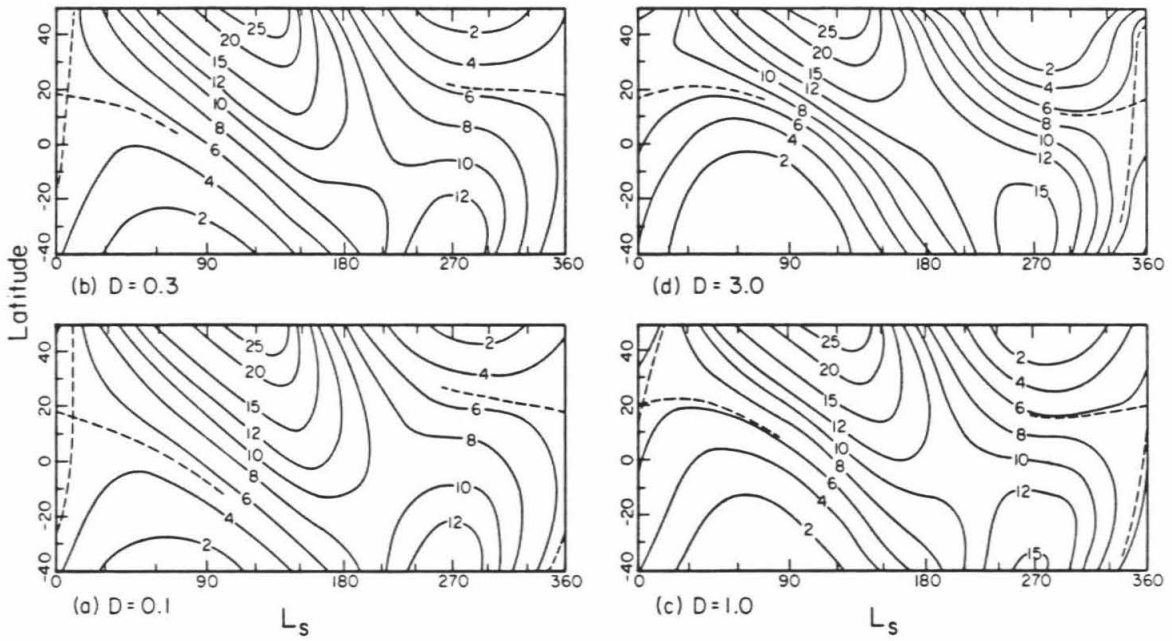


Figure 40: Results of the mid-latitude/equatorial coupled model for $\tau_a = 3$ days and various values of D .

each latitude. More-subtle features can also be examined, including the first rise in seasonal vapor being nearer to the equator. Dynamical effects cannot entirely be ruled out in explaining this effect. There are numerous examples of apparent up-gradient atmospheric transport and the subsequent concentration of a species away from its source (for instance, the global behavior of ozone on Earth, volcanic dust in the Earth's stratosphere, or water in the Earth's tropic regions). On Mars, circulation could conceivably create the maximum away from the polar cap edge if the water was transported south near the surface and upwelled and was concentrated at a low-latitude null in the circulation. The atmospheric circulation at this time likely does not have a well-defined null within this latitude range (see Leovy and Mintz, 1969; Pollack et al., 1981), such that a dynamical cause is unlikely, however.

The dashed line in Figure 35 shows the contour that goes through the "saddle point" in the data prior to the northern spring vapor increase. That the line extending upward also goes toward the right indicates that the first increase in vapor occurs nearer to the equator, as already pointed out. This type of behavior also shows up in some of the model results. In Figure 40 this line extends toward the right for $D \gtrsim 0.3 \text{ cm}^2/\text{s}$. Of course, the models with $D = 0$ (Figure 39) do not show this behavior. In (τ_a, D) space, the range of models with this type of behavior is $1.0 \leq \tau_a \leq 10$ days and $D \gtrsim 0.3 \text{ cm}^2/\text{s}$. In none of the models is the result as marked as the observations, however; the greatest effect obtained in the models can be seen in Figure 40, with $\tau_a = 3.0$, $D = 1.0$. Also, the models that produce the correct first increase in vapor have a larger-than-observed amplitude in the seasonal vapor curve at some latitudes. This may be an artifact of the way in which the surface fluxes are calculated in this type of model (see the next section, dealing with the pole-to-pole models). It is significant that the models which do incorporate regolith exchange can

reproduce in part this earlier rise of vapor near the equator; there is no reason *a priori* that this should be the case — the variation of temperature with latitude and season shows no marked variation within this region (Kieffer et al., 1977; Figure 30), and models with regolith exchange could easily have not reproduced this type of behavior.

To sum up the results of the models as regards the possible parameter values, the behavior of the models is consistent with the observations for τ_a and D that fall within the range $3 \leq \tau_a \leq 10$ days and $0 \leq D \leq 1.0 \text{ cm}^2/\text{s}$, respectively. If the first increase in vapor nearer the equator is not a dynamical effect but actually signifies the contribution from the regolith, then a range for D of $0.3 \leq D \leq 1.0 \text{ cm}^2/\text{s}$ is indicated.

The relative importance of the regolith versus transport can be assessed for this region of the planet given this range of the parameters. Figure 41 shows the relative contributions to the seasonal cycle for various values of τ_a and D . Given their range as above, it is seen that transport of vapor in from the polar regions supplies 12-28 units of vapor, while the regolith supplies 14-26. Thus, they contribute about equally to the cycle (to within a factor of two depending on what values for the parameters actually apply). Of course, the vapor transported in from the polar regions may also be coming from a source of adsorbed water within the regolith, or it may be supplied from ice deposits on the polar caps; this question will be addressed in the next section.

In Chapter II.A it was pointed out that there would be a net transport of vapor toward the south resulting from the annual gradient of vapor with latitude. This water would come from the north residual cap and would ultimately deposit onto the south residual cap, resulting in long-term exchange of water between the caps. The model discussed here allow an estimate to be

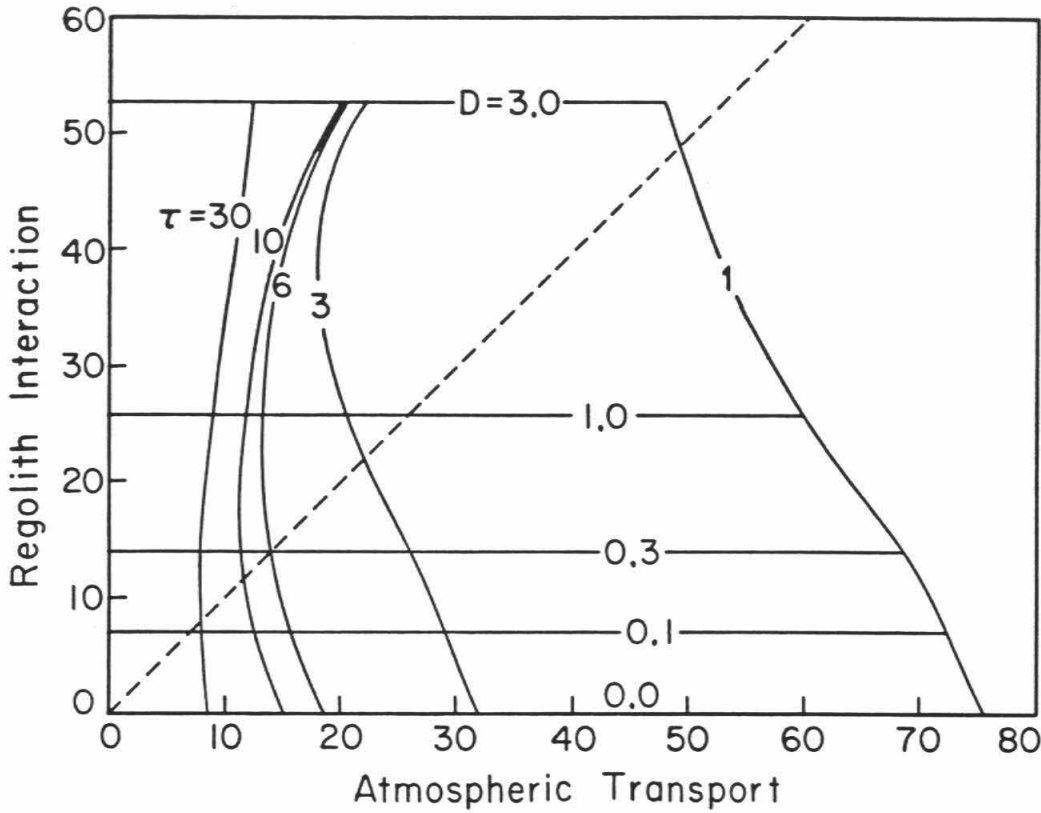


Figure 41: The relative importance of exchange of water with the regolith and atmospheric transport in producing the seasonal variation of water within the mid-latitude/equatorial region, shown as a function of τ_a (in days) and D (in cm^2/s). The axes are in units of 1.26×10^{18} g (or μm in the equatorial 10° latitude band), and represent water brought into the atmosphere in the region from the subsurface or from more-poleward regions. The inferred values of $0.3 \lesssim D \lesssim 1.0$ and $3 \lesssim \tau_a \lesssim 10$ imply that transport and regolith exchange supply roughly the same amount of water.

made of the amount of water moved south each year. For $3 \leq \tau \leq 10$ days, the mass of water transported toward the south is in the range $1.4 \times 10^{14} \leq m \leq 4.1 \times 10^{14}$ g/yr. $\tau = 5$ corresponds to $m = 1.8 \times 10^{14}$ g/yr. This compares with the upper limit obtained earlier of $\sim 4 \times 10^{14}$ g/yr (see Chapter II.A). If 1.8×10^{14} g water were removed from the north cap each year, it would correspond to removal of a layer of ice about 60 m deep from the cap over the course of 10^5 years. This is comparable to the thickness of the individual laminae in the polar layered terrain (Cutts et al., 1979). As the layers are thought to form one per 10^5 -year cycle of the orbital obliquity (e.g., Pollack, 1979), it is apparent that the long-term exchange of water between the caps may be significant in the formation and evolution of this terrain.

4. Global Processes and Models

In the previous section, models of the water behavior were constructed which included only the region between the maximum equatorward extent of the polar caps. This limitation enabled results to be obtained that were not dependent on an understanding of the behavior of the polar caps. In this section, a complete model is developed which will extend from pole to pole, including the seasonal advance and retreat of the polar caps. Results can then be obtained regarding the relative importance on a global scale of the various processes controlling the vapor cycle.

In this global model, the atmosphere and regolith are fully-coupled in terms of exchange of vapor (rather than coupling the atmosphere with the surface fluxes as was done in the mid-latitudes model). Thus, the complete model consists of an atmospheric layer and five subsurface layers at each of 18 latitudes. Each atmospheric box can communicate with the adjacent atmospheric boxes, exchanging vapor with timescale τ_a (as described before). Each atmospheric box can also exchange water with the regolith; this exchange is determined by the vertical number density gradient, which is governed by the amount of vapor in the atmosphere, by the amount of adsorbed water in the regolith, and by the subsurface temperatures. The regolith part of the model is essentially identical to the one-dimensional model with boundary conditions (see Chapter III.A), except that the atmospheric boundary condition now depends on the past history of the model rather than on the observed vapor behavior, and is therefore independent of the water vapor observations.

The seasonal advance of the CO₂ polar caps is that predicted by the thermal model of Kieffer et al. (1977). Because that model does not accurately predict the retreat of the caps (see Kieffer, 1979), the observed recession

(James, 1979; James et al., 1979) was included in the model. This was done by artificially removing any excess CO₂ ice from the surface at the appropriate seasons and recalculating the surface temperatures at each season.

Water vapor is allowed to condense onto the ground as ice whenever solid CO₂ is also present on the surface; the atmospheric water vapor above the CO₂ depletes with an e-fold time τ_f . The resulting models are relatively insensitive to the value of τ_f , and $\tau_f = \tau_a$ was used most often. This formulation is an oversimplification in that it is of course possible for water frost to be present on the surface even if CO₂ frost is not. At most seasons and at most non-polar latitudes, however, the surface warms sufficiently during the day, in the absence of CO₂ ice to buffer the temperatures, that significant water ice cannot remain on the ground. Water ice was inferred to be present at the VL-2 site when CO₂ ice probably was not (Jones et al., 1979), but the deposits there do not contain a significant amount of water relative to the global vapor budget (see Chapter II.A). As the model CO₂ cap retreats, water ice on the cap is placed back into the atmosphere, essentially instantaneously. The retreat of the cap past a particular 10° latitude bin is linear with time, and an amount of water which is proportionate to the fraction of the bin exposed is lost from the surface at each time step.

It is the boundary conditions at the north and south poles, in a sense, which drive the system. The southernmost latitude bin is taken to be a sink for vapor at all seasons, consistent with the perennial CO₂ covering observed in the south during the Viking year (Kieffer, 1979; Paige, 1981). The vapor abundance in the northernmost latitude bin is constrained by the observations (see Figure 2 or Figure 35). Account is thereby taken of the fact that the north residual cap acts as a source for vapor during the summer (Farmer et al., 1976). Uncertainties in the processes controlling the vapor abundance over the cap

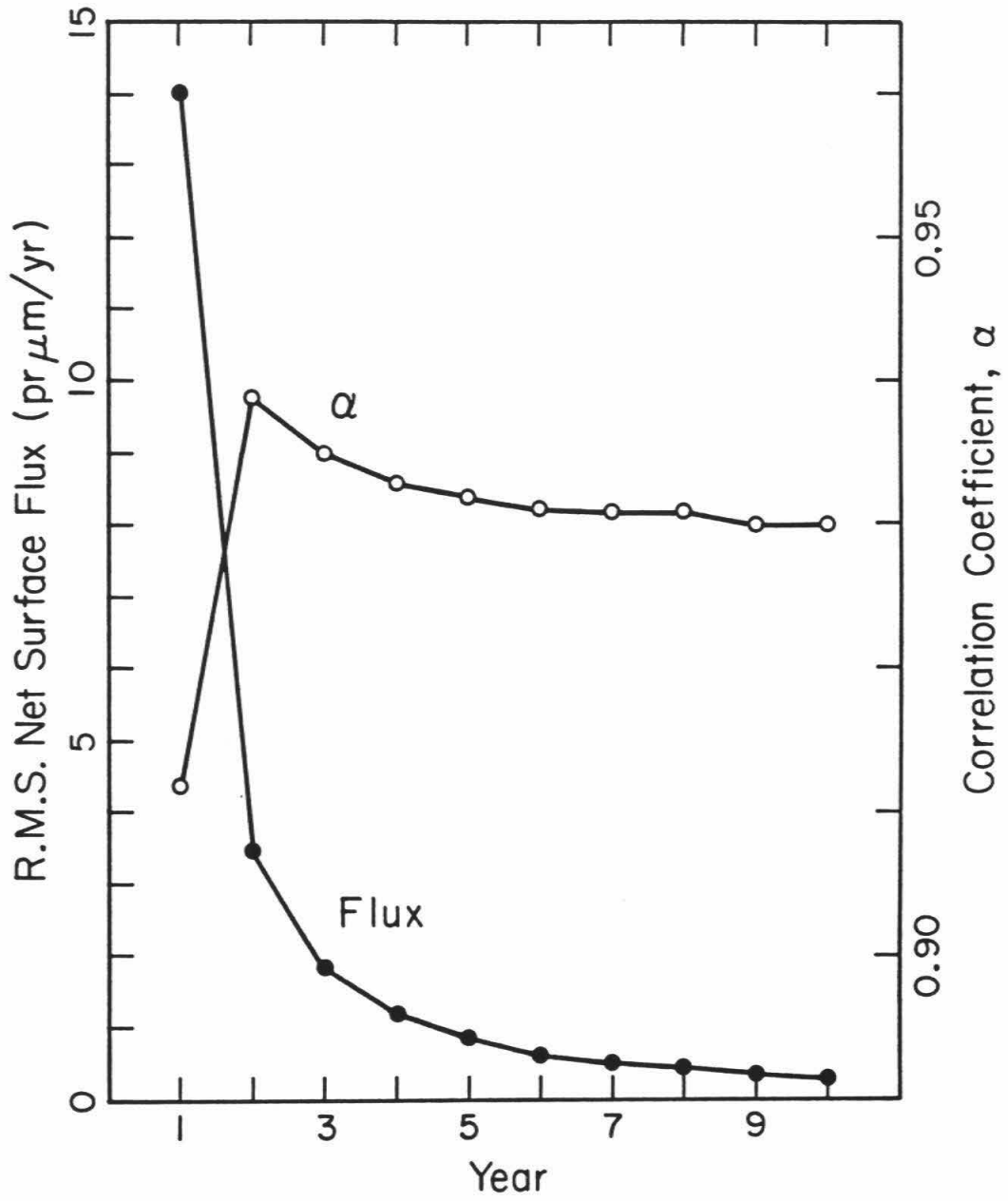
(such as saturation temperatures or vapor abundances, the polar cap albedo, etc.) make it difficult to calculate *a priori* the amount of water sublimed off the cap each summer (see, however, Toon et al., 1980); it is for this reason that the observed vapor abundances were used as the northern boundary condition.

The model is iterated for ten Martian years using a one Mars day timestep (which includes, however, the diurnal temperature variations within the regolith, as discussed earlier). This time is sufficiently long for the system to reach a steady state. Possible year-to-year variations in the various processes or the vapor behavior (see Chapter II.C) are ignored, and transport of water in non-vapor states is not included.

The models are compared with the observations (as represented by Figure 35) using a correlation coefficient similar to that described in the previous section. The coefficient measures the deviations from linear of a plot of the 1206 model points (18 latitudes by 67 times of year) versus the corresponding data points. Calculations were done several ways, including with no weighting scheme, normalizing each latitude band to its annual average (thereby examining only the shapes of the resulting seasonal curves), and weighting each latitude band by its area (cosine of latitude). The resulting coefficients were all quantitatively similar and show the same general trends; for simplicity, only those coefficients calculated with no weighting will be discussed.

Figure 42 shows the time evolution for one model of the resulting correlation coefficient and of the r.m.s. net flux of vapor from the sub-surface into the atmosphere. If the net surface flux is less than about one μm at a latitude band in a year, the resulting vapor behavior is essentially indistinguishable from that with zero flux. The figure shows that the system has essentially reached a steady state after ten years. Comparison of the resulting

Figure 42: Time-evolution of the global model, showing the behavior of the correlation coefficient and of the net flux from the surface. A nearly-steady state is reached after about ten years.



vapor abundances output in two consecutive years shows this same repeatability.

Figure 43 shows the resultant correlation coefficient as a function of the atmospheric mixing time constant τ_a and the regolith diffusivity D . The best-fitting model calculated is with $\tau_a = 2.5$ days and $D = 1.0 \text{ cm}^2/\text{s}$. Discussion follows regarding what the differences between the various models are and which models can be ruled out, if any.

Figure 44a-c shows the results of several of the models, in the form of contours of the vapor abundance as a function of latitude and season. These models all have $D = 0$ and different values of τ_a . The general trend in all of them is to produce the most vapor during local summer, due to the release of the vapor from the seasonal and residual (north only) polar caps. The non-smooth behavior seen in some places as vapor abundances increase results from the stepwise release of vapor into the atmosphere from the edge of the retreating polar cap, despite efforts to minimize this effect. Again, the biggest difference between these models is the speed with which vapor migrates from the polar regions toward the equator. Comparison of these plots with Figure 35 shows this to be the largest single effect in producing a good or poor fit.

Certainly, the case $\tau_a = 10$ days can be ruled out due to the inability of water to reach the equatorial region (compare Figure 44 and Figure 35). Interestingly, the global model for vapor presented by Davies (1981) would seem to be in a sense a subset of those considered here (although a very different set of assumptions controls the polar regions). His non-dust storm effective atmospheric diffusivity of $2. \times 10^5 \text{ m-deg/day}$ corresponds to τ_a in the formulation here of 30. days (similarly, his values of 10^7 and $3 \times 10^8 \text{ m-deg/day}$ during and between global dust storms correspond to $\tau_a = 0.6$ and 2.0 days,

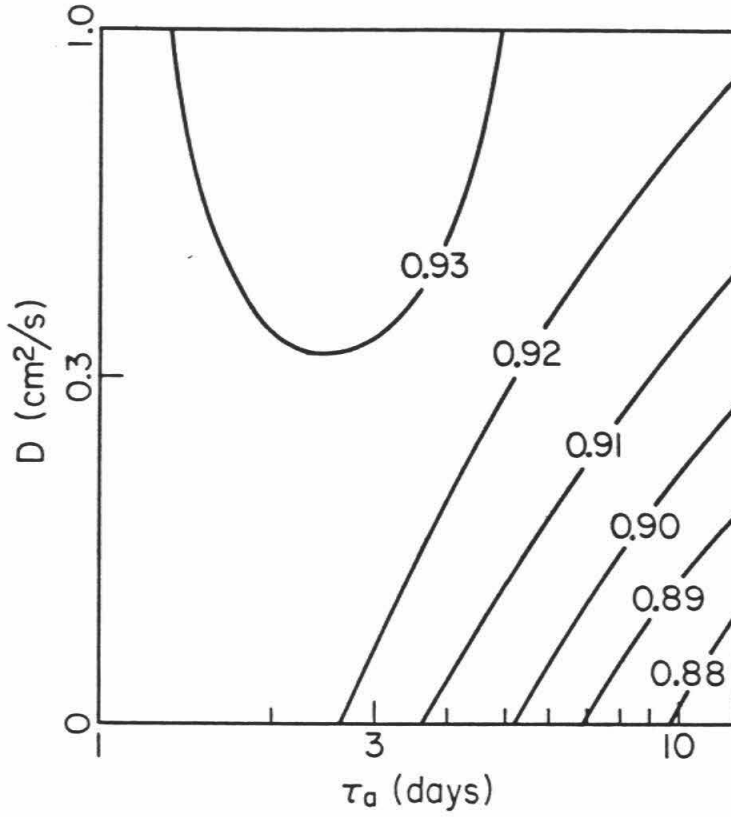
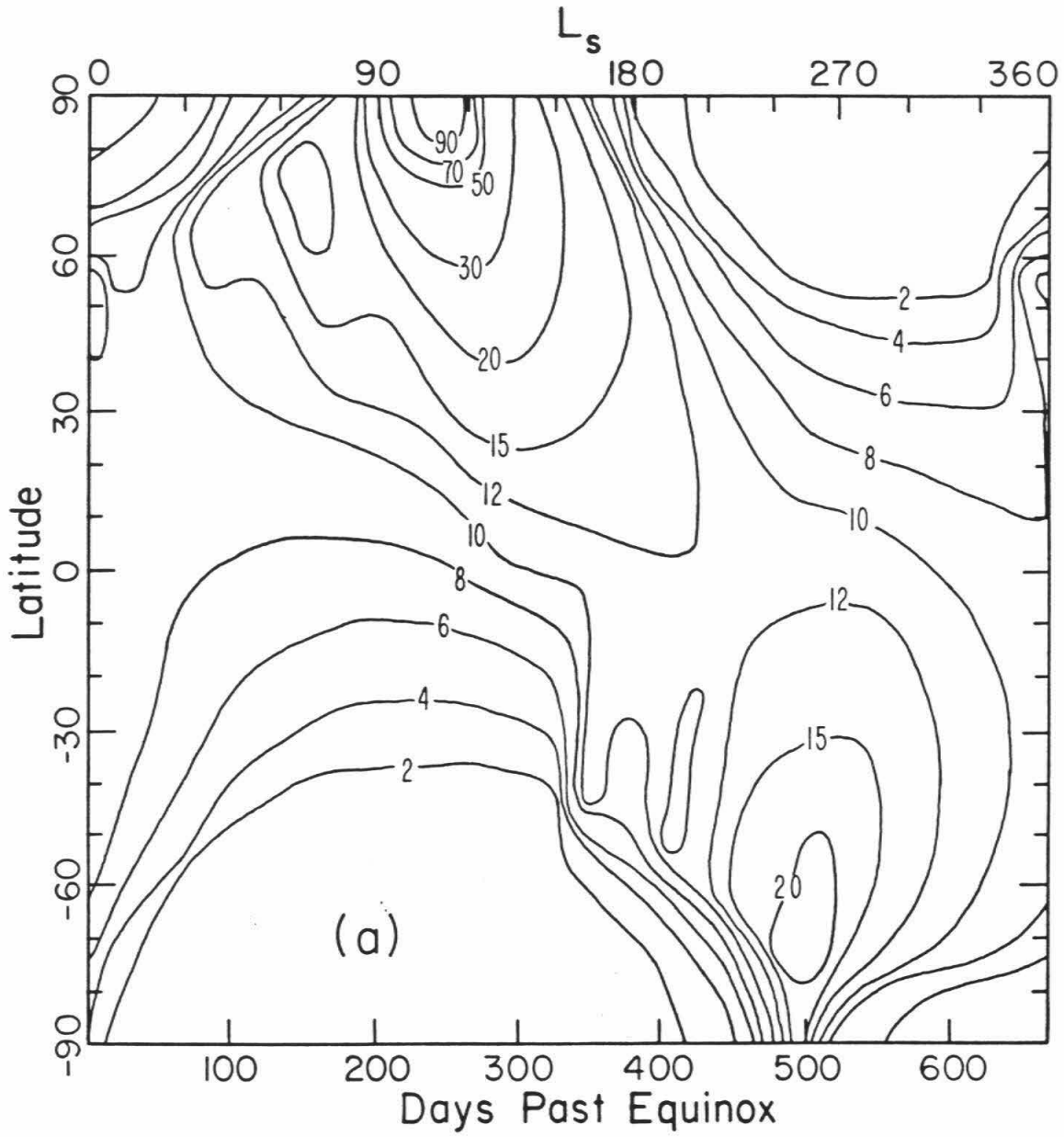
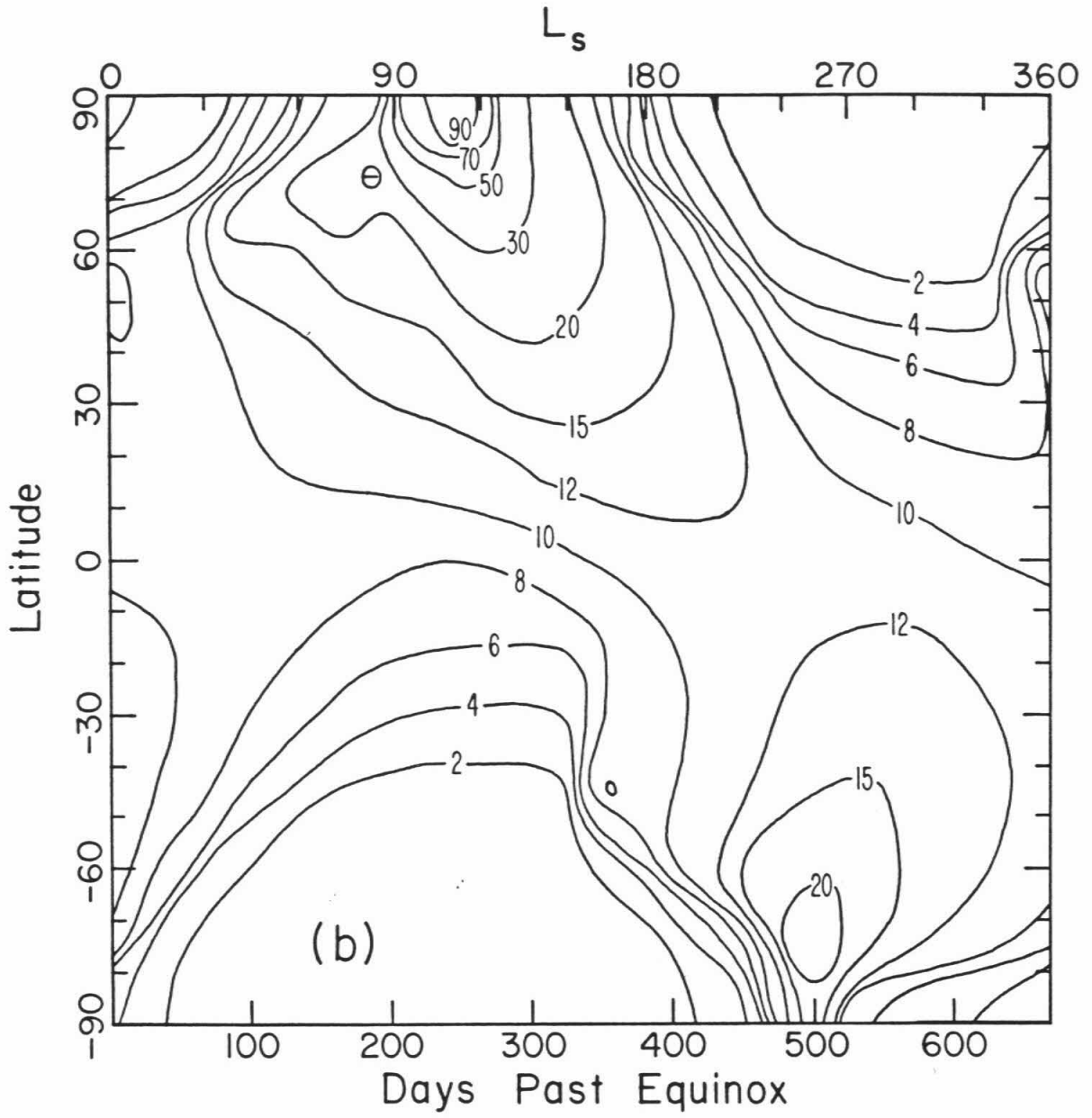
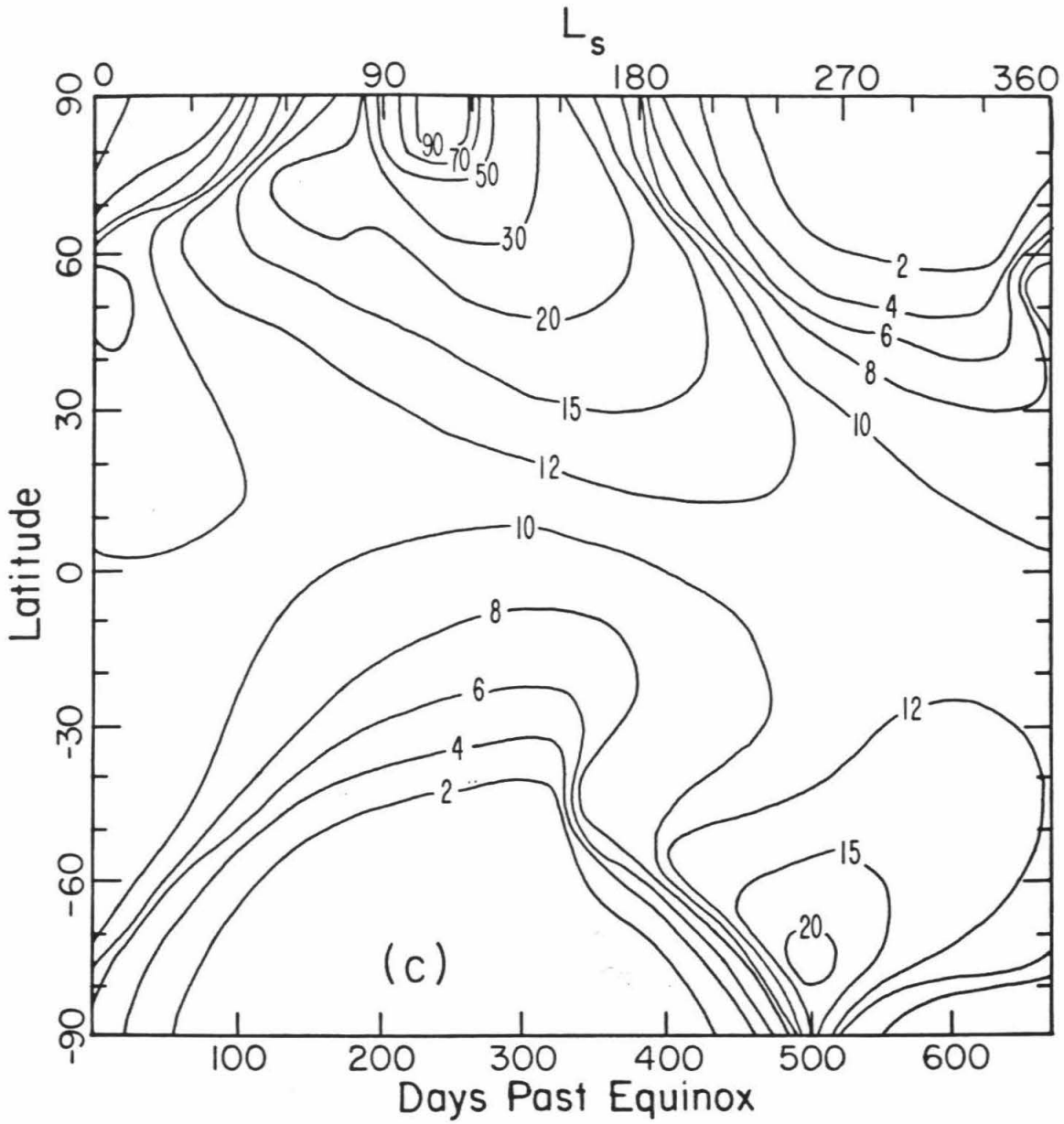


Figure 43: Contour plot of the correlation coefficient obtained comparing the data with the global model for coupled behavior of atmospheric transport and regolith exchange. Values are shown as a function of the regolith vapor diffusivity D and the meridional transport time constant τ_a . See text for details.

Figure 44: Results of the global coupled model for $D = 0$ and various values of τ_{α} . The contours are column vapor abundance (pr μm), and should be compared with the observations presented in Figure 35. (a) $\tau_{\alpha} = 2.5$. (b) $\tau_{\alpha} = 5.0$. (c) $\tau_{\alpha} = 10.0$.





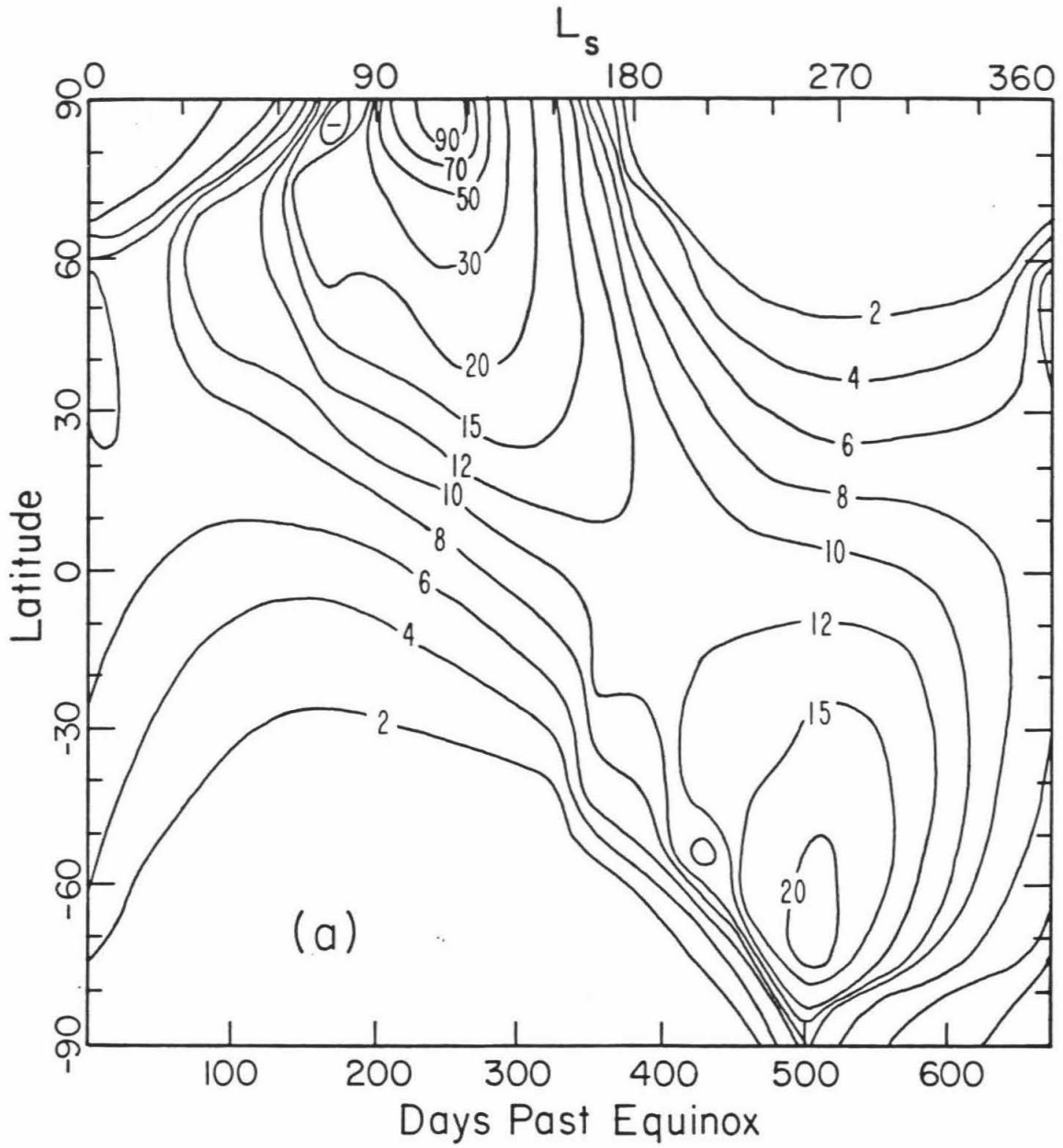


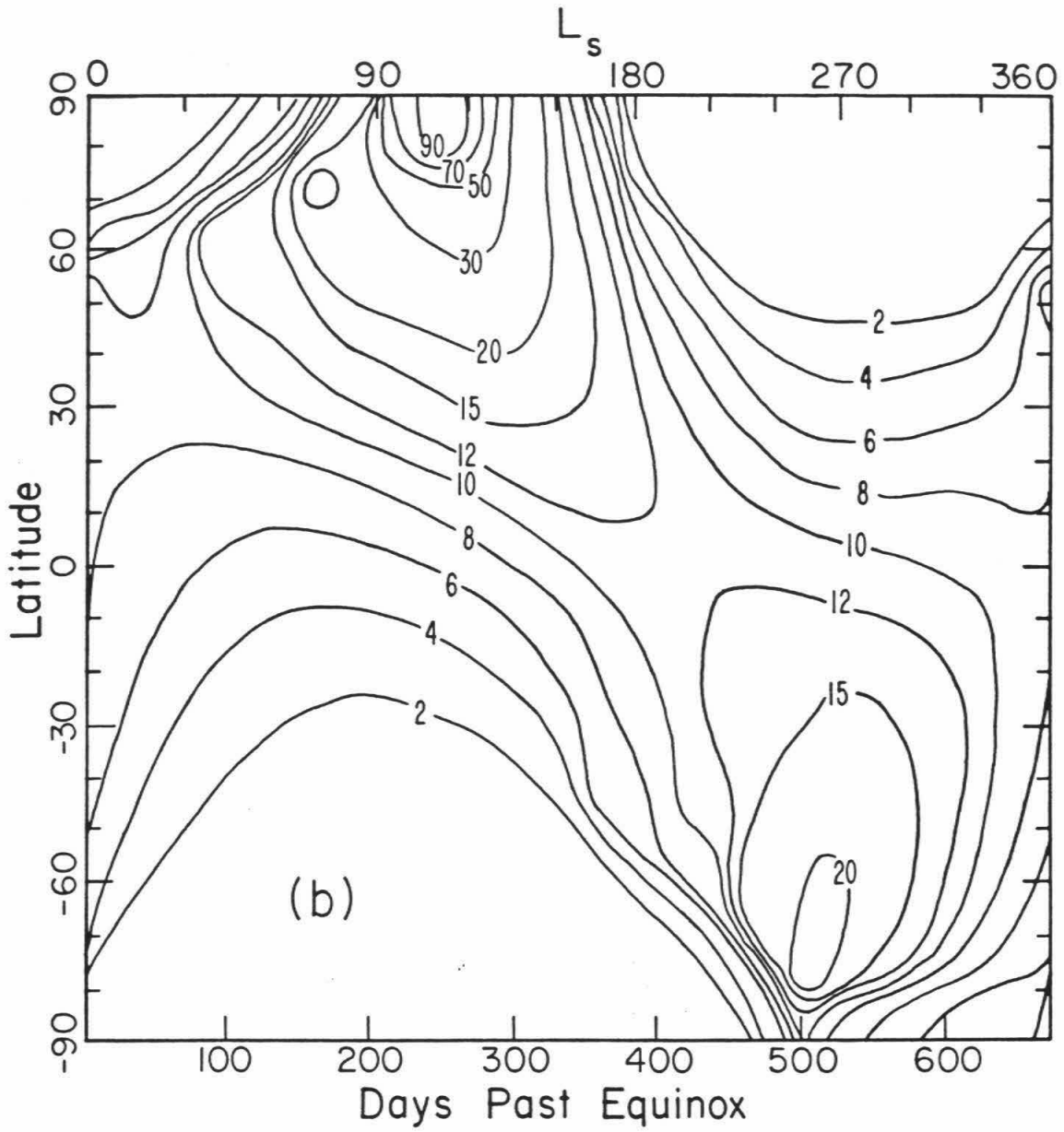
respectively). This low mixing explains the inability of his model to reproduce the amplitude of the non-polar regions' vapor behavior, while the good agreement of the polar behavior was explicitly built into his model via his assumptions of the saturation abundance; the saturation column abundance he uses does not relate one-to-one with surface or atmospheric temperature, and extends into regions of the planet that cannot be near saturation (e.g., ice remaining at $+60-70^\circ$ as late as $L_s = 80^\circ$ and appearing at 50° latitude as early as $L_s = 140^\circ$, and extending in the southern hemisphere as far north as -10° latitude where the average daily temperatures stay above 200 K).

None of the models with $D = 0$ succeed in producing as rapid a decline in the northern hemisphere vapor at the end of summer as is observed. This slower decline is especially evident from 40° to 70° latitude at $L_s \approx 150^\circ$. The fastest mixing times, $\tau_a \approx 1$ day, come closest to reproducing this decline, but these values are not physically reasonable. Atmospheric circulation in this region is likely to be predominantly due to baroclinic wave activity (e.g., Pollack et al., 1981, and others). There is very little wave activity at this season (Hess et al., 1979), however, such that a mixing time $\tau_a \gtrsim 10$ days is likely more appropriate at this season and latitude. The lack of a strong circulation is also evidenced by the existence of spiral clouds in the polar regions which cannot form and maintain when circulation is active (Gierasch et al., 1979). This evidence argues for a regolith sink for the vapor, which will be discussed below in more detail.

Figure 45 shows the seasonal vapor behavior produced by models which have $D = 1.0 \text{ cm}^2/\text{s}$. The effects of including regolith exchange are several: the location of the spring northern saddle point is moved earlier in time; there is a more rapid decline in the northern vapor abundances at the end of summer; and there is an increase in the amounts of vapor present during summer in the

Figure 45: Results of the global coupled model for (a) $\tau_a = 2.5$ and $D = 1.0$, and (b) $\tau_a = 5.0$ and $D = 1.0$.





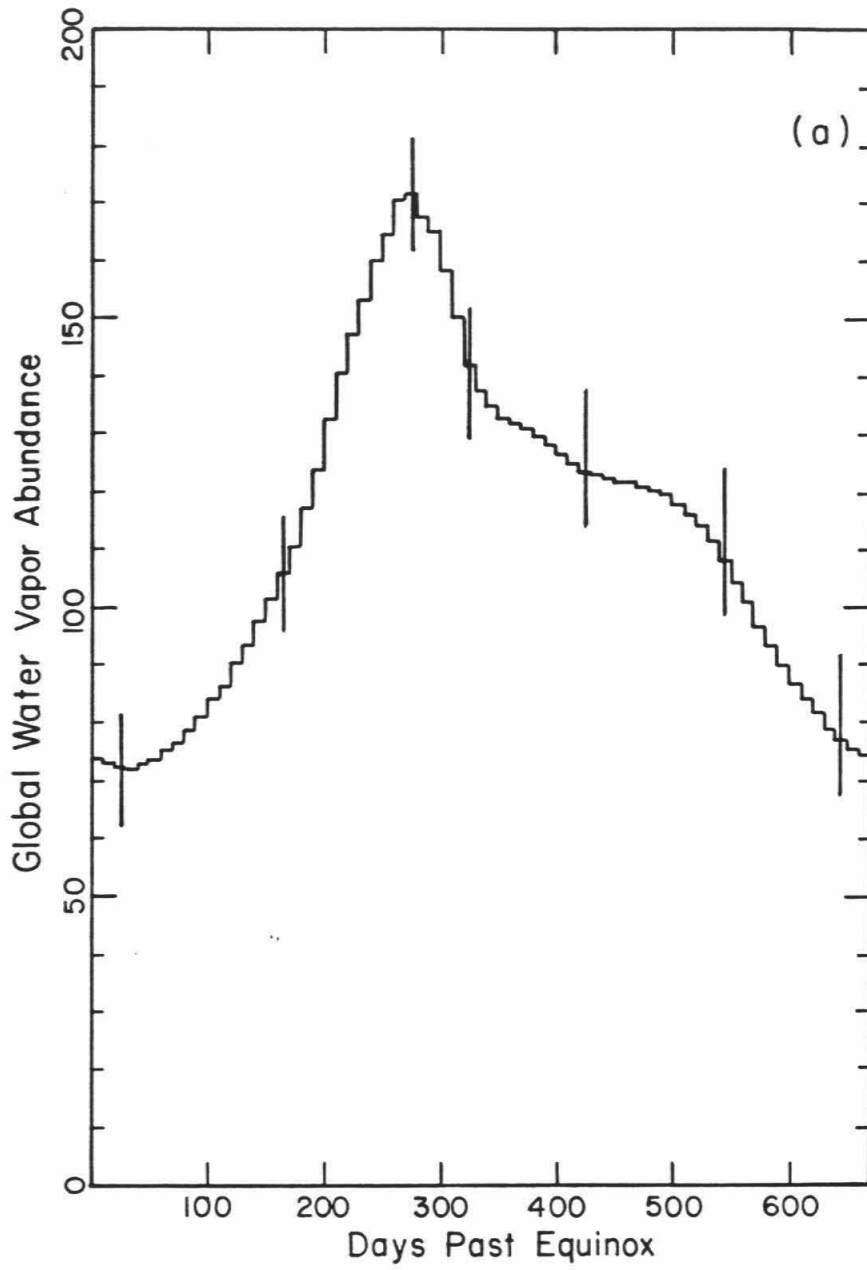
southern hemisphere. The saddle point occurs earlier, but is difficult to place due to the non-uniform release of vapor from the cap. Recall that in the mid-latitude/equatorial model, the first release of vapor at this season actually occurred nearer to the equator due to vapor coming from the regolith.

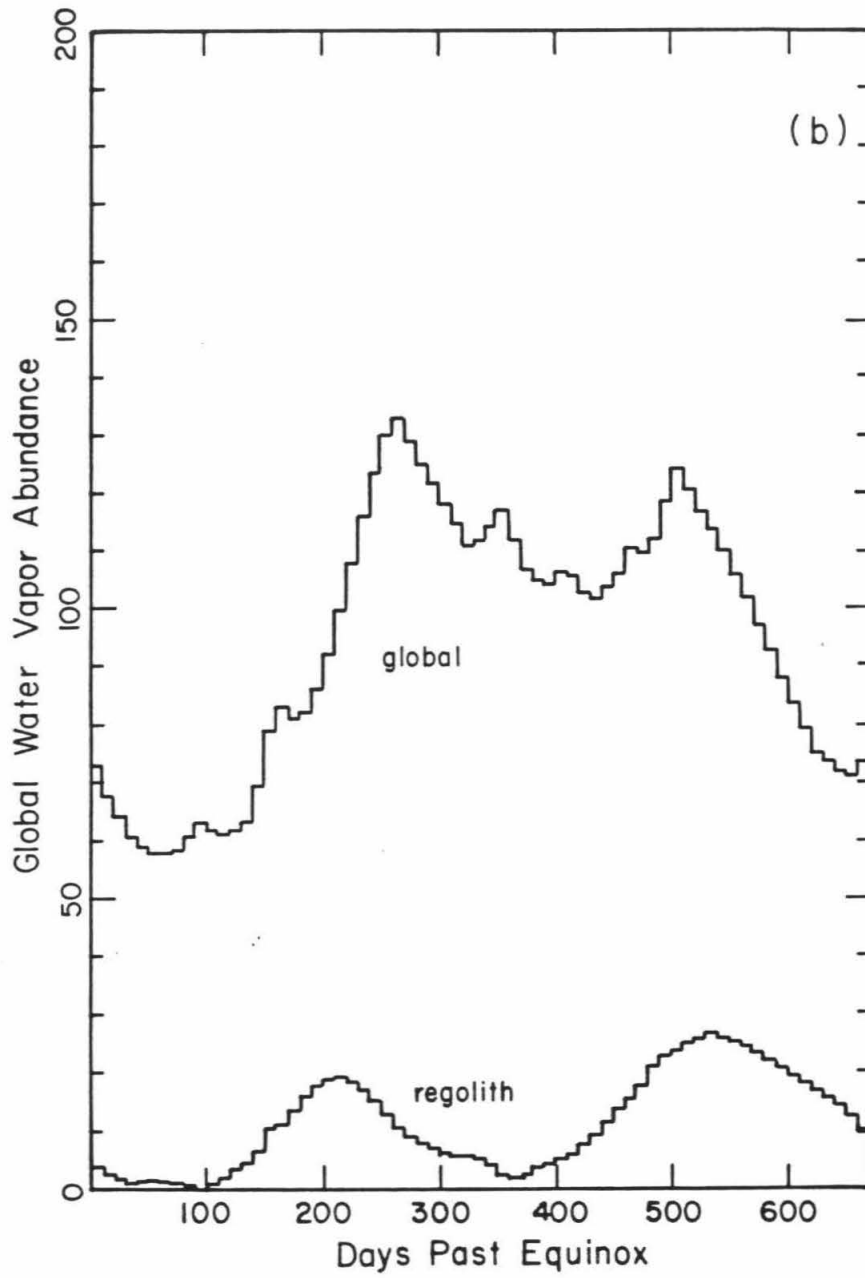
The more-rapid decline in vapor seen at the end of summer is due to vapor beginning to enter the regolith at this season, in addition to its being carried back to the residual northern cap. The effect of this regolith exchange is to make it appear as if the vapor moves quicker toward the equator (compare Figure 44 and 45 for $\tau_a = 5$ days). It should be pointed out that the decline in vapor is still not as rapid as was observed.

Figure 46 shows the seasonal variation of the total global vapor abundance, as observed and as predicted by the global model for $\tau_a = 2.5$ days, $D = 1.0 \text{ cm}^2/\text{s}$. For the model, the contribution to the global behavior of vapor exchanged with the regolith is also shown. Both model and data show the largest global abundances during northern summer. The fact that the seasonal amplitude of the model is less than the observations is due to the inability of the north polar vapor to be carried sufficiently far south toward the equator. This result can also be seen in Figures 44 and 45, which show less equatorial vapor at the peak than is observed (Figure 35). A similar plot for the $\tau_a = 1$ day model does have an amplitude as large as is observed; however, this value is unrealistically rapid for transport either via the equatorial Hadley cell or via the baroclinic wave activity, as discussed earlier. The model curve also shows an increase in global vapor during the southern winter, whereas the data show no such increase (although it may be partly concealed by the dust storms).

In order to examine these differences of the model results from the observations, a variety of models were calculated with non-constant properties.

Figure 46: (a) The seasonal variation of global water vapor abundance as observed by the MAWD. The values have been interpolated through the dust storms and a smooth line drawn. The vertical bars represent estimates of the worst-case uncertainties in the values. The units are 1.26×10^{13} g; 10 pr μm everywhere on the planet would result in a value of 134.4. (b) The same variation, as predicted by the global model with $\tau_a = 2.5$ and $D = 1.0$. Also shown is the contribution to the total due to vapor exchanged with the regolith. See text for discussion.





These include a time-varying atmospheric mixing constant τ_a , a latitudinal variation of D , and a time-varying vertical distribution of the vapor within the atmosphere.

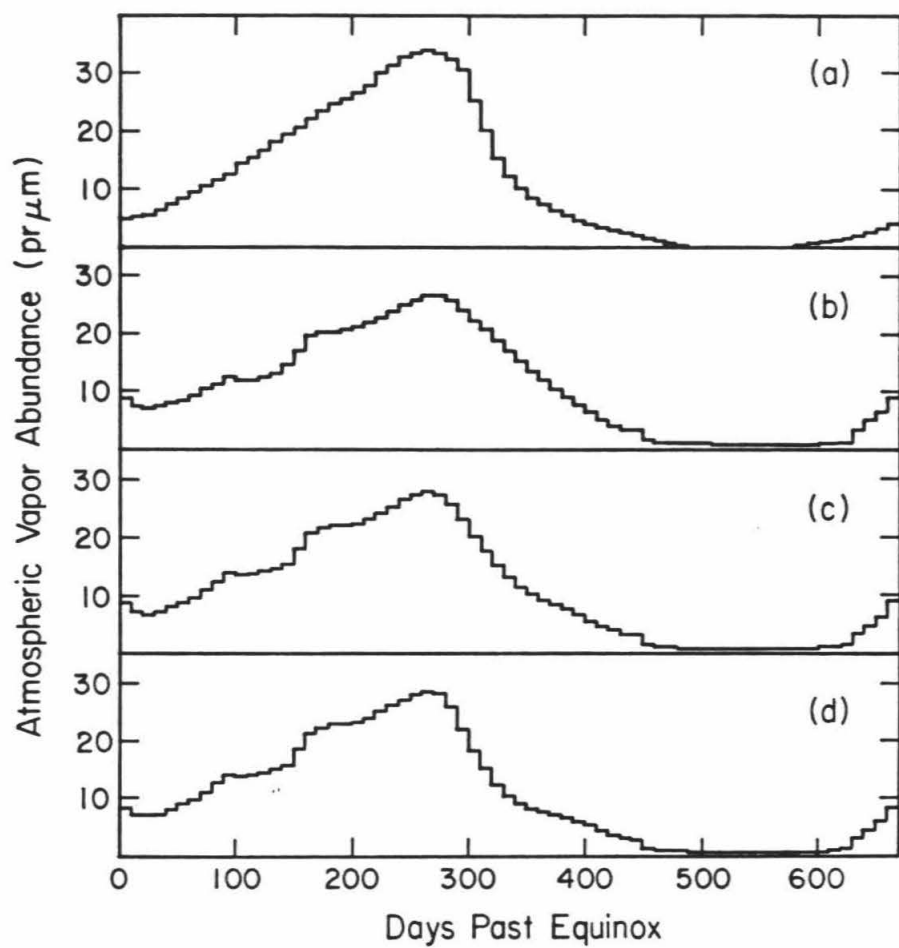
A time-dependent τ_a was chosen to account for the variability of the strength of the circulation. The various circulation models (Pollack et al., 1976, 1981; Leovy and Mintz, 1969; Moriyama and Iwashima, 1980) show that the strength of the equatorial Hadley cell may vary by a factor of four with season (see Table 7). Additionally, the more-poleward baroclinic wave activity occurs predominantly during the northern winter in the north, and is almost negligible during summer (Hess et al., 1979). The effects of airborne dust also increase the circulation (Haberle et al., 1980; Table 7), with the maximum strength occurring during northern winter. Therefore, a time-dependent τ_a was used, with the most rapid mixing occurring near $L_s = 270^\circ$, and less-rapid mixing at other seasons. The result was generally to improve the fit of the model, but only marginally. Part of the reason for the small effect is that the least amount of water globally is in the atmosphere during southern summer, so increased mixing plays only a small role. In the actual distribution of water there is almost no gradient of vapor during the southern summer (see Figure 3 or Figure 35), such that enhanced mixing can play only a small role in redistributing the water.

The increase in the modeled global vapor abundance during southern summer results from the combined effects of water being released from the receding polar cap and being exchanged with the subsurface (Figure 46); no similar increase is actually observed. To see the effects on this increase, models were run that had no regolith interaction south of -20° latitude. This latitude was chosen because of the sharp change in the surface thermal behavior which occurs there (Palluconi and Kieffer, 1981; see Figure 12). In theory, there should be a distinct relationship between the thermal inertia and the vapor diffusivity

D , due to the dependence of both properties on the regolith particle size. In practice, however, the factors which determine both properties are too complicated to allow derivation of a simple relationship between them, and this simple latitudinal dependence was chosen. The result was that the increase in vapor abundance during southern summer was lessened considerably, as expected, with a corresponding increase in the correlation coefficient obtained.

Finally, it was seen in Chapter II.B that the vertical distribution of the vapor varies with both location and season; there was insufficient information, however, to obtain its distribution uniquely as a function of these two variables. When the vapor is moved closer to the ground, the surface vapor density is enhanced and vapor diffuses into the regolith; conversely, if the vapor is distributed over a larger height, more vapor will be drawn from the ground. This effect was discussed also in Chapter III.A, regarding the one-dimensional models with boundary conditions. Models incorporating this effect were computed to see if surface enhancement of the vapor could cause the vapor to re-enter the regolith in the northern hemisphere at the end of summer such that the decline in atmospheric vapor would be as fast as was observed. Results at one latitude are shown in Figure 47, and indicate the large effect that a variable vertical distribution of the vapor can produce. Models incorporating this enhancement of the surface vapor density also show a better fit to the data, as measured by the correlation coefficient. Interestingly, this effect serves to increase the importance of the regolith in the seasonal cycle: by pumping more water into the ground at one season, more is available to come out the next year. In fact, these models also indicate the caution with which the other models should be treated: Any seasonal variation of the vertical distribution of the vapor will affect the exchange of vapor between the atmosphere and regolith, possibly significantly.

Figure 47: Seasonal behavior of vapor at latitude $+55^\circ$. (a) Smooth line through the observations (see Figure 35). (b) Modeled behavior, $\tau_a = 5.0$, $D = 1.0$. (c) Same as (b), except that the surface concentration of vapor is increased by a factor of two near day 300 to drive the vapor more rapidly back into the regolith. (d) Same as (b), except that surface vapor is increased by a factor of three.



Now that all of the models have been presented, it is appropriate to discuss whether the differences between them are significant, and what values of the parameters τ_a and D are likely to be appropriate. Those models with non-constant properties all fit the data better than those without, as measured by the correlation, α . Comparison of the results of the models in Figures 44 and 45, however, indicates that the more-complex models may not fit the data significantly better than the simplest ones (with $D = 0$). Therefore, comparison of the results of the models with $D = 0$ (Figure 44) with the observations (Figure 35) can provide interesting limits. Of the models shown in Figure 44, that with $\tau_a = 2.5$ days is the best fit, that with $\tau_a = 5$ yields a noticeably worse fit, and that with $\tau_a = 10$ is a considerably poorer fit. The correlation coefficients obtained are $\alpha = 0.92$, $\alpha = 0.90$, and $\alpha = 0.87$, respectively. For the case $D = 0$, then, models with $\alpha < 0.90$ can be ruled out. It is reasonable that this result will hold in general, for any D . Figure 43 shows that the constraint $\alpha > 0.90$ does not eliminate many models; examination of Figures 44 and 45 again substantiates this, in that few of the models appear to be significantly better or worse than the rest in reproducing the observations.

The relative importance of each process is shown in Figure 48 for a variety of different models calculated. Shown is the fractional contribution of each process to the variation of global atmospheric vapor at the time of the spring rise of vapor in the north. The contribution from the regolith is the amount of water desorbed from the subsurface and diffused into the atmosphere; of course, this contribution is zero when $D = 0$. The contribution from the seasonal polar cap is a measure of the amount of water held in that reservoir and released on retreat of the cap. That from the residual cap is the amount of water released from the northernmost 10° latitude band, and includes water deposited onto that region the previous season as well as new

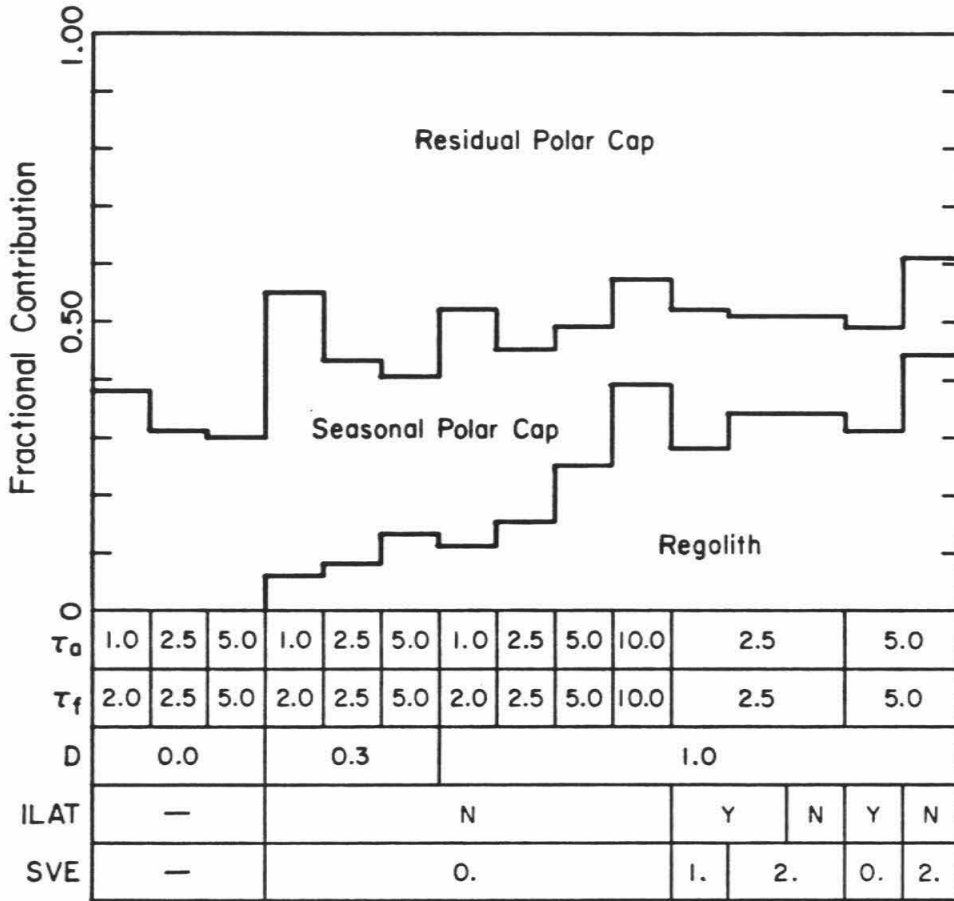


Figure 48: The relative importance of the regolith and the seasonal and residual polar caps in the global spring vapor behavior, expressed as a fraction of the total sum variation, as obtained in the global models for various parameter values. ILAT indicates whether the regolith south of -20° has the same vapor diffusivity as elsewhere (N) or zero diffusivity (Y). SVE indicates whether the near-surface vapor concentration is enhanced near day 300, and the amount by which it increases (0 = no enhancement, 1 = doubled, 2 = tripled).

water sublimed for the first time. There is a rough trade-off between water supplied from the regolith and from the seasonal cap, with the contribution from the residual cap remaining roughly constant at about half. From the data (Figure 6), the contribution due to the residual cap is seen to be no greater than about 40% of the total variability (as indicated by the fractional increase in global abundance after the residual cap is exposed at $L_s \approx 80^\circ$).

For the best estimate of the range of parameters, $3 \lesssim \tau_a \lesssim 6$ days and $0.3 \lesssim D \lesssim 1.0$ cm²/s, the contribution from the regolith is between 10 and 30% of the total variation. Complications to the models, such as enhancement of the surface vapor abundance at certain seasons, can boost this amount to almost 50% of the total. In all of the models, the amount of water present as frost in the seasonal polar caps can be significant, always being capable of supplying greater than 10% of the total water in the budget; this result is entirely consistent with the observations of water ice spectral features from the seasonal caps, as discussed in Chapter II.D.

5. Discussion

Because none of the models discussed in this section are capable of exactly reproducing the observations, it is apparent that not all of the relevant physics has been included. Deficiencies are probably present in several aspects of the models. The use of a simple diffusive-type mixing model is an obvious oversimplification. In reality, the strength of the meridional circulation will not be constant but will be a function of both latitude and season; in fact, the actual transport of vapor will be governed by a superposition of the three-dimensional distribution of vapor in the atmosphere with the global wind field, and will not in general be as simple as described.

The regolith must also be more complicated than was assumed here. Not only will the diffusivity D vary from place to place on the planet, but so might the subsurface composition or the degree of surface coverage by rocks (which can impede exchange of water). The surface thermal inertia varies by a factor of twenty from place to place as measured on a scale of tens of kilometers; smaller-scale variations undoubtedly occur. These variations most likely map in a complex yet unknown way into variations in the other properties also.

The polar cap behavior is also more complicated than discussed here. Certainly the factors controlling the behavior of the CO_2 part of the caps are only now beginning to be unraveled (Paige, 1981, 1982). That interaction of the atmospheric vapor with the polar caps will occur has been previously realized by Leighton and Murray (1966) and Leovy (1973). The details governing this interaction are poorly understood, especially regarding the formation of ice or clathrate mixed in with the CO_2 frost or the stability of the resulting frosts under Martian conditions. Such a basic phenomenon as the existence and radiative effects of a polar hood are only poorly known (Briggs and Leovy, 1974;

Christensen and Zurek, 1982). All of these uncertainties will affect the models discussed here.

Despite the large degree of simplification which went into the basic models, it is apparent that these simple models can explain the gross features of the seasonal vapor behavior, and that a number of results can be discussed with confidence. It is very revealing that the atmospheric mixing times (τ_a) which yield the best fit of the models to the data are within the range of values predicted based on both theory and observations; this correspondence indicates both the importance of transport of vapor in the seasonal water cycle and that the simple mixing model actually does account for a large fraction of the transport which occurs. There is thus no need to invoke significant transport of water in non-vapor states to explain the observations.

The importance of exchange of water between the atmosphere and the regolith is indicated in several ways. Given the possible range in the diffusion constant, $0.1 \leq D \leq 5.0 \text{ cm}^2/\text{s}$, it was seen that exchange must occur. D would have to be significantly less than 0.1 to result in insignificant interaction seasonally. Given the nature of the Martian surface, larger values are more likely (as discussed in Chapter III.A).

Given the best estimate of the properties of the atmosphere and regolith, $0.3 \lesssim D \lesssim 1.0 \text{ cm}^2/\text{s}$, it follows that both the regolith and the polar caps are important in the seasonal cycle. In the region between the polar caps, the regolith then accounts for roughly half of the vapor variability, while transport from the polar regions accounts for the remainder. Globally, the regolith supplies 10-40% of the seasonal water, the residual cap about 40%, and the seasonal caps the remainder.

It is difficult to separate the effects on the water cycle of the polar caps

and the regolith or to more uniquely determine their relative importance. The difficulty arises because both processes act, to first order, in the same directions, producing the largest amounts of vapor during the local summer and the least during the winter. This is because the sublimation of ice and the desorption of water are both thermally-driven processes, with higher temperatures resulting in greater atmospheric vapor abundances; the changing temperatures with season thus act in the same direction for both processes.

Despite the fact that the regolith contributes a large amount of the seasonal water, it is apparent that it is the behavior of the two polar caps which controls the seasonal cycle. This results from their control of the total amount of water in the atmosphere. For example, if the north residual cap never supplied water seasonally and acted as a perennial sink for water (as the south residual cap appears to do often), the atmosphere would rapidly be depleted of water as frost condensed out at the poles. With the north cap supplying water and the south cap removing it each year, a gradient of vapor from north to south is set up (see Chapter II.A). The amount of water in the regolith adjusts itself to be in equilibrium with the average amount of water in the atmosphere, and it is the seasonal variation superimposed on this average amount that the regolith and seasonal caps supply. The time that the regolith takes to respond to a change in imposed atmospheric vapor abundance is only a few years, at least insofar as affecting the seasonal exchange of water. This result can be seen in Figure 42, which shows that after several years, the flux of water from deeper layers is sufficiently small ($< 1 \text{ pr } \mu\text{m}/\text{year}$) that the seasonal cycle will not be affected. On a longer timescale, any changes in the albedo or temperature of the polar cap which can affect the amounts of water sublimed off of the residual cap seasonally will modify the latitudinal gradient of vapor; the regolith will respond locally, taking up or giving off enough water to again be

in equilibrium with the atmospheric abundances.

Thus, on the obliquity timescale, the changing insolation at the polar caps (e.g., Murray et al., 1973; Ward, 1974) will modify their temperatures and hence the amount of vapor in equilibrium over the cap. Atmospheric transport will mix the vapor between the polar caps to set up a gradient of water, and the regolith will respond in order to be in equilibrium with the atmosphere. The timescales for all of these processes support the interpretation: The equilibrium between the polar cap and the local atmosphere is established quite rapidly, probably with a timescale on the order of several days; this quickness is due to the rapidity with which ice can sublime off of the surface to fill the available holding capacity (see Ingersoll, 1970; Farmer, 1976; Toon et al., 1980). Given the atmospheric mixing times derived earlier, the timescale for setting up a latitudinal gradient of vapor in response to the polar vapor abundances is probably on the order of one to several years. Similarly, the timescale for the water in the regolith to equilibrate with the vapor in the atmosphere above it is less than several years (for equilibration down to a depth that is still capable of communicating with the atmosphere seasonally). Equilibration to deeper layers will take longer, but the effects near the surface or on the atmosphere will be very small on a seasonal basis. Because the insolation changes with a much longer timescale, the polar caps will be in equilibrium with the insolation, the global atmosphere will be in equilibrium with the polar caps, and the regolith will be in equilibrium with the atmosphere. Thus, the polar caps control the entire process.

Chapter IV

Concluding Remarks

It is appropriate at this point to summarize the major conclusions reached regarding the seasonal behavior of water vapor in the Mars atmosphere and to discuss further work which could substantiate these conclusions or allow further progress to be made in understanding the Mars water cycle.

Water vapor in the Mars atmosphere has been continuously mapped spatially and temporally for a period of more than one and one-half Mars years by the Viking Orbiter MAWD instruments. The column abundance varies spatially and seasonally, with up to about 100 μm over the summer north polar cap and down to essentially zero during the polar winter. The total vapor content of the atmosphere varies with season from an equivalent of about 1 to 2 km^3 of ice, with each hemisphere having its maximum abundance during the local summer season.

There is a notable asymmetry in the water behavior with respect to latitude, with the northern hemisphere containing up to twice as much vapor as the southern. This vapor gradient implies a net annual flow of vapor toward the south, at least during the year observed by Viking. The degree to which this northward flow may be balanced by flow toward the north resulting from and coincident in time with the global dust storms, when the vapor gradient may be tilted slightly in the other direction, is unknown, as is the effect of water transport in the form of clouds, adsorbed onto airborne dust grains, or during other years.

As northern summer approaches, vapor appears first in the region of $+20^\circ$ to $+40^\circ$ latitude. This fact is consistent with the regolith being a seasonal source of vapor (either from subsurface ice or adsorbed water) but not with the

receding seasonal polar cap being the principal source of water at low latitudes. After the peak of summer, the vapor abundances throughout the northern hemisphere decline too early to allow incorporation into the seasonal polar cap, suggesting that the sink is either the residual cap or the regolith. Because of the difficulty in transporting this vapor back to the residual cap sufficiently rapidly, much of it is probably exchanging with the regolith.

When the water vapor abundances are averaged over a Mars year, it is apparent that topography plays a large role in determining the spatial variability. The lowest places generally have the most vapor, while the highest have the least. While it helps in qualitatively understanding this type of behavior, the concept of a uniform mixing ratio throughout the whole atmosphere appears to be an over-simplification. If the effect of air mass is divided out, the remaining map of annual average abundance correlates with maps of either surface thermal inertia or bolometric albedo. High vapor abundances are associated with regions of low inertia and high albedo. This behavior can be understood as possibly arising from: 1) the effects of surface and subsurface temperatures on the adsorption, desorption, and diffusion of water vapor; or 2) the control exerted by surface reflectance and emission on the atmospheric vapor holding capacity via the atmospheric temperatures.

Comparison of the observations of water vapor made by the Viking MAWD with those made by the Mariner 9 IRIS and by Earth-based spectroscopists over the last twenty years shows a remarkable repeatability of the vapor cycle. The southern hemisphere summer of 1969 is the most notable exception, showing large vapor abundances similar to those seen during the northern summer season. A possible explanation is that this excess water sublimed off of the south residual cap; this would require the CO₂ frost (which was present throughout the summer during the Viking year) to sublime away first such that

the cap temperature were no longer buffered near 150 K, and could result from an increased radiative load on the cap due to a different degree of dust storm activity that year.

During the year observed by Viking, the strong latitudinal gradient of water and the existence of a cold trap at the south pole both imply a net transport of vapor toward the south and growth of the south cap. During years in which the CO_2 on the south cap disappears, large atmospheric vapor abundances will occur over the southern residual water ice cap; this will balance out, at least in part, the vapor gradient and possibly result in a net northward flow of vapor that year. An important, yet unanswered, question is whether this (possible) northward flow of vapor is less than, equal to, or greater than the southward flow seen during the Viking seasons, and whether the north water ice cap is thereby shrinking or growing on a net basis during the current epoch. The amount of vapor transported south during the Viking year is, however, entirely consistent with current theories regarding the formation and evolution of the polar layered terrain. The individual layers are believed to form one per obliquity cycle; the amount of water transported south in this time, at the rate inferred from the Viking data, is comparable to the amount of water which would be needed for formation of a single layer in that time.

Additional constraints on the water cycle can be obtained from infrared spectroscopy of the seasonal polar caps. Results indicate the presence of water frost on the surface, in some fashion mixed in with the CO_2 frost. There is no firm evidence, however, for significant quantities of ice lasting throughout the day in more-equatorial regions.

The vertical distribution of the vapor within the atmosphere can be obtained by comparison of the vapor abundances with the atmospheric

temperatures. The results generally indicate that the vapor is confined to a region of one to three scale heights extent. This height varies both as a function of latitude and of season, and can provide an important constraint on global models of regolith exchange. This distribution of vapor implies near-surface saturation at night and the formation of night and morning fogs at most locations and most seasons.

Observations of the Martian surface and atmosphere indicate the nearly ubiquitous presence of particulate material of size greater than $1\ \mu\text{m}$. A regolith of this material is capable of adsorbing large amounts of water onto the individual grains and of exchanging an amount seasonally which is significant with respect to the amount of vapor present in the atmosphere. This process must, in fact, be going on to some degree.

Models of the seasonal exchange of water with the regolith and the meridional transport allow estimates to be made of the relative importance of these processes. A model of the mid-latitude/equatorial region indicates that the regolith supplies roughly the same amount of water seasonally as does transport in from the more-poleward regions. A global model which also includes exchange of water with the seasonal and residual polar caps indicates that regolith exchange accounts for 10-40% of the global variation, while the north residual cap supplies about 40% of the water and the seasonal caps supply the remainder. These results could change significantly if the atmosphere is sufficiently diabolical in terms of the seasonal and spatial variability of the vertical distribution of vapor within the atmosphere or of the degree of correlation of the vapor distribution with the general circulation patterns.

The difficulty in reaching conclusions regarding the relative importance of those processes which may be responsible for controlling the vapor cycle, and

the large uncertainty inherent in those conclusions reached, lies in the fact that the two processes which may be of the most importance act in nearly the same direction. Exchange of water with the regolith and with the polar caps result, both separately and in tandem, in the largest vapor abundances being present during local summer and the least during winter. Thus, simple models of the major processes will not uniquely indicate the degree to which each may be responsible. It is then the more-subtle features of the models or the data, or the other observations relevant to the nature of the Mars surface, which may be called upon to determine the relative importance of each process.

The latitudinal gradient of water in the atmosphere implies a similar gradient in subsurface reservoirs of adsorbed water, in order for the atmosphere and regolith to be in equilibrium. The two will be in equilibrium due to the relative timescales for equilibration between the regolith and the local atmosphere, the atmosphere and the polar caps, and the caps and the insolation. It is because of the relative timescales that the polar caps generally control the global behavior of vapor, with the regolith and seasonal caps responding and adding a superposed seasonal variability. On longer timescales, such as the 10^5 -year obliquity timescale, it is again the polar caps which will control the behavior, with the atmosphere and the regolith responding appropriately.

Recalling the uncertainties in the conclusions reached here, it is of interest to examine the possibilities for further research which may arise over the next decade or so and which can help solve some of the ambiguities discussed here. Additional research will take the form of either new models or new observational constraints.

In terms of modeling, the most profitable venture might be to examine

the transport of vapor which would occur given the actual circulation patterns. A global circulation model like that of Pollack et al. (1981) or Haberle et al. (1980) would more-definitively answer the questions regarding the role played by transport of vapor or by the residual or seasonal polar caps. If such a model could then be coupled to a model of regolith exchange, like that discussed in Chapter III, the relative importance of the various cycles could be determined more precisely than was possible here. Models of the polar caps, like those being developed by Paige (1982), will also play an important role in understanding the water behavior on the seasonal and on longer timescales.

Analysis of existing data can also provide more clues as to the nature of the water cycle. Data on the distribution of clouds in the Mars atmosphere exist based on Viking and Mariner imagery (French et al., 1981; Kahn and Gierasch, 1982) and on Viking thermal mapping (Christensen and Zurek, 1982). Comparison of these data sets with the vapor observations and the inferred vertical distribution of vapor will aid considerably in understanding the role of condensates in the water cycle. Additionally, observations from the remaining Viking lander continue, and may aid in understanding the relationship between the vapor and the occurrence of dust storms or airborne or surface condensates.

Earth-based observations of Mars are still of continuing interest. Perhaps the most important would be to continue global or spatially-resolved observations of atmospheric vapor during the Martian southern summer season. This would allow possible confirmation of the 1969 type of southern behavior and would aid in understanding the activity of the south seasonal and residual caps. Observations of near-infrared spectra of the polar regions will aid in constraining the amounts of water ice present on or in the seasonal polar caps; the variability of water ice spectral features with latitude or with season would

be an important observation.

There has been much discussion lately regarding a future spacecraft mission to Mars to study its climate over the course of a Mars year. Several different observations would aid considerably in understanding the seasonal water cycle. Additional observations of the vapor column abundance, especially during the southern summer season, would add to the data set from Viking. Three-dimensional mapping would be of the most interest, however. Knowledge of the vertical distribution of vapor and its variability with location and season would prove invaluable as a constraint for models of the exchange of water with the regolith and with the polar caps. Being able to correlate the vapor abundances with the actual wind fields would provide similar boundary conditions for models of atmospheric transport. These few (!) pieces of data could provide conclusive answers regarding the relative importance of each process. Additional significant information would be obtained by spatially mapping the polar cap frosts with a near-infrared spectrometer, and by observing the seasonal cycles of dust and of CO₂ to see how they interact with each other and with the vapor. It would also be very informative if the locations of subsurface reservoirs (in the top meter or so) of adsorbed water or ice could be mapped over the planet, but the utility of this would be most apparent if it could be mapped with sufficient precision to look for seasonal variations in the subsurface water content and thus provide information on the seasonally-accessible reservoirs.

Adding the results of any one or more of the above-suggested lines of research would aid immensely in understanding the seasonal water cycle on Mars. This will then feed back immediately into a further understanding of the long-term behavior of and possible changes in the Mars climate, and in understanding the abundance and distribution of volatiles on Mars.

Considerable implications also exist for the Earth's climatic history, as many of the processes extant are similar, differing only in degree.

Bibliography

- Anderson, D.M., E.S. Gaffney, and P.F. Low, Frost phenomena on Mars, *Science* **155**, 319-322, 1967.
- Anderson, D.M., M.J. Schwarz, A.R. Tice, Water vapor adsorption by sodium montmorillonite at -5° C, *Icarus* **34**, 638-644, 1978.
- Arvidson, R.E., E.A. Guinness and S.W. Lee, Differential aeolian redistribution rates on Mars, *Nature* **278**, 533-535, 1979.
- Barker, E.S., Martian atmospheric water vapor observations: 1972-74 apparitions, *Icarus* **28**, 247-268, 1976.
- Barker, E.S., R.A. Schorn, A. Woszczyk, R.G. Tull, S.J. Little, Mars: detection of atmospheric water vapor during the southern hemisphere spring and summer season, *Science* **170**, 1308-1310, 1970.
- Barnes, J.R., Time spectral analysis of midlatitude disturbances in the Martian atmosphere, *J. Atmos. Sci* **37**, 2002-2015, 1980.
- Barnes, J.R., Midlatitude disturbances in the Martian atmosphere: A second Mars year, *J. Atmos. Sci.* **38**, 225-234, 1981.
- Barrer, R.M., Surface and volume flow in porous media, in *The Solid-Gas Interface* (E.A. Flood, ed.), Marcel Dekker, Inc., New York, p. 557-609, 1967.
- Brass, G.W., Stability of brines on Mars, *Icarus* **42**, 20-28, 1980.
- Briggs, G.A., The nature of the residual Martian polar caps, *Icarus* **23**, 167-191, 1974.
- Briggs, G.A. and C.B. Leovy, Mariner 9 observations of the Mars polar hood, *Bull. Am. Met. Soc.* **55**, 278-296, 1974.
- Briggs, G., K. Klaasen, T. Thorpe, J. Wellman, W. Baum, Martian dynamical phenomena during June-November 1976: Viking orbiter imaging results, *J. Geophys. Res.* **82**, 4121-4149, 1977.
- Briggs, G.A., W.A. Baum, and J. Barnes, Viking orbiter imaging observations of dust in the Martian atmosphere, *J. Geophys. Res.* **84**, 2795-2820, 1979.
- Brunauer, S., L.E. Copeland, and D.L. Kantro, The Langmuir and BET theories, in *The Solid-Gas Interface* (E.A. Flood, ed.), Marcel Dekker, Inc., New York, p. 77-103, 1967.
- Budyko, M.I., *Climatic Changes*, American Geophysical Union, Washington, D.C., 1977.
- Carr, M.H. and G.G. Schaber, Martian permafrost features, *J. Geophys. Res.* **82**, 4039-4054, 1977.
- Carr, M.H., H. Masursky, W.A. Baum, K.R. Blasius, G.A. Briggs, J.A. Cutts, T. Duxbury, R. Greeley, J.E. Guest, B.A. Smith, L.A. Soderblom, J. Veverka, J.B. Wellman, Preliminary results from the Viking orbiter imaging experiment, *Science* **193**, 766-776, 1976.
- Carslaw, H.S. and J.C. Jaeger, *Conduction of Heat in Solids*, 2nd ed., Oxford University Press, London, 1959.

- Christensen, P.R., Martian dust mantling and surface composition: Interpretation of thermophysical properties, *J. Geophys. Res.*, in press, 1982.
- Christensen, P.R. and R.W. Zurek, Martian north polar ice clouds, *Bull. Am. Astron. Soc.*, in press, 1982.
- Clark, B.C., Implications of abundant hygroscopic minerals in the Martian regolith, *Icarus* **34**, 645-665, 1978.
- Clark, R.N., The surface condensates on Mars observed by Viking: Frost layers several tenths of a millimeter thick, *Lunar and Planetary Science XI*, Lunar and Planetary Institute, Houston, 160-161, 1980.
- Clark, R.N., The spectral reflectance of water-mineral mixtures at low temperatures, *J. Geophys. Res.* **86**, 3074-3086, 1981a.
- Clark, R.N., Water frost and ice: the near-infrared spectral reflectance 0.65-2.5 μm , *J. Geophys. Res.* **86**, 3087-3096, 1981b.
- Clark, R.N. and T.B. McCord, Mars residual north polar cap: Earth-based spectroscopic confirmation of water ice as a major constituent and evidence for hydrated minerals, *J. Geophys. Res.* **87**, 367-370, 1982.
- Conrath, B.J., Thermal structure of the Martian atmosphere during the dissipation of the dust storm of 1971, *Icarus* **24**, 36-46, 1975.
- Conrath, B., R. Curran, R. Hanel, V. Kunde, W. Maguire, J. Pearl, J. Pirraglia, J. Welker, and T. Burke, Atmospheric and surface properties of Mars obtained by infrared spectroscopy on Mariner 9, *J. Geophys. Res.* **78**, 4267-4278, 1973.
- Cutts, J.A., K.R. Blasius, and W.J. Roberts, Evolution of Martian polar landscapes: Interplay of long-term variations in perennial ice cover and dust storm intensity, *J. Geophys. Res.* **84**, 2975-2994, 1979.
- Davies, D.W., The vertical distribution of Mars water vapor, *J. Geophys. Res.* **84**, 2875-2880, 1979a.
- Davies, D.W., The relative humidity of Mars' atmosphere, *J. Geophys. Res.* **84**, 8335-8340, 1979b.
- Davies, D.W., The Mars water cycle, *Icarus* **45**, 398-414, 1981.
- Davies, D.W. and L.A. Wainio, Measurements of water vapor in Mars' antarctic, *Icarus* **45**, 216-230, 1981.
- Davies, D.W., C.B. Farmer and D.D. La Porte, Behavior of volatiles in Mars' polar area: A model incorporating new experimental data, *J. Geophys. Res.* **82**, 3815-3822, 1977.
- Fanale, F.P., Martian volatiles: Their degassing history and geochemical fate, *Icarus* **28**, 179-202, 1976.
- Fanale, F.P. and W.A. Cannon, Exchange of adsorbed H_2O and CO_2 between the regolith and atmosphere of Mars caused by changes in surface insolation, *J. Geophys. Res.* **79**, 3397-3402, 1974.
- Fanale, F.P. and W.A. Cannon, Mars: CO_2 adsorption and capillary condensation on clays — Significance for volatile storage and atmospheric history, *J. Geophys. Res.* **84**, 8404-8414, 1979.

- Fanale, F.P., W.B. Banerdt, R.S. Saunders, L.A. Johansen, and J.R. Salvail, Seasonal carbon dioxide exchange between the regolith and atmosphere of Mars: Experimental and theoretical results, *J. Geophys. Res.*, in press, 1982.
- Farmer, C.B., Liquid water on Mars, *Icarus* **28**, 279-289, 1976.
- Farmer, C.B. and P.E. Doms, Global seasonal variation of water vapor on Mars and the implications for permafrost, *J. Geophys. Res.* **84**, 2881-2888, 1979.
- Farmer, C.B. and D.D. La Porte, The detection and mapping of water vapor in the Martian atmosphere, *Icarus* **16**, 34-46, 1972.
- Farmer, C.B., D.W. Davies, D.D. La Porte, Mars: Northern summer ice cap — water vapor observations from Viking 2, *Science* **194**, 1339-1341, 1976.
- Farmer, C.B., D.W. Davies, A.L. Holland, D.D. La Porte, and P.E. Doms, Mars: Water vapor observations from the Viking orbiters, *J. Geophys. Res.* **82**, 4225-4248, 1977.
- Fjeldbo, G., D. Sweetnam, J. Brenkle, E. Christensen, D. Farless, J. Mehta, B. Seidel, W. Michael, Jr., A. Wallio, M. Grossi, Viking radio occultation measurements of the Martian atmosphere and topography: Primary mission coverage, *J. Geophys. Res.* **82**, 4317-4324, 1977.
- Flasar, F.M. and R.M. Goody, Diurnal behavior of water on Mars, *Planet. Space Sci.* **24**, 161-181, 1976.
- French, R.G., P.J. Gierasch, B.D. Popp, R.J. Yerdon, Global patterns in cloud forms on Mars, *Icarus* **45**, 468-493, 1981.
- Gierasch, P. and R. Goody, A study of the thermal and dynamical structure of the Martian lower atmosphere, *Planet. Space Sci.* **16**, 615-646, 1968.
- Gierasch, P.J. and R.M. Goody, The effect of dust on the temperature of the Martian atmosphere, *J. Atmos. Sci.* **29**, 400-402, 1972.
- Gierasch, P., P. Thomas, R. French and J. Veverka, Spiral clouds on Mars: A new atmospheric phenomenon, *Geophys. Res. Lett.* **6**, 405-408, 1979.
- Goody, R. and M.J.S. Belton, Radiative relaxation times for Mars. A discussion of Martian atmospheric dynamics, *Planet. Space Sci.* **15**, 247-256, 1967.
- Guinness, E.A., R.E. Arvidson, D.C. Gehret, and L.K. Bolef, Color changes at the Viking landing sites over the course of a Mars year, *J. Geophys. Res.* **84**, 8355-8364, 1979.
- Haberle, R.M., C.B. Leovy, and J.B. Pollack, Some effects of global dust storms on the atmospheric circulation of Mars, *Bull. Amer. Astron. Soc.* **12**, 725, 1980.
- Hamilton, K.H., The effect of solar tides on the general circulation of the Martian atmosphere, *J. Atmos. Sci.* **39**, 481-485, 1982.
- Hanel, R., B. Conrath, W. Hovis, V. Kunde, P. Lowman, W. Maguire, J. Pearl, J. Pirraglia, C. Prabhakara, B. Schlachman, G. Levin, P. Straat, T. Burke, Investigation of the Martian environment by Infrared Spectroscopy on Mariner 9, *Icarus* **17**, 423-442, 1972.
- Hess, S.L., The vertical distribution of water vapor in the atmosphere of Mars, *Icarus* **28**, 269-278, 1976.

- Hess, S.L., R.M. Henry, C.B. Leovy, J.A. Ryan, J.E. Tillman, Meteorological results from the surface of Mars: Viking 1 and 2, *J. Geophys. Res.* **82**, 4559-4574, 1977.
- Hess, S.L., J.A. Ryan, J.E. Tillman, R.M. Henry, C.B. Leovy, The annual cycle of pressure on Mars measured by the Viking Landers 1 and 2, *Geophys. Res. Lett.* **7**, 197-200, 1979.
- Houck, J., J.B. Pollack, C. Sagan, D. Schaack, J. Decker, High altitude infrared spectroscopic evidence for bound water on Mars, *Icarus* **18**, 470-480, 1973.
- Huguenin, R.L., Mars: Possible occurrence of near-surface liquid H₂O brines in the Solis Lacus region (-25°, 85°), *Lunar and Planetary Science X*, 596-597, 1979.
- Huguenin, R.L., Salt storms on Mars? *Bull. Amer. Astron. Soc.* **12**, 723, 1980.
- Huguenin, R.L. and S.M. Clifford, Implications of Martian 'Oases', Third Intl. Colloq. Mars, Lunar and Planetary Institute, Houston, 121-123, 1981.
- Hunt, G.R., Spectral signatures of particulate minerals in the visible and near-infrared, *Geophysics* **42**, 501-513, 1977.
- Ingersoll, A.P., Mars: Occurrence of liquid water, *Science* **168**, 972-973, 1970.
- Jakosky, B.M. The effects of non-ideal surfaces on the derived thermal properties of Mars, *J. Geophys. Res.* **84**, 8252-8262, 1979.
- Jakosky, B.M., Seasonal buffering of atmospheric H₂O and CO₂ by the Martian regolith, *Bull. Am. Astron. Soc.* **13**, 707-708, 1981.
- Jakosky, B.M. and C.B. Farmer, The seasonal and global behavior of water vapor in the Mars atmosphere: Complete global results of the Viking atmospheric water detector experiment, *J. Geophys. Res.*, **87**, 2999-3019, 1982.
- Jakosky, B.M. and D.O. Muhleman, The longitudinal variation of the thermal inertia and the 2.8 centimeter brightness temperature of Mars, *Astrophys. J.* **239**, 403-409, 1980.
- Jakosky, B.M. and D.O. Muhleman, A comparison of the thermal and radar characteristics of Mars, *Icarus*, **45**, 25-38, 1981.
- James, P.B., Recession of Martian north polar cap: 1977-1978 Viking observations, *J. Geophys. Res.* **84**, 8322-8334, 1979.
- James, P.B. and K. Lumme, Martian south polar cap boundary: 1971 and 1973 data, *Icarus*, in press, 1982.
- James, P.B. and G.R. North, The seasonal CO₂ cycle on Mars: An application of an energy balance climate model, *J. Geophys. Res.*, in press, 1982.
- James, P.B., G. Briggs, J. Barnes, A. Spruck, Seasonal recession of Mars' south polar cap as seen by Viking, *J. Geophys. Res.* **84**, 2889-2922, 1979.
- Jones, K.L., R.E. Arvidson, E.A. Guinness, S.L. Bragg, S.D. Wall, C.E. Carlston, and D.G. Pidek, One Mars year: Viking Lander imaging observations, *Science* **204**, 799-806, 1979.
- Joseph, J.H., W.J. Wiscombe, and J.A. Weinman, The delta-Eddington approximation for radiative flux transfer, *J. Atmos. Sci.* **33**, 2452-2459, 1976.

- Kahn, R. and P.J. Gierasch, Analysis of cloud forms from Mars orbiter imaging, Abstracts 4th Annual Meeting of Planet. Atmos. Princ. Investigators, NASA, p. 173, 1982.
- Kahn, R., R. Goody, and J. Pollack, The Martian twilight, *J. Geophys. Res.* **86**, 5833-5838, 1981.
- Kieffer, H.H., Near infrared spectral reflectance of simulated Martian frosts, Ph.D. thesis, California Institute of Technology, 1968.
- Kieffer, H.H., Spectral reflectance of CO₂-H₂O frosts, *J. Geophys. Res.* **75**, 501-509, 1970a.
- Kieffer, H., Interpretation of the Martian polar cap spectra, *J. Geophys. Res.* **75**, 510-514, 1970b.
- Kieffer, H.H., Soil and surface temperatures at the Viking landing sites, *Science* **194**, 1344-1346, 1976.
- Kieffer, H.H., Mars south polar spring and summer temperatures: A residual CO₂ frost, *J. Geophys. Res.* **84**, 8263-8288, 1979.
- Kieffer, H.H., S.C. Chase, E.D. Miner, G. Munch, G. Neugebauer, Preliminary report on infrared radiometric measurements from the Mariner 9 spacecraft, *J. Geophys. Res.* **78**, 4291-4312, 1973.
- Kieffer, H.H., S.C. Chase, Jr., T.Z. Martin, E.D. Miner, F.D. Palluconi, Martian north pole summer temperatures: Dirty water ice, *Science* **194**, 1341-1344, 1976a.
- Kieffer, H.H., S.C. Chase, Jr., E.D. Miner, F.D. Palluconi, G. Munch, G. Neugebauer, T.Z. Martin, Infrared thermal mapping of the Martian surface and atmosphere: First results, *Science* **193**, 780-786, 1976b.
- Kieffer, H.H., P.R. Christensen, T.Z. Martin, E.D. Miner, F.D. Palluconi, Temperatures of the Martian surface and atmosphere: Viking observations of diurnal and geometric variations, *Science* **194**, 1346-1351, 1976c.
- Kieffer, H.H., T.Z. Martin, A.R. Peterfreund, B.M. Jakosky, E.D. Miner, and F.D. Palluconi, Thermal and albedo mapping of Mars during the Viking primary mission, *J. Geophys. Res.* **82**, 4249-4291, 1977.
- Kong, T.Y. and M.B. McElroy, Photochemistry of the Martian atmosphere, *Icarus* **32**, 168-189, 1977.
- Kunde, V.G., Water vapor variations in the atmosphere of Mars from Mariner 9 IRIS, *Bull. Am. Astron. Soc.* **5**, 297, 1973.
- Larson, H.P. and U. Fink, Identification of carbon dioxide frost on the Martian polar cap, *Astrophys. J.* **171**, L91-L95, 1972.
- Leighton, R.B. and B.C. Murray, Behavior of carbon dioxide and other volatiles on Mars, *Science* **153**, 136-144, 1966.
- Leovy, C.B., Exchange of water vapor between the atmosphere and surface of Mars, *Icarus* **18**, 120-125, 1973.
- Leovy, C.B., Observations of Martian tides over two annual cycles, *J. Atmos. Sci.* **38**, 31-39, 1981.
- Leovy, C. and Y. Mintz, Numerical simulation of the atmospheric circulation and climate of Mars, *J. Atmos. Sci.* **26**, 1167-1190, 1969.

- Lindal, G.F., H.B. Hotz, D.N. Sweetnam, Z. Shippony, J.P. Brenkle, G. Hartsell, R.T. Spear, W.H. Michael, Jr., Viking radio occultation measurements of the atmosphere and topography of Mars: Data acquired during 1 Martian year of tracking, *J. Geophys. Res.* **84**, 8443-8456, 1979.
- List, R.J., *Smithsonian Meteorological Tables*, Smithsonian Institution, Washington, D.C., 1951.
- Martin, L.J., North polar hood observations during Martian dust storms, *Icarus* **26**, 341-352, 1975.
- Martin, T.Z., Mean thermal and albedo behavior of the Mars surface and atmosphere over a Martian year, *Icarus*, **45**, 427-446, 1981.
- Martin, T.Z. and H.H. Kieffer, Thermal infrared properties of the Martian atmosphere. 2. The 15 μm band measurements, *J. Geophys. Res.* **84**, 2843-2852, 1979.
- Martin, T.Z., A.R. Peterfreund, E.D. Miner, H.H. Kieffer and G.E. Hunt, Thermal infrared properties of the Martian atmosphere. 1. Global behavior at 7, 9, 11, and 20 μm , *J. Geophys. Res.* **84**, 2830-2842, 1979.
- McCord, T.B., R.L. Huguenin, G. Johnson, Photometric imaging of Mars during the 1973 opposition, *Icarus* **31**, 293-314, 1977.
- McCord, T.B., R.N. Clark, and R.L. Huguenin, Mars: Near-infrared spectral reflectance and compositional implication, *J. Geophys. Res.* **83**, 5433-5441, 1978.
- McCord, T.B., R.N. Clark, and R.B. Singer, Mars: Near-infrared spectral reflectances of surface regions and compositional implications, *J. Geophys. Res.* **87**, 3021-3032, 1982.
- Mooney, R., A.G. Keenan and L.A. Wood, Adsorption of water vapor by montmorillonite. I. Heat of desorption and application of BET theory, *J. Am. Chem. Soc.* **74**, 1367-1371, 1952.
- Moriyama, S. and T. Iwashima, A spectral model of the atmospheric circulation of Mars: A numerical experiment including the effects of the suspended dust and the topography, *J. Geophys. Res.* **85**, 2847-2860, 1980.
- Moroz, V.I., The infrared spectrum of Mars (λ 1.1 - 4.1 μ), *Sov. Astron.* **8**, 273-281, 1964.
- Moroz, V.I., and L.V. Ksamfomaliti, Preliminary results of astrophysical observations of Mars from Mars-3, *Icarus* **17**, 408-422, 1972.
- Muhleman, D.O., Microwave emission from the Moon, in *Thermal Characteristics of the Moon* (J.W. Lucas, ed.), 51-81, MIT Press, Cambridge, Mass., 1972.
- Murray, B.C., W.R. Ward and S.C. Yeung, Periodic insolation variations on Mars, *Science* **180**, 638-640, 1973.
- North, G.R., Theory of energy-balance climate models, *J. Atmos. Sci.* **32**, 2033-2043, 1975.
- Paige, D.A., Annual radiation balance of the Martian polar regions, *Third Int'l. Coll. Mars*, Lunar and Planetary Institute, Houston, Texas, 179-181, 1981.
- Paige, D.A., Radiative properties of the subliming seasonal polar caps of Mars, *Bull. Am. Astron. Soc.*, in press, 1982.

- Palluconi, F.D., and H.H. Kieffer, Thermal inertia mapping of Mars from 60° S to 60° N, *Icarus* **45**, 415-426, 1981.
- Peterfreund, A.R., and H.H. Kieffer, Thermal infrared properties of the Martian atmosphere, 3, Local dust clouds, *J. Geophys. Res.* **84**, 2853-2863, 1979.
- Pimentel, G.C., P.B. Forney, K.C. Herr, Evidence about hydrate and solid water in the Martian surface from the 1969 Mariner infrared spectrometer, *J. Geophys. Res.* **79**, 1623-1634, 1974.
- Pollack, J.B., Climatic change on the terrestrial planets, *Icarus* **37**, 479-553, 1979.
- Pollack, J.B., and Y.L. Yung, Origin and evolution of planetary atmospheres, *Ann. Rev. Earth Planet. Sci.* **8**, 425-487, 1980.
- Pollack, J.B., D. Pitman, B.N. Khare, C. Sagan, Goethite on Mars: A laboratory study of physically and chemically bound water in ferric oxides, *J. Geophys. Res.* **75**, 7480-7490, 1970.
- Pollack, J.B., C.B. Leovy, Y.H. Mintz, and W. Van Camp, Winds on Mars during the Viking season: predictions based on a general circulation model with topography, *Geophys. Res. Lett.* **3**, 479-482, 1976.
- Pollack, J.B., D. Colburn, R. Kahn, J. Hunter, W. Van Camp, C.E. Carlston, and M.R. Wolf, Properties of aerosols in the Martian atmosphere, as inferred from Viking Lander imaging data, *J. Geophys. Res.* **82**, 4479-4496, 1977.
- Pollack, J.B., D.S. Colburn, F.M. Flasar, R. Kahn, C.E. Carlston, and D. Pidek, Properties and effects of dust particles suspended in the Martian atmosphere, *J. Geophys. Res.* **84**, 2929-2945, 1979.
- Pollack, J.B., C.B. Leovy, P.W. Greiman, Y. Mintz, A Martian general circulation experiment with large topography, *J. Atmos. Sci.* **38**, 3-29, 1981.
- Ryan, J.A. and R.D. Sharman, H₂O frost point detection on Mars? *J. Geophys. Res.* **86**, 503-511, 1981.
- Ryan, J.A., R.M. Henry, S.L. Hess, C.B. Leovy, J.E. Tillman, and C. Walcek, Mars meteorology: Three seasons at the surface, *Geophys. Res. Lett.* **5**, 715-718, 1978.
- Sellers, W.D., A climate model based on the energy balance of the Earth-atmosphere system, *J. Appl. Meteor.* **8**, 392-400, 1969.
- Sharman, R.D. and J.A. Ryan, Mars atmosphere pressure periodicities from Viking observations, *J. Atmos. Sci.* **37**, 1994-2001, 1980.
- Sharp, R.P. and M.C. Malin, Channels on Mars, *Geol. Soc. Amer. Bull.* **86**, 593-609, 1975.
- Sinton, W.M., On the composition of Martian surface materials, *Icarus* **6**, 222-228, 1967.
- Slipher, E.C., *The Photographic Story of Mars*, Sky Publishing Corp., Cambridge, MA, 1962.
- Smith, S.A. and B.A. Smith, Diurnal and seasonal behavior of discrete white clouds on Mars, *Icarus* **16**, 509-521, 1972.
- Smythe, W.D., Spectra of hydrate frosts: Their application to the outer solar system, *Icarus* **24**, 421-427, 1975.

- Soderblom, L.A., K. Edwards, E.M. Eliason, E.M. Sanchez, M.P. Charette, Global color variations on the Martian surface, *Icarus* **34**, 446-464, 1978.
- Spinrad, H., G. Munch, L.D. Kaplan, The detection of water vapor on Mars, *Astrophys. J.* **137**, 1319-1321, 1963.
- Tillman, J.E., R.M. Henry, S.L. Hess, Frontal systems during passage of the Martian north polar hood over the Viking Lander 2 site prior to the first 1977 dust storm, *J. Geophys. Res.* **84**, 2947-2955, 1979.
- Toon, O.B., J.B. Pollack and C. Sagan, Physical properties of the particles composing the Martian dust storm of 1971-1972, *Icarus* **30**, 663-696, 1977.
- Toon, O.B., J.B. Pollack, W. Ward, J.A. Burns, K. Bilski, The astronomical theory of climatic change on Mars, *Icarus* **44**, 552-607, 1980.
- Trenberth, K.E., Seasonal variations in global sea level pressure and the total mass of the atmosphere, *J. Geophys. Res.* **86**, 5238-5246, 1981.
- Tull, R.G. and E.S. Barker, Ground-based photoelectric measures of H₂O on Mars during the Mariner 9 encounter, *Bull. Am. Astron. Soc.* **4**, 372, 1972.
- U.S. Geological Survey, Topographic map of Mars, Map I-961, U.S. Geological Survey, Washington, D.C., 1976.
- Wall, S.D., Analysis of condensates formed at the Viking 2 lander site: The first winter, *Icarus*, **47**, 173-183, 1981.
- Ward, W.R., Climatic variations on Mars. I. Astronomical theory of insolation, *J. Geophys. Res.* **79**, 3375-3386, 1974.
- Ward, W.R., Present obliquity oscillations of Mars: Fourth-order accuracy in orbital e and I , *J. Geophys. Res.* **84**, 237-241, 1979.
- Wechsler, A.E. and P.E. Glaser, Pressure effects on postulated lunar materials, *Icarus* **4**, 335-352, 1965.
- Wechsler, A.E., P.E. Glaser, and J.A. Fountain, Thermal properties of granulated materials, in *Thermal Characteristics of the Moon* (J.W. Lucas, ed.), 215-241, MIT Press, Cambridge, Mass., 1972.
- Wiscombe, W.J. and S.G. Warren, A model for the spectral albedo of snow. I: Pure snow, *J. Atmos. Sci.* **37**, 2712-2733, 1980.
- Zisk, S.H. and P.J. Mouginis-Mark, Anomalous region on Mars: Implications for near-surface liquid water, *Nature* **288**, 735-738, 1980.
- Zurek, R.W., Diurnal tide in the Martian atmosphere, *J. Atmos. Sci.* **33**, 321-337, 1976.
- Zurek, R.W., Martian great dust storms: An update, *Icarus*, in press, 1982a.
- Zurek, R.W., manuscript in preparation, 1982b.

Better is the end of a thing than the beginning thereof.

—Ecclesiastes 7:8

The world is round and the place which may seem like the end
may also be only the beginning.

—Ivy Baker Priest